Universidade de Aveiro Departamento de Engenharia Cerâmica e do Vidro
2010

Dmitry Kiselev

Microscopia de Força Piezoeléctrica de Relaxors Ferroelectricos

Piezoresponse Force Microscopy of Ferroelectric Relaxors

Universidade de Aveiro Departamento de Engenharia Cerâmica e do Vidro
2010

Dmitry Kiselev

Microscopia de Força Piezoeléctrica de Relaxors Ferroelectricos

Piezoresponse Force Microscopy of Ferroelectric Relaxors

Dissertação apresentada à Universidade de Aveiro para cumprimento dos requisitos necessários à obtenção do grau de Doutor em Ciência e Engenharia de Materiais, realizada sob a orientação científica do Dr. Andrei Kholkine, Investigador Coordenador do Departamento de Engenharia Cerâmica e do Vidro e do CICECO da Universidade de Aveiro

Dissertation presented to University of Aveiro to obtain the PhD degree in Materials Science and Engineering, under the scientific guidance of Dr. Andrei Kholkine, Research Coordinator of the Department of Ceramics and Glass Engineering and CICECO of the University of Aveiro

I acknowledge the Portuguese Foundation for Science and Technology (FCT) for their financial support through a PhD grant (SFRH/BD/22391/2005)

o júri

presidente

Prof. Amadeu Mortágua Velho da Maia Soares

Professor Catedratico do Departamento de Biologia da Universidade de Aveiro

Prof. Senentxu Lanceros-Méndez

Professor Associado do Departamento de Física da Universidade do Minho

Prof. Dr. Yuriy Genekovich Pogorelov

Professor Associado do Departamento de Fisica da Universidade do Porto

Prof. Dr. Vitor Brás de Sequeira Amaral

Professor Catedratico do Departamento de Fisica da Universidade de Aveiro

Prof. Dr. Maria Elisabete Jorge Vieira Costa

Professora Auxiliar da Universidade de Aveiro

Dr. Andrei Leonidovitch Kholkine

Investigador Coordenador do Departamento de Engenharia Cerâmica e do Vidro da Universidade de Aveiro

acknowledgments

Thinking back to the four years I spent in Aveiro, it is impressive how much people I got to know. Some of them gave a contribution to the work I performed here in Aveiro, many others made me feel at home.
I would like to express my sincere gratitude to my supervisor, Dr. Andrei Kholkine, for his faith, guidance and support throughout the course of my Ph.D research.

I have tremendous respect to Dr. Andrei Kholkine for his knowledge, wisdom and passion for research. I benefited from his guidance in every aspect and step during my Ph.D study, the discussions we held and all those sparking suggestions he made regarding my research, his patience when correcting my papers, proposals and thesis, and his assistance on my preparation for seminar and conference talks. I deeply appreciate all this invaluable help. In addition, he has been always excited about every small step forward I have made. He always made me and other group members feel that we could do anything. This is the exact feeling I have been dreaming to be a materials scientist.

Also, I would like to thank Dr. Igor Bdikin who has given me great help in almost all equipment and facilities setup. He generously shared all its knowledge and experience with experimental PFM techniques. Without its help my research would not be so successful.

I also would like to express my gratitude to the rest of my committee members: Prof. Amadeu Mortágua Velho da Maia Soares, Prof. Senentxu Lanceros-Méndez, Prof. Vitor Amaral, Prof. Yuriy Pogorelov and Prof. Elisabete Costa for their invaluable, insightful comments and suggestions that improved the quality of this work.

I would like to express provided to Dr. Karlis Bormanis (Latvia), Dr. Maria Kozec (Slovenia) (PLZT ceramics), and Dr. P. Rehring (USA) (PZN-4.5%PT single crystals) for the granted samples.

I would also like to acknowledge the contribution of my friends and colleagues from the Department of Ceramics and Glass Engineering for their valuable help, empathy and friendship during all these years, from the administrative and technical staff to all PhD and Posdoc students of the 3rd floor, as well as all the members of Ferroelectric Group.

I also must acknowledge Dr. Andrei Salak and Dr. Nikolai Vyshatko for the help with sample preparation and the experimental part (dielectric measurements) of this work. Moreover, I would like to thanks to Dr. Brahim Dkhil, from the Ecole Centrale Paris, for his useful remarks and suggestions in the discussion of relaxor properties of ceramics and single crystals.

Finally, I greatly acknowledge the financial support PhD fellowship SFRH/BD/22391/2005 from the Fundação para a Ciência e a Tecnologia

The most important acknowledgment was saved for last. I would like to express my gratitude to my Family. They have been constantly providing faith, encourage and enjoyment during my PhD study.

palavras-chave

Microscópia da Força Atómica, materiais ferroeléctricos, properiedades dieléctricas, ferroeléctricas, piezoeléctricas, domíneos, clusters nanopolar, fractal, a evolução do domínio

resumo

Nesta tese, ferroeléctricos relaxor (I dont know uf the order is correct) de base Pb das familias (Pb,La)(Zr,Ti)O_3 (PLZT), $Pb(Mg_{1/3},Nb_{2/3})O_3$-$PbTiO_3$ (PMN-PT), $Pb(Zn_{1/3},Nb_{2/3})O_3$-$PbTiO_3$ (PZN-PT) foram investigados e analisados. As propriedades ferroeléctricas e dieléctricas das amostras foram estudadas por métodos convencionais de macro e localmente por microscopia de força piezoeléctrica (PFM).

Nos cerâmicos PLZT 9.75/65/35 o contraste da PFM à escala nanometrica _ foi investigado em função do tamanho e orientação dos grãos. Apurou-se que a intensidade do sinal piezoeléctrico das nanoestruturas diminui com o aumento da temperatura e desaparece a 490 K (La mol. 8%) e 420 K (9,5%). Os ciclos de histerese locais foram obtidos em função da temperatura. A evolução dos parâmetros macroscópicos e locais com a temperatura de superfície sugere um forte efeito de superfície nas transições de fase ferroeléctricas do material investigado. A rugosidade da parede de domínio é determinada por PFM para a estrutura de domínio natural existente neste ferroeléctrico policristalino. Além disso, os domínios ferroeléctricos artificiais foram criados pela aplicação de pulsos eléctricos à ponta do condutor PFM e o tamanho de domínio *in-plane* foi medido em função da duração do pulso. Todas estas experiências levaram à conclusão de que a parede de domínio em relaxors do tipo PZT é quase uma interface unidimensional. O mecanismo de contraste na superfície de relaxors do tipo PLZT é medido por PFM

As estruturas de domínio versus evolução da profundidade foram estudadas em cristais PZN-4,5%PT, com diferentes orientações através da PFM. Padrões de domínio irregulares com tamanhos típicos de 20-100 nm foram observados nas superfícies com orientação <001> das amostras unpoled?. Pelo contrário, os cortes de cristal <111> exibem domínios regulares de tamanho mícron normal, com os limites do domínio orientados ao longo dos planos cristalográficos permitidos. A existência de nanodomínios em cristais com orientação <001> está provisoriamente (wrong Word) atribuída à natureza relaxor de PZN-PT, onde pequenos grupos polares podem formar-se em coindições de zero-field-cooling (ZFC). Estes nanodomínios são considerados como os núcleos do estado de polarização oposta e podem ser responsáveis pelo menor campo coercitivo para este corte de cristal em particular. No entanto, a histerese local piezoelétrica realizada pelo PFM à escala nanométrica indica uma mudança de comportamento de PZN-PT semelhante para ambas as orientações cristalográficas investigadas. A evolução das estruturas de domínio com polimento abaixo da superfície do cristal foi investigada. O domínio de ramificações e os efeitos de polarização de triagem após o polimento e as medições de temperatura têm sido estudados pela PFM e pela análise SEM. Além disso, verificou-se que a intensidade do sinal piezoeléctrico a partir das estruturas de nanodomínio diminui com o aumento da temperatura, acabando por desaparecer aos 430 K (orientaçáo <111>) e 470 K (orientação <100>). Esta diferença de temperatura nas transições de fase local em cristais de diferentes orientações é explicada pelo forte efeito de superfície na transição da fase ferroelétrica em relaxors.

A comutação da polarização em relaxor ergódico e nas fases ferroeléctricas do sistema PMN-PT foram realizadas pela combinação de três métodos, Microscopia de Força Piezoeléctrica, medição de um único ponto de relaxamento eletromecânico e por ultimo mapeamento de espectroscopia de tensão. A dependência do comportamento do relaxamento na amplitude e tempo da tensão de pulso foi encontrada para seguir um comportamento logarítmico universal com uma inclinação quase constante. Este comportamento é indicativo da progressiva população dos estados de relaxamento lento, ao contrário de uma relaxação linear na presença de uma ampla distribuição do tempo de relaxamento. O papel do comportamento de relaxamento, da não-linearidade ferroeléctrica e da heterogeneidade espacial do campo na ponta da sonda de AFM sobre o comportamento do ciclo de histerese é analisada em detalhe. Os ciclos de histerese para ergódica PMN-10%PT são mostrados como cineticamente limitados, enquanto que no PMN, com maior teor de PT, são observados verdadeiros ciclos de histerese ferroeléctrica com viés de baixa nucleação.

keywords

Piezoelectricity, Ferroelectricity, Relaxors, PLZT ceramics, PZN-PT single crystals, PFM, domain, nanopolar clusters, fractal, domain evolution, piezoelectric loops, relaxation

abstract

In this thesis, Pb-based relaxor ferroelectrics of the $(Pb,La)(Zr,Ti)O_3$ (PLZT), $Pb(Mg_{1/3},Nb_{2/3})O_3$-$PbTiO_3$ (PMN-PT), $Pb(Zn_{1/3},Nb_{2/3})O_3$-$PbTiO_3$ (PZN-PT) families were investigated and analyzed. Ferroelectric and dielectric properties of the samples were studied by conventional macroscopic methods and locally by piezoresponse force microscopy (PFM).

In PLZT 9.75/65/35 ceramics the nanoscale PFM contrast was investigated as a function of grain size and grain orientation. It was found that the intensity of piezoresponse signal from nanodomain structure decreases with temperature and it disappears at 490 K (La mol. 8%) and 420 K (9.5%). Local hysteresis loops were obtained as a function of temperature. The evolution of the macroscopic and local parameters with temperature suggests strong surface effect on ferroelectric phase transition in the investigated materials. The domain wall roughness is determined with PFM for the natural domain structure existing in this polycrystalline ferroelectric. Besides, artificial ferroelectric domains were created by application of voltage pulses to the conducting PFM tip, and the in-plane domain size was measured as a function of pulse duration. All these experiments result in the conclusion that the domain wall in PZT-type relaxors is quasi one-dimensional interface. The mechanism of the surface contrast in PLZT-type relaxors is uncovered by PFM.

Domain structures vs. depth evolution was studied in PZN-4.5%PT crystals with different orientation via PFM. Irregular domain patterns with the typical sizes 20-100 nm were observed on the (001)-oriented surfaces of unpoled samples. On the contrary, (111) crystal cuts exhibit normal micron-size regular domains with the domain boundaries directed along allowed crystallographic planes. The existence of nanodomains in (001)-oriented crystals is tentatively attributed to the relaxor nature of PZN-PT where small polar clusters may form under zero-field-cooling (ZFC) conditions. These nanodomains are considered as the nuclei of the opposite polarization state and can be responsible for the smaller coercive field for this particular crystal cut. However, local piezoelectric hysteresis performed by PFM on the nanometer scale indicates similar switching behavior of PZN-PT for both investigated crystallographic orientations. Evolution of the domain structures with polishing below the crystal surface has been investigated. The domain branching and polarization screening effects after polishing and temperatures measurements have been studied by PFM and SEM analysis. In addition, it was found what the intensity of piezoresponse signal from nanodomain structures decreases with temperature and finally disappears at 430 K (<111> orientation) and 470 K (<100> orientation). This difference of the temperature of local phase transitions for crystals of different orientaions is explained by strong surface effect on ferroelectric phase transition in relaxors.

Polarization switching in ergodic relaxor and ferroelectric phases in the PMN-PT system is studied using Piezoresponse Force Microscopy, single point electromechanical relaxation measurements, and voltage spectroscopy mapping. The dependence of relaxation behavior on voltage pulse amplitude and time was found to follow a universal logarithmic behavior with a nearly constant slope. This behavior is indicative of the progressive population of slow relaxation states, as opposed to a linear relaxation in the presence of a broad relaxation time distribution. The role of relaxation behavior, ferroelectric non-linearity, and the spatial inhomogeneity of the tip field on hysteresis loop behavior is analyzed in detail. The hysteresis loops for ergodic PMN-10%PT are shown to be kinetically limited, while in PMN with larger PT content, true ferroelectric hysteresis loops with low nucleation biases are observed.

Natura sic voluit

Dmitry Kiselev

Piezoresponse Force Microscopy of Ferroelectric Relaxors

Table of Contents

List of Common Abbreviations and Symbols

FeRAM	Ferroelectric Random Access Memory
DRAM	Dynamic Random Access Memory
MEMs	Miniaturized Electromechanical Systems
SPM	Scanning Probe Microscope
AFM	Atomic Force Microscope
RROC	Apex radius of AFM tip
TM-AFM	Tapping Mode AFM
SSPM	Scanning Surface Potential Microscopy
C-AFM	Conductive AFM
PFM	Piezoresponse Force Microscopy
VPFM	Vertical Piezoresponse Force Microscopy
LPFM	Lateral Piezoresponse Force Microscopy
PFS	Piezoresponse Force Spectroscopy
TM	Tapping Mode
PR_{phase}	Piezoresponse Phase
$PR_{amplitude}$	Piezoresponse Amplitude
LA	Lock-in Amplifier
PSD	Phase Sensitive Detector
TEM	Transmission Electron Microscopy
NMR	Nuclear Magnetic Resonance
PLM	Polarized Light Microscopy
SEM	Scanning Electron Microscopy
R	Rhombohedral Phase
T	Tetragonal Phase
M	Monoclinic Phase
O	Orthorhombic Phase
C	Cubic Phase

M_A, M_B, M_C	Monoclinic phases
HR-XRD	High-Resolution synchrotron X-ray Diffraction
XRD	X-ray diffraction
ZFH	Zero-field-heating
ZFC	Zero-field-cooling
MPB	Morphotropic Phase Boundary
PMN-*x*PT	Lead Magnesium Niobate-Lead Titanate - (1-x)$Pb(Mg_{1/3}Nb_{2/3})O_3$-*x*$PbTiO_3$, "x" is the PT-content usually in mol. %; where it is given as an absolute fraction, the inferred value should be clear.
PZN-*x*PT	Lead Zinc Niobate-Lead Titanate - (1-*x*)$Pb(Zn_{1/3}Nb_{2/3})O_3$-*x*$PbTiO_3$
PZT	Lead Zirconate Titanate - $Pb(Zr,Ti)O_3$
PTO	Lead Ttitanate - $PbTiO_3$
PLZT	Lead Lanthanum Zirconate Titanate - $(Pb,La)(Zr,Ti)O_3$
FE	Ferroelectric Phase
PE	Paraelectric Phase
AFE	Anti-Ferroelectric Phase
RFE	Relaxor Ferroelectrics
DW	Domain Wall
AC	Alternative Current
DC	Direct Current
FTT	Fast Furie Transformation
KWW	Kolrausch-Williams-Watts
SRBRF	Spherical Random Bond Random Field Model
PNR	Polar Nanoregions
WKG	Westphal-Kleemann-Glinchuk Model
LGD	Landau-Ginzburg-Devonshire Thermodynamic Theory
P-E	Polarization-Electric Field
D_i	Electric Displacement

ε_0	Dielectric Permittivity of the Vacuum (8.85×10^{-12} F/m)
ε_{ij}	Dielectric Permittivity
ε''	Imaginary Part of the Permittivity
ε'	Real Part of the Permittivity
ε_{max}	Maximum of the Permittivity
χ'	Dielectric Susceptibility
d	Characteristic Wave Vector of the Domain
a, b, c	Unit Cell Parameters
β, γ, δ	Constants
k_{33}	Electromechanical Coupling Factor
V	Volume of the Unit Cell
hkl	Miller Indexes
d_{hkl}	Spacing between Atomic Planes
G	Gibbs' Free Energy
P_i	Total Polarization
P_R	Remanent Polarization
P_S	Spontaneous Polarization
E	Electric Field
E_C	Coercive Field
T_f	Freezing Temperature
T_B	Burns Temperature
T_0	Curie-Weiss Temperature
T^*	Intermediate Temperature
T_C	Curie Temperature
T_{C1}	Temperature of Rhombohedral Phase Transition
T_{C2}	Temperature of Tetragonal Phase Transition
T_m	Temperature of Peak Permittivity
ΔT	Temperature Change
σ_{ij}	Stress

d_{ijk}	Piezoelectric Coefficients
v	Poisson's Ratio
δ_{ij}	Kronecker Delta
α	Angle of Poling Direction between the [001] and [111] Crystallographic Orientations
α_{ij}	Coefficient of Thermal Expansion
ξ	Correlation Function
χ'	Dielectric Susceptibility
n	Refractive Index
ζ	Roughness of the Domain Wall
μ	Dynamic Exponent
tanδ	Tangent of the Loss Angle
V	Voltage
U_A	Activation Energy
W_e	Elastic Energy
ω	Frequency
C_p	Capacitance of a Parallel Plane Capacitor
R	Parallel Resistance
C_o	Linear Capacitor (~1 μF)
C_x	Ferroelectric Material Capacitor
A	Area of the Electrodes
τ	Relaxation (aging) Time
b, t_0	Parameters
Δt	Time Needed for a Single Scan
F_{con}	Contact Force
σ_i	Surface Charge Density
Φ	Phase
X, Y, Z	Directions
Z_e	Ellipsoidal Ring

Z_c	Central Peak
Z_0	Position-Independent Offset
ε_i	Eccentricities
φ	Rotation Angle
H	Hamiltomian
S_i	Order Parameter
J_{ij}	Random Bond Interaction
h_i	Random Local Electric Field
g	Local Field Factor
N	Number of Polar Clusters
[…]	Direction
$\langle ... \rangle$	Equivalents directions
(…)	Plane
↔	Phase Transition

Introduction

Disordered systems including magnetic spin and cluster glasses [1], ferroelastic martensites [2], dipolar and quadrupolar glasses [3], ferroelectric relaxors [1], structural glasses [4], as well as more exotic matter such as vortex lattices in superconductors [5] have been under extensive theoretical and experimental research for the last 5 decades. This interest is precipitated by the unique properties emerging as the results of disorder interaction with order parameter, including high magnetic and electromechanical coupling constants, tunability of dielectric and magnetic responses, as well as unique memory effects. By now, many of theoretical concepts formulated on the quest to understand the physics of disordered systems, such as Edwards-Anderson models for spin glasses [2] and spherical random bond-random field model for relaxors [6] have become the bedrock of statistical physics.

Ferroelectric relaxors are a prototypical example of disordered ferroic systems. These materials have been originally discovered by Smolensky and co-workers in 1954 [7,8] and were initially believed to undergo unusual *diffuse* phase transitions associated with the broad and frequency dispersive variations of dielectric permittivity as a function of temperature. The origins of these behaviors were traced to the presence of *polar nanoregions* (PNRs) of 1-5 nm size [9], the dynamics of which underpins fascinating relaxor properties. The resurgence of interests to relaxors in the last decades is largely related to applications, e.g., ultrasonic medical and underwater imaging [10, 11], actuators and optical elements [12], as well as to emergent theoretical concepts [13]. Relaxors have been extensively studied using macroscopic time-resolved spectroscopies, including a broad range of phenomena from non-exponential relaxations common for disordered systems [14], to complex dynamic phenomena such as spectral hole burning [15] and memory effects [16]. Significant progress in atomistic understanding of relaxors has been achieved using model Hamiltonian, density-functional theory [17], and optical [18], neutron [19] and x-ray scattering [20]. Despite the progress, many aspects of mesoscopic relaxor physics are still unresolved, including the existence and nature of order parameter, the mechanisms of PNR reorientation, and the details of bias- and temperature-induced phase transitions.

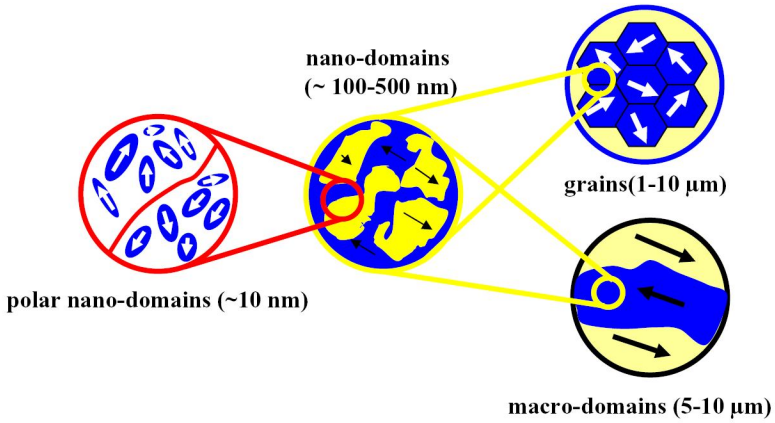

Figure 1. Proposed hierarchy of length scales in ferroelectric relaxors.

The behavior of ferroelectric materials is governed by complex multiscale phenomena where hierarchy of the domain states is typically observed. This is especially complicated in relaxors where at least three levels of domain states have been discovered [21, 22, 23, 24]. The upper scale is determined by the macroscopic grains in ceramics [25] or micron-sized regular domains in ferroelectric-relaxor solid solutions with high concentration of ferroelectric component [21] (Figure 1). Below this level, nanoscale (10-150 nm) random domains were found and they reflect the polar inhomogeneity that is the main feature of relaxors. And finally, the smallest rotatable unit, PNRs should exist in these material but these were only evaluated by scattering techniques or modeling.

It is therefore necessary to understand and to control the domain states in relaxors that are directly related to their performance as sensors and actuators. As is seen in the increasing number of publications in this field during the past decade, nanoscale investigation of ferroelectric properties of thin films and bulk ceramics from micron to nanoscales has gained high importance but these were rarely applied to ferroelectric relaxors. In this regard, *piezoresponse force microscopy* (PFM) is a powerful tool for investigating properties of ferroelectric relaxors at the nanoscale. PFM is a scanning probe technique based on the converse piezoelectric effect that is present in all ferroelectric materials. This technique allows both the detection and the modification of the ferroelectric states (using the same experimental setup) with a resolution down to 10 nm.

The invention of the PFM in the mid-90ies was the transformative change in capability of probing electromechanically coupling on the nanoscale. The first measurements of bias-induced strains in piezoelectric materials by a scanning probe came in 1991 based on scanning acoustic microscopy [26] and STM [27]. Piezoelectric measurement [28] and ferroelectric domain visualization [29,30] by atomic force microcopy were reported in 1992-1994. Papers by Takata *et al* [31,32] (strain imaging via tunneling acoustic microscopy), Franke *et al* [33], Kolosov *et al* [34], Gruverman *et al* [35,36], and Hidaka *et al.* [37] followed in 1994-1997. The early imaging applications were the harbinger of current advances in PFM-based probes, ranging from ferroelectrics and multiferroic [38,39,40] to III-V nitrides [41,42] to polymers [43,44,45,46,47], and biological systems [48,49,50,51], and recently to strongly correlated oxides [52,53] and energy storage and conversion materials. The development of fast PFM imaging [54,55] and spectral imaging modes [56,57,58,59] holds promise for probing polarization states in relaxors, and, their evolution with temperature and dc field.

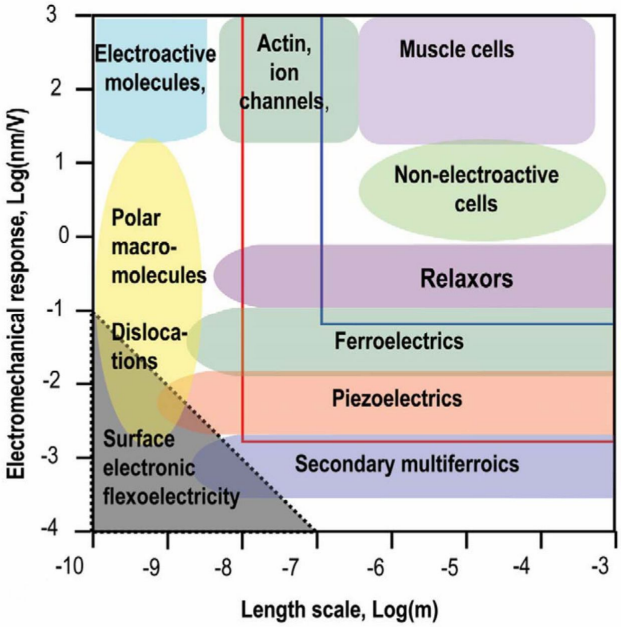

Figure 2. Electromechanical response roadmap depicting the relationship between length scale and system response. The blue and red lines correspond to areas accessible by nanoindentation and scanning probe microscopy, respectively [60].

The roadmap in Figure 2 illustrates the sensitivity and length scales for electromechanical phenomena associated with bias-induced transformations, as well as presents limits of PFM and piezoelectric nanoindentation measurements. Note that a broad spectrum of phenomena will become accessible with a 1–1.5 order of magnitude increase in resolution and ~1–2 order of magnitude increase in sensitivity, providing a clear perspective for technique development. The individual challenges on this pathway are (a) technique development to increase resolution, selectivity and sensitivity; (b) atomistic control of environment; (c) identifying appropriate material and defect systems; and (d) theory.

It can be thus stated that relaxors materials where *several hierarchical domain states* (from nm to tens of μm) typically exist present a unique object for PFM since their rich physical phenomena can be conveniently accessed via PFM. Relaxors have many features useful for applications which mechanism is still not understood – high dielectric constant, giant piezocoefficient, and hysteresis less strain. It is believed that all these can be analyzed and explained with the help of PFM which is the best technique for studying polarization at the nanoscale. Therefore, the primary focus of this research was to investigate the nanoscale properties of major Pb-based relaxor families including single crystals $Pb(Mg_{1/3}Nb_{2/3})O_3$ (PMN), $(1-x)Pb(Mg_{1/3}Nb_{2/3})O_3$-$xPbTiO_3$ (PMN-xPT) and $(1-x)Pb(Zn_{1/3}Nb_{2/3})O_3$-$xPbTiO_3$ (PZN-xPT), and polycrystalline ceramics $(Pb,La)(Zr,Ti)O_3$ (PLZT) via various AFM/PFM techniques combined with the macroscopic studies such as dielectric behavior and polarization hysteresis loops.

The present thesis is organized in five chapters. *Chapter 1* is dedicated to literature review aiming at introducing the reader to the state-of-art in respect to following issues: the fundamentals of the piezoelectric and ferroelectric phenomena, description of the related PFM technique and relevant prior research on relaxor ferroelectric crystals and ceramics, their domain structure, crystalline phase states of the materials and possible phase transition, are reviewed.

The experimental setup for the processing and characterization, including PLZT ceramics and PZN-xPT single crystals growth and characterization as well as *atomic force microscopy* (AFM) ferroelectric domain writing and imaging techniques are described in *Chapter 2*.

The obtained results are presented, analyzed and discussed in the next two chapters. In *Chapter 3*, the results regarding the study of relaxor PLZT ceramics are discussed. Structural, dielectric, ferroelectric and piezoelectric characterization data are used to describe the PLZT x/65/35 ceramics, with La concentration ranging from 5 to 11 %. With increasing La concentration, an evolution of macro-domains → micron-domains → PND (polar nano domains) → PNR was found. The PLZT ceramics with high concentration of La (>9at.%) preserve the domain contrast at the nanoscale, even if the macroscopic properties do not exhibit any ferroelectricity. Random network of maze nanopolar patterns is a direct consequence of La-induced disorder and have to be investigated as a function of temperature in order to observe the freezing of polar nanoclusters.

In contrast, *Chapter 4* reports on the experimental investigation of the nanoscale properties of the PZN-xPT, PMN and PMN-xPT relaxor single crystals at different orientation cuts under different temperature. Irregular domain patterns with the typical sizes 20-100 nm were observed on the (001)-oriented surfaces of unpoled samples. On the contrary, (111) crystal cuts exhibit normal micron-size regular domains with the domain boundaries directed along allowed crystallographic planes. The existence of nanodomains in (001)-oriented crystals is tentatively attributed to the relaxor nature of PZN-PT where small polar clusters may form under zero-field-cooling (ZFC) conditions. The PFM imaging indicates the presence of labyrinthine domain structures even in ergodic PMN-10%PT compositions, indicative of a non-cubic symmetry at least in the surface layer. In PMN-35%PT, ferroelectric domains with high wall roughness are observed, whereas PMN-32%PT demonstrates the coexistence of ferroelectric and labyrinthine domains. The comparison of vertical and lateral PFM suggests that the observed in-plane contrast can be ascribed purely to cross-talk between vertical and lateral signals, and no evidence for in-plane domains is obtained. It is shown that local hysteresis loops in relaxors are fundamentally different form those in ferroelectrics. In relaxors (PMN-10%PT), the local loops are kinetically limited, while in “normal” ferroelectrics (PMN-32%PT and PMN-35%PT) the loops seem to be dominated by the spatial dispersion of the polarization only.

The last Chapter of this thesis is to list the general conclusions of the present work and to outline some future work for complementing it.

References

[1] Binder K. and Young A.P., "Spin glasses: Experimental facts, theoretical concepts, and open questions" *Rev. Mod. Phys*. **58**, 801 (1986).

[2] V. Wadhawan, *Introduction to Ferroic Materials*, CRC Press (2000).

[3] Kleemann W.," Random-field induced antiferromagnetic, ferroelectric and structural domain states" *Int. J. Mod. Phys*. **7**, 2469 (1993).

[4] Angell C.A., "Perspective on the glass transition" *J. Phys. Chem. Solids* **49**, 863 (1988).

[5] Blatter G., Feigelman M.V., Geshkenbein V.B., Larkin A.I., and Vinokur V. M., "Vortices in high-temperature superconductors" *Rev. Mod. Phys*. **66**, 1125 (1994).

[6] Pirc R. and Blinc R., "Spherical random-bond–random-field model of relaxor ferroelectrics" *Phys. Rev. B* **60**, 13470 (1999).

[7] a) Smolensky G. A. and Isupov V. A., *Sov. Phys. Tech. Phys* 1954, *24*, 1375. b) Smolensky G. A. and Agranovskaya A. I., *Sov. Phys. Tech. Phys.* 1958, *3*, 1380.

[8] Smolensky G. A., Bokov V. A., Isupov V. A., Krainik N. N., Pasynkov R. E., Sokolov A. I., Yushin N. K. *Ferroelectrics and Related Materials*, Gordon and Breach, NY, (1981).

[9] Burns G. and Dacol F.H., "Crystalline ferroelectrics with glassy polarization behavior" *Phys. Rev. B*, 28, 2527 (1983).

[10] Cross L. E., in *Ferroelectric Ceramics* (eds. N. Setter and E. Colla), Birkhausen, Berlin, (1993).

[11] Bokov A. A. and Ye Z.-G., "Recent progress in relaxor ferroelectrics with perovskite structure" *J. Mat. Sci*. **41**, 31 (2006).

[12] Waser R. (ed.), Nanoelectronics and Information Technology: Advanced Electronic Materials and Novel Devices. Wiley-VCH, Berlin, (2005).

[13] Kutnjak Z., Petzelt J., and Blinc R., "The giant electromechanical response in ferroelectric relaxors as a critical phenomenon" *Nature* **441**, 956 (2006).

[14] Jonscher A.K., *Dielectric Relaxation in Solids*, Chelsea Dielectric Press, (1983).

[15] Kircher O., Schiener B., and Bohmer R., "Long-lived dynamic heterogeneity in a relaxor ferroelectric" *Phys. Rev. Lett.* **81**, 4520 (1998).

[16] G.Y. Xu, P.M. Gehring, and G Shirane, "Persistence and memory of polar nanoregions in a ferroelectric relaxor under an electric field" *Phys. Rev. B* **72**, 214106 (2005).

[17] Grinberg I., Shin Y.H., and Rappe A. M., "Molecular dynamics study of dielectric response in a relaxor ferroelectric" *Phys. Rev. Lett.* **103**, 197601 (2009).

[18] Toulouse J., Jiang F., Svitelskiy O., Chen W., and Ye Z.G., "Temperature evolution of the relaxor dynamics in $Pb(Zn_{1/3}Nb_{2/3})O_3$: A critical Raman analysis", *Phys. Rev. B* **72**, 184106 (2005).

[19] Matsuura M., Hirota K., Gehring P.M., Ye Z.G., Chen W., and Shirane G., "Composition dependence of the diffuse scattering in the relaxor ferroelectric compound $(1-x)Pb(Mg_{1/3}Nb_{2/3})O_3-xPbTiO_3$ ($0\leq x\leq 0.40$)" *Phys. Rev. B*, **74**, 144107 (2006**)**.

[20] Egami T., "Local Structure of Ferroelectric Materials" *Annu. Rev. Mater. Res*.**37**, 297 (2007) and references therein.

[21] Lehnen P., Kleemann W., Woike Th., Pankrath R. "Ferroelectric nanodomains in the uniaxial relaxor system $Sr_{0.61}À_xBa_{0.39}Nb_2O_6:Ce_x\ 3^{+}$" *Phys. Rev. B*, **64**, 224109 (2001).

[22] Bdikin I. K., Shvartsman V. V., and Kholkin A. L. "Nanoscale domains and local piezoelectric hysteresis in $Pb(Zn_{1/3}Nb_{2/3})O_3$-4.5%$PbTiO_3$ single crystals" *Appl. Phys. Lett.* **83**, 4232 (2003).

[23] Shvartsman V. V. and Kholkin A. L., "Domain structure of $0.8Pb(Mg_{1/3}Nb_{2/3})O_3$-$0.2PbTiO_3$ studied by piezoresponse force microscopy" *Phys. Rev. B* **69**, 014102 (2004).

[24] Vakhrushev S. B., Naberezhnov A. A., Dkhil B., Kiat J.-M., Shvartsman V., Kholkin A., Dorner B., and Ivanov A. In Fundamental Physics of Ferroelectrics 2003, Williamsburg, VA, USA, 2003, edited by P. K. Davies and D. J. Singh, AIP Conf. Proc. No. **677**, 74(AIP, Melville, NY, 2003).

[25] Shvartsman V. V., Kholkin A. L., Orlova A., Kiselev D., Bogomolov A. A., and Sternberg A, "Polar nanodomains and local ferroelectric phenomena in relaxor lead lanthanum zirconate titanate ceramics " *Appl. Phys. Lett.* **86**, 202907 (2005).

[26] Güthner P., Glatz-Reichenbach J. and Dransfeld K., "Investigation of local piezoelectric properties of thin copolymer films" *J. Appl. Phys*. **69**, 7895 (1991).

[27] Birk H., Glatz-Reichenbach J., Jie L., Schreck E., and Dransfeld K, "The local piezoelectric activity of thin polymer films observed by scanning tunneling microscopy" *J. Vac. Sci. Technol*. *B* **9**, 1162 (1991).

[28] Güthner P. and Dransfeld K., „Local poling of ferroelectric polymers by scanning force microscopy" *Appl. Phys. Lett.* **61**, 1137 (1992).

[29] Luthi R., Haefke H., Grütter P., Güntherodt H-J., Szcześniak L., and Meyer K.P.. "Surface and domain structures of ferroelectric GASH crystals studied by scanning force microscopy" *Surf. Sci. Lett.* **285**, L498 (1993).

[30] Bae M. K., Horiuchi T., Hara K., Ishibashi Y., and Matsushige K., "Direct observation of domain structures in triglycine sulfate by atomic force microscope" *Jpn. J. Appl. Phys.,* Part 1 **33,** 1390 (1994).

[31] Takata K., Kushida K., Torii K., and Miki H.,"Strain imaging of lead-zirconate-titanate thin film by tunneling acoustic microscopy", *Jpn. J. Appl. Phys.,* Part 1 **33,** 3193 (1994).

[32] Takata K., " Strain-imaging observation of a $Pb(Zr,Ti)O_3$ thin film" *J. Vac. Sci. Technol. B* **14,** 882 (1996).

[33] Franke K., Besold J., Haessler W., and Seegebarth C., "Modification and detection of domains on ferroelectric PZT films by scanning force microscopy" *Surf. Sci. Lett.* **302,** L283 (1994).

[34] Kolosov O., Gruverman A., Hatano J., Takahashi K., and Tokumoto H., "Nanoscale Visualization and Control of Ferroelectric Domains by Atomic Force Microscopy" *Phys. Rev. Lett.* **74**, 4309 (1995).

[35] Gruverman A., Kolosov O., Hatano J., Takahashi K., and Tokumoto H.," Domain structure and polarization reversal in ferroelectrics studied by atomic force microscopy" *J. Vac. Sci. & Technol. B* **13,** 1095 (1995).

[36] Gruverman A., Auciello O., and Tokumoto H., "Nanoscale investigation of fatigue effects in Pb(Zr,Ti)O3 films" *Appl. Phys. Lett.* **69,** 3191 (1996).

[37] Hidaka T., Maruyama T., Sakai I., Saitoh M., Wills L. A., Hiskes R., Dicarolis S. A., and Amano J., " Characteristics of PZT thin films as ultra-high density recording media" *Integr. Ferroelectr.* **17,** 319 (1997).

[38] *Scanning Probe Microscopy of Electrical and Electromechanical Phenomena at the Nanoscale,* edited by S. V. Kalinin and A. Gruverman (Springer, Berlin, 2007).

[39] *Nanoscale Characterization of Ferroelectric Materials: Scanning Probe Microscopy Approach,* edited by M. Alexe and A. Gruverman (Springer, Berlin, 2004).

[40] *Nanoscale Phenomena in Ferroelectric Thin Films,* edited by S. Hong (Kluwer, Dordrecht, 2004).

[41] Rodriguez B. J., Gruverman A., Kingon A. I., Nemanich R. J., and Ambacher O., "Piezoresponse force microscopy for polarity imaging of GaN" *Appl. Phys. Lett.* **80**, 4166 (2002).

[42] Stoica T., Calarco R., Meijers R., and Lüth H., "Nanoscale imaging of surface piezoresponse on GaN epitaxial layers" *Appl. Surf. Sci*. **253,** 4300 (2007).

[43] Rodriguez B. J., Jesse S., Kalinin S. V., Kim J., Ducharme S., and Fridkin V.," Nanoscale polarization manipulation and imaging of ferroelectric Langmuir-Blodgett polymer films" *Appl. Phys. Lett.* **90,** 122904 (2007).

[44] Matsushige K., Yamada H., Tanaka H., Horiuchi T., and Chen X. Q., "Nanoscale control and detection of electric dipoles in organic molecules" *Nanotechnology* **9,** 208 (1998).

[45] Kimura K., Kobayashi K., Yamada H., Horichi T., Ishida K., and Matsushige K., "Orientation control of poly(vinylidenefluoride-trifluoroethylene) crystals and molecules using atomic force microscopy" *Appl. Phys. Lett.* **82,** 4050 (2003).

[46] Gysel R., Stolichnov I., Tagantsev A. K., Setter N., and Mokrý P., "Restricted domain growth and polarization reversal kinetics in ferroelectric polymer thin films" *J. Appl. Phys.* **103**, 084120 (2008).

[47] Gaynutdinov R. V., Lysova O. A., Tolstikhina A. L., Yudin S. G., Fridkin V. M., and Ducharme S., "Polarization switching kinetics at the nanoscale in ferroelectric copolymer Langmuir–Blodgett films" *Appl. Phys. Lett.* **92,** 172902 (2008).

[48] Halperin C., Mutchnik S., Agronin A., Molotskii M., Urenski P., Salai M., and Rosenman G., "Piezoelectric effect in human bones studied in nanometer scale" *Nano Lett.* **4,** 1253 (2004).

[49] Kalinin S. V., Rodriguez B. J., Jesse S., Thundat T., and Gruverman A., "Electromechanical imaging of biological systems with sub-10 nm resolution" *Appl. Phys. Lett.* **87,** 053901 (2005).

[50] Minary-Jolandan M. and Yu M-F, "Nanoscale characterization of isolated individual type I collagen fibrils: polarization and piezoelectricity" *Nanotechnology* **20,** 085706 (2009).

[51] Binetti V. R., Schiffman J. D., Leaffer O. D., Spanier J. E., and Schauer C. L., "The natural transparency and piezoelectric response of the Greta oto butterfly wing" *Integr. Biol.* **1**, 324 (2009).

[52] Mamin R. F., Bdikin I. K., and Kholkin A. L., "Locally induced charged states in La0.89Sr0.11MnO3 single crystals" *Appl. Phys. Lett.* **94**, 222901 (2009).

[53] Kholkin A., Bdikin I., Ostapchuk T., and Petzelt J., "Room temperature surface piezoelectricity in $SrTiO_3$ ceramics via piezoresponse force microscopy" *Appl. Phys. Lett.* **93**, 222905 (2008).

[54] Nath R., Chu Y. H., Polomoff N. A., Ramesh R., and Huey B. D., "High speed piezoresponse force microscopy: <1 frame per second nanoscale imaging" *Appl. Phys. Lett.* **93**, 072905 (2008).

[55] Polomoff N. A., Premnath R. N., Bosse J. L., and Huey B. D., "Ferroelectric domain switching dynamics with combined 20 nm and 10 ns resolution" *J. Mat. Sci.* **44**, 5189 (2009).

[56] Jesse S., Lee H. N., and Kalinin S. V., "Quantitative mapping of switching behavior in piezoresponse force microscopy" *Rev. Sci. Instrum.* **77**, 073702 (2006).

[57] Jesse S., Rodriguez B. J., Choudhury S., Baddorf A .P., Vrejoiu I., Hesse D., Alexe M., Eliseev E. A., Morozovska A. N., Zhang J., Chen L. Q., and Kalinin S. V. *Nature Mater.* **7**, 209 (2008).

[58] Kalinin S. V., Jesse S., Rodriguez B. J., Chu Y. H., Ramesh R., Eliseev E. A., and Morozovska A. N., "Probing the role of single defects on the thermodynamics of electric-field induced phase transitions" *Phys. Rev. Lett.* **100,** 155703 (2008).

[59] Ovchinnikov O., Jesse S., Guo S., Seal K., Bintachitt P., Fujii I., Trolier-McKinstry S., and Kalinin S. V., " Local measurements of Preisach density in polycrystalline ferroelectric capacitors using piezoresponse force spectroscopy" *Appl. Phys. Lett.* **96**, 112906 (2010).

[60] Kalinin S.V., Rodriguez B. J., Jesse S., Maksymovych P., Seal K., Baddorf A. P., Kholkin A., Proksch R., "Local bias-induced phase transitions" *Materials Today* **11**, 16 (2008).

Chapter 1

Background on Ferroelectric Materials

Fundamentals

It is the purpose of this Chapter to provide a brief description of the ferroelectric and piezoelectric phenomena in ferroelectrics and related materials for electronic and memory applications. Firstly, the fundamental issues associated with the ferroelectric phenomena such as phase transitions, appearance of domains, and switching of polarization vector will be outlined, followed by a brief description of the basic physical properties and structures of common ferroelectric materials including relaxors. A short introduction to the scanning probe techniques, especially Piezoresponse Force Microscopy, will be also given.

§1.1 Piezoelectric Materials

Discovery of the Piezoelectric Effect

The piezoelectric effect (surface charge from mechanical pressure) was discovered in 1880 by the Curie brothers, Pierre and Jacques. Since then, piezoelectricity has been found in many naturally occurring materials such as tourmaline, quartz, topaz, cane sugar, and Rochelle salt. The Curie brothers experimentally discovered that a surface charge could be measured when a mechanical stress was applied to certain crystals that had been given a surface treatment. The brothers also discovered that there was a relationship between temperature and surface charge intensity. The Curie brothers, however, did not predict the converse piezoelectric effect (deformation under electric field). It was not until 1881 when Gabriel Lippmann, Marie Curie's thesis advisor, proved mathematically that the converse piezoelectric effect was possible, so that the Curie brothers quickly completed experiments to show that it was indeed present.

Perovskites and the Discovery of Ferroelectricity

Perovskite is the name for the general class of crystals that are composed on the basic chemical formula ABO_3. These crystals have the ability to reorient their polarization direction

through the application of external loads over a range of temperatures (ferroelectricity), something that is not seen in all piezoelectric materials. Although ferroelectricity was previously proposed, it was not until 1921 that this phenomenon was experimentally discovered in single crystal Rochelle salt specimens [1]. Water-soluble Rochelle salt (sodium potassium tartrate tetrahydrate) and potassium dihydrogen phosphate (KDP) were the only two ferroelectric materials known until barium titanate ($BaTiO_3$). To summarize, chronological information is provided for the discovery of early ferroelectric crystals in Table 1.1.

The exact history of the discovery of barium titanate is unclear because much of the initial research began in secrecy in the early 1940s during World War II for the use in high dielectric-constant capacitors. After the conclusion of the War, much of the research that was accomplished in secrecy was published and the source of the high dielectric constant was determined to be due to the ferroelectric behavior [2, 3].

The discovery of lead zirconate titanate, $Pb(Ti,Zr)O_3$ (PZT), came about in the early 1950s [4] and offered increased properties over barium titanate including lower dielectric loss and higher Curie points [5]. PZT is a solid solution of lead zirconate $PbZrO_3$ (PZ) and lead titanate $PbTiO_3$ (PT) where the ratio between the components can be varied, changing material properties. In addition, additives such as lanthanum can be included in the solid solution to affect the constitutive behavior. The variability in PZT materials properties due to mixture ratios led to the discovery of the morphotropic phase boundary (MPB) where exceptional piezoelectric coefficients were observed [6]. Efforts to grow single PZT crystals failed [7], stalling major single crystal research until the early 1990s.

Table 1.1 A partial list of early ferroelectric crystals.

Name and Chemical Formula	**Curie Temperature, T_C (^oC)**	**Spontaneous Polarization, P_S ($\mu C/cm^2$)**	**Year in which reported**
Rochelle Salt $NaKC_4H_4O_6 \cdot 4H_2O$	23	0.25	1921
Potassium Dihydrogen Phosphate KH_2PO_4 (KDP)	-150	4	1935
Potassium Dihydrogen Arsenate KH_2AsO_4	-177	5	1938
Potassium Dideuterium Phosphate KD_2PO_4	-60	5.5	1942
Barium Titanate $BaTiO_3$	120	26	1945
Lead Titanate $PbTiO_3$	490	>50	1950
Potassium Niobate $KNbO_3$	415	30	1951
Lead Zirconate Titanate* $Pb(Zr_xTi_{1-x})O_3$	~350	>40	1952

*polycrystalline ceramics

It was not until the early 1950s that lead-based relaxor ferroelectric materials with the chemical formula of $Pb(B',B'')O_3$, where B' is a low valence cation and B" is a high valence cation, were discovered by the group of Smolenski [8,9]. Materials with this chemical structure were shown to not display Curie-Weiss behavior, instead having a diffuse dielectric permittivity around the Curie point. Of the many interesting relaxor materials discovered, lead magnesium niobate, $Pb(Mg_{1/3}Nb_{2/3})O_3$ (PMN), proved to be the most promising [10]. PMN was shown to have a minimal electrical conductivity [11] and an unhysteretic electrostrictive effect [12,13], making it useful for many applications, such as micro-positioning systems.

In the late 1970s, it was discovered that the solid solutions of PMN and PT have properties intermediate between relaxors and normal ferroelectrics [14]. This finding was quickly followed by the discovery of the morphotropic phase boundary (MPB) with PT, above which the electrostrictive behavior of PMN-xPT was replaced by a more normal ferroelectric response seen in other materials [15]. This led to the creation of the phase diagram which

showed a MPB separating the room temperature stable rhombohedral and tetragonal phases and enhanced dielectric and piezoelectric properties [16].

Although the growth of PMN single crystals was initially reported in the early 1960s [9, 17], it was not until the late 1960s that another solid solution representing relaxor single crystal family, lead zinc niobate $Pb(Zn_{1/3}Nb_{2/3})O_3$ (PZN), was found [18,19]. It was discovered that the behaviour of single crystals $(1-x)Pb(Zn_{1/3}Nb_{2/3})O_3$-$xPbTiO_3$ (PZN-PT) was composition [20] and orientation [21,22] dependent, with some compositions and crystallographic directions exhibiting extremely large piezoelectric behavior. This work was followed by the studies of single crystal PMN-PT in the early 1990s [22,23] and renewed the interest in ferroelectric materials.

Discovery of New Monoclinic Phases

Since the discovery of a new monoclinic phase in ceramic solid solutions $Pb(Zr,Ti)O_3$ (PZT) in 1999 [24] several works were published to understand the mechanisms responsible for high piezoelectric response of these materials. This monoclinic phase was observed for PZT compositions near the morphotropic phase boundary, initially interpreted as the coexistence of the rhombohedral (F_R) and tetragonal (F_T) ferroelectric phases, at room temperature in the composition temperature phase diagram [6]. Based on subsequent studies, supported by different techniques such as high-resolution synchrotron x-ray powder diffraction [25,26,27]. Raman spectroscopy [28,29] dielectric measurements [30] and theoretical electromechanical studies [31] the MPB was redefined assuming the monoclinic phase as responsible for high piezoelectric response in PZT ceramics [32].

Within a short time interval, another monoclinic phase was also observed in similar solid solution PMN-PT [33] which also exhibits an analogous MPB between the rhombohedral and tetragonal ferroelectric phases in the PMN-PT composition-temperature phase diagram as observed in PZT. The PMN-PT is known for its exceptional electromechanical properties, sometimes one order of magnitude larger than classical PZT ceramics [34]. Subsequent to these studies, the monoclinic structure was considered as a natural link between the tetragonal and rhombohedral phases in PZT or PMN-PT phase diagram that remains under intense

investigations. A comprehensive review on advances to understand the role of the monoclinic phases on structure and high piezoelectricity in lead-based solid solutions was published in 2002 [35].

Today single crystal and ceramic ferroelectrics continue to be an exciting research area that promises even further discoveries.

§1.2 Piezoelectricity

The piezoelectric effect is associated with a lack of charge symmetry about the center of a unit cell. A unit cell is the smallest three-dimensional atomic structure periodically repeated throughout the crystalline structure that still shows the crystal symmetry [6]. There are 21 classes of crystals that do not have a center of symmetry, with 20 of those classes being piezoelectric (Figure 1.1). The remaining non-piezoelectric class, *432* point group, does not show a piezoelectric effect because of the combination of other symmetry elements. Each piezoelectric crystal class has a symmetry which is reflected in the materials properties such as compliance, piezoelectric constants, and dielectric permittivity [36]. The piezoelectric effect is not found exclusively in crystalline materials.

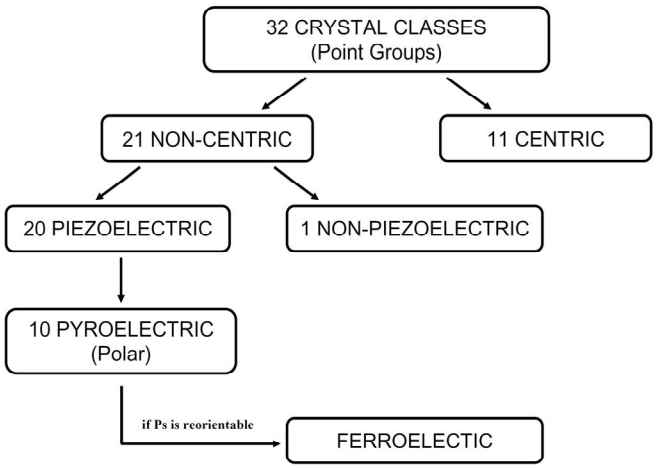

Figure 1.1 Relationship between piezoelectrics, pyroelectrics and ferroelectrics.

As mentioned above, all the ferroelectric materials are pyroelectric/piezoelectric, while not all the piezoelectric materials possess ferroelectric properties. The relationships between piezoelectrics, pyroelectrics and ferroelectrics are illustrated in Figure 1.1.

All ferroelectric materials are indeed piezoelectric (see Figure 1.1 for a crystal classification). As already mentioned, piezoelectricity is the ability of certain crystalline materials to develop an electrical charge proportional to an applied mechanical stress [7]. This is also called the direct piezoelectric effect. Piezoelectric materials also show a converse effect, where a geometric strain (deformation) is produced on the application of a voltage. The direct and converse piezoelectric effects can be expressed in tensor notation as,

$$P_i = d_{ijk}\sigma_{jk} \quad \text{(direct piezoelectric effect)}, \tag{1.1}$$

$$x_{ij} = d_{kij}E_k \quad \text{(converse piezoelectric effect)}, \tag{1.2}$$

where P_i is the polarization generated along the i-axis in response to the applied stress σ_{jk}, and d_{ijk} (= d_{kij}) is the piezoelectric coefficient. For the converse effect, x_{ij} is the strain generated in a particular orientation of the crystal on the application of electric field E_k along the k-axis.

Certain kinds of polymers have been found to exhibit electromechanical behavior including rubber, wood fiber and silk. Figure 1.2 shows a schematic of a cubic (a) and tetragonal (b) unit cell for lead titanate $PbTiO_3$. The non-piezoelectric cubic unit cell is referred to as the paraelectric phase and is found above the material specific Curie point. As the material is cooled passing the Curie point a spontaneous polarization, P_S, is formed by a phase transformation into the tetragonal phase. The tetragonal phase has transverse isotropic symmetry and six possible spontaneous polarization directions along the principal axes.

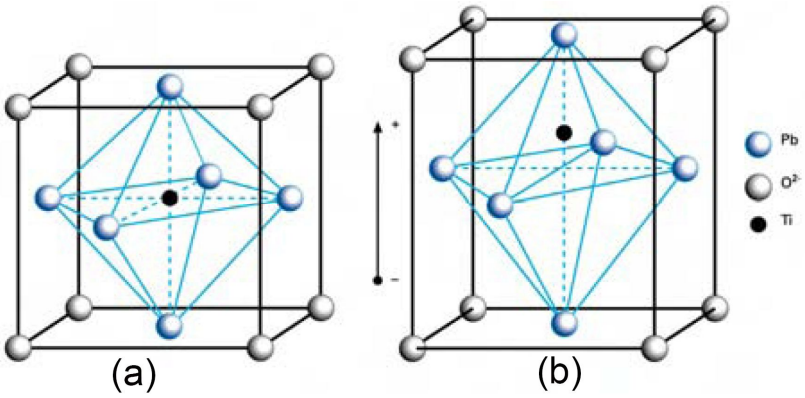

Figure 1.2 Unit cell of perovskite structure $PbTiO_3$ (a) cubic structure in paraelectric state; (b) tetragonal structure in ferroelectric state.

§1.3 Ferroelectricity

Ferroelectric materials are a subgroup of piezoelectric materials. Materials which fall into this category have a spontaneous polarization within a defined temperature range and the ability to reorient their spontaneous polarization through the application of an external field [37]. A net remanent polarization may be produced in a multidomain ferroelectric material by applying a dc electric field greater than the coercive field. This is defined as poling. The reorientation of spontaneous polarization in ferroelectric materials is principally controlled by the motion of domain walls. Domains are regions of a ferroelectric material which share the same spontaneous polarization direction. The boundary between neighboring domains is called a domain wall. Reorientation of the polarization of unit cells in an unconstrained ferroelectric single crystal due to an applied field results in translation of domain walls. Polarization reorientation within one phase can be induced by either applied stress (ferroelastic switching) or electric field (ferroelectric switching). Ferroelectric polycrystalline material behavior is more complicated as each of the randomly oriented grains is a constrained single crystal subjected to local stress and electric field due to grain boundaries and local inhomogeneities.

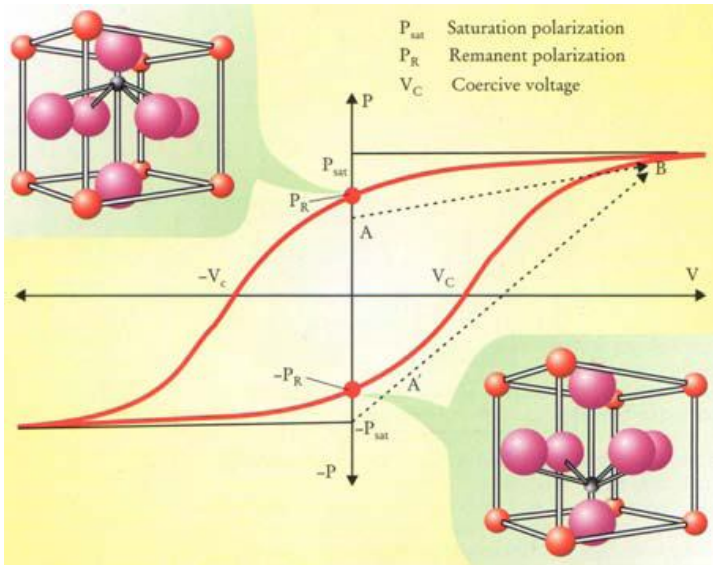

Figure 1.3 Hysteretic loop between the polarization and the electric field of a ferroelectric materials, where two remanent polarizations P_R correspond to two low energy stable states.

An unpoled polycrystalline ferroelectric material initially has no remanent strain or electric displacement.

Different from dielectric materials, the switchability of the spontaneous polarizations causes the hysteretic relationship between the polarization and the electric field as shown in Figure 1.3, which is characteristic of the ferroelectric materials. The finite polarization in the absence of the electric field is called remnant polarization, denoted as P_R. The voltage at which polarization changes direction is called coercive field V_c.

Ferroelectric materials usually undergo structural phase transition from high temperature non-ferroelectric phase to low temperature ferroelectric phase, which is a result of lowering the total free energy of the system. The first transition (if there is more than one structure transition) temperature to a ferroelectric phase is called *Curie Temperature* T_c. Close to the Curie temperature in the paraelectric state, the dielectric constant behaves with temperature according to Curie-Weiss law is

$$\varepsilon = \frac{C}{T - T_0}, \tag{1.3}$$

where ε is the permittivity of the material, C is the Curie constant and T_0 is the Curie-Weiss temperature. The Curie-Weiss temperature T_0 is, in general, different from the Curie point T_C. For first order transitions $T_0<T_C$, while for second order phase transitions $T_0=T_C$. At the low temperature ferroelectric state, the two lower stable states correspond to spontaneous polarization ($+P_R$, $-P_R$) as shown in Figure 1.3.

The ferroelectric phase transition in the equilibrium state can be treated phenomenologically by the Landau-Ginzburg-Devonshire (LGD) thermodynamic theory [38,39].

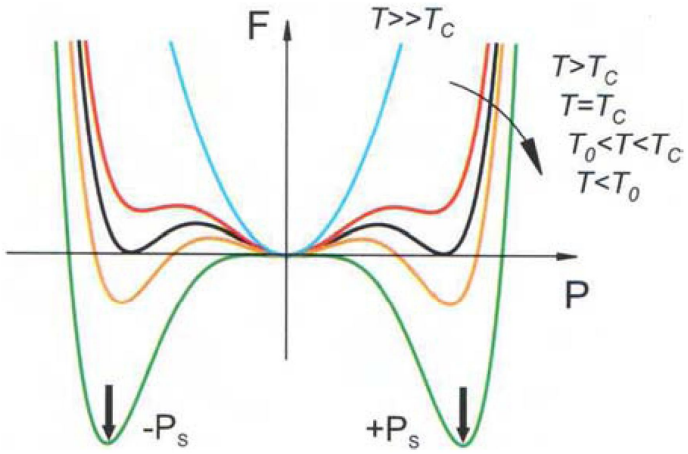

Figure 1.4 The free energy as a function of polarization for a ferroelectric with a first-order phase transition as a function of temperature.

The theory describes the macroscopic picture of ferroelectrics based on Gibbs free energy, which is expressed as

$$G = G_0 + \frac{1}{2}\beta(T - T_0)P^2 + \frac{1}{4}\gamma P^4 + \frac{1}{6}\delta P^6, \tag{1.4}$$

where β, γ and δ are constants. β and δ are found to be positive in all known ferroelectrics, while γ can be either positive or negative in case of second order and first order phase transition, respectively. Figure 1.4 shows the characteristic curves of the Gibbs free energy (G) *vs.* polarization for ferroelectrics with a first-order transition in different temperature ranges.

T_0, T_C, T_1, and T_2 are a series of special temperatures characterizing the transition from the ferroelectric to paraelectric phase.

Other ferroelectrics show diffuse phase transition behavior. An additional subset in the diffuse ferroelectrics, called "*relaxors*", will be discussed separately later on. General property changes with ferroelectric phase transitions are schematically summarized in Figure 1.5 [40].

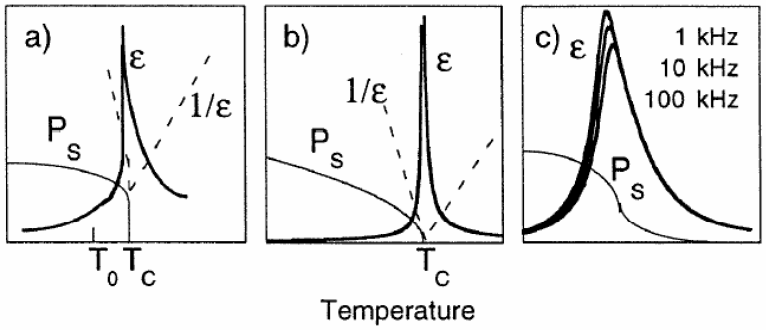

Figure 1.5 Schematic temperature dependence of the dielectric permittivity (ε) and spontaneous polarization (P_S) for (a) a first- and (b) a second-order ferroelectric and (c) for a relaxor ferroelectric [28].

As exemplified by several perovskite-type compounds [e.g., $Pb(Mg_{1/3}Nb_{2/3})O_3$, $Pb_xLa_{1-x}(ZrTi)O_3$] and tungsten-bronze-type compounds [e.g., $(Sr_{1-x}Ba_x)Nb_2O_6$], relaxors can be distinguished from normal ferroelectrics such as $BaTiO_3$ and PZT, by the presence of a broad, diffused and dispersive dielectric peak on cooling over the so-called transition temperature, T_m, at which the permittivity is maximum for a given frequency (see Figure 1.5(c)). In relaxor ferroelectrics, the Curie-Weiss law is not completely obeyed close to T_m.

Ferroelectric Domains

When ferroelectric materials are cooled down from high temperature, the crystal is subdivided to regions with different spontaneous polarization orientations to minimize the electrostatic energy of depolarization fields and the elastic energy due to mechanical constraints. The region that has the uniform spontaneous polarization orientation is called a ferroelectric domain. For a fully compensated ferroelectric single crystal of a suitable

orientation, a single domain state is the lowest free energy. However, in most cases, different domains will form which is driven by electrical or mechanical boundary conditions. As exemplified by $PbTiO_3$, six equivalent polarizations can possibly form in the crystal depending on the stress and electric field conditions in the crystal during the cooling. The domains with polarization parallel to the main c-axis, are called *c* domains, while the domains with polarization perpendicular to c-axis are called *a* domains. The boundary between different domains is called *domain wall* whose typical size corresponds to few unit cells. If the angle between the spontaneous polarization orientations of the neighboring domains is 180º, the domain wall is called the 180º domain wall; if the angles are not 180º, for example, they are 90º, 71º, as in a tetragonal or rhombohedral structure, respectively, these domain walls are called 90º or 71º domain walls, or generally, the non-180º domain walls.

In the tetragonal structure, both 180º and 90º domain walls can form in the crystal; however, the formation mechanism is notably different. The formation of both the 180º and 90º domain walls can minimize the depolarization field by compensating for the surface charge in an unpoled ferroelectric ceramics, but only the formation of the 90º domain wall can release the elastic energy stored in the crystal. Moreover, both the 180º and non-180º domain wall motion will increase the dielectric properties, while only non-180º domain wall motion will affect the piezoelectric response. Because the lattice parameters of the unit cells at both sides of 180º domain wall are the same, the movement of the 180º domain wall will not induce piezoelectric strain. However, the different lattice parameters along the 90º domain wall will induce large piezoelectric strain [41,42]: in the tetragonal crystal, the strain induced will approach the tetragonality of the crystal and increase the piezoelectric properties as shown in [43] and illustrated in Figure 1.6. It is worth mentioning that the movement of 180º domains wall can increase the apparent piezoelectric response when the applied electric field reaches the coercive field. This is due to the fact that the amount of domains that have the same spontaneous polarization orientation with the electric field increase and these domains expand along the electric field direction, while the amount of domains with opposite polarization direction decreases and the domains shrink under the electric field [44].

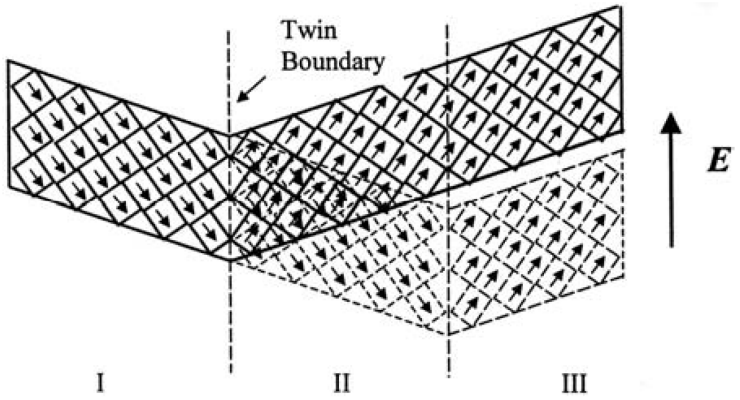

Figure 1.6 Movement of 90º domain and induced piezoelectric strain.

The general ferroelectric domain structure in equilibrium is a result of minimizing the overall mechanical and electrostatic energies:

$$W_{tot} = W_M + W_E + W_{DW} + W_S = \min, \tag{1.5}$$

where W_M is the elastic energy, W_E is the electric energy, W_{DW} is the domain wall energy, and W_S is the surface energy. The static ferroelectric domain structure in single crystals, powders, and ceramics has been observed by many techniques including optical microscopy, scanning electron microscopy, transmission electron microscopy, and, recently, atomic force microscopy. In ferroelectric ceramics, each region of the material is not free to deform due to the surrounding constraint, so complicated domain patterns form consisting of randomly oriented grains/domains.

Ferroelectric domain structure is the most important factor that determines the ferroelectric properties of a ferroelectric material, together with domain nucleation and domain wall mobility. The way how the material splits up into domains at the formation of the ferroelectric phase depends very much on the mechanical and electrical boundary conditions imposed on the sample, as well as on the nature of the sample itself.

§1.4 Relaxor Ferroelectrics

Relaxor ferroelectric materials are distinguished by their dispersive dielectric response and diffuse phase transformations about the temperature at which maximum dielectric permittivity is measured, T_m [45]. Relaxor ferroelectrics also show a decrease in hysteresis and remanent polarization as the temperature is increased to T_m, frequency dependent ferroelectric/dielectric properties and optical isotropy (the structure remains unchanged across T_m) when there is no external field.

Recently, solid solutions of PMN-*x*PT [12,46] and PZN-*x*PT [47] have been developed for use in engineered structures. The addition of the ferroelectric PT to relaxor PMN or PZN forms a complex solid solution system with enhanced electromechanical properties [48]. The addition of PT was also shown to increase the temperature at which the maximum dielectric permittivity was found [49]. Extensive work has been done on the growth of relaxor PMN-*x*PT and PZN-*x*PT single crystals by the flux method, top-cooled solution growth, bottom-cooled solution and the Bridgman techniques [50,51,52]. Presently, it remains difficult and expensive to manufacture large single crystals with minimal fluctuations in piezoelectric properties [53,54] for academic research or industrial applications [55].

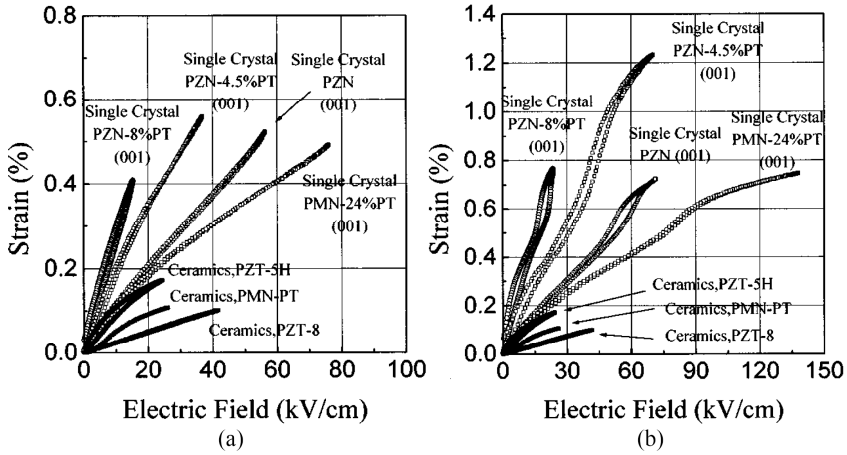

Figure 1.7 Electric field induced strain for various compositions of relaxor single crystals and ferroelectric polycrystals. Low electric field excursions (a) produce nearly linear material response while at elevated electric fields (b) the initiation of phase transformations are apparent from the presence of hysteresis and nonlinear change in the electromechanical response [47].

Figure 1.7 shows the strain behavior of various compositions of PMN- and PZN-based single crystals and polycrystalline specimens due to unipolar electric field loading [47].

Because of the symmetry in single crystals certain crystallographic orientations exhibit larger electromechanical couplings and reduced non-linearity and hysteresis. Experimental investigations have principally focused on the (001) cuts due to the large electromechanical coupling factor (k_{33} > 90%), piezoelectric constant (d_{33} > 2500 pC/N), dielectric permittivity (ε_{33} ≥5000) and low dielectric loss (≤ % 1). Park and Shrout [48] have experimentally measured longitudinal strains as high as 1.7% in single crystal PZN-8%PT under a ~120 kV/cm electric field. As the crystallographic orientation is changed to the <111> crystal cut the measured longitudinal strain decreases. The exceptional materials properties have been related to the specific domain and phase states [42].

Implementation of relaxor single crystals in applications can be challenging. Their constitutive behavior is rate-dependent as well as sensitive to temperature, electric field, and stress [6]. They generally have a low coercive field, when compared to polycrystalline materials, which limits their usage range unless a bias field is applied [6]. Further understanding of the nonlinear electromechanical response, domain evolution, phase evolution, and effects of composition on this behavior are important components of the implementation of these materials in new applications.

§1.5 Phase Transitions in Relaxor Ferroelectrics

Ferroelectrics have recently seen a resurgent of interest particularly due to the discovery of such materials with large dielectric susceptibility and piezoeffect. In particular, relaxor ferroelectrics have found applications in industry with optical applications such as phase conjugate mirrors, piezoelectric sensors and actuators. The ferroelectric nature of the materials considered in this section arises from the competition between order and disorder due to the structural composition, and this in turn can lead to dramatically high static and dynamical properties in the material [56]. Relaxor ferroelectrics can be categorized into two structural families: perovskites with complex composition and bronze tungsten structure [57]. In relaxors there is a distinct transition from high temperature with polar nanodomains to a

state that exhibits relaxor behavior. The nature of the transition and composition of the relaxor state are still debated.

Ferroelectrics versus Relaxors

A useful starting point to understand the qualitative features of relaxors is to contrast them with the "normal" ferroelectrics which are better understood. The distinction between ferroelectrics (FE) and relaxor ferroelectrics (RFE) can be distinguished by three qualitatively different features in the temperature dependence of the dielectric susceptibility, as shown in Figure 1.8.

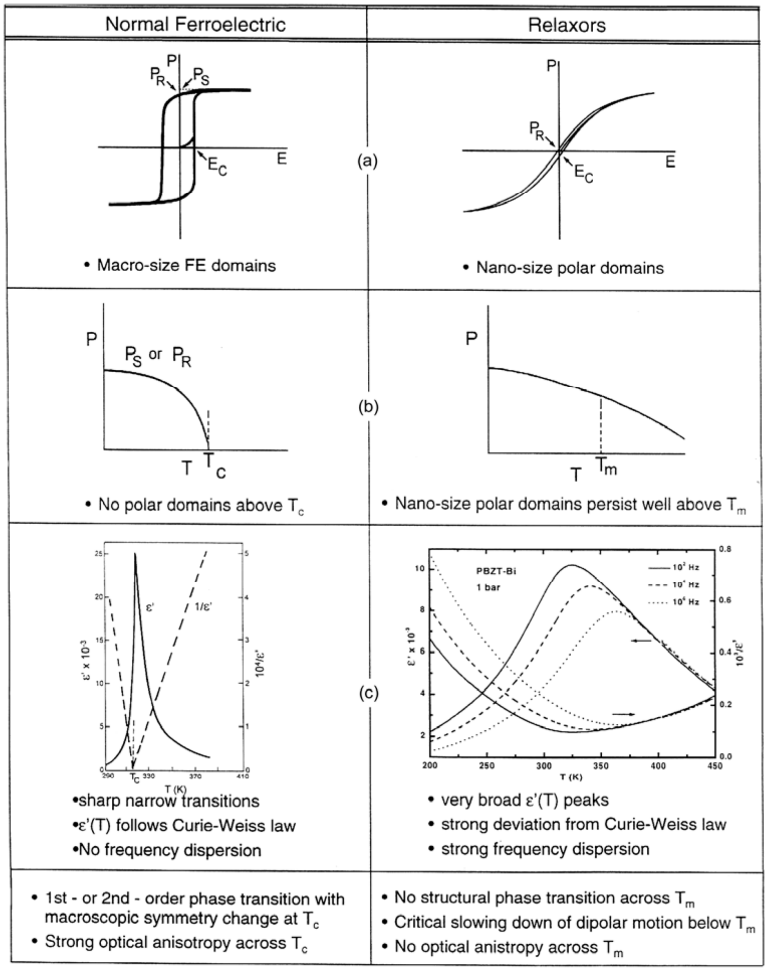

Figure 1.8 Comparison between "normal" and relaxor ferroelectrics [56].

Firstly, in "normal" ferroelectrics the real part of the dielectric susceptibility, $\chi'(T)$ shows a Curie-Weiss law behavior at the transition temperature T_C, whereas in relaxors the dielectric peak does not diverge at T_m but it is rather broad and rounded. This rounded peak position at T_m characterizes the dynamic of the polar clusters and/or nanodomains and T_f, being the limit of T_m at zero frequency, marks the dynamic freezing temperature or glass like transition [56]. Secondly, there is a strong frequency dependence in the peak position, T_m, of $\chi'(T)$. Lastly, the polarization in FE goes to zero at T_C and in the relaxors the polarization extends well beyond T_m [58]. The fact that there is zero polarization at T_C in normal FE whereas in the relaxor there is no vanishing of the polarization shows that the polar nanodomains persist well beyond T_m [56].

While the normal ferroelectric has a hysteresis loop that at zero field retains large polarization, in the relaxor this zero field polarization is significantly smaller owing to the fact that the nanodomains are randomly distributed. It is possible to create a large polarization when there is a sufficiently large external electric field, but once the field is removed polarization returns to being small owing to the randomness of the domains. Finally, it should be noted that in FEs there is a macroscopic structural change at T_C and this does not occur in RFEs across T_m [56]. Due to these qualitatively different features one then should not expect the transitions in FEs to have the same mechanism in RFEs.

One of the most extensively studied relaxor ferroelectrics is $PbMg_{1/3}Nb_{2/3}O_3$. To probe the transition from a glassy state to the long range ferroelectric ordered state several different experimental techniques have been used. Those include pyroelectric measurements, nuclear magnetic resonance (NMR), dielectric spectroscopy and X-ray and neutron scattering. First, we begin by looking at the high temperature and the nature of the phase there. At very high temperature the thermal fluctuations are so strong, so that there are no well-defined dipoles in the sample. As the temperature is reduced, polar nanodomains begin to form at a temperature T_B, the Burns temperature [57, 58]. Recently, it was reported that the main feature characterizing T_B is the off-centering of Pb-ions from their special position giving rise to dynamic polar regions [59]. A lot of anomalies around T_B were reported and the first evidence for the formation of polar nanodomains at T_B was obtained by measuring the refractive index n as a function of temperature. Evidence for polar nanodomains well above T_m is also seen in measurements of the dielectric susceptibility, as illustrated in Figure 1.9. The departure from

the Curie-Weiss behavior becomes more severe as T decreases. This stems from the fact that the polarization correlations lead to the increased size of nanodomains [56].

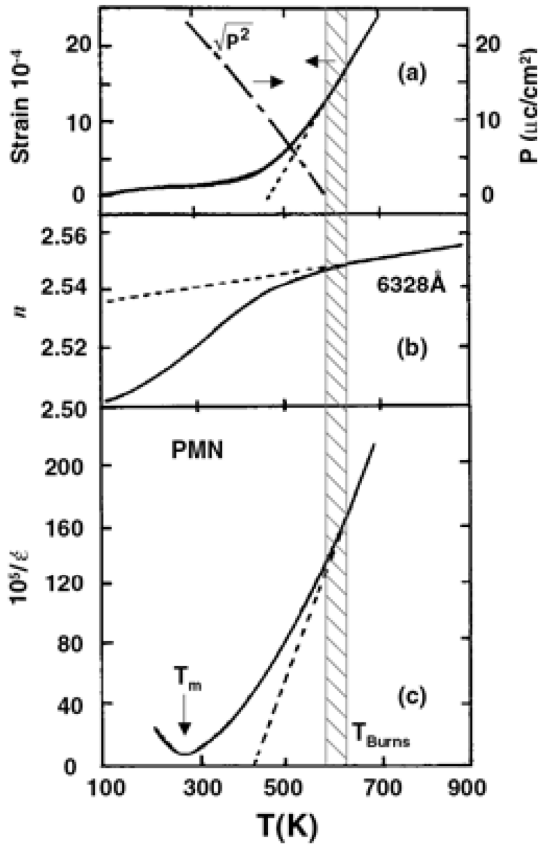

Figure 1.9 Deviations from linearity at T_B measured by the index of refraction and reciprocal dielectric constant [56].

Consequently, the polar nanoregions (PNRs) affect the behaviour of the crystal dramatically, giving rise to unique physical properties. For this reason, the state of crystal at $T<T_B$ is often considered as the new phase different from the PE one. At temperatures close to T_B the PNRs are mobile and their behaviour is ergodic. On cooling, their dynamics slow down enormously and at a low enough temperature, T_f (typically hundreds degrees below T_B), the PNRs in the canonical relaxors become frozen into a nonergodic state, while the average symmetry of the crystal still remains cubic. Similar kind of nonergodicity is characteristic of a dipole glass (or spin glass) phase. It is also worth mentioning that a new intermediate

temperature referred as T^* was also reported [60,61]. At this temperature some dynamical polar regions which appeared at T_B become static at T^* and and this is reflected in several measurements including x-ray diffraction, acoustic emission or Raman spectroscopy. The existence of PNRs was observed by neutron and X-ray elastic diffuse scattering around the reciprocal lattice points [62,63]. In PMN crystals, significant diffuse scattering appears at $T < T_B$ with the intensity increasing with decreasing temperature. This effect resembles the scattering caused by FE critical fluctuations, but an important difference (found in synchrotron X-ray experiments [63]) is that the shape of wave vector dependence of scattering intensity at large distances from the reciprocal lattice point deviates from a Lorentzian function. This means [63] that the PNRs are more compact than the usual FE critical fluctuations and have better defined borders. The correlation length (ξ) of the atomic displacements contributing to the diffuse scattering, which is a measure of the size of PNR, can be derived from the experiment: it is inversely proportional to the width of the diffuse (Lorentzian) peak. According to the recent high resolution neutron elastic diffuse scattering study of PMN [64], the size of the emerging PNRs is very small (ξ is around 1.5 nm) and practically temperature independent at high temperatures (Figure 1.10).

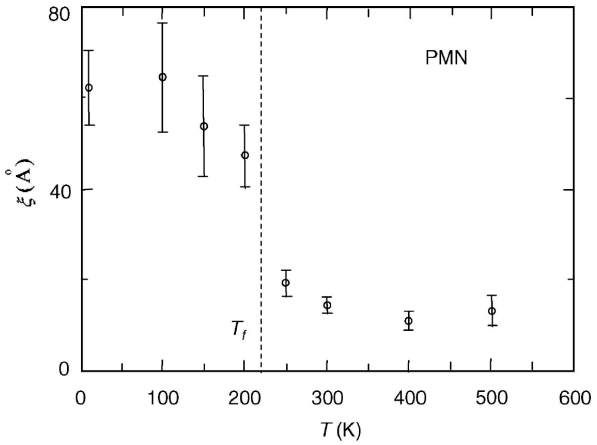

Figure 1.10 Average size of PNRs in the $Pb(Mg_{1/3}Nb_{2/3})O_3$ crystal (determined from diffuse neutron scattering) as a function of temperature. Vertical dashed line corresponds to T_f [64].

The perovskite unit cell parameter being ~0.4 nm, each PNR is composed of only few unit cells. Below about 300 K, ξ begins to grow on cooling, reaching ~7 nm at 10 K. The most significant growth is found around T_f the so called freezing temperature. Qualitatively the same behaviour was observed in the bulk of PZN crystals (the structure of PZN surface layers is different) but the size of PNRs is larger: they grow from ~7 nm at high temperatures to ~18 nm at 300 K [65]. From the analysis of the relation between ξ and the integrated intensity of scattering, it was concluded [64] that the number of PNRs also increases on cooling, but in contrast to the temperature evolution of ξ, the increase begins right from T_B and at $T \approx T_f$ a sharp decrease of this number occurs (presumably due to the merging of smaller PNRs into larger ones). Below T_f the number of PNRs remains practically the same at any temperature.

§1.6 Origin and Evolution of PNRs: Models and Theories

Although the very existence of PNRs in relaxors seems to be doubtless, the cause and mechanisms of their formation are not conclusively understood. At temperatures higher than T_B the structure and properties of relaxors closely resemble those of normal displacive ferroelectrics. When a relaxor becomes compositionally ordered after high temperature annealing (without changing the chemical composition), a sharp ferro- or antiferroelectric (AFE) phase transition is observed. These facts seemingly suggest that the relaxor crystal tends to be ferro- or antiferroelectric at low temperatures, but the quenched compositional disorder somehow prevents the normal transition into the phase with macroscopic FE or AFE order from happening. Instead, the PNRs appear. There exist different approaches to explain the formation of PNRs. All of them can be schematically subdivided into two categories. The models of the first category [66, 67, 68] consider the PNRs as a result of local "phase transitions" or phase fluctuations, so that the crystal consists of nanosize polar islands embedded into a cubic matrix in which the symmetry remains unchanged (as shown in Figure 1.11(a)). The models of the second category assume the transition to occur in all regions of the crystal and the crystal consists of low-symmetry nanodomains separated by the domain walls but not by the regions of cubic symmetry [69, 70] (the example is shown in Figure. 1.11(b)). Note that these two situations can hardly be distinguished experimentally by structural

examinations [71] because the *local* symmetry of cubic matrix is not expected to be cubic and the thickness of domain walls (i.e. the regions where polarization is not well-defined) is comparable with the size of nanodomains.

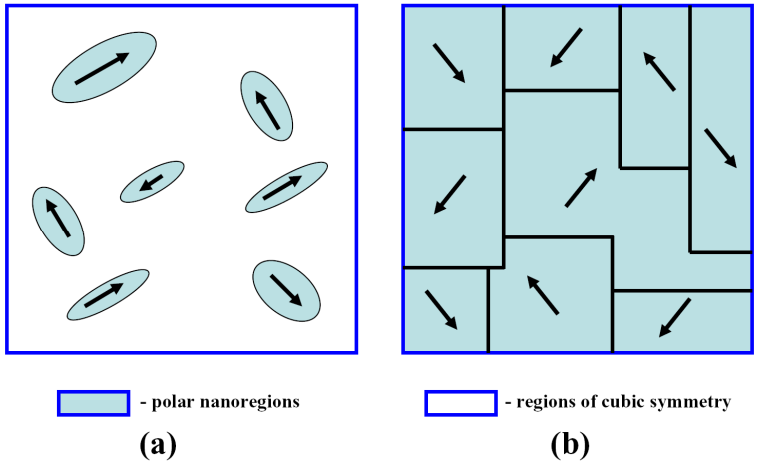

Figure 1.11 Schematic representation of PNRs in relaxors according to the different models.

The second category is represented by the random-field model proposed by Westphal, Kleemann and Glinchuk (WKG model) [69, 72], who applied the results of theoretical work by Imry and Ma [73] to the relaxors. It was shown in Ref. [73] that in the systems with a continuous symmetry of order parameter, a second-order phase transition should be destroyed by quenched random local fields conjugate to the order parameter. Below the Curie temperature the system becomes broken into small-size domains (analogy of PNRs) instead of forming a long-range ordered state. It should be emphasized that this model does not consider the trivial case of the local spontaneous polarization which is directed parallel to the quenched field when the field is strong enough. Instead, the situation is determined by the interplay of the surface energy of domain walls and the bulk energy of domains in the presence of *arbitrary weak* random fields [73].

For displacive transitions, continuous symmetry means that the spontaneous deformation is incommensurate with the PE lattice. However, this is not the case for the perovskite ferroelectrics in which the spontaneous deformation and the polarization (order parameter) are aligned along definite crystallographic directions (e.g. the <111> directions for

the rhombohedral phase). Nevertheless, when the number of allowed directions is large (e.g. eight for the rhombohedral phase), the symmetry of the order parameter can be considered quasi-continuous and this approach appears to be applicable. The disordered distribution of the heterovalent ions inherent to the compositionally disordered structure (e.g. Nb^{5+} and Mg^{2+} ions in PMN) provides the source for quenched random electric fields.

Ishchuk [70] analyzed the thermodynamic potential in the framework of Landau phenomenological theory for the systems in which the energies of the FE and AFE phases are close to each other. It was shown that the state with coexisting FE and AFE domains may have lower thermodynamic potential than the homogeneous (FE or AFE) state. This effect is due to the interactions (electrostatic and elastic) between the FE and AFE domains. It was suggested that relaxors are just the crystals in which this effect occurs. In other words, the nonpolar regions, coexisting with PNRs (FE domains), are the domains of AFE structure.

The best-known model of the first category was developed in the early works by Isupov and Smolenskii [66,74]. Due to the compositional disorder the concentrations of different ions (e.g. Mg^{2+} and Nb^{5+} in PMN) are subject to quenched spatial fluctuations. As the FE Curie temperature (T_C) depends on the concentration, spatial fluctuations of local T_C are expected. It was suggested that upon cooling, local FE phase transitions occur first in those regions where T_C is higher, whereas the other parts of the crystal remain in the PE phase. Therefore, PNRs are simply the regions with elevated Curie temperature.

Several other models use the microscopic approach and consider the structural evolution and formation of PNRs in terms of interatomic interactions. The FE lattice distortion in the ordinary perovskites is known to be determined by a delicate balance between the electrostatic (dipole-dipole) interactions and the short-range repulsions. Hybridization between the oxygen 2*p* states and electronic states of cations (covalent bonding) is able to change this balance, influencing thereby the phase transition temperature [75]. In the compositionally ordered (translationally symmetric) crystals, exactly the same forces affect all the atoms of a certain type because they have the same coordination neighbourhood. In the case of compositional disorder, the ions of different types may be found in the neighbouring unit cells in the same crystallographic positions (e.g. in the B-sublattice of PMN, both Mg and Nb ions are the nearest neighbors of Nb ions). The interatomic interactions which would cause ferro-

or antiferroelectric order in the compositionally ordered state become random in this case, and as a result, the long-range polar order is disturbed. The models described below emphasize the importance of different interactions: the interactions under random local electric fields only (including dipole-dipole interactions) [66], and the dipole-dipole interactions together with random short-range repulsions [76] or random covalent bonding [77].

In the random field theory developed for relaxors by Glinchuk and Farhi (GF model) [67] (see also Ref. [78] in which the related papers are reviewed), the transition is regarded as an order-disorder one, i.e. at high temperature the crystal is represented by a system of reorientable dipoles. These random-site dipoles are embedded in highly polarizable "host lattice". The dipole-dipole interactions are indirect (they occur via the host lattice) and random. Nevertheless, according to the theory, they should lead to uniformly directed local fields and thus to FE ordering at low temperature (in contrast to *direct* dipole-dipole interactions which can lead to a dipole glass state). Thus to explain the absence of macroscopic FE order in relaxors, additional sources of random local electric fields are considered. These additional fields can be static (coming from quenched compositional disorder, lattice vacancies, impurities and other imperfections) or dynamic (associated with shifts of non-ferroactive ions from the special positions). In contrast to the fields considered in the WKG model, these fields should be rather large (larger than critical value) to destroy the long-range FE order. The FE order parameter, phase transition temperature T_C, linear and nonlinear dielectric susceptibilities are calculated within the framework of statistical theory using the distribution function for local fields. It is found that, depending on the model parameters (concentration of dipoles, other field sources and the host lattice correlation length), the low-temperature phase can be FE, dipole glass, or mixed ferroglass. In the temperature interval between T_C and T_B, the short-range clusters may appear, in which the reorientable dipoles are ferroelectrically correlated (i.e. PNRs). This might be related to the recently evidenced T^* temperature. In the ferroglass state, these clusters coexist with the macroscopic regions in which the dipoles are coherently ordered.

One of the models recently proposed for relaxors is the "spherical random bond random field model" (*SRBRF*). In experiments conducted with quadrapole perturbed NMR and measurements on the nonlinear susceptibility it is suggested that the experimental results

could fit into this model's framework [79]. The ^{93}Nb NMR line shape and the probability distribution of the polarization was shown to be Gaussian at all temperatures, which means that the order parameter should be a variable length continuous vector field rather than fixed length field like in dipolar glasses. The vector field is associated with the reorientable polar clusters but subject to a constraint on the square of the total polarization.

The Hamiltonian describing these clusters is given by

$$H = -\frac{1}{2}\sum_{ij} J_{ij}\vec{S}_i \cdot \vec{S}_j - \sum_i \vec{h}_i \cdot \vec{S}_i - g\sum_i \vec{E}_i \cdot \vec{S}_i \,, \tag{1.6}$$

where J_{ij} is the random bond interaction, h_i is the random local electric field, and the last term is the effective local field, with local field factor g [79].

The order parameter S_i is proportional to the dipole moment at the i^{th} site in that cluster and it is discrete with finite number of orientations. The order parameter is subject to the constraint that

$$\sum_i \vec{S}_i^2 = 3N \,, \tag{1.7}$$

where N is the number of polar clusters. It is assumed, like in dipolar glasses, that the random bonds are infinitely ranged with a Gaussian probability distribution, and to simplify the calculations it is assumed that the components of S_i vary continuously [79]. This model is what is known as the spherical random bond random field model.

§1.7 Scanning Probe Microscopy

The main technique used in this thesis for the investigation of relaxor ferroelectrics is the Scanning Force Microscope (SFM). Several SFM modes are capable to image domain pattern at crystal surfaces.

The basic idea of all Scanning Probe Microscopy (SPM) is to take a local probe and bring it that close to the investigated sample that one or several detectable interactions between tip and sample occur. One of these interactions is adjusted to a preselected value by correcting the tip-sample separation with a feedback. Now the local probe is scanned line by

line over a surface area. The feedback adjusts the selected interaction to the desired value at any time. By monitoring the tip position (output of the feedback loop) a surface on which the selected interaction equals the desired value is obtained.

In first approximation, the selected interaction must only depend on the tip-sample separation but not on other local properties of the sample. Therefore, the tip-sample separation is roughly a map of surface topography. In practice many other quantities influense the used interaction. This results in a mixing of topography and these quantities. If these quantities dominate, there will generally be no tip-sample separation at which the desired value is reached and no stable feedback is possible while scanning.

The movement of the tip towards and away from the sample is realized by piezoelectric element. A precision better that one nanometer is required. The scanning of the tip is also done by piezoelectric transducers.

The first scanning probe microscope has been the scanning tunneling microscope (STM) [80]. A sharpened wire is used as a probe. The interaction used for establishing the feedback is the tunneling current between the tip and the conducting sample when a voltage is applied. The STM offers atomic resolution in real space.

In order to enable the measurement of insulating samples the SFM has been invented [81]. The probe is a micro fabricated tip attached at one end of a microscopic cantilever-type spring. The opposite end of the cantilever is attached to the scanner. Any force acting on the tip will results in a deflection of the cantilever. The deflection is measured, e.g., by deflecting a laser beam on it and detecting the change in reflection angle.

The piezoresponse mode was introduced by Güthner and Dransfeld [82]. The idea is to monitor the local electromechanical vibrations of the ferroelectric sample caused by an AC voltage applied between an electrode below the sample and the tip. This oscillation is sensed by the tip. Feedback is established in the contact mode. By measuring not only the cantilever movements normal to the sample but also lateral oscillations, the direction of the spontaneous polarization can be detected even when it is parallel to surface. The piezoresponse mode is discussed in detail in Chapter 3.

The piezoresponse mode offers an excellent separation of the topography and domain contrast. This allows the measurement of untreated surfaces of crystals and thin films. In

addition, it is the only SFM mode which allows the detection of the spontaneous polarization in the plane of the sample.

§1.8 Piezoresponse Force Microscopy in Relaxors

The unique properties of relaxor ferroelectrics have raised fundamental interest in understanding the mesoscopic structures in these materials, including micro- and nanodomain populations, polarization distributions, and their evolution with external electric field and temperature. This interest prompted a limited number of studies on relaxors using SFM [83] and, later on, Piezoresponse Force Microscopy (PFM) [84]. Abplanalp *et al.* [85] observed diffuse domains with irregular 180º-domain walls and domain structure that resembled a fingerprint pattern in an unpoled $Pb(Zn_{1/2}Nb_{2/3})O_3$-8% $PbTiO_3$ single crystal using both out-of-plane (vertical) and in-plane (lateral) PFM measurements (Figure 1.12).

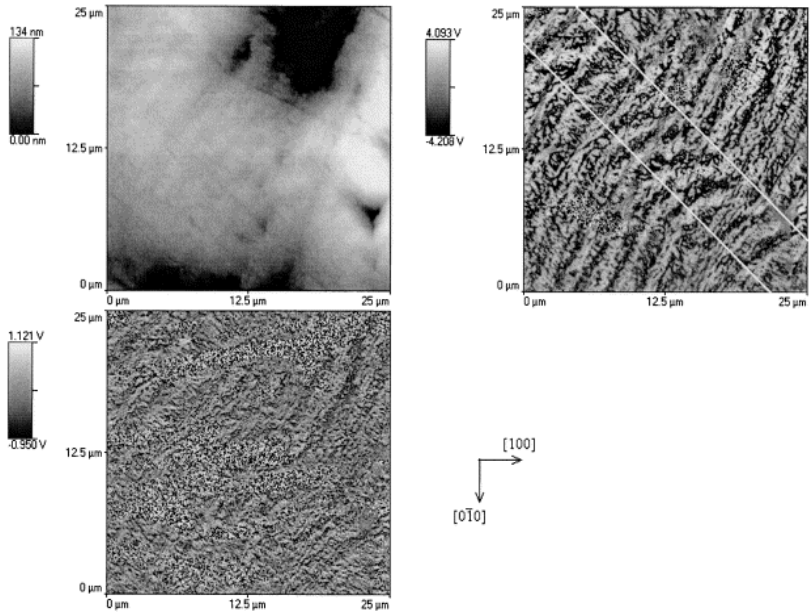

Figure 1.12 Piezoresponse mode SFM scan of the domains in PZN-PT. Added white diagonal lines correspond to the preferred orientation of the ferroelastic (110) domain walls. Topography (upper left), out-of-plane (upper right) and in-plane (lower left) piezoelectric response are displayed [85].

Ferroelastic domains were also observed and the switching of antiparallel domains was demonstrated with the application of +/-30 V. Similar domain patterns were revealed in relaxor $PbMg_{1/3}Nb_{2/3}O_3$-10%$PbTiO_3$ (PMN-10%PT) single crystals by Vakhrushev *et al.* [86] and, later on, by Bai *et al.* [87], and Bdikin *et al.* [88] in PZN-PT. In subsequent studies, Shvartsman and Kholkin [89] and Salak *et al.* [90] measured the temperature dependence of the electromechanical response in PMN-20%PT single crystals and in $BaTiO_3$ ceramics doped with $La(Mg_{1/2}Ti_{1/2})O_3$, respectively. In PMN-20%PT, ferroelectric domains were found to contain PNRs that existed above T_C. Similarly, in the doped $BaTiO_3$, the electromechanical response due to ferroelectric domains disappeared above T_C, while small residual domains could be observed. Interestingly, even above the transition temperature, local hysteresis loops could still be measured. The observed nanoscale behavior was found to correlate with the macroscopic studies [90]. Vertical and lateral PFM have also been employed to measure the domain structure in PMN-30%PT crystals [91] and in relaxor lead lanthanum zirconate-titanate ceramics (PLZT) [92]. The complex domain structure observed in relaxor PLZT (La content 9.75%) was attributed to a La-induced disorder and a correlation length of ~50 nm was determined using autocorrelation of the PFM images. Recently, Shvartsman and Kholkin [93] observed nanodomains well above the structural phase transition by PFM, and attributed this behavior to a transient relaxor-ferroelectric state near the surface of the crystal. In principle, PNRs should exist in relaxors below T_B (~650 K) but their direct study is hampered by their small size (~0.5 – 5 nm) and apparent dynamic character. However, these measurements were not detailed enough to comprehensively study the relaxor behaviour by PFM and judge on the behaviour of nanodomains as a function of their composition, temperature and applied electric field.

§1.9 Objectives

This thesis is devoted to the detailed investigation of three groups of ferroelectric relaxor materials by PFM: these are relaxor $(1-x)Pb(Mg_{1/3}Nb_{2/3})O_3$-$xPbTiO_3$ (PMN-PT) and $(1-x)Pb(Zn_{1/3}Nb_{2/3})O_3$-$xPbTiO_3$ (PZN-PT) single crystals and polycrystalline relaxor ceramics

(Pb,La)(Zr,Ti)O_3 (PLZT). The most attention is given to the nanoscale inhomogeneities in these materials and their roles in the enhancement of materials properties.

The materials list is broad enough and it is thought that studying the nanodomain features and polarization dynamics will stem further light on the nature of the relaxor state as shortly outlined below.

- Lanthanum doping in ferroelectric Pb(Zr,Ti)O_3 is believed to disturb the long-range Coulomb interaction, which shifts the formation of spontaneous polarization to low temperatures (below T_c). It is known that with high La-content the ceramics exhibit relaxor properties (6%<x<12%) or both relaxor and ferroelectric features for x<6%. In relaxor PLZT the cooling in the electric field gives rise to the transition into relaxor nonergodic ($E<E_C$) or ferroelectric states ($E>E_C$). The polar structure of relaxor PLZT ceramics with different La content (x=5-12%) and its temperature evolution will be studied for samples with different histories (aged, cooled through the phase transition temperature under electric fields of various strengths). Particular attention will be paid to the study of influence of microstructure on the domain patterns (size effect, interaction between polar regions and grain boundaries, etc) and temperature studies. The obtained results will be used for the explanation of formation of relaxor state in PLZT ceramics.
- Domain-engineered states in PMN-PT or PZN-PT single crystals have been interpreted as homogeneous intermediate low-symmetry phases. However, as discussed in the introduction, structural inhomogeneous entities (i.e. PNRs) are known to exist over a wide composition range for relaxor-normal crystalline solution. Clearly, it is reasonable to suggest that intermediate phases could be related to PNRs. The natural question is how the PNRs are related to these phases. To address this question, a comprehensive investigation of phase transformation on the macroscale and study of domain structure at the nanoscale is needed. The electric field-induced piezoresponse and transformation of polar structure in single crystals of solid solutions PMN-xPT (x=0-10% and 30-40%) and PZN-xPT (x=4.5%) will be investigated in this thesis. Also, a direct observation of induced polar structures under different voltages will be undertaken. This should allow us to elucidate the nature of the relaxor-ferroelectric phase transition in PMN-PT

crystals with low PT content (x=0-10%). In addition, an investigation of solid solutions of composition close to morphotropic phase boundary (x=30-40% for PMN-PT) will be undertaken to investigate the role of nanoscale domains and mechanism responsible for extremely high piezoelectric effect and electrically induced strain observed in these materials. Based on obtained results of the stability of induced domains the artificial domain patterns will be investigated in these crystals that should help to improve further their performance (so-called *domain nanoengineering*). The part of the thesis aims at resolving the above-described paradigms by examining domain structures of the bulk PZN-4.5%PT single crystals. This composition far from the MPB was intentionally chosen in order to simplify the analysis of the observed domain patterns.

All in all, we will use Piezoresponse Force Microscopy to study the evolution of the domain structure on *a nanometer length* scale for PLZT x/65/35 and PMN-x%PT with different x, and PZN-4.5%PT single crystal. PFM seems to be an excellent tool to study ferroelectric domain inhomogeneities due to the high resolution and sensitivity. Therefore, details of the PFM methods will be discussed in the following chapter.

A more general discussion of the results obtained is provided in Chapters 3 and 4, where different approaches common to all of them are presented. Since sizes of the smallest mesoscopic structures investigated were approaching the experimental resolution limit, a discussion of the limitations of the method as well as of potential improvements is also included.

References

[1] Valasek J., "Piezoelectric and allied phenomena in Rochelle Salt" *Phys. Rev.* **17**, 475 (1921).

[2] Von Hippel A., Breckenridge R.G., Chesley F.G., and Tisza L., "High dielectric constant ceramics" *Ind. Eng. Chem.* **38**, 1097 (1946).

[3] Wul B.M. and I.M. Goldman, "Dielectric constants of titanates of metals of the second group" *Dokl. Akad. Nauk SSSR* **46**, 154 (1945).

[4] Jaffe B., Roth R.S., and Marzullo S., "Properties of piezoelectric ceramics in solid-solution series lead titanate-lead zirconate-lead oxide: tin oxide and lead titanate-lead hafnate", *United States Bureau of Standards Journal of Research* **55**, 239 (1955).

[5] Crawford A.E., "Lead zirconate piezoelectric ceramics" *British Communications and Electronics* **6**, 516 (1959)

[6] Jaffe B., Cook W.R., and Jaffe H., Piezoelectric Ceramics London: New York, Academic Press. (1971).

[7] Liu X., E.F. McCandlish, L.E. McCandlish, K. Mikulka-Bolen, R. Ramesh, F. Cosandey, G.A. Rossetti Jr, and R.E. Riman, "Single-crystal-like materials by the self-assembly of cube-shaped lead zirconate titanate (PZT) microcrystals", *Langmuir* **21**, 3207 (2005).

[8] Smolenskii G.A. and Agranovskaya A.I., "Dielectric polarization of number of complex compounds" *Soviet Physics Solid State* **1**, 1429 (1960).

[9] Smolenskii G.A., Isupov V.A., Agranovyskaya A.I., and Krainik N.N., "New ferroelectrics of complex composition IV" *Soviet Physics - Solid State* **2**, 2651 (1961).

[10] Kamzina L.S., Krainik N.N., Smolensky G.A., and Trepakov V.A., "Photoinduced phenomena in lead magnesium niobate crystal at the diffuse phase transition" *Ferroelectrics* **18**, 113 (1976).

[11] Bonner W.A., Dearborn E.F., Geusic J.E., Marcos H.M., and Van Uitert L.G., "Dielectric and electro-optic properties of lead magnesium niobate" *Appl. Phys. Lett*. **10**, 163 (1967).

[12] Cross L.E., Jang S.J., Newnham R.E., Nomura S., and Uchino K., "Large electrostrictive effects in relaxor ferroelectrics" *Ferroelectrics* **23**, 187 (1980).

[13] Jang S.J., Uchino K., Nomura S., and Cross L.E., "Electrostrictive behavior of lead magnesium niobate based ceramics" *Ferroelectrics* **27**, 31 (1979).

[14] Jang S.J., Uchino K., Nomura S., and Cross L.E., "Electrostrictive behavior of lead magnesium niobate based ceramic dielectrics" *Ferroelectrics* **27**, 31 (1979).

[15] Pan, W.Y., Gu W.Y., Taylor D.J., and Cross L.E., "Large piezoelectric effect induced by direct current bias in PMN:PT relaxor ferroelectric ceramics" *Japanese Journal of Applied Physics, Part 1: Regular Papers & Short Notes* **28**, 653 (1989).

[16] Choi, S.W., Shrout T.R., Jang S.J., and Bhalla A.S., "Morphotropic phase boundary in $Pb(Mg_{1/3}Nb_{2/3})O_3$-$PbTiO_3$ system" *Mater. Lett.* **8**, 253 (1989).

[17] Smolenskii, G.A. and Agranovskiya A.I., "Dielectric polarization of number of complex compounds". *Soviet Physics -- Solid State* **1**, 1429 (1960).

[18] Nomura, S., Yonezawa M., Doi K., Nanamatsu S., N. Tsubouchi, and M. Takahashi, "Crystal structure and piezoelectric properties of $Pb(Zn_{1/3}Nb_{2/3})O_3$- $PbTiO_3$ solid solution" *NEC Research & Development,* **29**, 15 (1973).

[19] Yonezawa M., Doi K., Nanamatsu S., Tsubouchi N., Takahashi M., Nomura S., "Crystal structure and piezoelectricity of the system $Pb(Zn_{1/3}Nb_{2/3})O_3$- $PbTiO_3$ " *Journ. of Jap. Soc. on Powder* **16**, 253 (1969).

[20] Kuwata, J., Uchino K., and Nomura S., "Phase transitions in the $Pb(Zn_{1/3}Nb_{2/3})O_3$-$PbTiO_3$ system" *Ferroelectrics* **37**, 579 (1981).

[21] Kuwata, J., Uchino K., and Nomura S., "Dielectric and piezoelectric properties of $0.91Pb(Zn_{1/3}Nb_{2/3})O3$-$0.09PbTiO_3$ single crystals" *Jpn J. Appl. Phys*, Part 1: *Regular Papers & Short Notes*, **21**, 1298 (1982).

[22] Park, S.-E. and Shrout T.R., "Characteristics of relaxor-based piezoelectric single crystals for ultrasonic transducers" *IEEE Transactions on Ultrasonics, Ferroelectrics, and Frequency Control*, **44**, 1140 (1997).

[23] Lopath, P.D., Park S.-E., Shung K.K., and Shrout T.R.. Ultrasonic transducers using piezoelectric single crystal perovskite. 1996. East Brunswick, NJ, USA: IEEE, Piscataway, NJ, USA.

[24] Noheda B., Cox D. E., Shirane G., Gonzalo J. A, Park S. –E. and Cross L.E., "A monoclinic ferroelectric phase in the $Pb(Zr_{1-x}Ti_x)O_3$ solid solution" *Appl. Phys. Lett*. **74**, 2059 (1999).

[25] Noheda B, Gonzalo J. A., Cross L. E, Guo R., Park S. –E, Cox D. E. and Shirane G, "Tetragonal-to-monoclinic phase transition in a ferroelectric perovskite: The structure of $PbZr_{0.52}Ti_{0.48}O_3$" *Phys. Rev. B* **61**, 8687 (2000).

[26] Guo R., Cross L. E., Park S. –E., Noheda B, Cox D. E and. Shirane G, "Origin of the High Piezoelectric Response in $PbZr_{1-x}Ti_xO_3$" *Phys. Rev. Letters* **84**, 5423 (2000).

[27] Noheda B, Gonzalo J. A., Caballero A, Mouse C, Cox and Shirane D. E, "New features of the morphotropic phase boundary in the $Pb(Zr_{1-x}Ti_x)O_3$ system" *Ferroelectrics* **237**, 541 (2000).

[28] Souza Filho A. G, Lima. Ayala K. C. V., A. P, Guedes I, Freire P. T. C, Mendes Filho J., Araújo E. B. and Eiras J. A., "Monoclinic phase of $PbZr_{0.52}Ti_{0.48}O_3$ ceramics: Raman and phenomenological thermodynamic studies" *Phys. Rev. B* **61**, 14283 (2000).

[29] Lima A. K., Souza Filho., A. G., Ayala A. P.,. Mendes Filho J,. Freire P. T. C, Melo F.E. A., Araújo E. B. and. Eiras J. A, "Raman study of morphotropic phase boundary in $PbZr_{1-x}Ti_xO_3$ at low temperatures" *Phys. Rev. B* **63**, 184105 (2001).

[30] Mishra R. S. K., Pandey D., Lemmens H. and Tendeloo G. Van, "Evidence for another low-temperature phase transition in tetragonal $Pb(Zr_xTi_{1-x})O_3$ (x=0.515,0.520) " *Phys. Rev. B* **64,** 054101 (2001).

[31] Topolov V. Y. and Turik A. V., "A new monoclinic phase and features of stress relief in $PbZr_{1-x}Ti_xO_3$ solid solutions" *Phys J..: Condens. Matter* **13**, L771 (2001)

[32] Noheda B., Cox D. E.,. Shirane G, Guo R., Jones B. and Cross L. E., "Stability of the monoclinic phase in the ferroelectric perovskite $PbZr_{1-x}Ti_xO_3$" *Phys. Rev. B* **63**, 014103 (2001).

[33] Noheda B., Cox D. E., Shirane G.,. Gao J and Ye Z. G., "Phase diagram of the ferroelectric relaxor $(1-x)PbMg_{1/3}Nb_{2/3}O_3$-$xPbTiO_3$" *Phys. Rev. B* **66**, 054104 (2002).

[34] Viehland D., Amin A.and Li J. F., "Piezoelectric instability in 〈 011〉 -oriented $Pb(B_{1/3}^{I}B_{2/3}^{II})O_3$–$PbTiO_3$ crystals" *Appl. Phys. Lett.* **79**, 1006 (2001).

[35] Noheda B., "Structure and high-piezoelectricity in lead oxide solid solutions" *Current Opinion in solid State and Materials Science* **6**, 27 (2002).

[36] Nye J.F., Physical properties of crystals: their representation by tensors and matrices. London: Oxford University Press, Oxford, (1967).

[37] IEEE Standard Definitions of Primary Ferroelectric Terms. ANSI/IEEE Std 180-1986

[38] Lines M. E. and Glass A. M., Principles and Applications of Ferroelectrics and Related Materials. Oxford, (1977).

[39] Strukov B. A. and Levanyuk A. P.. "Ferroelectric Phenomena in Crystals". Springer-Verlag Berlin Heidelberg, (1998).

[40] Damjanovic D., "Ferroelectric, dielectric and piezoelectric properties of ferroelectric thin films and ceramics" *Rep. Prog. Phys.* **61**, 1267 (1998).

[41] Tsurumi T., Kumano Y., Ohashi N., Takenaka T., and Fukunaga O., "90º domain reorientation and electric-field-induced strain of tetragonal lead zirconate titanate ceramics" *Jpn. J. Appl. Phys*. **36**, 5970 (1997).

[42] Tsurumi T., Y. Kumano, N. Ohashi, and O. Fukunaga. "Contribution of 90 domains in electric-field-induced strain of PZT ceramics", *Journal of the Korean Physical Society*, **32**, S1241 (1998).

[43] Burcsu E., Ravichandran G., and Bhattacharya K., "Large strain electrostrictive actuation in barium titanate". *Appl. Phys. Lett*., **77**, 1698 (2000).

[44] Chen L. and Roytburd A. L., "180° ferroelectric domains as elastic domains" *Appl. Phys. Lett.* **90**, 102903 (2007).

[45] Smolenskii G.A., "Physical phenomena in ferroelectrics with diffused phase transition" *J. Phys. Soc. Jpn*. **28**, 26 (1970).

[46] Nomura S. and Uchino K., "Recent applications of PMN-Based electrostrictors" *Ferroelectrics* **50**, 197 (1983).

[47] Kuwata J., Uchino K., and Nomura S., "Phase transitions in the $Pb(Zn_{1/3}Nb_{2/3})O_3$ -$PbTiO_3$ system" *Ferroelectrics* **37**, 579 (1981).

[48] Park S.E. and Shrout T.R., "Ultrahigh strain and piezoelectric behavior in relaxor based ferroelectric single crystals",*J. Appl. Phys*. **82**, 1804 (1997).

[49] Haertling G.H., "Ferroelectric ceramics: history and technology" *J. Am. Ceram. Soc.* **82**, 797 (1999).

[50] Harada K., S. Shimanuki, T. Kobayashi, S. Saitoh, and Y. Yamashita, "Crystal growth and electrical properties of $Pb[(Zn_{1/3}Nb_{2/3})0.91\text{-}Ti0.09]O_3$ single crystals produced by solution Bridgman method" *J. Am. Ceram. Soc.***81**, 2785 (1998).

[51] Harada K., S. Shimanuki, T. Kobayashi, Y. Yamashita, and S. Saitoh, "Growth of high-quality $Pb[(Zn_{1/3}Nb_{2/3})0.91\text{-}Ti0.09]O_3$ single crystals by excess ZnO addition". *J. Am. Ceram. Soc.* **85**, 145 (2002).

[52] Kobayashi T., S. Shimanuki, S. Saitoh, and Y. Yamashita, "Improved Growth of Large Lead Zinc Niobate Titanate Piezoelectric Single Crystals for Medical Ultrasonic Transducers" *Jpn. J. Appl. Phys.*,**36**, 4 (1997).

[53] Bhaumik I., G. Singh, S. Ganesamoorthy, A.K. Karnal, M.K. Tiwari, and V.S. Tiwari, "Compositional variation in 0.65 $PbMg_{2/3}Nb_{1/3}O_3$- $0.35PbTiO_3$ single crystals grown by high temperature solution growth technique" *Cryst. Res. Technol.*,**42**, 356 (2007).

[54] Karaki T., M. Adachi, Y. Hosono, and Y. Yamashita, "Distribution of piezoelectric properties in Pb[(Mg1/3Nb2/3)0.7Ti0.3]O3 single crystal" *Jpn. J. Appl. Phys.* **41**, 402 (2002).

[55] Ye Z.G., "Crystal chemistry and domain structure of relaxor piezocrystals" *Curr. Opin. Solid State Mater. Sci.*, **6**, 35 (2002).

[56] Samara G., "The relaxational properties of compositionally disordered ABO3 perovskites" *J. Phys., Conds. Matter* **15** R367 (2003).

[57] Cross L.E.,"Relaxor ferroelectrics: an overview" *Ferroelectrics* **151**, 305 (1994).

[58] Cross L.E., "Relaxor ferroelectrics" *Ferroelectrics* **76**, 241 (1987).

[59] Dmowski W., Vakhrushev S. B., Jeong I.-K., Hehlen M. P., Trouw F., and Egami T., "Local lattice dynamics and the origin of the relaxor ferroelectric behavior" *Phys. Rev*. Lett. 100, 137602 (2008).

[60] Roth M., Mojaev E., Dul'kin E., Gemeiner P., and Dkhil B., "Phase transition at a nanometer scale detected by acoustic emission within the cubic phase $Pb(Zn_{1/3}Nb_{2/3})O_3$-$xPbTiO_3$ relaxor ferroelectrics." *Phys. Rev. Lett.* 98, 265701 (2007).

[61] Dkhil B., Gemeiner P., Al-Barakaty A., Bellaiche L., Dul'kin E., Mojaev E., and Roth M., "Intermediate temperature scale T* in lead-based relaxor systems" *Phys. Rev. B* 80, 064103 (2009)

[62] Vakhrushev S.B., Kvyatkovsky B.E., Nabereznov A. A., Okuneva N. M. and Toperverg B. P., "Glassy phenomena in disordered perovskite-like crystals " *Ferroelectrics* **90**, 173 (1989).

[63] Vakhrushev S ., Nabereznov A., Sinha S . K., Feng Y. P. and Egami T., "Synchrotron X-ray scattering study of lead magnoniobate relaxor ferroelectric crystals" *J. Phys. Chem. Solids* **57**, 1517 (1996).

[64] Xu G., Shirane G., Copley J. R. D. and Gehring P. M., "Neutron elastic diffuse scattering study of $Pb(Mg_{1/3}Nb_{2/3})O_3$ " *Phys. Rev. B* **69**, 064112 (2004).

[65] Stock C., Birgeneau R. J., Wakimoto S., Gardner J. S., Chen W., Ye Z. -G. and. Shirane G, "Universal static and dynamic properties of the structural transition in $Pb(Zn_{1/3}Nb_{2/3})O_3$ " *ibid.* **69**, 094104 (2004).

[66] Smolenskii G. A., "Physical phenomena in ferroelectrics with diffuse phase transitions" *J. Phys. Soc. Jpn.* **28**, (Supl.) 26 (1970)

[67] Glinchuk M. D. and Farhi R., "A random field theory based model for ferroelectric relaxors" *J. Phys.: Condens. Matter* **8**, 6985 (1996).

[68] Bokov A. A. "Ferroelectric domains and polar clusters in disordered structures" *Ferroelectrics* **190**, 197 (1997).

[69] Westphal V., Kleemann W. and Glinchuk M. D., "Diffuse phase transitions and random-field-induced domain states of the ''relaxor'' ferroelectric $PbMg_{1/3}Nb_{2/3}O_3$" *Phys. Rev. Lett.* **68**, 847 (1992).

[70] Ishchuk V. M., "Was it necessary to introduce the notion "relaxor ferroelectrics"? - the problem of phase transitions in $(Pb,Li_{1/2}\text{-}La_{1/2})(Zr,Ti)O_3$, $(Pb,La)(Zr,Ti)O_3$, $Pb(Mg_{1/3}Nb_{2/3})O3$, $Pb(In_{1/2}Nb_{1/2})O_3$ and related materials. 1 model conceptions" *Ferroelectrics* **255** 73 (2001).

[71] De Mathan N., Husson E., Calvarin G., Gavarri J . R.,. Hewat A. W and Morell A., "A structural model for the relaxor $PbMg_{1/3}Nb_{2/3}O_3$ at 5 K" *J. Phys. Condens. Matter* **3**, 8159 (1991).

[72] Kleemann W., "Random-field induced antiferromagnetic, ferroelectric and structural domain states" *Int. J. Mod. Phys. B* **7** 2469 (1993).

[73] Imry Y. and Ma S . -K., "Random-Field Instability of the Ordered State of Continuous Symmetry", *Phys. Rev. Lett.* **35**, 1399 (1975).

[74] Isupov V. A. "Ferroelectric and antiferroelectric perovskites $PbB'_{0.5}B''_{0.5}O_3$", *Ferroelectrics* **289** 131 (2003).

[75] Cohen R. E., "Origin of ferroelectricity in perovskite oxides" *Nature* **358** 136 (1992).

[76] Bokov A. A., "Influence of disorder in crystal structure on ferroelectric phase transitions" *JEPT* **84**, 994 (1997).

[77] Egami T., "Atomistic mechanism of relaxor ferroelectricity" *Ferroelectrics* **267**, 101 (2002).

[78] Glinchuk M. D., "Relaxor ferroelectrics: from Cross superparaelectric model to random field theory" *British Ceramic Trans.* **103** (2004) 76.

[79] Pirc R. and Blinc R., "Spherical random-bond–random-field model of relaxor ferroelectrics" *Phys. Rev. B* **60**, 13470 (1999).

[80] Binning G and Roher H. "Scanning tunneling microscopy" *Helv. Phys. Acta* **55**(6), 726-735 (1982)

[81] Binning G., Quate C.F. and Gerber "Atomic force microscope" *Phys.Rev.Lett* **59**(6), 930-933 (1986)

[82] Güthner P. and Dransfeld K. "Local poling of ferroelectrics polymers by scanning force microscopy" *Appl.Phys.Lett.* **61**(9), 1137-1139 (1992).

[83] Yu H., Gopalan V., Indel J. S., and Randall C. A., "Domain switching and electromechanical properties of pulse poled $Pb(Zn_{1/3}Nb_{2/3})O_3$–$PbTiO_3$ crystals" *J. Appl. Phys*. **89**, 561 (2001).

[84] Lehnen P., Kleemann W., Woike T., and Pankrath R., "Ferroelectric nanodomains in the uniaxial relaxor system $Sr_{0.61}$-x$Ba_{0.39}Nb_2O_6$:Ce^{3+}" *Phys. Rev. B* **64**, 224109 (2001).

[85] Abplanalp M., Barošová D., Bridenbaugh P., Erhart J., Fousek J., Günter P., Nosek J., and Šulc M., "Ferroelectric domain structures in PZN–8%PT single crystals studied by scanning force microscopy" *Solid State Comm.* **119**, 7 (2001).

[86] Vakhrushev S. B., Naberezhnov A. A., Dkhil B., Kiat J.-M., Shvartsman V., Kholkin A., Dorner B., and Ivanov A., *AIP Conf. Proc.* **67**, 74 (2003).

[87] Bai F., Li J.-F., and Viehland D., "Domain hierarchy in annealed (001)-oriented $Pb(Mg_{1/3}Nb_{2/3})O_3$-x%$PbTiO_3$ single crystals" *Appl. Phys. Lett.* **85**, 2313 (2004).

[88] Bdikin I. K., Shvartsman V. V., and Kholkin A. L. "Nanoscale domains and local piezoelectric hysteresis in $Pb(Zn_{1/3}Nb_{2/3})O_3$-4.5%$PbTiO_3$ single crystals" *Appl. Phys. Lett.* **83**, 4232 (2003).

[89] Shvartsman V. V. and Kholkin A. L., "Domain structure of $0.8Pb(Mg_{1/3}Nb_{2/3})O_3$-$0.2PbTiO_3$ studied by piezoresponse force microscopy" *Phys. Rev. B* **69**, 014102 (2004).

[90] Salak A. N., Shvartsman V. V., Seabra M. P., Kholkin A. L., and Ferreira V. M., "Ferroelectric-to-relaxor transition behaviour of $BaTiO_3$ ceramics doped with $La(Mg_{1/2}Ti_{1/2})O_3$" *J. Phys.: Condens. Matter* **16,** 2785 (2004).

[91] Zeng H. R., Yu H. F., Hui S. X., Li G. R.,. Luo H. S, and Yin Q. R., "Domain orientation imaging of PMN–PT single crystals by vertical and lateral piezoresponse force microscopy" *J. Cryst. Growth* 267, 194 (2004).

[92] Shvartsman V. V., Kholkin A. L., Orlova A., Kiselev D., Bogomolov A. A., and Sternberg A, "Polar nanodomains and local ferroelectric phenomena in relaxor lead lanthanum zirconate titanate ceramics" *Appl. Phys. Lett.* **86**, 202907 (2005).

[93] Shvartsman V. V. and. Kholkin A. L, "Evolution of nanodomains in $0.9PbMg1_{/3}Nb_{2/3}O_3$-$0.1PbTiO_3$ single crystals" *J. Appl. Phys.* **101**, 064108 (2007).

Chapter 2

Materials Processing and Experimental Techniques

This Chapter is devoted to the details of the experimental procedure including the short description of sintering of PLZT ceramics and growth of single crystals, as well as methods used to orient and cut the samples. Besides, detailed description of the experimental techniques used for the characterization of both ceramics and single crystals is included.

Also, after describing the experimental setup, the operating principle of AFM will be illustrated, followed by a more detailed description of relevant AFM modes. Then the PFM operating principle will be explained along with the experimental procedures employed for domain imaging and quantitative PFM characterization. Finally, attention is devoted to the description of probes which are necessary for PFM measurements.

§ 2.1 Sample Preparation

PLZT Ceramics

$Pb_{1-x}La_x\left(Zr_yTi_{1-y}\right)_{1-x/4}O_3$ (*PLZT x/y/1-y*) ceramic samples (y=65 %, x=5–13 %) were sintered in the Institute of Physics of the Latvian Academy of Sciences and in Jozef Stefan Institute, Slovenia. Big disc-like ceramic samples (diameters of about 2 cm and thickness of 1.5 mm) were cut in several pieces to enable measurements by different techniques.

Let us consider in a more detail the process of synthesis the PLZT ceramics from the Latvian Institute of Physics. Figure 2.1 shows the flow chart used for the synthesis of PLZT powder by the *peroxohydroxopolymer (PHP) method*. The starting salts — $TiCl_4$, $ZrOCl_2 \cdot 8H_2O$, and $La(NO_3)_3 \cdot 6H_2O$ were dissolved in water. Coprecipitation occurs when various cations in the solution precipitate simultaneously. Control of the solution conditions – concentration, temperature, pH, mixing – is essential in order to yield a perfectly mixed precursor. The metal ions are coordinated by hydroxy (OH^-) or aqua (H_2O) ligands, depending on the charge (z) of the metal cation and the pH of the solution. Cations with z = 4 form all types of complexes over the whole pH range: $[M{-}OH_2]^{z+}$ $[M{-}OH]^{(z-1)+} + H^+ \leftrightarrow [M{=}O]^{(z-2)+} + 2H^{+3,5}$. To form a hydroxypolymer the concentration of metallic cation was at least 1.5 g ion/l for titanium and zirconium and 2.4 g ion/l for lanthanum, with pH about 9. From a mixed

solution of the corresponding metallic salts $TiCl_4$, $ZrOCl_2$, $La(NO_3)_3$ with 25% NH_4OH the hydroxopolymer of TiO_2–ZrO_2–La_2O_3 was obtained by coprecipitation as a curd-snow like deposit without any liquid phase. After calcination at 1000 ºC for 4 h white powder consisting of $TiO_2 \cdot ZrO_2 \cdot La_2O_3$ oxides was obtained.

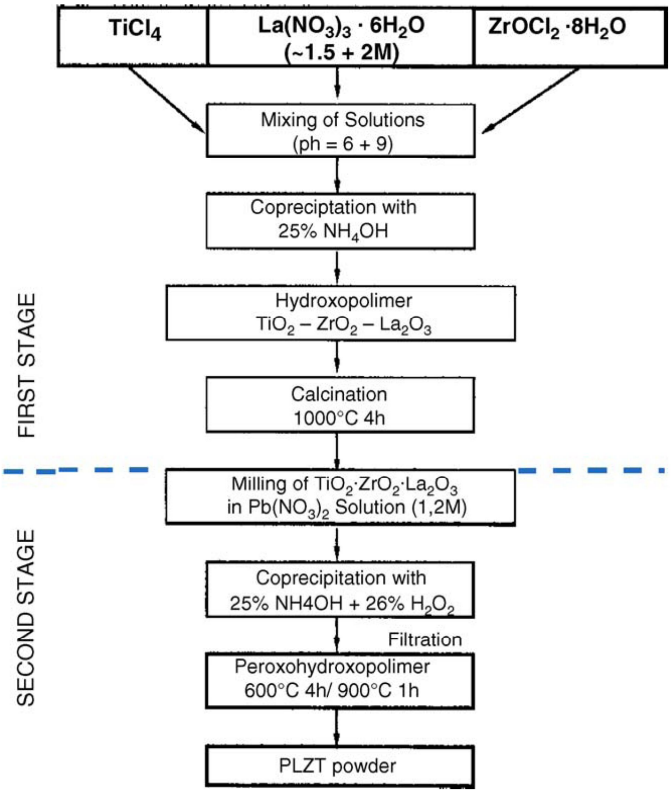

Figure 2.1. Flow chart for synthesis PLZT powder by peroxyhydroxypolymer method.

At the second stage PbO was introduced into the white powder consisting of mixed oxides of titanium, zirconium, lanthanum. The white powder of mixed Ti, Zr, La oxides was milled in $Pb(NO_3)_2$ solution of approximately 1.2M concentration for 10 h in a ball mill. After milling the suspension was coprecipitated by a reagent consisting of 25% NH_4OH and 26% H_2O_2. The obtained deposit after filtration was annealed at 600 ºC for 4 h, yielding an amorphous PLZT nanopowder. After the second calcination at 900 ºC for 1 h a crystalline powder of PLZT was obtained.

Finally, transparent PLZT ceramics were produced with a two-stage hot-pressing sintering process. The first stage was performed at 1150–1180 ºC for 1 h in vacuum with 20 MPa pressure. The second stage was performed at 1150–1200 ºC for 1–40 h depending on size of the pellet (15–90 mm in diameter) at a pressure 20 MPa in air or in O_2-rich atmosphere. In this way, chemically pure, high-quality ceramics were produced.

On the contrary, samples from Jozef Stefan Institute (Slovenia) were prepared by a conventional *mixed-oxide method* from commercial oxides. Stoichiometric mixtures of PbO (99.9+% Aldrich, Germany), ZrO_2 (99% Tosoh, Japan), TiO_2 (99.8% Alfa Aesar, Germany) and $La(OH)_3$ were used. $La(OH)_3$ was obtained from 99.99% La_2O_3 (Alfa Aesar, Germany) by equilibrating it in a humid atmosphere. The starting powders were homogenized in a planetary mill at 200 rpm for 2 h. After drying, the mixtures were calcined at 900 °C for 2 h, re-milled and re-calcined. After second calcination, the powders were milled in an attritor mill and dried. The powders were then uniaxially pressed under 100 MPa pressure and additionally isostatically pressed under 500 MPa. The PLZT compacts were then put in an alumina crucible, covered with a powder of an identical composition to and then sintered at 1200 °C for 1h in the oxygen atmosphere.

PZN-PT Single Crystals

The single crystals of PZN-4.5%PT were provided by Dr. P. Rehring (Penn State University) in the framework of the Single Crystal Initiative.

The starting agents PbO, ZnO, Nb_2O_5 and TiO_2 with a purity of 99.9% were weighed according to the stoichiometry (95.5% $Pb(Zn_{1/3}Nb_{2/3})O_3$–4.5%$PbTiO_3$) and thoroughly mixed in a mortar. The mixture was then placed into a platinum crucible and sintered at above 850 °C for 8 h. The sintered materials were mixed with the same ratio of PbO flux and ground homogeneously in an agate mortar with a pestle. Then the mixture was loaded into a Pt crucible with dimensions of Ø50 × 300 mm. In order to obtain large size crystals, special procedure was applied to the bottom of the crucible to eliminate poly-nuclei. The crucible was

sealed and moved to a refractory tube filled with alumina powder to support the crucible and prevent PbO evaporation at high temperature.

The final growth of PZN-PT was carried out in a home-made modified Bridgman furnace. The furnace was composed of three temperature zones: the high temperature zone for melting raw materials, the temperature gradient zone for crystallizing and the low temperature zone for annealing as-grown crystals. The furnace temperature was set to about 1150–1200 °C. After the raw materials were soaked for 10 h, the samples were lowered at 0.5 mm/h. Then the furnace was cooled to room temperature at a rate of 80 °C/h. As-grown ingot was taken out from the crucible and PZN-PT crystals were separated from the solidified flux by leaching in hot HNO_3 solution for more than 24 h. The crystals were then oriented along <001> direction and cut in the form of the platelets with major faces normal to these directions. The thickness of the plates was 200–300 μm. These samples had a yellow color, the cubic shape with the edge length up to 6 mm, and the cube faces parallel to the {001} cubic planes.

PMN-PT Single Crystals

The PMN–PT ingots were grown by using the vertical Bridgman (VB) method at the Institute of Physics of Rostov-on-Don State University. At first, the high purity oxide powders of PbO MgO, Nb_2O_5, and TiO_2 were employed to synthesize the raw materials for crystal growth in the stoichiometric ratio in a heated furnace through the columbite precursor method to improve the melt homogeneity and prohibit the formation of the parasitic pyrochlore phase. The oxides were mixed by ball-milling with zirconia balls in ethanol for 5 h and dried at about 90 °C for 2 h. Then, the presynthesized materials were charged into the Pt crucible with diameter of 26 mm, which was designed to avoid the side-wall nucleation and to decrease the chance of leakage. A Pt lid was welded to seal the crucible to prevent the component volatilization, reduce the composition variation and control the atmosphere. Then the charged Pt crucible was placed into a vertical Bridgman furnace. The Bridgman crystal growth was carried out by gradually lowering the crucible from the high temperature zone to the cold zone in the temperature gradient of about 17 °C/cm. The growth rate was 0.5 mm/h. The as-grown

ingot was oriented along pseudocubic <0 0 1> directions and cut into $5 \times 5 \times 0.5$ mm^3 pieces The samples were polished and supplied with Au electrodes

§ 2.2. Characterization

Scanning Electron Microscopy (SEM)

Scanning Electron Microscopy (SEM) is a type of electron microscope that images the sample surface by scanning it with a high-energy beam of electrons in a raster scan pattern. The resolution of the SEM can approach a few nm and it can operate at magnifications that are easily adjusted from about 10x to 300,00x. Not only a topographical information is produced by the SEM, but the composition near surface regions of the material can be obtained [1].

In SEM, a source of electrons is focused (in vacuum) into a fine probe that is rastered over the surface of the specimen (Figure 2.2). As the electrons penetrate the surface, a number of interactions occurs that can result in the emission of electrons or photons from the surface. A reasonable fraction of the electrons emitted can be collected by appropriate detectors, and the output can be used to modulate the brightness of a cathode ray tube (CRT) whose *x*- and *y*-inputs are driven , so that to raster the electron beam. In this way, an image is produced on the CRT; every point that the beam strikes on the sample is mapped directly onto a corresponding point on the screen.

The principal images produced in SEM are of three types: secondary electron images, backscattered electron images, and elemental X–ray maps. Secondary and backscattered electrons are conventionally separated according to their energies. They are produced by different mechanisms. Secondary electrons result from the inelastic scattering of electrons from the beam (primary electrons) with atomic electrons. During this process, some energy is transferred to atomic electrons which allows them to exit the solid. When the energy of the emitted electron is less than 50 eV, by convention it is referred to as a secondary electron. Higher energy electrons are primary electrons that have been scattered without loss of kinetic energy (i.e., elastically) by the nucleus of an atom.

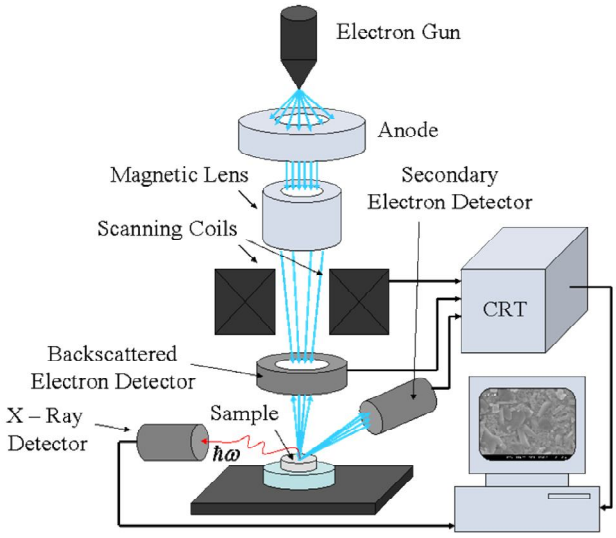

Figure 2.2 Schematics of the operation principle of SEM.

An additional electron interaction in SEM occurs when the electron from the beam (primary electron) collides with the surface and ejects a core electron from an atom. The excited atom will decay to its ground state by emitting a characteristic X–ray photon. The X–ray emission signal can be sorted by energy in energy dispersive X–ray detector. This forms the basis of the Energy dispersive X-ray Spectrometry (EDS), which is described below.

Energy Dispersive X-Ray Spectrometry (EDS)

Energy Dispersive X-ray Spectrometry (EDS) is an analytical technique used for the elemental analysis or chemical characterization of a sample. As a type of spectroscopy, it relies on the investigation of a sample through interactions between electromagnetic radiation and matter, analyzing X-rays emitted by the matter in response to being hit with charged particles. Its characterization capabilities are due in large part to the fundamental principle that each element has a unique atomic structure allowing X-rays that are characteristic of an element's atomic structure to be identified uniquely from each other. Most modern EDS systems can detect X-rays from all the elements in the periodic table above beryllium, Z = 4, if present in sufficient quantity.

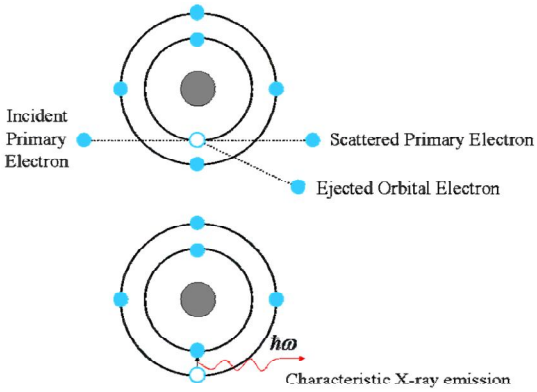

Figure 2.3 Schematic of the inner shell ionization and subsequent de-excitation by X-ray emission.

X-rays are produced as a result of the ionization of an atom by high-energy radiation wherein an inner shell electron is removed [1]. To return the ionized atom to its ground state, an electron from a higher energy outer shell fills the vacant inner shell and, in the process, releases an amount of energy equal to the potential energy difference between the two shells. This excess energy, which is unique for every atomic transition, will be emitted by the atom as an X-ray photon. For example, if the K shell is ionized and the ejected K-shell electron is replaced by an electron from the L shell, the emitted X-ray is labeled a characteristic Kα1 X-ray (Figure. 2.3). The hole that exists in the L shell will be filled by an electron from a higher shell, say the M shell, if one exists. This M – L transition may result in the emission of another X-ray, labeled in turn according to the one of the many M – L transitions possible. The cascade of transitions will continue until the last shell is reached. Thus, in an atom with many shells, many emissions can result from a single primary ionization.

The SEM images were taken for all the compositions studied by PFM. The magnifications were different for most samples and varied from 1000x to 6000x depending on the size of topographical features to be dispalyed.

X-ray Study of PZN-PT Crystals

The single crystal diffractometer available within the X-ray suite was a Gemini R from Oxford Diffraction.

The Gemini R is a Kappa geometry goniometer equipped with dual wavelength (Cu/Mo) fine focus X-ray sources, graphite monocromators and Enhance optics. The detector is a Ruby CCD area detector, which allows for extremely fast data collection of the entire Ewald sphere. The Oxford Diffraction CrysAlisPro software enables data collection, data intergration and absorption corrections to be made, and is used in conjunction with refinement software such as ShelX or Jana. For low temperature experiments (80-400 K) an Oxford Cryosystems "Cobra" is attached to the system. Additionally an optical stereomicrosope is used for mounting and alignment of samples.

X-ray diffraction studies were performed with DRON-2 and SIEMENS (D 500) diffractometers, using CuKα radiation. The samples were aligned with their *b** and *c** directions in the horizontal scattering plane (*a**, *b** and *c** it's axes in reciprocal lattice).

Lattice Parameters of the Crystals

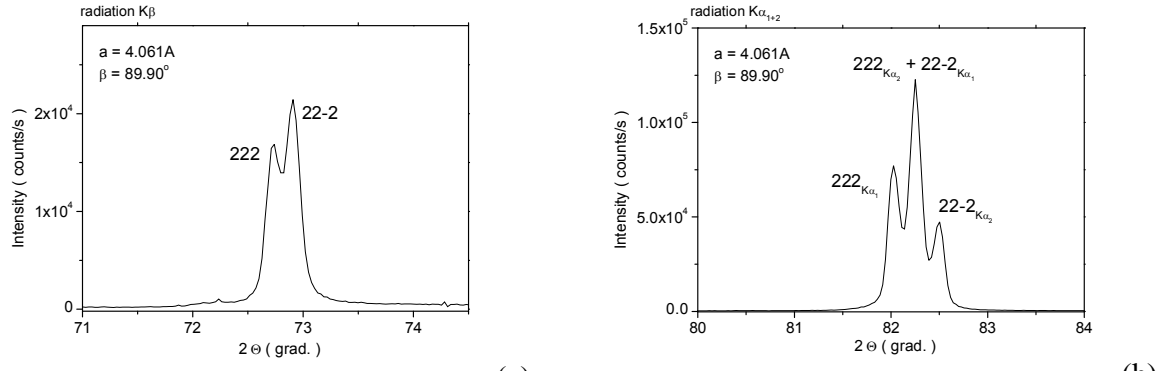

(a) (b)

Figure 2.4 X-ray diffractogram along [1 1 1] direction for the (111) oriented PZN-4.5PT single crystal (Θ–2 Θ scanning). (222) KCu β - (a) and (222) KCu α□ - (b).

The selected crystals were measured 5 mm across (mostly 4 · 3 mm^2) and up to 0.3 mm in thickness. Their single crystalline nature was confirmed by X-ray diffraction methods (Figure 2.4). The crystal structure is rhombohedral with the lattice parameters a = 4.061 Å and β =89.90°. The X-ray diffractogram of a crystal along [111] directions (Figure 2.4) shows double (hhh) and (hh-h) peaks, corresponding to apparent twinning of the crystals.

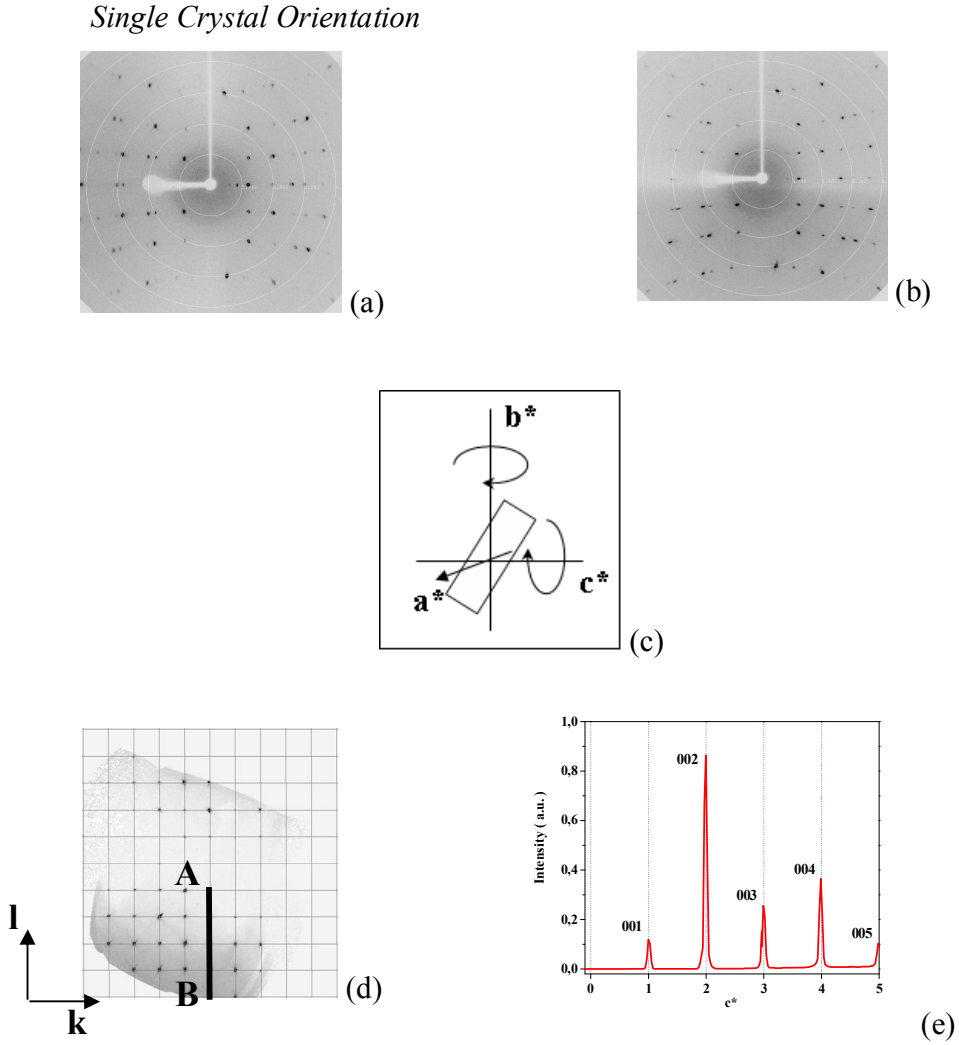

Figure 2.5 2D X-ray diffraction images, obtained by step rotation about axis b* (a) and c* (b). Schematic of the crystal orientation (c). Reciprocal space image (d) and cross-section along A-B line (e).

The X-ray diffraction images of the sample were obtained while rotating around *b** and *c** axes. From the 2D patterns (Figure 2.5 a,b), the point group symmetry in reciprocal space is close to *mmm*, i.e. it is definitively orthorhombic.

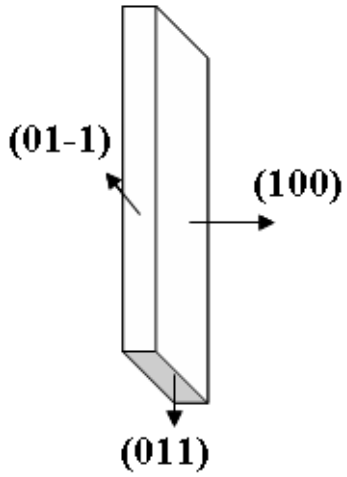

Figure 2.6 Schematic of the crystallographic orientation of the crystals.

This is manifested, for example, in the closeness of the values of the parameters *a, b* and *c* and α, β and γ ~ 90°. Then, precession photographs were taken with CuKα radiation for *0 k l* layer. The 0-layer (0kl) precession pattern is shown as an example in Figure 2.5(d). From X-ray diffraction images the orientation of the crystals has been determined as shown on Figure 2.6.

From XRD data may be conclude what investigated PZN-xPT crystals were (111) and (100) orientations with disorientation angle less 1° of wide side and (011) - lateral sides. Crystals have twinning structure with same volumes of the twins. Crystallographic lattice parameters are correspond to composition x=4.5%.

Electroding and Surface Preparation

Prior to making dielectric and PFM measurements, the samples were polished to obtain smooth and parallel surfaces. The ceramics and oriented crystals were polished to the desired thicknesses by using several abrasives in the following order:

- silicon carbide paper;
- diamond paste (15 μm, 6 μm, 3 μm, 1 μm, and 0.25 μm)
- colloidal silica aqueous suspension (~ 0.05 μm)

Submicron polishing was performed only when required by certain experiments, such a PFM domain studies. The final surface area of the polished samples used in this study varied from 5 × 5 mm^2, while the final thicknesses were about 100 to 200 μm.

Two different kind of electrodes, silver and gold, were applied to samples according to the measurement type and temperature range after polishing. For the dielectric properties as a function of temperature, the silver paste (Heraeus C1000) was applied on the surface and then fired at 400 °C for 30 min with the heating rate of 2 ºC/min. For polarization hysteresis (P-E) and temperature measurements, the samples were covered with gold. Gold electrodes (thickness ~ 80 nm) were sputtered onto the whole area of the parallel polished facets using a Polaron E5000 vacuum sputtering system working with argon partial pressure of 0.2 mtorr, acceleration voltage of 1.2 kV, and emission current of 12 mA.

For domain observation via Piezoresponse Force Microscopy, only one facet (upper facet) of the samples (single crystals and ceramics) was polished similarly to the method previously described, and colloidal-silica aqueous suspension (~ 0.05 μm) was used in the end.

Dielectric Characterization

For most applications of ferroelectric materials, dielectric properties, e.g., dielectric permittivity (ε) and dielectric loss ($tan\ \delta$), are important parameters which provide a great deal of information for understanding polarization mechanism. Commonly, the dielectric

permittivity or dielectric constant is obtained from the capacitance measurements under an *ac* electric field and is a function of frequency. Generally, this measurement is performed in the frequency range from several Hz to hundred MHz or even GHz. Thus, assuming that the sample is a capacitor filled with a dielectric medium (the ferroelectric sample), the relative permittivity (ε_r) can be obtained taking into account the sample thickness (t) and the area of the electrodes (A), using the following expression,

$$\varepsilon_r = \frac{Ct}{\varepsilon_0 A}, \tag{2.1}$$

where C is the measured capacitance and ε_0 is the dielectric permittivity of vacuum (8.85 × 10^{-12} F/m). In addition, dielectric losses are obtained from the ratio of the imaginary part (ε'') to the real part ($\varepsilon' = \varepsilon_r$) of the permittivity, where ε'' given by

$$\varepsilon'' = \omega RC, \tag{2.2}$$

where ω is the frequency and R is the resistance. This information is necessary to get insight into the domain activity, phase transitions and overall quality of the samples. Typically, tan $\delta<0.02$ is considered to indicate high quality of the sample is terms of loss factor.

Dielectric properties were measured from room temperature up to 450 ºC under heating and cooling rates 1 ºC/min using a Hewlett-Packard precision LCR-meter (Model HP4284A) connected to a PC via a GPIB card and working in the frequency range from 100 Hz to 1 MHz. The temperature was controlled using an Eurotherm 2404 controller and a thermocouple positioned very close to sample without touching it, reaching a temperature control with a precision of ±0.5 ºC. Prior each measurement, a correction for the stray capacitance of the sample holder and connecting wires was performed using the LCR-meter which is necessary to separate the capacitance of the sample from other spurious capacitances.

Ferroelectric Hysteresis Measurements

To confirm the ferroelectric properties of the studied ceramics and single crystals, the polarization-electric field (P-E) hysteresis loops were measured using a modified Sawyer-Tower circuit (see Figure 2.7).

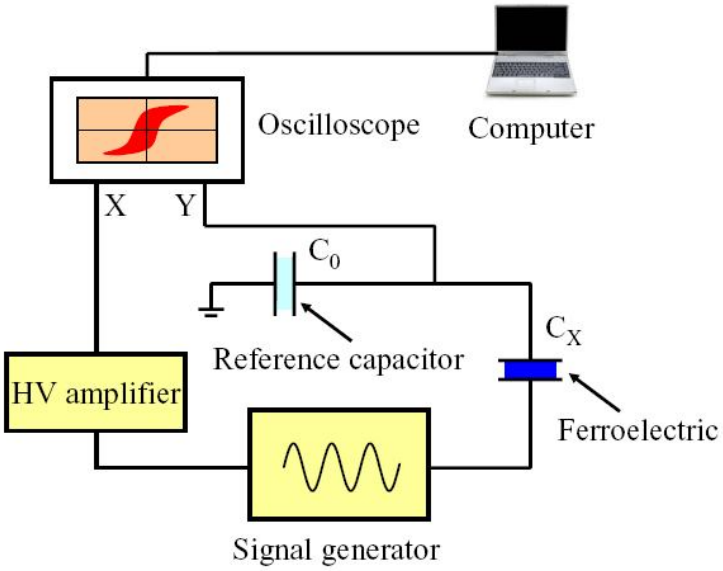

Figure 2.7 Sawyer-Tower circuit used for P-E hysteresis loop acquisition in bulk ceramics and single crystals.

An alternating voltage is applied across the electrodes on the ferroelectric sample (C_x) connected to the horizontal channel an oscilloscope, hence the signal plotted on the horizontal channel of the oscilloscope (V_x) is proportional to the electric field across the sample (E), which can be calculated considering the sample thickness (t),

$$E = \frac{V}{t}. \tag{2.3}$$

C_0 is a linear capacitor with a large capacitance of ~ 1 μF that is connected in series with the ferroelectric material C_x in such a way that most of the voltage drops across the sample. The voltage across the linear capacitor $C_0(V_y)$ is therefore proportional to the

polarization (P) of the ferroelectric material, which is calculated tacking into account the area of the electrodes (A), using the following expression:

$$P = \frac{C_0 V_y}{A}. \tag{2.4}$$

A typical loop for a ferroelectric material is shown in Figure 1.3. The observation of the *P-E* hysteresis loop is frequently used for the identification of ferroelectrics as well as for the determination of the spontaneous (P_S) and remanent (P_r) polarizations and the coercive field (E_C) of the studied material. All these parameters can be computed from the recorded hysteresis loop as well as the value of relative permittivity (ε_r) calculated from the slope of the *P-E* linear behavior at saturation:

$$P = \varepsilon_r \varepsilon_0 E. \tag{2.5}$$

The hysteresis loops were measured in a sinusoidal electric field at a frequency of 50 Hz and at amplitudes up to 20 kV/cm. The measurements were carried out in the temperature range from 25 to 130 °C. During P-E hysteresis measurements, the samples were submerged in silicon oil to prevent arcing. The hysteresis loop was visualized and recorded using a digital oscilloscope (LeCroy WaveRunner LT322) and the acquired data was saved on a floppy disk. Once again, because of the small transverse size of the samples, a correction for the stray capacitance of the sample holder and connecting wires was necessary to separate the P-E hysteresis loop of the sample from the linear contribution due to stray capacitance.

§ 2.3 Analysis of Nanoscale Properties (AFM, PFM)

Piezoresponse Force Microscopy (PFM) is an Atomic Force Microscopy (AFM) technique. In this paragraph, after describing the experimental setup, the operating principle of AFM will be illustrated, followed by a more detailed description of certain AFM modes. Then the PFM operating principle will be explained along with the experimental procedures

employed in order to perform domain imaging and quantitative characterization. Finally, attention is devoted to the description of probes which are necessary for PFM measurements.

§ 2.3.1 Experimental Setup

The representation in Figure 2.8 shows the setup, including all the components of the measurement equipment. The latter is composed of commercial Scanning Probe Microscopy (SPM) systems by Agilent and Bruker (microscope, controllers, and signal access module), an external lock-in amplifier and relative control computers. The SPM systems include Multimode Veeco (currently Bruker) Microscope (with Nanoscope IIIA Controller) and Agilent AFM/SPM Microscope (with PicoSPM II 3500 Controller) (Figure 2.9), associated controllers, built in lock-in amplifier, signal access module and a control computer.

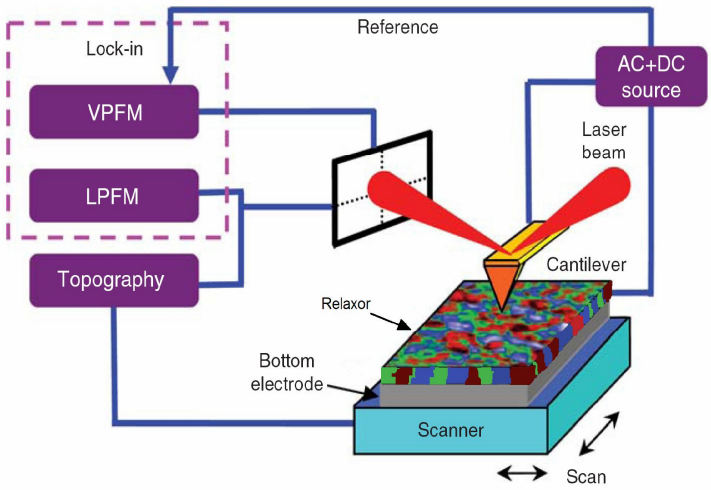

Figure 2.8 Schematic representation of the PFM experimental setup.

These systems were used for the standard topography and polarization imaging in all studied materials. To perform quantitative characterization, the external lock-in amplifier (LA) was used in connection with the SPM system (only for Multimode Veeco (Bruker) Microscope). For this purpose, the signals from and to the microscope are acquired by the LA via a signal access module. The output data from the LA are retrieved, elaborated and stored

by the computer. During these operations the SPM computer runs custom procedures, controlling probe movements and voltage signals. To have proper synchronization during the operation, an additional signal is sent by the SPM system. It is used as triggering signal for the procedures controlling the LA.

Atomic Force Microscope

In general, SPM instruments include a vast range of microscopes sharing the principle of a proximity probe imaging a surface by lateral scanning. With the advent of Scanning Tunneling Microscopy (STM) in 1981 [2], the most widely used techniques nowadays are STM, Near-field Scanning Optical Microscopy (NSOM) and AFM. AFM is currently the most broadly employed tool in the SPM family, since it can measure a wide range of surface properties on any kind of materials, ranging from topography to surface potential, from electrical to magnetic properties. Moreover, the measurements can be performed under normal (ambient) temperature and pressure, thus not requiring special environmental conditions. Its resolution in the Z direction is of the order of subnanometer, while the lateral one is limited by the tip radius of curvature, i.e., in the order of few tens of nanometers.

(a) (b)

Figure 2.9 Images of the AFMs used: Multimode Veeco (Bruker) (with Nanoscope IIIA Controller) (a) and PicoScan (with PicoPlus 3500 Controller) from Agilent (b).

Operating Principle

AFM is based on a *probe*, constituted by a sharp tip at the end of a flexible cantilever. The tip has the height of the order of micrometers and a radius of curvature of generally 10-20 nm. Upon proximity to a surface, the cantilever reacts to the forces between the tip and the investigated surface, deflecting in first approximation according to Hooke's law. Various kinds of atomic forces are involved in such interaction, among which the van der Waals force is the dominant one. By scanning the tip over the surface under investigation, the cantilever reacts to the topography of the sample. A feedback loop monitoring the cantilever's deflection keeps either the tip at a constant distance to the surface or the contact force constant (depending on the scanning mode used) by moving the probe downwards or upwards. Such movement gives the topography of the scanned surface.

The deflection of the cantilever is measured by the optical lever mode. A laser light from a solid-state diode is reflected off the back of the cantilever and collected by a *photodetector*. It consists of closely spaced photodiodes (Figure 2.10) whose output signal is collected by a differential amplifier. Angular displacement of cantilever results in one photodiode collecting more light than the other photodiode, producing an output signal. Therefore, the detector keeps track of the cantilever's deflection.

The utilization of a quadrupole photodiode enables to separate vertical and lateral contributions to the signal:

$$S_V = \frac{(A+B)-(C+D)}{(A+B+C+D)}$$

$$S_L = \frac{(A+C)-(B+D)}{(A+B+C+D)} \qquad (2.7)$$

The differential signal between the top and bottom elements provide a measure of the vertical deflection S_V of the cantilever. Similarly, the differential signal between the sum of the

two left elements and the sum of the two right elements provides a measure of the torsion in the cantilever S_L.

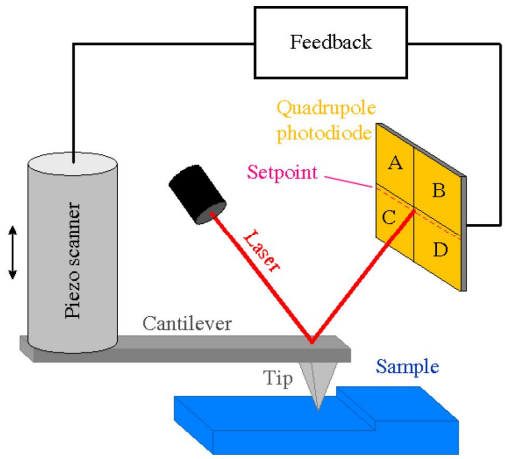

Figure 2.10 Schematic of AFM in contact mode. When the cantilever deflects in reaction to a feature on the surface, the laser signal on the photodetector moves away from the vertical setpoint. The feedback loop, via the scanner, adjusts the vertical position of the probe until the position is restored.

To accurately track the surface topography, a *Z feedback* method is employed. For any mode used to image a surface, a setpoint is assigned, determining the distance or the contact force with the sample. The Z *feedback* continuously compares the signal from the photodetector to the setpoint and regulates the probe's vertical position in order to keep the two at the same value. This is achieved by sending a voltage input to the *scanner*, on which the probe is mounted. The scanner is a tube made of a piezoelectric ceramic, which allows precise positioning both along the Z axis and the lateral axes. Surface imaging is operated by raster movement of the scanner in X and Y direction. Each line of the selected area is scanned forth (*trace*) and back (*retrace*), an operating mode useful for setting the proper scanning parameters and detect artifacts in the scanned image.

§ 2.3.2 AFM Modes

Of the many modes in which the AFM can operate, the following ones can be used in conjunction with the PFM.

Tapping Mode or Amplitude Modulation

The most widely employed AFM mode for topography imaging is the Tapping Mode (TM) or amplitude modulation. The TM-AFM operates by scanning the probe across the sample surface, while the cantilever is oscillated by a piezoactuator. Operation can take place in ambient and liquid environments. In the first case, the cantilever oscillates at or near its resonance frequency with amplitude ranging typically from 10 nm to 100 nm. In liquid, the oscillation need not be at the cantilever resonance. The tip slightly "taps" on the sample surface during scanning, contacting the surface at the bottom of its swing. Variations in the tip-surface average distance make the oscillation amplitude to change. The feedback loop monitors the RMS of the oscillation, acquired by the photodetector and keeps it constant at the setpoint value by vertical movements of the scanner.

Its vertical position at each (X,Y) data point is stored in the computer to form the topographic image of the sample surface.

With respect to contact mode AFM (which will be described in the following section), TM-AFM has several advantages:

- Higher lateral resolution on most samples (1 to 5 nm)
- Lower forces and less damage to soft samples imaged in air
- Lateral forces virtually eliminated

and one drawback:

- Slightly slower scan speed than in contact mode AFM

Contact Mode

Contact mode is the basic option for a series of measurements of surface properties, including conductive AFM and PFM. The probe is brought towards the surface by extending the Z scanner. When the tip enters in contact with the surface the cantilever starts bending. The extension of the Z scanner stops when the cantilever deflection reaches the predetermined setpoint, corresponding to a chosen contact force. Scanning over the surface features causes the cantilever deflection to change. The feedback loop regulates the vertical Z scanner position in a way to maintain the deflection equal to the setpoint. The recorded Z scanner movement gives the topography.

The contact force can be determined by performing the so-called force-distance procedure. It consists of the 2-stage movement of Z scanner, so that the probe first approaches the surface and then retracts from it. The deflection of the cantilever is plotted versus this movement, as shown in Figure 2.11. Starting from a non-contact position the probe descends towards the surface. The cantilever is not bent and the deflection remains constant (black line, segment 1), until in proximity of the surface the tip is pulled down by attractive forces. The tip comes in contact with it and the cantilever bends downwards, with a decrease in deflection (segment 2). Once in contact, a further descent of the probe makes the contact force to increase, and the cantilever bends upward with a consequent increase in deflection (segment 3). When the Z scanner is moving in the reverse direction, the probe starts ascending, the force decreases and the cantilever relaxes (red line, segment 4). Attractive forces between the tip and the surface make the tip to hold on it, causing the cantilever to bend downward (segment 5). The deflection decreases further until the spring force of the cantilever overcomes the attractive forces (segment 6) at the pull-off point. The cantilever comes back to the non-contact position (segment 7).

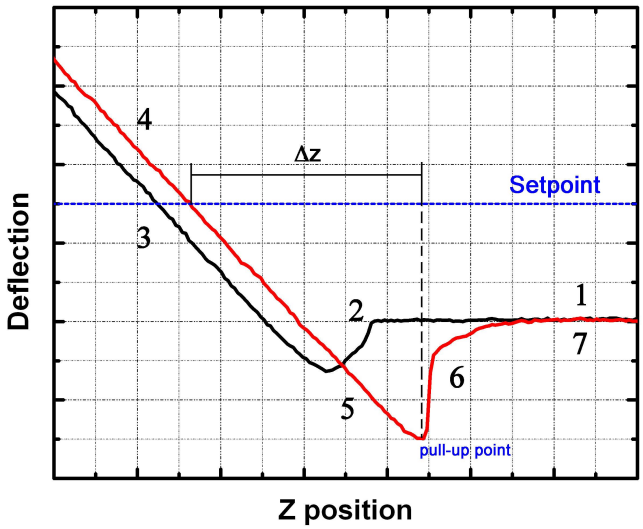

Figure 2.11 A typical force-distance plot. The black and red lines represent the response from the tip approaching to and retracting from the surface.

The choice of the deflection setpoint defines the contact force. By the obtained force curve it is possible to calculate the actual contact force maintained by the feedback loop during the measurements. The vertical deflection of the cantilever corresponds to the Z scanner movement. Therefore, if the spring constant of the cantilever k is known, by applying Hooke's law it is possible to calculate the contact force F_{con}:

$$F_{con} = k \cdot \Delta z \,, \tag{2.8}$$

where z is the distance covered by the Z scanner to bring the cantilever deflection from the setpoint to the pull-up point. Typical contact forces employed are in the range of 10^{-9} *N*. In addition, this procedure allows the calibration of the signal detected by the photodetector, by determining the *deflection sensitivity*. The Z sensitivity represents the Z deflection value versus the Z scanner movement (provided that the latter has been calibrated properly). It follows that the sensitivity is calculated by the slope of the force plot in the contact regime (segments 4 and 5 in Figure 2.11).

Contact mode implies the following advantages:

- High scan speed
- Only AFM technique which can reach "atomic resolution"
- More effective on rough surfaces with extreme changes in vertical topography and disadvantages:
- Lateral forces can distort features in the image.
- Forces normal to the tip-sample interaction can be high in air due to capillary forces from the adsorbate layer
- Lateral forces and high normal forces can result in reduced spatial resolution and damage of soft samples

§ 2.3.3 Piezoresponse Force Microscopy

History of PFM

The motivation for the development of PFM was the necessity of nondestructive local measurement of the polarization at nanoscale. In the ideal case, the local electromechanical response can be linked to local polarization through the piezoelectric constant tensor. In fact, its components are related to the polarization vector by the Devonshire theory via the electrostriction coefficient [3, 4, 5], as described in §1.4.

In the first half of the 90's several groups modified an AFM setup using the tip as movable electrode in order to detect polarization in ferroelectric samples. In 1991 the group of Dransfeld [6] used a scanning tunneling microscope (STM) to measure the piezoelectric coefficient in a vinylidene fluoridetrifluoroethilene (P(VDF-TrFE)) sample provided with a top gold electrode. Applying an alternating voltage across the sample, they induced a vibration, which was extracted by a lock-in amplifier connected to the feedback loop of the STM operating in constant current mode. By doing that, they were able to measure the local longitudinal piezoelectric coefficient d_{33} and relative hysteresis loop. The d_{33} value varied over the surface, and they could not exclude that it came from variations of tunnelling conditions of the gold electrode. In the same year, the same group [7] used a scanning near field acoustic

microscope (SNAM) to measure piezoelectricity in the same material. By applying an alternating field, without need of top electrode, the induced vibration signal was extracted by lock-in techniques. Local d_{33} measurements and its hysteresis loop could be obtained, but with lateral resolution more than 1 μm. Finally, one year later [8] the same group employed an AFM using the tip as top electrode for both polarizing and detecting (by applying alternate voltage) polarization micron-size domains in P(VDF-TrFE).

Later, several groups used PFM for investigating the piezoelectric properties of PZT thin films [9,10,11] and pointing the attention on ferroelectrics in view of data storage application, as Hidaka proposed in 1996 [12]. The increasing application of ferroelectrics in miniaturized systems and memories led to a growing necessity of characterization of these materials at the nanoscale. The technique evolved with the combination of vertical and lateral PFM, and the area of research expanded over different materials [13,14,15,16]. Domain dynamics was investigated by Gruverman [17] and the group of Triscone [18], along with the study of their functional properties by Alexe [19,20].

On the other hand, the need for a proper interpretation of the data obtained by PFM pushed other groups to study the processes underlying PFM measurements. At the very beginning of the new millennium, Kalinin et al. [21,22,23] studied the electrostatic and mechanical influence on the measuring process. As it will be described in §2.1.1, they found that the electrostatic contribution to the piezoresponse is predominant with respect to the electromechanical contribution for low contact forces (“weak indentation regime”), while it is negligible for high contact forces (“strong indentation regime”), still being within the limit of elastic deformation of the sample. They found that the piezoresponse depends strongly on the experimental conditions and, in particular, on the mechanical properties of the cantilevers, as observed also by Harnagea [24]. Specifically, they realized that the piezoresponse is strongly affected by the frequency of the excitation voltage, which must be below the resonance frequency of the cantilever.

Harnagea et al investigated the relationship between the piezoelectric tensor and the polarization [25]. They showed that the piezoelectric tensor, and thus the measurements in PFM, is strongly dependent on the angle between the spontaneous polarization and the vertical

displacement measured by PFM. The relationship is straightforward only under certain conditions.

In 2006, Jungk et al. [26] elaborated a vectorial analysis of the PFM mechanism for the detection of the piezoresponse signal. In particular, they claimed that the presence of background noise from the experimental system is responsible for many irregularities in PFM measurements. In the same year, Peter et al. [27] attributed the main error in the quantitative PFM acquisition to the existence of various adsorbates on the surface, suggesting that operation in vacuum after *in-situ* heating is recommended.

PFM Operating Principle

Piezoresponse Force Microscopy is an extension of contact mode AFM technique, and is based on the converse piezoelectric effect. Using the AFM tip as a top electrode, an electric field is imposed over the investigated sample. For this purpose, the sample is usually grown/supplied with a bottom electrode. In response, ferroelectric material (being also a piezoelectric) changes its local dimensions due to piezoelectric effect.

As shown by equation 1.3, the induced piezoelectric strain is a linear function of the applied electric field. The piezoelectric tensor relates the strain to the applied field. The piezoelectric coefficient of major interest is the longitudinal coefficient d_{33}. As the PFM experimental environment is configured, it is assumed that the modulation voltage generates a field in the Z direction, corresponding to the direction normal to the surface of the sample. For example for thin films, this field can be regarded as homogeneous in the volume under the tip provided the thickness is less than the contact area. Following this assumption, formula 1.2 can be written as:

$$x_z = d_{33} E_z . \tag{2.9}$$

The Z component of the electric field can be calculated by dividing the applied voltage by the sample thickness. In the same way, by dividing the induced displacement in the Z

direction by the thickness of the sample, the Z strain component is obtained. Therefore equation 2.9 can be written as:

$$\Delta z = d_{33} V \,, \tag{2.10}$$

with Δz positive for upward polarization and negative for downward polarization.

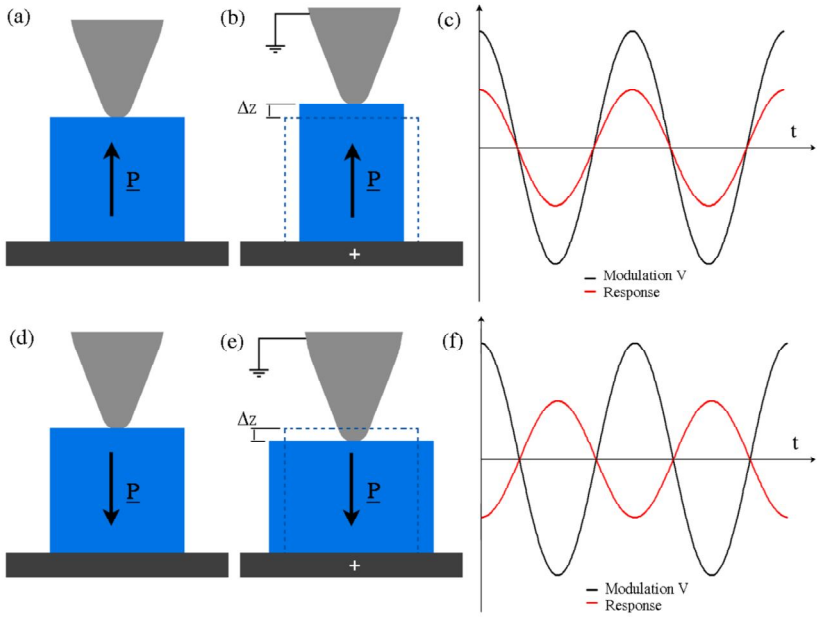

Figure 2.12. Principle of the phase shift in piezoresponse. In case of a volume with upward polarization (a), the application of an upward field makes the volume expand (b) and contract for downward field. Therefore, the vibration induced by alternating field is in phase with the excitation (or modulation) voltage (c). For a domain with downward polarization (d), the volume contracts for upward field (e) and the vibration is out of phase with the modulation voltage.

Given the small magnitude of the piezoelectric effect, the electromechanical response to an applied DC field is typically in the order of subnanometer. In fact, considering a ferroelectric with d_{33}=50 pm/V, an applied voltage of 4 V induces a displacement Δz=2 Å. The resolution of the AFM is very close to this value. Furthermore, surface roughness is commonly of the order of nanometers, thus topography features easily hinder the piezoelectric change. This inconvenience is solved by the use of an alternating voltage

$V = V_{AC}\sin(\omega t)$ (*modulation voltage*) combined with lock-in techniques. The modulation voltage generates an alternating field across the sample, which forces it to vibrate. The phase Φ of such a vibration depends on the polarization direction inside the sample. If the latter has the same direction with the applied field, the vibration of the sample is in phase with respect to the modulation voltage ($\Phi \approx 0$). Conversely, for opposite directions it is out of phase ($\Phi \approx 180º$, see Figure 2.12). Considering the previous assumption for which the voltage is applied from the bottom electrode (zero phase applied field pointing upwards), the electromechanical vibration of the sample can be represented by:

$$\Delta z(t) = d_{33}V_{AC}\sin(\omega t + \Phi). \tag{2.11}$$

Such a vibration is superimposed on the topography signal, which, as already mentioned, is an order of magnitude larger. The piezoelectric vibration is extracted from the overall signal using a lock-in amplifier. The signal extracted is referred as *piezoresponse* signal [28] and is composed of phase and amplitude (PR_{phase} and $PR_{amplitude}$). It can be represented as:

$$PR = d_{33}V_{AC}\cdot\cos(\Phi)\,, \tag{2.12}$$

being Φ the PR_{phase} and $d_{33}V_{AC}$ the $PR_{amplitude}$, related to direction and magnitude of the out-of-plane polarization vector, respectively.

In the same way, the direction and magnitude of the *lateral piezoresponse* can be extracted. In fact, as described in §2.2.1, the utilization of a quadrupole photodiode allows separating vertical and lateral signals. Therefore, lateral vibrations of the sample can be extracted from the latter. The lateral piezoresponse is related to the transverse component of the piezoelectric tensor, i.e. to the in-plane polarization. Thus, using both vertical and lateral piezoresponses, a three-dimensional picture of the polarization state can be mapped.

Hysteresis Measurements

As asserted in §1.3, the occurrence of a ferroelectric P-E hysteresis loop is a necessary condition fo ferroelectricity. Since the piezoelectric tensor is intrinsically related to the polarization, the occurrence of a piezoelectric hysteresis is a proof of ferroelectricity, too. Thus PFM is a suitable tool for the detection of ferroelectricity in a material. The piezoelectric hysteresis loop measurement makes it possible to locally characterize the piezo/ferroelectric properties.

Hysteresis loops are acquired in order to gain information about the switching behavior of the polarization. They are obtained by sweeping the DC voltage from zero to above the positive and then back below the negative coercive voltage. At each value of voltage the piezoresponse is measured. The plot of the PR_{phase} evidences the coercive voltage for positive and negative voltages. The effective piezoelectric coefficient is simply calculated by dividing the $PR_{amplitude}$ by the modulation voltage. The obtained d_{33} *hysteresis loop* is characterized by two zero values corresponding to coercive voltages values. These are the result of the balancing of the responses from the switched and non-switched polarization domains during the switching process. After the nascent domain propagates through the thickness underneath the tip, the full response is recovered and piezoresponse reaches the saturation. By plotting PR_{ampl}*cosPR_{phase}, a *piezoresponse hysteresis loop* is obtained. From this, various characteristic paramters of ferroelectrics can be evaluated [29, 30]:

- forward and reverse coercive biases are defined as the two zero piezoresponse points V^+ and V^-.
- imprint I_m that is present in case of asymmetry of the hysteresis is defined as $I_m = (V^+ + V^-)/2$.
- forward and reverse saturation responses R^+_S and R^-_S: the values of piezoresponse corresponding to saturated polarization, measured at maximum and minimum DC voltage value.
- forward and reverse remanent responses R^+_0 and R^-_0, measured at zero DC voltage value.

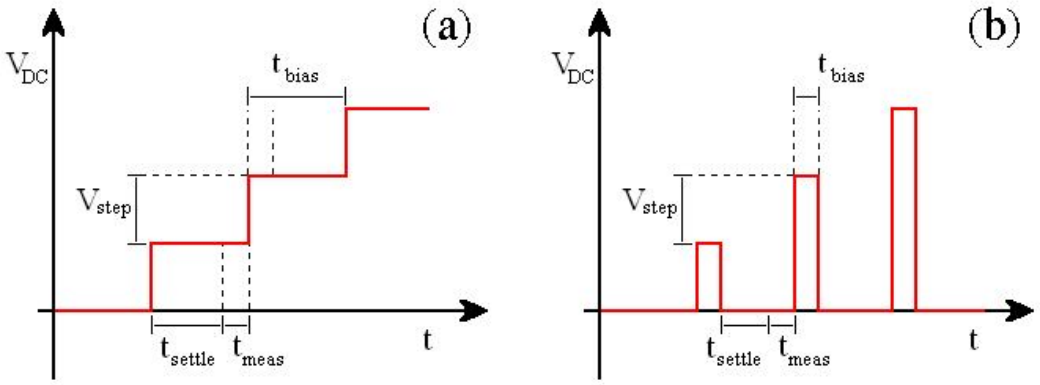

Figure 2.13 *DC* voltage waveforms for the in field (a) and remanent (b) hysteresis loops.

Hysteresis loops can be obtained by two different procedures, which determine the shape of the loop and values of the corresponding paramters:

- In-field hysteresis loops are obtained by measuring the piezoresponse in the presence of electric field. The DC voltage is thus ramped in steps of duration t_{bias}, and the piezoresponse is measured after a time t_{settle} during the step (Figure 2.13(a));
- Remanent hysteresis loops are the result of measuring the piezoresponse after the field is turned off. Therefore, the voltage is pulsed for a time t_{bias}, and after a time t_{settle} the piezoresponse is measured after the time t_{meas} (Figure 2.13(b)). In this way, the tip-surface electrostatic interaction is reduced and the piezoelectricity is investigated without the influence of the DC voltage previously applied. The actual remanent piezoresponse is detected, so the retention characteristics of the ferroelectric are revealed.

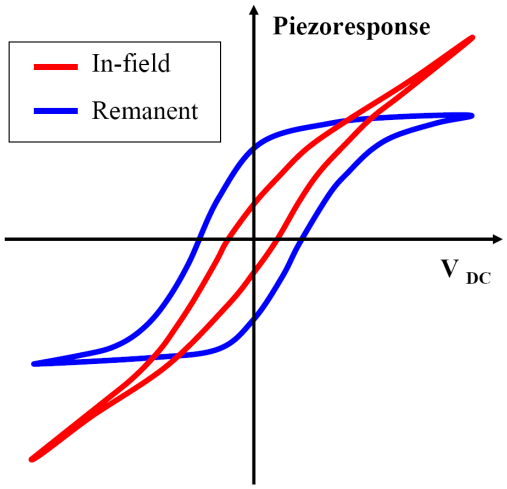

Figure 2.14 Schematic piezoresponse hysteresis loops of continuous dc ("in-field loop") and pulse DC modes ("remanent loop").

A big difference in the loops obtained by the two procedures is the piezoresponse behavior after the switching from one polarization state to the other (see to Figure 2.16). Whereas the remanent loop is saturated under high voltage, the in-field loop contains a linear part. The linear part can be used to estimate the electrostatic interaction between the film and the sample.

The results shown in this thesis are obtained with remanent hysteresis loops only, since in the absence of DC field the electrostatic interactions vanish.

Theory of Domain Switching via PFM

The progress in experimental studies has stimulated a parallel development of theoretical models to relate measured contrast and PFM hysteresis loop parameters to the materials properties. A number of such models are based on the interpretation of phenomenological characteristics of piezoresponse hysteresis loops similar to macroscopic P-E loops, such as slope, imprint bias, coercive bias, remanent response, and work of switching [20, 31]. A number of authors attempted to relate local PFM hysteresis loops and macroscopic *P-E* measurements, often demonstrating good agreement between the two [32, 33]. Several

groups combined local detection by PFM with a uniform switching field imposed through the thin top electrode to study polarization switching in ferroelectric capacitor structures. Spatial variability in switching behavior was discovered by Gruverman et al. and attributed to strain [34] and flexoelectric [35] effects and defect influence [36]. The analysis of the tip-induced domain growth process during hysteresis loop measurements in Piezoresponse Force Spectroscopy (PFS) should include the individual stages delineated in Figure 2.15, i.e., domain nucleation and growth for forward bias sweep, with either reverse domain nucleation or shrinkage on reverse bias sweep. A number of phenomenological models have been developed based on the classical work of Landauer [37], where domain nucleation in ferroelectrics under a homogeneous electric field was studied. In the original work by Abplanalp [38], polarization reversal in the inhomogeneous electric field of an AFM tip for a semi-ellipsoidal domain with infinitely thin domain walls under the absence of charge compensation was first considered.

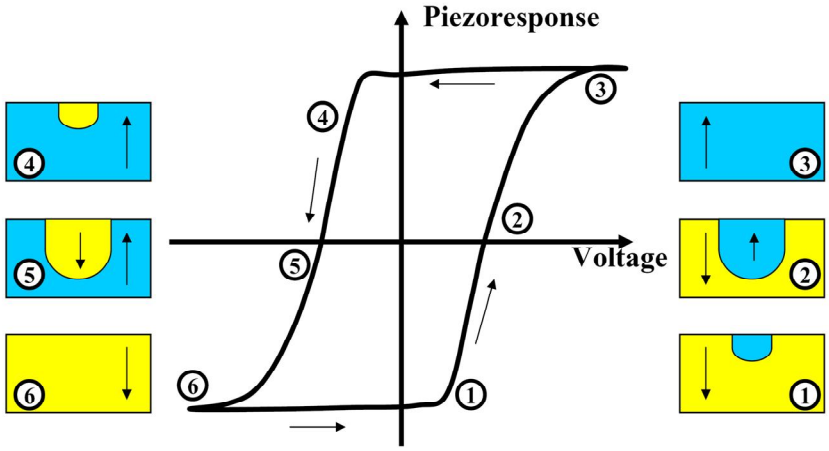

Figure 2.15 Schematics of hysteresis loop and domain growth process during PFM hysteresis. The domain structure at the characteristic points of the forward (right) and reverse (left) branches of the hysteresis loop is also shown. Arrows indicate the polarization direction.

The tip was modeled using a point charge system. It was also predicted that due to the finite charge-surface separation, domain nucleation requires nonzero nucleation bias. This voltage threshold for domain nucleation in the *inhomogeneous* electric field of an AFM tip

was then studied by Molotskii [39], Kalinin *et al.* [40], Emelyanov [41], and Morozovska and Eliseev [42] using a variety of tip models, as described below.

Using Landauer model and a point-charge approximation for the electric field of an AFM tip, Molotskii [43] obtained elegant closed-form analytical expressions for the domain size dependence on the applied voltage in the case when the surface charges were completely compensated by the external screening ones. Kalinin *et al.* [40] considered the domain nucleation allowing for the electromechanical coupling inside a ferroelectric medium using both the sphere-plane model of the AFM tip and a rigorous solution for the tip-surface indentation problem. It was shown numerically and analytically that the domain nucleation is possible above the threshold value of voltage applied to the tip, i.e., a potential barrier for nucleation exists. Depending on the activation energy, the domain nucleation was classified in terms of first and second order phase transitions. Similar results were later obtained by Emelyanov [41], who considered the nucleation of semi-ellipsoidal domains by voltage modulated AFM in ferroelectric film within the framework of classical thermodynamic approach. He analyzed the switching in thin films and classified stages of the switching process and proved that semi-ellipsoidal domains are unstable and transform into cylindrical domains spanning over the thickness of the film when reaches the bottom electrode.

Recently Morozovska and Eliseev [42] have developed the thermodynamic theory of nanodomain tailoring in thin ferroelectric films allowing for semiconducting properties, screening, and size effects. The analytical results proved that the nucleation of a cylindrical domain grown through the thin film is similar to the first order phase transition. However, the screening effect on the semi-ellipsoidal domain formation in thicker films, ferroelectric hysteresis and piezoelectric response were not considered.

In the following paper [44], the authors extended the thermodynamic theory for hysteresis loop formation in PFM and analyzed the effects of surface screening and finite conductivity of the material. These results were compared with experimental studies, elucidating the role of kinetic effects and pinning on domain formation.

§ 2.4 Appendix

AFM Probes

The core of atomic force microscopy is the probe. Its characteristics determine the properties revealed and the goodness of the measurement. Therefore, the selection of a proper probe is a critical step, and is driven by several parameters, which sometimes contradictory and should be compromised between pro and contra. An AFM probe is constituted by three major components (Figure 2.16). The substrate is the body of the probe, by which it is handled and positioned on the sample holder to be connected to the piezoelectric scanner of the AFM. The cantilever is the portion projecting off of the substrate. Commonly, it is several hundred of microns in length (L), few tens of microns in width (w) and few microns thick (d). The tip is situated at the end of the cantilever. It is usually of pyramidal shape, ending with a sharp edge having a radius of curvature (R_{ROC}) of tens of nanometers. This size determines the lower limit for lateral resolution. The sidewalls angles of the tip determine the ability to detect steep features on a sample surface. The resonance frequency (ω) and the spring constant (k) are important parameters depending on the measurement to be performed, along with the resistivity (R).

As R_{ROC} is the decisive factor for the lateral resolution, it is desirable to have it and keep it as small as possible. In contact mode measurements (as in the case of PFM) the friction and following wear leads to broadening of the edge of the tip, with consequent loss in resolution (blunt tips). The same phenomenon is decisive for the lifetime of probes with coated tips employed for electrical measurements. Thus great care has to be taken in determining the contact force and keeping it as low as possible in order to limit the action of friction. For the aforementioned reasons, the utilization of a probe with low spring constant cantilever is recommended in order to ensure a proper contact with the surface while maintaining a low contact force. In the same operation mode, the collection of debris on the tip, apart from leading to loss in resolution, may lead to artifacts in the imaging of the surface.

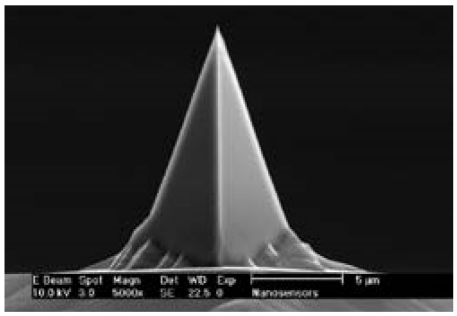

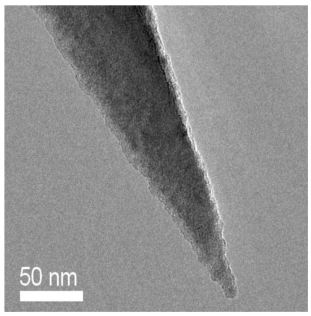

Cantilever data:

Technical Data	Nominal Value	Specified Range
Thickness /µm	4	3.0 - 5.0
Mean Width /µm	30	22.5 - 37.5
Length /µm	125	115 - 135
Force Constant /(N/m)	42	10 - 130
Resonance Frequency /kHz	330	204 - 497

Figure 2.16. SEM images and technical characteristics of the used cantilevers (PPP-NCH from Nanosensors™).

In AFM measurements and, in particular in PFM operation mode, the choice of the probe is critical for the quality of the measurement.

Piezoresponse measurements are influenced to a great extent by electrostatic interaction, as it will be pointed out in Chapter 3. In particular, such influence is conversely proportional to the cantilever spring constant [45]. Therefore, while a brittle cantilever (such as NANOSENSORS™ PPP-CONT) is usually used for contact mode measurements, on the other hand for PFM measurements it is more convenient to employ stiff cantilevers (such as NANOSENSORS™ PPP-NCH). A second parameter to consider is the cantilever's resonance frequency. The modulation voltage for operating in PFM is usually in the range 5-50 kHz, and up to 100 kHz for particular experiments. Having, for obvious reasons, the modulation frequency to be far away from the resonance, a cantilever with high resonance frequency is required.

As described, the contact force is calculated by measuring the vertical deflection of the cantilever and knowing its spring constant k. k values stated by the manufacturers are subject to variations. If the applied force has to be known with high accuracy (i.e. with error <5%), k has to be determined. The Sader method can be used for calculating both the normal and

torsional spring constants [46]. The Sader method for calibrating the normal spring constant of rectangular AFM cantilevers is represented by the formula:

$$k = 0.1906\rho w^2 LQ\omega^2 \Gamma_i^f(\omega), \tag{2.13}$$

where ρ represents the density of air, Q the quality factor, Γ_i the imaginary component of the hydrodynamic function [47]. The quality factor and the actual resonance frequency of the free cantilever are obtained by the use of special software. This operates by measuring the thermal vibration of the cantilever, individuating the resonance peak and fitting it. By measuring L and ω of the cantilever, the spring constant is calculated by Eq. 2.13 In a similar way, the torsional spring constant can be calculated.

Lock-in Amplifier

To perform single data measurements of the piezoresponse signal, an external LA is used. The LA used for this study is a dual-phase SR830 DSP Lock-In Amplifier from Stanford Research Systems, which is controlled by means of a *LabView* script via a *GPIB* connection.

Generally, LAs are used to detect and measure very small AC signals. Accurate measurements may be made even when the small signal is obscured by the noise being many orders of magnitude larger [48]. Typical experiments involve an exciting signal (V_{ref}) at a fixed frequency determining a response signal (V_{sig}):

$$\begin{aligned} V_{ref} &= A_{ref}\cos\left(\omega_{ref}t + \varphi_{ref}\right) \\ V_{sig} &= A_{sig}\cos\left(\omega_{ref}t + \varphi_{ref}\right) \end{aligned} \tag{2.14}$$

where φ_{ref} and φ_{sig} are the phase shifts, ω_{ref} and ω_{sig} are the frequencies, and A_{ref} and A_{sig} are the amplitudes. The LA extracts from V_{sig} the component at ω_{ref}. This is achieved by a phase-sensitive detector (PSD) which multiplies the two signals. The output of the PSD is

$$V_{PSD} = \frac{1}{2} V_{ref} V_{sig} \left[\cos\left(\left(\omega_{ref} - \omega_{sig} \right) t + \varphi_{sig} - \varphi_{ref} \right) + \cos\left(\left(\omega_{ref} + \omega_{sig} \right) t + \varphi_{sig} + \varphi_{ref} \right) \right]. \tag{2.15}$$

By passing V_{PSD} through a low pass filter, all the AC signals are removed from it. The only case when a signal passes through the filter is $\omega_{ref} = \omega_{sig}$ for which the first term in the previous formula becomes a DC signal of the form:

$$V_{PSD} = \frac{1}{2} V_{ref} V_{sig} \cos\left(\varphi_{sig} - \varphi_{ref} \right). \tag{2.16}$$

Therefore, all the components but the one at the reference frequency are removed by the action of the low pass filter. By adjusting φ_{ref} to match φ_{sig}, the PSD signal is maximized, so that V_{sig} can be measured. Conversely, if the phase difference is $\pi/2$, the signal is null. This is the kind of operation possible if a single-phase LA, i.e. with only one PSD, is used.

If V_{ref} is not an internal source of the LA and its phase shift cannot be adjusted, a second PSD is necessary. Dual-phase LA makes use of two PSDs. The second PSD operates with a reference signal shifted $\pi/2$, so that it's output is:

$$V_{PSD2} = \frac{1}{2} V_{ref} V_{sig} \sin\left(\varphi_{sig} - \varphi_{ref} \right). \tag{2.17}$$

Discarding from the two PSD signals the known V_{ref}, it is possible to obtain two quantities representing the signal as a vector:

$$\begin{aligned} X &= V_{sig} \cos(\Delta\varphi) \\ Y &= V_{sig} \sin(\Delta\varphi) \end{aligned} \tag{2.18}$$

By X and Y the magnitude of V_{sig} and the phase difference can be calculated:

$$R = \sqrt{X2 + Y2}$$
$$\Delta\varphi = \arctan\left(\frac{Y}{X}\right) \tag{2.19}$$

In the case of PFM, the LA has as V_{ref} the modulation signal, V_{sig} the signal from the photodiode and extracts the piezoresponse by calculating $R=PRamplitude$ and $\Delta\varphi=PRphase$

Resolution in PFM Experiments

In a typical PFM experiment, the sharp tip plays the role of a movable top electrode. Since usually the thickness of the studied sample is much larger than the tip-sample contact area (5-20 nm), the probing electric field is strongly inhomogeneous and measured PFM response comes from a small volume around the contact point. This provides a high spatial resolution of the PFM method. The natural way to estimate the lateral resolution in the PFM experiment is to measure the width of a domain wall between two antiparallel domains. While the intrinsic width of 180° domain walls in ferroelectrics is expected to be a few unit cells [49, 50, 51], the domain walls measured in a PFM experiment are typically thicker (tens of nm) and, therefore, reflect primarily the spatial resolution of the PFM. Experimentally, the width of the domain wall image, *w*, is estimated from the profile of the piezoresponse signals across the wall, which is fitted by a suitable function, e.g., by the one used to describe the polarization profile in the mean field theory of ferroelectrics [52].

$$PR(x) = PR \cdot \tanh\left[\frac{(x - x_0)}{w}\right]. \tag{2.20}$$

Figure 2.17 illustrates the profile of the PFM signal across the 180° domain wall measured in PLZT ceramics. The apparent width of the domain wall obtained from the best fit to Eq. 2.20 is about 65 nm.

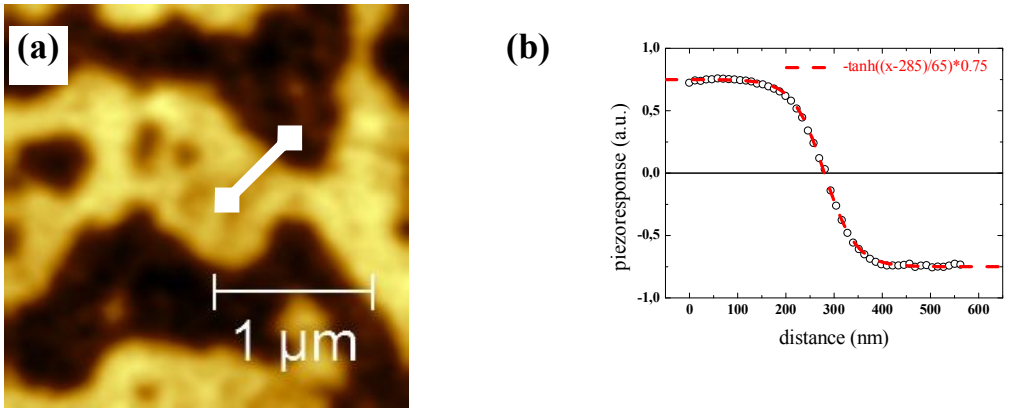

Figure 2.17. The VPFM image of PLZT ceramics: (a) Bright and dark contrasts correspond to domains with the spontaneous polarization oriented up and down to the figure plane, respectively. The cross-section of the piezoresponse image across the 180° domain wall (b). The broken line is the best fit to Eq. (2.20).

The theory of the resolution in PFM was recently considered by Kalinin *et al* [53]. They have shown that for the system with 180° domain walls, the piezoresponse may be presented as a convolution of a function describing the spatial distribution of material properties, and as a function related to the probe parameters (it is assumed that piezoelectric and dielectric properties are uniform across the sample thickness).

One of the traditional resolution criteria used in optics is the Rayleigh two-point resolution limit – two Gaussian shaped image features of similar intensity can be resolved, if the intensity at the midpoint between them is less than 81% of the maximum [54]. If the object transfer function has a Gaussian shape, the Rayleigh two-point resolution criterion may be defined as $w_r=1/qr$ for which $F(q_r)=0.58F(0)$. Kalinin *et al.* [40] showed that in the PFM experiment, the Rayleigh resolution correlates with the measured width of the domain wall. Moreover, the quantitative determination of material properties from the PFM experiment requires that typical domain size exceeds w_r. Nevertheless, the features with smaller size may still be resolved by PFM. The minimal feature size detectable against the noise corresponds to the information limit defined from the condition $N(q)=F(q)$. However, the intensity of the PFM signal in that case starts to scale with the feature size and no reliable information about

material properties can be obtained. For PFM, the information limit may be considerably smaller than the Rayleigh resolution.

The dependencies of the resolution on the tip size, as well as on the sample parameters (thickness, material), were studied experimentally by Jungk *et al*. [55]. They found that for the metal coated tips, the width of the measured walls scales linearly with the tip radius. For the uncoated Si tip, the broader domain walls were measured. It was explained as an effect of the dielectric SiO_2 layer formed on the tip surface. As a result, the probe is electrically separated from the sample surface and the electric field is less localized leading to reduced spatial resolution. No effect of the material parameters (dielectric permittivity, elastic and piezoelectric constant) on the resolution was found. The thinnest domain wall width (measured for the tip with the radius 15 nm) was only 17 nm.

Recently, Rodriguez *et al.* [56] reported that the measured width of the domain wall can be as small as 3 nm when the measurements are done not in the ambient condition (air) but in a liquid environment. They suggested that the mobile ions present in the solution screen the long range electrostatic interactions from the conical parts of a tip, at distances greater than the Debye length enhancing localization of the probing field in the tip-surface junction. Owing to the strong inhomogeneity of the probing electric field the signal in the typical PFM experiment is collected mainly from the surface layer, whose thickness is a function of the dielectric permittivity, and contact conditions and is unknown, in general.

Due to the strong inhomogeneity of the probing electric field, the signal in the typical PFM experiment is collected mainly from a surface layer, whose thickness is a function of the dielectric permittivity and contact conditions, and is typically unknown. To overcome this limitation, the domain structure may be visualized through the top electrode of a ferroelectric capacitor [57]. In this case, the electric voltage may be applied either via the tip or using an external wire attached to the top electrode. In the latter case, the tip is used only for the detection of the piezoelectric displacement. In this configuration, the probing electric field is uniform and a measured response is generated by the entire sample thickness. This method allows the quantitative study of the dynamics of domain walls and polarization reversal mechanisms in ferroelectric capacitors. The drawbacks of this approach are a substantially smaller lateral resolution and an inability to measure lateral (LPFM) signal.

References

[1] Brundle C.R., Evans C.A., and Wilson S. *"Encyclopedia of Materials Characterization"*, Butterworth – Heinemann (1992).

[2] Binnig G., Rohrer H., Gerber Ch. and Weibel E., "Surface studies by Scanning Tunneling Microscopy" *Phys. Rev. Lett.* **49**, 57 (1982).

[3] Devonshire A. F., Theory of barium titanate - part I, *Philos. Mag.* **40**, 1040 (1949).

[4] Devonshire A.F., Theory of barium titanate - part II, *Philos. Mag.* **42**, 1065 (1951).

[5] Smolenskii G.A., Bokov V.A., Isupov V.A., Krainik N.N., Pasynkov R.E., Sokolov A.I., Ferroelectrics and Related Materials, New York, Cordon and Breach (1984).

[6] Birk H., Glatz-Reichenbach J., Jie L., Schreck E., and Dransfeld K., "Thew local piezoelectric activity of thin polymer films observed by scanning tunneling microscopy" *J. Vac. Sci. Technol. B* **9**, 1162 (1991).

[7] Güthner P., Glatz-Reichenbach J., and Dransfeld K., "Investigation of local piezoelectric properties of thin copolymer films" *J. Appl. Phys.* **69**, 7895 (1991).

[8] Güthner P. and Dransfeld K., "Local poling of ferroelectric polymers by scanning force microscopy" *Appl. Phys. Lett.* **61**, 1137 (1992).

[9] Franke K., Besold J., Haessler W., and Seegebarth C., "Modification and detection of domains on ferroelectric PZT films by scanning force microscopy" *Surf. Sci. Lett.* **302**, 283 (1994).

[10] Gruverman A., Auciello O., and Tokumoto H., "Scanning force microscopy for the study of domain structure in ferroelectric thin films" *J. Vac. Sci. Technol. B* **14**, 602 (1996).

[11] Gruverman A., Auciello O., and Tokumoto H., "Nanoscale investigation of fatigue effects in $Pb(Zr,Ti)O_3$ films" *Appl. Phys. Lett.* **69**, 3191 (1996).

[12] Hidaka T., Maruyama T., Saitoh M., Mikoshiba N., Shimizu M., Shiosaki T., Wills L. A., Hiskes R., Dicarolis S. A., and Amano Jun, "Formation and observation of 50 nm polarized domains in $_{PbZr1-x}Ti_xO_3$ thin film using scanning probe microscope" *Appl. Phys. Lett.* **68**, 2358 (1996).

[13] Eng L. M., Güntherodt H. J., Rosenman G., Skliar A., Oron M., Katz M., and Eger D., "Nondestructive imaging and characterization of ferroelectric domains in periodically poled crystals" *J. Appl. Phys.* **83**, 5973 (1998).

[14] Eng L. M., Güntherodt H. J., Schneider G. A., Kopke U., and Saldana J. M., "Nanoscale reconstruction of surface crystallography from three-dimensional polarization distribution in ferroelectric barium–titanate ceramics" *Appl. Phys. Lett.* **74**, 233 (1999).

[15] Abplanalp M., Eng L., and Günter P., "Mapping the domain distribution at ferroelectric surfaces by scanning force microscopy" *Appl. Phys. A* **66**, 231 (1998).

[16] Roelofs A., Böttger U., Waser R., Schlaphof F., Trogisch S., and Eng L.M., "Differentiating 180º and 90º switching of ferroelectric domains with three-dimensional piezoresponse force microscopy" *Appl. Phys. Lett.* **77**, 3444 (2000).

[17] Gruverman A., Tokumoto H., Prakash A. S., Aggarwal S., Yang B., Wuttig M., Ramesh R., Auciello O., and Venkatesan T., "Nanoscale imaging of domain dynamics and retention in ferroelectric thin films" *Appl. Phys. Lett.* **71**, 3492 (1997).

[18] Tybell T., Paruch P., Giamarchi T., and Triscone J. M., "Domain wall creep in epitaxial ferroelectric $Pb(Zr_{0.2}Ti_{0.8})O_3$ thin films" *Phys. Rev. Lett.* **89**, 097601 (2002).

[19] Alexe M., Gruverman A., Harnagea C., Zakharov N. D., Pignolet A., Hesse D., and Scott J. F., "Switching properties of self-assembled ferroelectric memory cells" *Appl. Phys. Lett.* **75**, 1158 (1999).

[20] Alexe M., Harnagea C., Hesse D., and Gösele U., "Polarization imprint and size effects in mesoscopic ferroelectric structures" *Appl. Phys. Lett.* **79**, 242 (2001).

[21] Kalinin S. V. and Bonnell Dawn A., "Imaging mechanism of piezoresponse force microscopy of ferroelectric surfaces" *Phys. Rev. B* **65**, 125408 (2002).

[22] Kalinin S. V., Karapetian E., and Kachanov M., "Nanoelectromechanics of piezoresponse force microscopy" *Phys. Rev. B* **70**,184101 (2004).

[23] Jesse S., Baddorf A. P. and Kalinin S. V., "Dynamic behaviour in piezoresponse force microscopy" *Nanotechnology* **17**, 1615 (2006).

[24] Harnagea C., Alexe M., Hesse D., and Pignolet A., "Contact resonances in voltage modulated force microscopy" *Appl. Phys. Lett.* **83**, 338 (2003).

[25] Harnagea C., Pignolet A., Alexe M., and Hesse D., "Piezoresponse Scanning Force Microscopy: What quantitative information can we really get out of piezoresponse measurements on ferroelectric thin films" *Integr. Ferr.* **44**, 113 (2002).

[26] Jungk T., Hoffmann A., and Soergel E., "Quantitative analysis of ferroelectric domain imaging with piezoresponse force microscopy" *Appl. Phys. Lett.* **89**, 163507 (2006).

[27] Peter F., Kubacki J., Szot1 K., Reichenberg B., and Waser R., "Influence of adsorbates on the piezoresponse of $KNbO_3$" *Phys. Stat. Sol. (a)* **203**, 616 (2006).

[28] Gruverman A., Auciello O., and Tokumoto H., "Scanning force microscopy: application to nanoscale studies of ferroelectric domains" *Integr. Ferr.* **19**, 49 (1998).

[29] Jesse S., Lee H. N. and Kalinin S. V., "Quantitative mapping of switching behavior in piezoresponse force microscopy" *Rev.Sci.Instrum.* **77**, 073702 (2006).

[30] Wu A., Vilarinho P .M. , Shvartsman V. V., Suchaneck G., and Kholkin A.L. "Domain populations in lead zirconate titanate thin films of different compositions via piezoresponse force microscopy" Nanotechnology **16**,2587 (2005)

[31] Saya Y., Watanabe S., Kawai M., Yamada H., and Matsushige K., "Investigation of Nonswitching Regions in Ferroelectric Thin Films Using Scanning Force Microscopy" *Jpn. J. Appl. Phys.*, **39**, 3799 (2000).

[32] Harnagea C., Pignolet A., Alexe M., Hesse D., and Gosele U., "Quantitative ferroelectric characterization of single submicron grains in Bi-layered perovskite thin films"*Appl. Phys.A: Mater. Sci. Process*. **70**, 261 (2000).

[33] Ricinschi D., Noda M., Okuyama M., Ishibashi Y., Iwata M., and Mitoseriu L., "A Landau-theory-based computational study of in-plane and out-of plane polarization components role in switching of ferroelectric thin films" *J. Korean Phys. Soc*. **42**, S1232 (2003).

[34] Gruverman A., Rodriguez B. J., Kingon A. I., Nemanich R. J., Cross J. S., and Tsukada M., "Spatial inhomogeneity of imprint and switching behavior in ferroelectric capacitors" *Appl. Phys. Lett*. **82**, 3071 (2003).

[35] Gruverman A., Rodriguez B. J., Kingon A. I., Nemanich R. J., Tagantsev A. K., Cross J. S., and Tsukada M., "Mechanical stress effect on imprint behavior of integrated ferroelectric capacitors" *Appl. Phys. Lett*. **83**, 728 (2003).

[36] Dehoff C., Rodriguez B. J., Kingon A. I., Nemanich R. J., Gruverman A., and Cross J. S., "Atomic force microscopy-based experimental setup for studying domain switching dynamics in ferroelectric capacitors" *Rev. Sci. Instrum*. **76**, 023708 (2005).

[37] Landauer R., "Electrostatic Considerations in BaTiO3 Domain Formation during Polarization Reversal" *J. Appl Phys.* **28**, 227 (1957).

[38] Abplanalp M., Dr. Nat. Sci. thesis, Swiss Federal Institute of Technology, (2001).

[39] Molotskii M., "Generation of ferroelectric domains in films using atomic force microscope" *J. Appl Phys*. **97**, 014109 (2005).

[40] Kalinin S. V., Gruverman A., Rodriguez B. J., Shin J., Baddorf A. P., Karapetian E., and Kachanov M., "Nanoelectromechanics of polarization switching in piezoresponse force microscopy" *J. Appl Phys.* **97**, 074305 (2005).

[41] Emelyanov A. Yu., "Coherent ferroelectric switching by atomic force microscopy" *Phys. Rev. B* **71**, 132102 (2005).

[42] Morozovska A. N. and Eliseev E. A., "Screening and size effects on the nanodomain tailoring in ferroelectrics semiconductors" *Phys. Rev. B* **73**, 104440 (2006).

[43] Molotskii M., "Generation of ferroelectric domains in atomic force microscope", *J. Appl. Phys.* **93**, 6234 (2003).

[44] Morozovska A. N., Kalinin S. V., Eliseev E. A., and Svechnikov S. V., "Local Polarization Switching in Piezoresponse Force Microscopy" *Ferroelectrics* **354**, 198 (2007)

[45] Harnagea C., Pignolet A., Alexe M., Hesse D., and Gösele U., "Quantitative ferroelectric characterization of single submicron grains in Bi-layered perovskite thin films" *Appl.Phys. A* **70**, 261 (2000).

[46] Green C. P., Lioe H., Cleveland J. P., Proksch R., Mulvaney P. and Sader J. E., "Normal and torsional spring constants of atomic force microscope cantilevers" *Rev. Sci. Instrum*. **75**, 1988 (2004).

[47] Sader J. E., "Frequency response of cantilever beams immersed in viscous fluids with applications to the atomic force microscope" *J. Appl. Phys*. **84**, 64 (1998).

[48] Stanford Research Systems, DSP Lock-In Amplifier model SR830, user manual (1999).

[49] Zhirnov V.A. "A contribution to the theory of domain walls in ferroelectrics" *Sov. Phys. JETP* **8**, 822 (1959).

[50] Padilla J., Zhong W., Vanderbilt D., "First-principles investigation of 180° domain walls in $BaTiO_3$" *Phys. Rev. B* **53**, R5969 (1996).

[51] Meyer B., Vanderbilt D. "*Ab initio* study of ferroelectric domain walls in $PbTiO_3$". *Phys. Rev. B* **65**, 104111 (2005).

[52] Strukov B.A., Levanyuk A.P. Ferroelectric phenomena in crystals: physical foundations. Spinger. Berlin. (1998)

[53] Kalinin S.V., Jesse S, Rodriguez B.J., Shin J., Baddorf A.P., Lee H.N., Borisevich A., Pennycook S.J. "Spatial resolution, information limit, and contrast transfer in piezoresponse force microscopy", *Nanotechnology* **17**, 3400 (2006).

[54] Born M., Wolf E. "Principles of Optics", Pergamon Press, Oxford (1975).

[55] Jungk T., Hoffmann A., Soergel E. "Impact of the tip radius on the lateral resolution in piezoresponse force microscopy" *New Journal of Physics* **10**, 013019 (2008).

[56] Rodriguez B.J., Jesse S., Baddorf A.P., Kalinin S.V. "High resolution electromechanical imaging of ferroelectric materials in a liquid environment by piezoresponse force microscopy" *Phys. Rev. Lett.* **96**, 237602 (2006).

[57] Gruverman A., Rodriguez B.J., Dehoff C., Waldrep D., Kingon A.I., Nemanich R.J., Cross J.S. "Direct studies of domain switching dynamics in thin film ferroelectric capacitors" *Appl. Phys. Lett* **87**, 082902 (2005).

Chapter 3

Investigation of Polar Nanodomain Structures in Relaxor Ceramics $Pb_{1-x}La_x(Zr_yTi_{1-y})_{1-x/4}O_3$ (PLZT x/y/1-y, x=5-13, y=65)

This chapter is devoted to the study of the nano and meso-scale properties of PLZT ceramics by using piezoresponse force microscopy. Comparison with macrosocopic properties will be done in order to get insight into the microscopic mechanisms involved in the relaxor ferroelectric properties of ceramics with a special attention to the grain effect i.e. far and close to the grain boundary. Our aim was to develop new approaches and methodologies in order to highlight the advantages to use PFM in the investigation of such complex and inhomogeneous systems at a nanoscale, and thus to reveal that PFM is a real powerful tool.

§ 3.1 Macroscopic Ferroelectric Properties of PLZT Ceramics

Introduction to PLZT Ceramics

Ferroelectric ceramics for piezoelectric applications historically have been formulated from a number of compositions and solid solutions including $BaTiO_3$, $PbTiO_3$, PbN_2O_6, $NaNbO_3$, PZT, and PLZT.

PZT ceramics are almost always used with a dopant, a modifier, or other chemical constituent or constituents to improve and to optimize their basic properties for specific applications.

Examples of these additives include off-valent *donors*, such as Nb^{5+} replacing Zr^{4+} or La^{3+} replacing Pb^{2+}, to counteract the natural *p*-type conductivity of the PZT and, thus, increase the electrical resistivity of the materials by at least 3 orders of magnitude. The donors are usually compensated by A-site vacancies. These additives (and vacancies) enhance domain reorientation; ceramics produced with these additives are characterized by square hysteresis loops, low coercive fields, high remanent polarization, high dielectric constants, maximum coupling factors, higher dielectric loss, high mechanical compliance, and reduced aging.

One system that embraces all compositional aspects of the dielectric, piezoelectric, pyroelectric, ferroelectric, and electrooptic ceramics is the PLZT system [1].

These materials are ferroelectric and are characterized by the presence of normal micron-sized domain structures in the low-temperature product state in the unpoled condition. La

modification (x) of PZT ceramics $Pb_{1-x}La_xZr_yTi_{1-y}$ (PLZT x/y/1-y) is known to result in the destabilization of the long-range ferroelectric order. With increasing La impurity content, the evolution of polar order has been shown to occur through a common sequence of domain like states for PLZT x/65/35 including: normal micron-sized domains and polar nanodomains (or clusters), as illustrated in Figure 3.1.

In the structure strongly disordered, relaxor ferroelectric behavior is observed. In these materials, the cluster state has been shown to be long lived at temperatures significantly below that of the average transformation temperature (T_m), as indicated by the dielectric response characteristics.

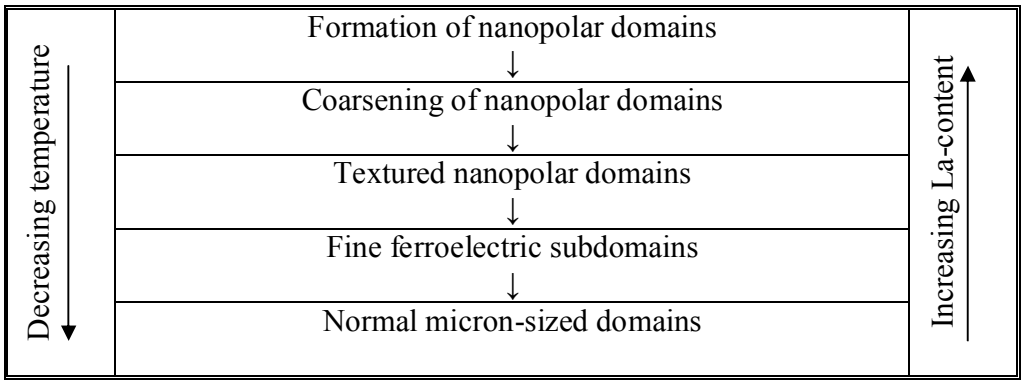

Figure 3.1 Common sequence of domain-like states observed with increasing La content in PLZT ceramics [2].

Viehland *et al.* [3] have shown that this long-lived polar cluster state is characterized by a glass-like behavior in the macroscopic response characteristics, similar to dipolar and quadrupolar glasses. The observed freezing behavior in relaxors clearly indicates the presence of a correlated freeze-out of polarization fluctuations, however it is not yet clear whether this correlated freeze-out involves a phase transformation into a state with a long-range ‘‘glassy’’ order parameter or rather the development of a finite-range order parameter on the mesoscopic scale.

In the weakly disordered condition, the macroscopic properties of PLZT are characterized by the decrease of remanent polarization, coercive field, c/a ratio and phase transformation

temperature with increasing La content [4].

In order to understand the nanoscale properties of PLZT ceramics, we first studied the major dielectric and ferroelectric properties of the samples.

The microstructure of the ceramics was investigated using a SEM. It was also used to carry out qualitative and quantitative tests of local chemical composition (via EDS) of ceramics.

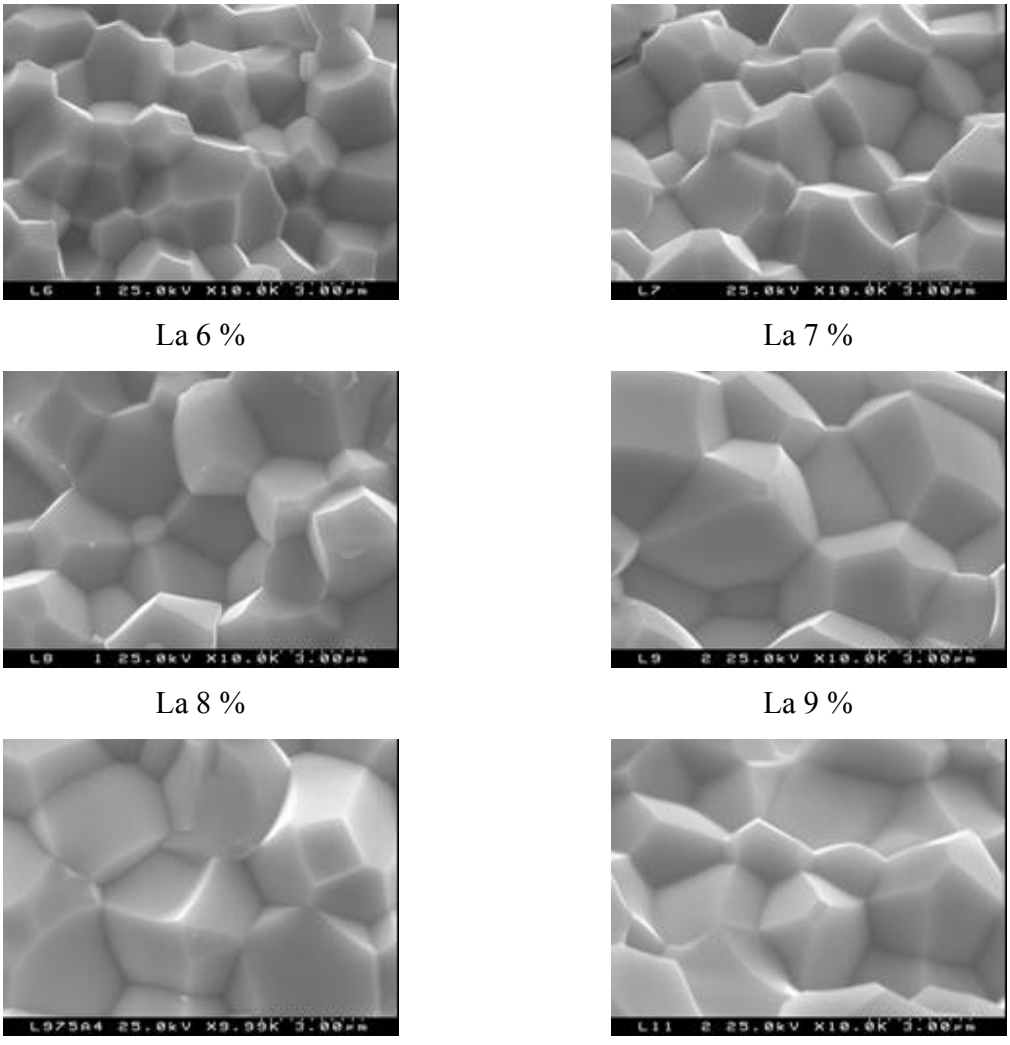

La 6 % La 7 %

La 8 % La 9 %

La 9.75 % La 11 %

Figure 3.2 SEM micrographs of fractured PLZT ceramics prepared with different amounts of lanthanum.

SEM images of PLZT with different La contents are presented in Figure 3.2. The fine-grained microstructure is quite uniform, with internal and grain-boundary porosity virtually nonexistent. No secondary phases or unreacted starting reagents were observed in any of the compositions. It should also be noticed that La modification resulted in a significant decrease in the grain size. The average grain size was decreased from 5–7 μm for 11/65/35 to 2-3 μm for 6/65/35.

Dielectric Characterization

Figure 3.3 shows the temperature dependence of the dielectric permittivity $\varepsilon(T)$ for PLZT-x/65/35 with $8\% \leq x \leq 13\%$. The dielectric permittivity of PLZT decreases rapidly with increasing La concentration. Simultaneously, the temperature of dielectric permittivity maximum T_m gradually decreases, almost linearly. The dielectric permittivity curves show broad diffuse maxima near the phase transition, especially for compositions with x>7%.

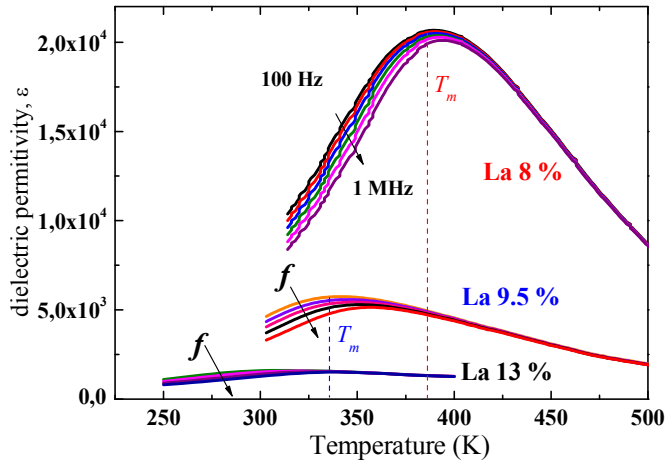

Figure 3.3 Temperature dependence of the dielectric permittivity $\varepsilon(T)$ for PLZT x/65/35ceramics measured at different frequencies.

Dielectric measurements in PLZT 8/65/35 revealed that at room temperature there is only a small frequency dispersion of the permittivity, a behavior being typical for a normal

ferroelectric. However, it was noticed that the frequency dispersion becomes more pronounced with increasing temperature, and small shift in T_m (the temperature of the dielectric maximum) with measurement frequency was detected. This suggests that the ceramic exhibits properties somewhere between a classical ferroelectric material and a relaxor. Relaxor behavior is apparent in 9.5/65/35 and 13/65/35 compositions. The data are fully compatible with earlier results [2,5].

Figure 3.4 shows the dielectric permittivity as a function of temperature for PLZT-13/65/35, which evidences the strong dependence of the dielectric permittivity $\varepsilon(T)$ on frequency in the region of phase transition. This is characteristic of relaxor materials: as the frequency increases, the value of ε_{max} decreases and T_m shifts to higher temperatures.

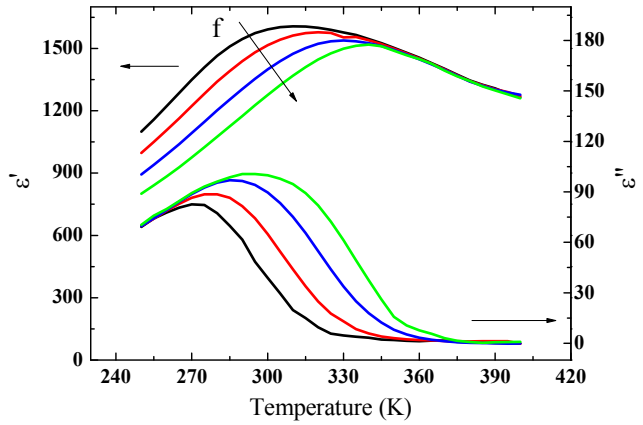

Figure 3.4 Temperature dependence of the real (ε') and imaginary (ε'') part of complex permittivity of PLZT 13/65/35 ceramics, measured at different frequencies: 1 kHz, 10 kHz, 100 kHz and 1 MHz.

The frequency dependence of the dielectric constant can provide direct information on the dynamic processes occurring in ferroelectric relaxors. That is, we performed the Vogel-Fulcher analysis [6] of the frequency dependence of the dielectric constant maximum temperature (T_m) in PLZT 9.75/65/35 ceramics as shown in Figure 3.5. The attempt frequency $\nu_0 = 2 \times 10^6$ Hz, the average activation energy $U = E_a/k_B = 0.03$ eV and the freezing temperature $T_f = 290 \pm 2$ K, were obtained by fitting the $1/T_m$ vs. ln ν curve with the following expression:

$$\nu = \nu_0 \exp\left[-\frac{E_a}{k_B\left(T_m - T_f\right)}\right] \tag{3.1}$$

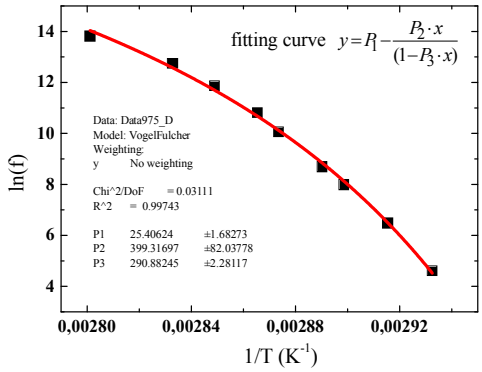

Figure 3.5 The fit of the frequency dependence of the temperature of the dielectric maximum using Vogel-Fulcher relationship for PLZT 9.75/65/35 where the solid points are the experimental data and the solid line is the curve fitting.

Independently of the analyzed frequency dependence, the maxima of the dielectric constant and dielectric loss vs. temperature are not coincident with the freezing temperature (T_f), which is the temperature where the ergodicity is effectively broken. This is a typical feature of the relaxor ferroelectric materials, where the ergodic state (where the long-range interaction between the ferroelectric clusters is practically absent) is effectively broken at T_f, and not at T_m. In fact, the ergodicity is broken due to the divergence of the longest relaxation time in the vicinity of 290 K, i.e., the temperature where the ferroelectric state (with long-range interactions) can also be induced by applying sufficiently high electric fields, as in pyroelectric or dielectric experiments with high applied bias fields.

P-E Hysteresis Loops

Macroscopic ferroelectric properties of PLZT ceramics were verified by the ferroelectric hysteresis measured with Sawyer-Tower method.

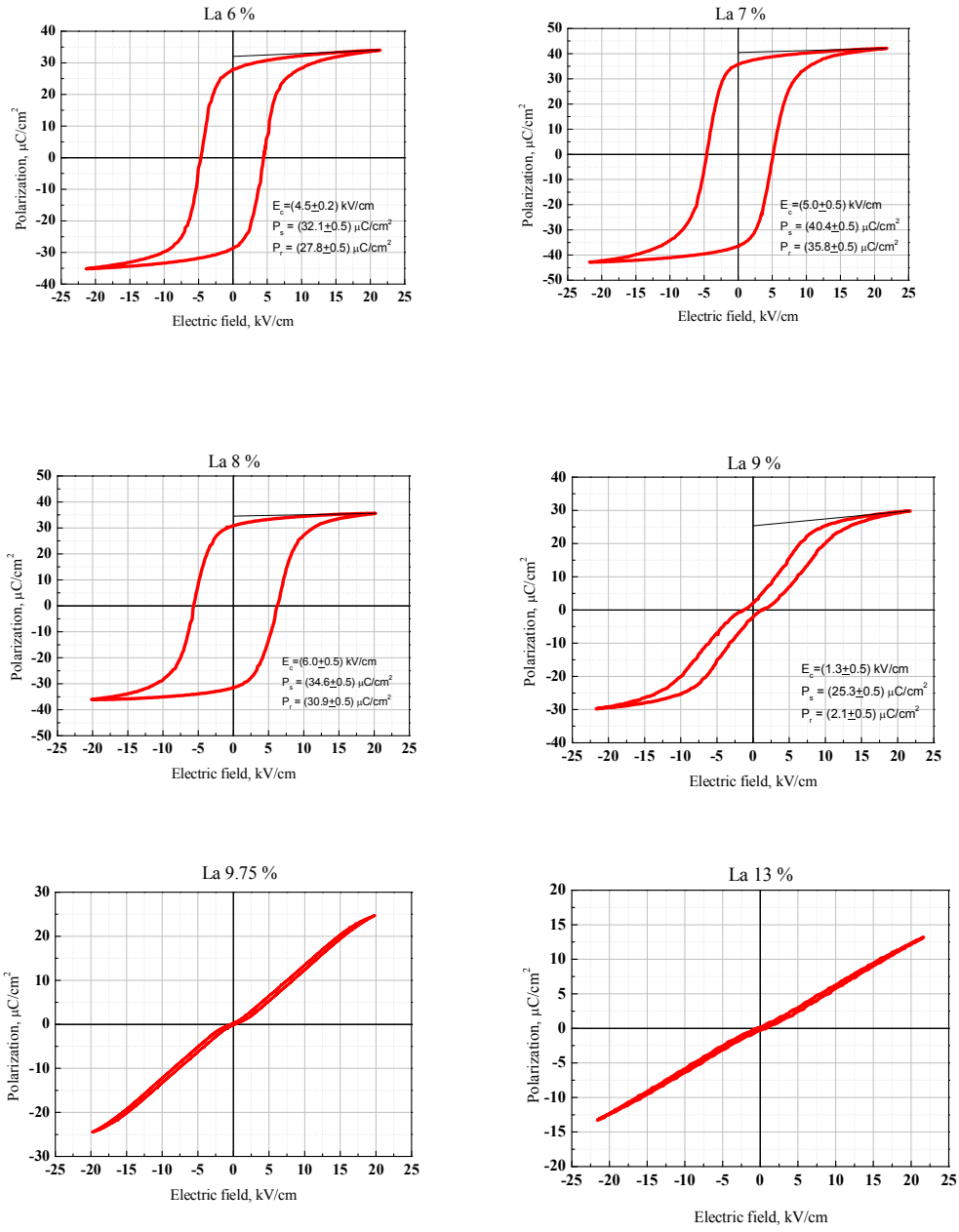

Figure 3.6 *P–E* hysteresis loops of the PLZT *x*/65/35 ceramics (for *x* = 6–13 La mole %) measured at 50 Hz at room temperature

Room-temperature *P–E* loops for the x/65/35 compositional sequence are shown in Figure 3.6. It is clear from the Figure that with La doping ferroelectric-type loops (for the compositions

between 6/65/35 and 8/65/35) are progressively changed to double loops with some features of antiferroelectric ordering at around La 9% mol. For PLZT 9.75/65/35 and 13/65/35 the hysteretic behavior disappears completely and the *P-E* curve becomes a so-called "slim-loop", as commonly observed for ferroelectric relaxor materials. The PLZT phase diagram indicates that there is a region of pseudocubic symmetry. Within this region compositions do not possess permanent remanent polarization at room temperature. The plausible reason could be attributed to the increasing of grain size and the decreasing of rhombohedrality when the La content increases.

Table 3.1 summarizes obtained ferroelectric parameters of used PLZT ceramics for different La concentrations.

Table 3.1: Ferroelectric parameters for PLZT x/65/35 ceramics.

PLZT composition	E_C, kV/cm	P_S, μC/cm^2	P_R, μC/cm^2	T_m (1 kHz), K	ε_m (1 kHz)	E_a, eV	T_f, K	υ_0, Hz
La 6 %	4.5±0.5	32.1±0.5	27.8±0.5	421	7562			
La 7 %	5.0±0.5	40.4±0.5	35.8±0.5	392	7058			
La 8 %	6.0±0.5	34.6±0.5	30.9±0.5	380	9633	0.06	340±2	3.6×10^9
La 9 %	1.3±0.5	25.3±0.5	2.1±0.5	352	8236	0.03	320±2	4.8×10^8
La 9.75 %	0	23.7±0.5	0	335	5582	0.03	290±2	2×10^6
La 13 %	0	13.2±0.5	0	295	1500			

To summarize, firstly, La addition shifts T_m to lower temperatures (T_m = 390, 335 and 300 K for 8, 9.75 and 13/65/35, respectively,), and secondly, dielectric constant decreases with increasing La content (21000, 5500 and 1700 for 8, 9.75 and 13/65/35, respectively). Dilutions of the permittivity and a reduction in T_m as a function of increasing La concentration have been previously observed [7].

§3.2 Nanoscale Domain Structure in Relaxor PLZT x/65/35 Ceramics

In this section we present the results of experimental investigation of nanoscale domain structures visualization of the surface domain patterns by PFM. The irregular polarization patterns are associated with the formation of a glassy state, where random electric fields destroy the long-range ferroelectric order.

The typical topography and piezoresponse images of relaxor PLZT 9.5/65/35 ceramics are shown in Figure 3.7 (a,b).

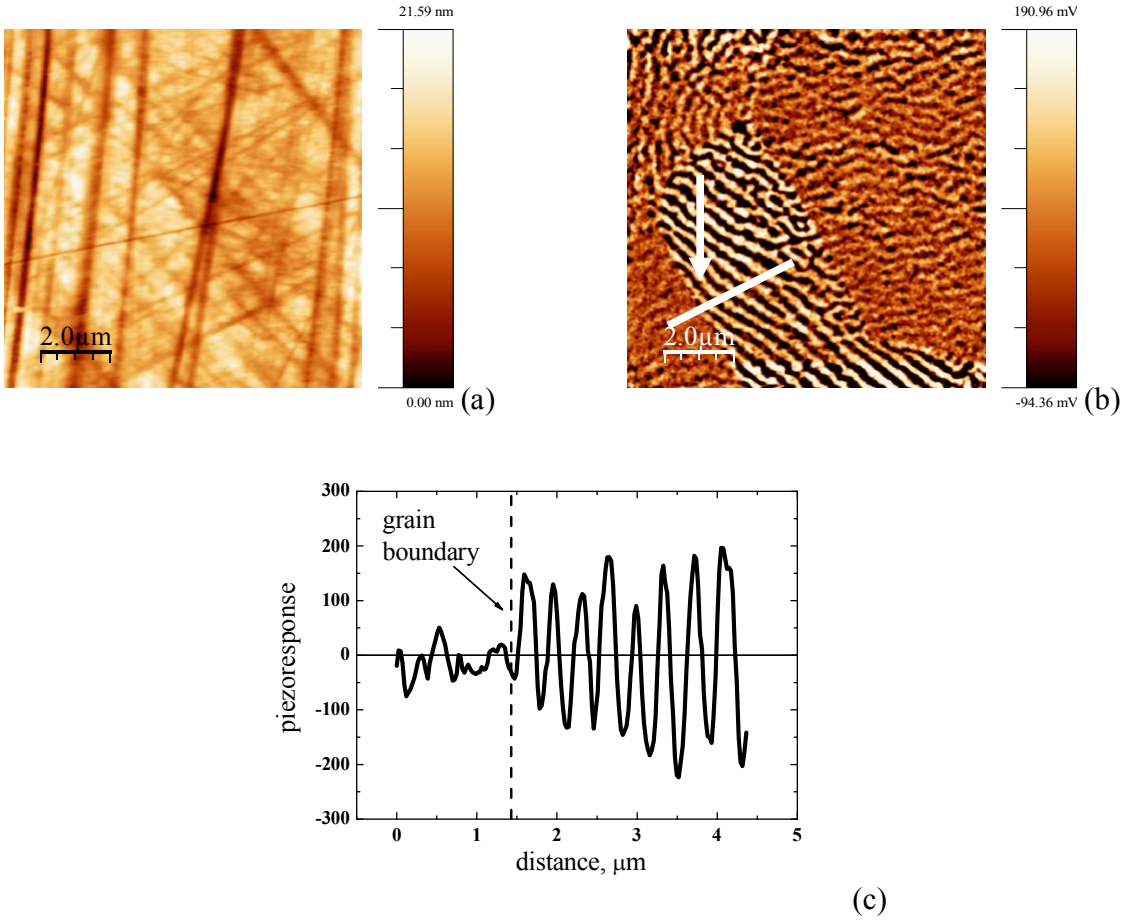

Figure 3.7 Typical topography (a) and piezoresponse (b) images of PLZT 9.5/65/35 ceramics. Cross-section of piezoresponse image (c) shows the variation of the contrast in adjacent grains.

Figure 3.7(a) shows the topography of the PLZT ceramics obtained by SPM. The main features in the topography are the surface scratches. It was found that each grain consists of a large number of fine labyrinth-type nanodomains with an alternating piezoresponse signal (corresponding to opposite polarization directions) as can be judged from the domain cross-section in Figure 3.7 (c). While no grains can be seen in the topography image owing to rigorous polishing, grains having different crystallographic orientation are distinguished in the piezoresponse image due to the different magnitude of piezoresponse contrast in different grains (see contrast change in Figure 3.7 (c)). Indeed, longitudinal piezoelectric coefficient is strongly dependent on the angle between the direction of applied electric field and polarization orientation. This allows studying various grain size effects as will be described below.

The nanoscale domain structures for different La concentration in PLZT ceramics by PFM are shown in Figure 3.8. Fine domains with mottled contrast are observed in x/65/35 (where $6 \leq x \leq 9$ La mole %) ceramics. Bright and dark areas correspond to domains with opposite vertical component of polarization. This contrast becomes gradually more pronounced with decrease lanthanum concentration. Decreasing La concentration to 7% results in coarsening of the domains. A comparison with microstructure shows that the grain size visualized by PFM is compatible with SEM reasults on fractured samples.

The PFM images contain the piezoelectric response of the domain structure integrated over some subsurface layer, which depth depends on applied AC voltage. These domains have no preference of one orientation against the other, so in the macroscopic sense the ceramics are not polar (consistent with electrical measurements).

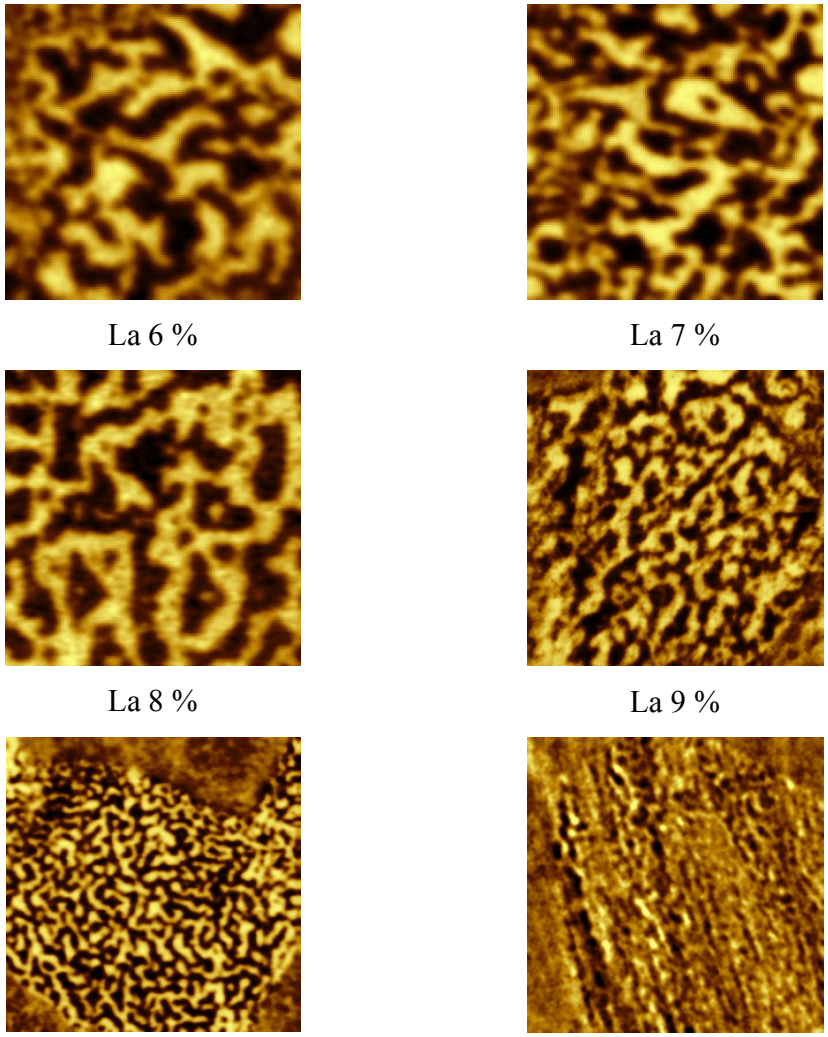

Figure 3.8 Nanoscale structures in PLZT x/65/35 ceramics visualized by PFM. Size for all images is 4×4 μm^2.

It has to be noticed that the piezoelectric signal varies from grain to grain thus giving a possibility of grain visualization. These compositions (PLZT x/65/35) are within the rhombohedral ferroelectric phase region and have eight domain states with spontaneous polarization vectors oriented in the directions of cube diagonals of the prototype cubic phase. The multi-domain states with different orientations will give variable piezoresponse observed in the

amplitude image in the PFM mode. These multi-domains will contribute to local effective piezoelectric constants measured by PFM.

Figure 3.9 shows the evolution of the histograms of the local piezoresponse at different La content calculated from scans in Figure 3.8.

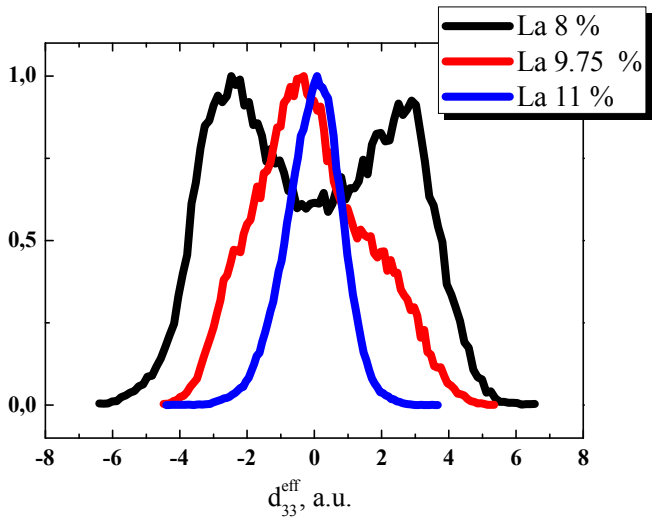

Figure 3.9 The histograms of the piezoresponse signal PLZT ceramics at different La content.

The histogram of the piezoresponse signal reflects the distribution of domains of different polarities. It was observed that, for PLZT 8/65/35, the piezoresponse distribution is approximately symmetric relative to domains of both signs. These distributions may be treated as a superposition of three separate contributions: two from the polar phase (with the peaks at positive and negative d_{33} values) and one from the nonpolar phase (maximum near d_{33}=0). The positions of the ‘‘polar’’ peaks can be considered to be effective values of the intrinsic piezoresponse inside a single polar region, d_{33}, while the ratio between the maxima of the polar and nonpolar contributions is a measure of the relative amount of the polar phase.

§3.3 Grain Size Effect and Local Disorder in Polycrystalline Relaxors

In this section we present an analysis of the local correlation radius and effect of the grain boundaries and grain size on the nanodomain structure. The obtained dependences are consistent with both the mechanical stress effect of impinging grains and the composition gradient in the PLZT grain and allows for better understanding of the dielectric properties of disordered ferroelectrics.

Figure 3.10 (a) shows the representative piezoresponse image of the individual PLZT grain consisting of a large number of "labyrinth"-type random nanodomains characteristic for this composition. As was discussed earlier, see §3.2., the random polarization patterns are mostly 180º domains with the polarization vector direction having an arbitrary angle with the sample plane. This angle depends on the crystallographic orientation of the grain and polarization direction lying along pseudocubic [111] axes and thus determines the absolute value of the piezoelectric contrast. As well documented in the literature, the appearance of these domains is due to the quenched random electric fields associated with La^{3+} doping at the Pb^{2+} sites. For the quantitative data analysis we applied an autocorrelation function method, which has been successfully used for the topographic data evaluation [8]. Indeed, the value of the piezoresponse signal, *D*, taken from the measured contrast is proportional to the local polarization value. Therefore, its autocorrelation function:

$$C(r_1, r_2) = \sum_{x,y} D(x,y)D(x+r_1, y+r_2) \tag{3.2}$$

should be equivalent to a polarization-polarization correlation function. As was reported earlier (see, e.g. [9]) the average correlation function can be fitted with the following equation: $C(r) \propto \exp\left[(r/\xi)^{-2h}\right]$, where *r* is the radius, ξ is the correlation length, and *h* is the exponent parameter [8]. This fitting determines the surface correlation length which is, in principle, the measure of the polarization disorder/order in these relaxor ceramics. The strict relationship between the surface correlation length and its "true" bulk value (that determines peculiar dielectric properties of relaxors) is not clear but it is believed that ξ is directly related to average

size of "frozen" by defects PNRs and thus can serve as a measure of the polarization disorder on the surface of polycrystalline relaxor ferroelectrics. Because the grains in studied PLZT ceramics are quite coarse (d~5-7 μm, at least one order of magnitude greater than the calculated correlation length) it is possible to determine this ξ parameter as a function of the coordinate inside the grain.

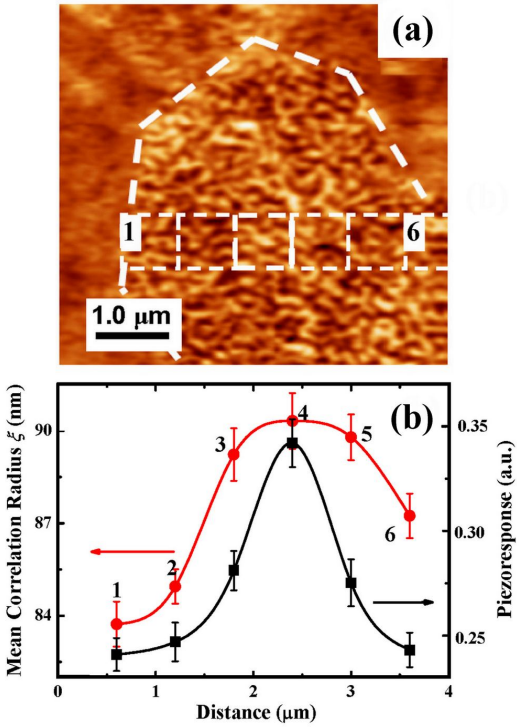

Figure 3.10 Representative piezoresponse image of the individual PLZT 9.75/65/35 grain (a) and variation of the correlation length ξ, and average piezoresponse across the grain (b). The values of ξ, are taken from scans shown in square boxes in (a).

This is illustrated in Figure 3.10(a) where the value of ξ was measured as a function of distance in six square boxes (scans). It is clear that the correlation length varies with the position being greater in the center of the grain while gradually decreasing upon approaching the grain boundary. This decrease is typically around 10-20% being several times greater than measurement error. This behavior was noted in several tens of grains investigated by PFM and thus indicates that the polarization disorder notably increases close to the grain boundary (most

significant variation starts at ~1-1.5 μm). There are several reasons that can qualitatively explain the increase of the polarization disorder in the vicinity of the grain boundaries. First, it can be tentatively attributed to the compressive mechanical stress arising at the grain boundaries upon cooling from sintering temperature. The origin of the stress is due to directional differences in thermal expansion coefficients, plastic deformation or elastic properties. In ferroelectric materials, the stress may also appear due to structural distortion arising upon ferroelectric phase transition. As was shown by G. Samara [10, 11] the application of compressive hydrostatic pressure to relaxors leads to an apparent decrease of the correlation radius, i.e., to the reduction of the dimensions of PNRs. This results in the shift and broadening of the dielectric maximum in several relaxor systems including PLZT [11]. For example, the correlation length is decreased by a factor of 2 when the pressure changes from the atmospheric one to 20 kbar in PLZT 12/40/60. At much higher pressures, the correlation length may increase again [12] but this pressure cannot be achieved during normal ceramic sintering. The measurements of the correlation length reported in this work are consistent with the mechanical pressure effect [11] and thus may be responsible for the grain size dependence in PLZT ceramics reported in the past (see [13] and references therein). Indeed, fine-grain PLZT ceramics exhibit much more diffuse phase transition as compared to coarse-grain samples [9].

An alternative explanation of the observed spatial dependence of the correlation length is due to the compositional gradients across the grain. This is reminiscent to the first model of relaxors (Smolenski model [14]) where the peculiar dielectric response is explained by the local fluctuations of the Curie points due to compositional disorder. Indeed, Lin and Chang [15] have reported segregation of defects and second phases at the PLZT grain boundaries during hot pressing under PbO excess. This resulted in a gradient of La concentration upon approaching the grain boundary. This behavior could be, in turn, translated into the variation of the correlation length as it s known that La substitution disrupts long-range ferroelectric order and leads to a pronounced diffuseness of the phase transition.

Another important feature of the observed grain effect is that the average value of the piezoelectric response (proportional to the average value of the polarization) also decreases upon approaching grain boundary closely following the correlation length dependence (see Figure

3.10(b)). It means that the mechanical stress and/or composition gradients may be responsible for the broad variation of the dielectric and piezoelectric properties in polycrystalline relaxors. Since the correlation length is sensitive to the position inside the grain, it is natural to expect that its value taken on a larger scale (several microns) will depend on the grain size, too.

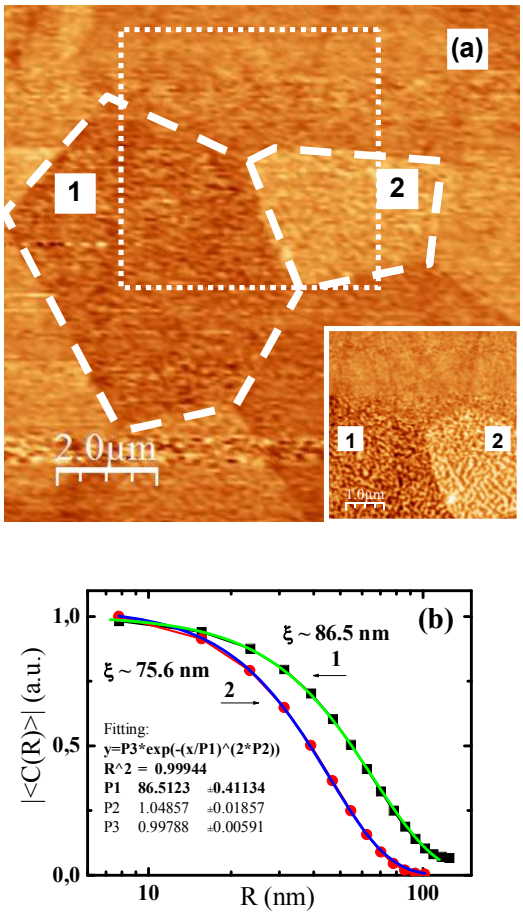

Figure 3.11 Piezoresponse images of two neighboring grains (a) and the corresponding autocorrelation functions (b) showing difference of the correlation lengths in grains of different dimensions. The inset presents a zoom of the piezoresponse images in two grains (1,2) from the selected area.

This is illustrated in Figure 3.11 where the autocorrelation function is shown for two neighboring grains (the grain structure is shown at two different scales, Figure 3.11(a), and the

grain boundary of two grains is allocated by a dashed line) of different sizes having different maximum contrast. It is clearly seen that the correlation length [see Figure 3.11(b)] is greater for bigger grain (*1*) thus confirming the above assumption. The correlation length as a function of the grain size is shown in Figure 3.12.

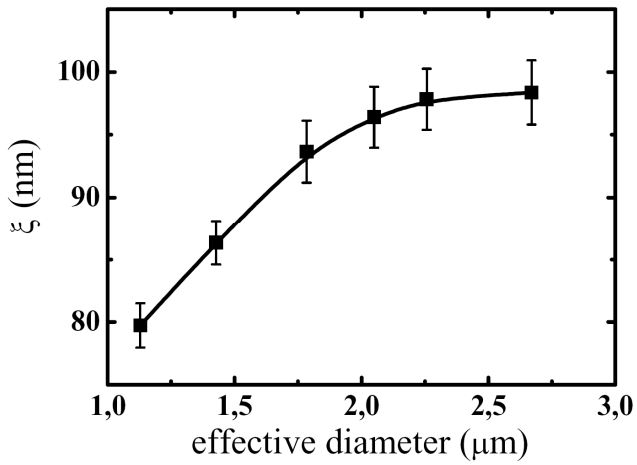

Figure 3.12 Average correlation length in PLZT ceramics taken over entire grain as a function of its effective diameter.

At least five grains of the same size but of different contrast were chosen in order to average the possible effect of the grain orientation on the observed dependence. The correlation length is about 80 nm in grains of micron-size dimensions and rapidly increases to about 100 nm for the grains with the size 2-3 μm. These data are consistent with those shown in Figure 3.10 which demonstrates the spatial dependence of the correlation length. It is obvious that the increase of ξ should occur mainly at 1 μm<d<2 μm (d is the grain size) and saturate in bigger grains where the grain boundary effect is not that significant. It should be also mentioned that the data shown in Figure 3.12 are consistent with the previous reports on the dielectric size effect in PLZT ceramics [13]. These measurements indicate that most changes of the dielectric response occur at the grain sizes 1 μm<d<2.5 μm and saturate in ceramics with bigger grains. Thus the local measurements in relaxor ceramics give clear insight into the origin of the deterioration of the dielectric response with decreasing its grain size [13]. In this way, we can explain the

broadening of the dielectric peak in PLZT ceramics with decreasing grain size [13]. Indeed, in small grains we can expect smaller correlation length and its larger variation across the grain. This means that the local phase transition and freezing temperatures should be also inhomogeneous inside the material giving rise to the broader distribution of the relaxation times and thus to the broader dielectric peak. The measurements of the correlation length can be thus useful for the understanding of the nature of diffuse phase transformations in polycrystalline ferroelectrics.

§3.4 2D Mapping Disorder in Polycrystalline Relaxors

In this section, we developed an advanced experimental procedure, which is based on the PFM measurements of local lattice vibrations and involves the Fast Fourier Transform (FFT) analysis of random polarization patterns. The maps of amplitude, radius, eccentricity, rotation, and width of the spatial correlation spectrum were extracted from the obtained piezoresponse images.

To analyze the image texture, 128x128 pixel sub-image centered at $(x_1, y_1) = (64,64)$ was chosen in the corner of the 3.000x3.000 full image. The 2D FFT transform is performed within the selected region, and resulting 2D data set was fitted using phenomenological function Z_{2D} as described below. Here, the function is chosen such as to reproduce the central peak and the ring, and allow for texture/preferential orientations (i.e. cross-section is ellipse rather then rotationally invariant). After fitting, the sub-image is shifted by 64 points, and fit was repeated. The fitting parameters are plotted as 2D maps for Mod (3000/64) = 46 points. This process thus allows extended 2D version compared to analysis in *paragraph 3.3*. Note that adjacent points are not independent [since sub-images overlap by half], but next nearest neighbors are independent. Hence, gradients in the texture images are gradual if span more then 2 adjacent pixels.

The phenomenological fitting function is

$$Z_{2D} = Z_e + Z_c + Z_0, \tag{3.3}$$

where Z_e and Z_c are ellipsoidal ring and central peak contributions, respectively, and Z_0 is position-independent offset. The functions

$$Z_e = A_1 \exp\left(-\frac{(a-d)^2}{s_1^2}\right), \tag{3.4}$$

$$Z_c = A_2 \exp\left(-\frac{b^2}{s_2^2}\right), \tag{3.5}$$

where A_1 and A_2 are the intensities of the texture and central peak, d is the characteristic wave vector of the domain, and s_1 and s_2 are corresponding widths. The coordinates are defined as

$$a^2 = x_2^2 + \left(y_2/(1-\varepsilon_1)\right)^2, \tag{3.6}$$

$$b^2 = x_2^2 + \left(y_2/(1-\varepsilon_2)\right)^2, \tag{3.7}$$

where ε_1 and ε_2 are eccentricities. Finally, $x_2 = x\cos\varphi + y\sin\varphi$ and $y_2 = -x\sin\varphi + y\cos\varphi$, where x, y correspond to the components of wave vector and φ is rotation angle. The maps of 9 independent parameters (2 amplitudes, 2 eccentricities, 2 widths, radius, angle, offset) are plotted as 2D maps.

In order to analyze the distribution of nanodomains over the area containing several grains, we performed large scans (30x30 μm^2 with the resolution 3000x3000 pixels) (Figure 3.13(a)) and made Fast Fourier Transform (FFT) analysis in windows containing 128x128 pixels (Figure 3.13(b)). Since the pixel size (10x10 nm^2) is much smaller than the domain size, each window reproduces domain distribution with sufficiently high accuracy. On the other hand, there are enough features in the selected windows for the FFT analysis.

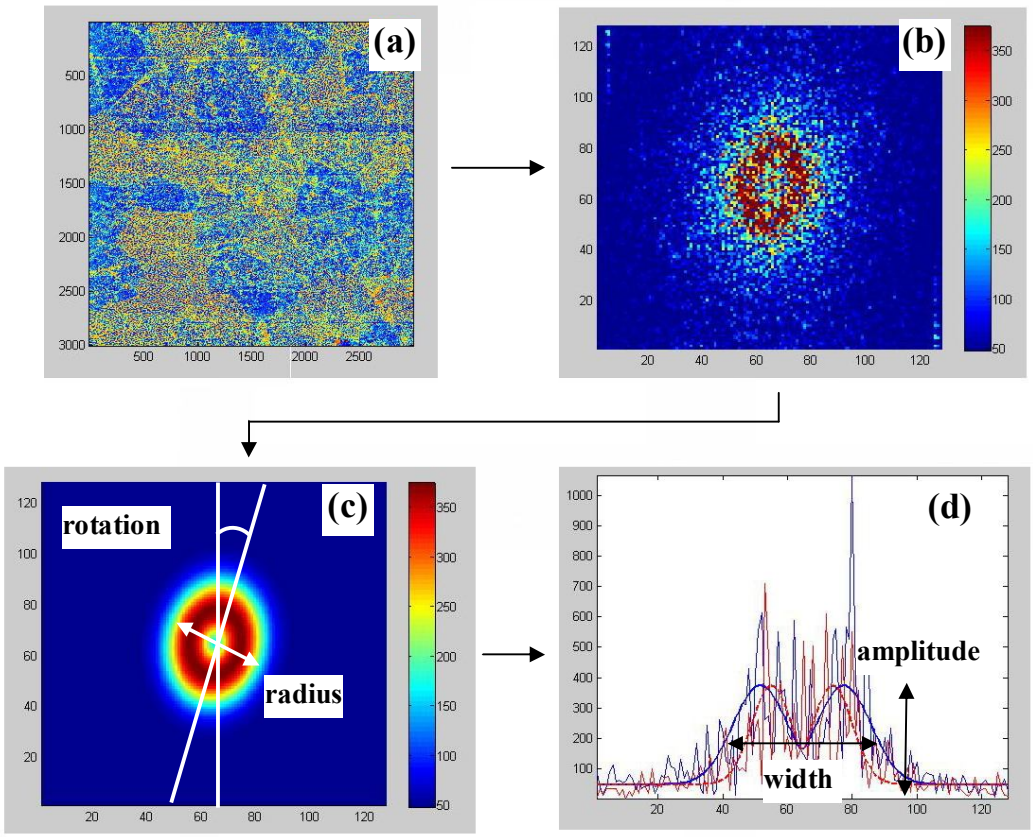

Figure 3.13 The interface (step-by-step) of a program for plotting maps images after 2D-FFT procedure. (a) – piezoresponse image of PLZT ceramics, (b) - Fast Fourier Transform (FFT), (c) – FFT after smoothing, (d) – cross-section from (c).

Figure 3.14 represents an example of the FFT processing of the selected windows where different parameters such as amplitude, radius, eccentricity, rotation, and width of the spatial correlation spectrum could be extracted.

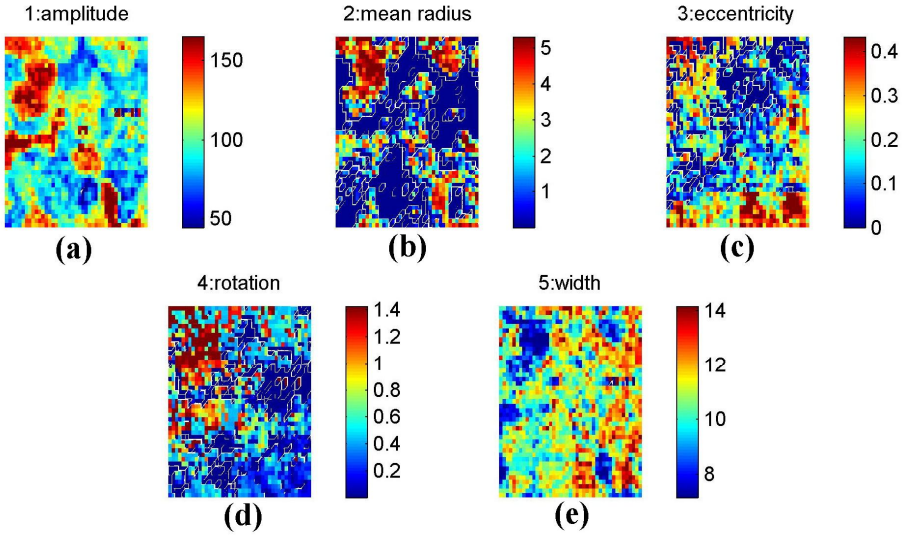

Figure 3.14 Example of the FFT processing of the selected windows where different parameters such amplitude (a), radius (b), eccentricity (c), rotation (d) and width (e) of the spatial correlation spectrum could be extracted.

The results are shown in Figure 3.15 together with original phase image of the contrast and grain boundaries denoted by dashed lines.

The microscopic mechanism involved in relaxors is still puzzling as it is difficult to deal with the nanoscale inhomogeneities whose observation depends on the length and time scale of the experimental probe. Besides, it is believed that the properties cannot be explained without considering hierarchical structures and dynamics underlying the need of multiscale tools going from atomic scale to large ferroelectric domains. Figure 3.15 is the first attempt to map different parameters of the polarization distribution obtained while observing the microstructure of ceramics (visible grains in Figure 3.15(a) after our FFT procedure. Among the parameters we could extract, the amplitude (Figure 3.15 (b), the radius (Figure 3.15 (c), and the width of the spatial spectrum (Figure 3.15 (d) are of great importance as new features can be revealed because they correspond to the average piezocoefficient – or, in other words, the polarization strength-, the correlation length, and the distribution of the characteristic length scales, respectively.

These pictures complement classical maze-like domain images obtained by PFM (Figure

3.15 (a)) in relaxor materials and show clearly that this method provides a powerful and unique tool for investigation of inhomogeneous or disordered materials at the mesoscale. It is worth noting that whereas the classical PFM phase displays polarization inhomogeneities at the nm scale, the 2D-FFT processing provides information at an upper (meso)scale, as the inhomogeneities revealed with PFM phase is no more evidenced and instead new and larger sized features are seen.

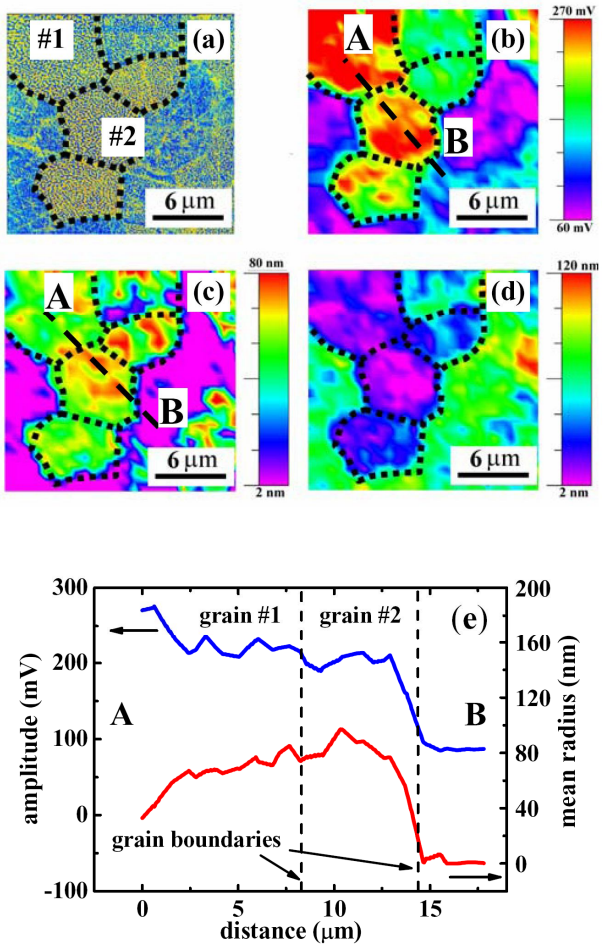

Figure 3.15 Original phase image (a) of the contrast comprising several grains, maps of the amplitude (b), the radius (c) and the width (d) after FFT procedure, (e) variation of the piezoresponse (blue line) and radius (red line) across the two neighboring grains (for b,c).

Let us start by looking at the amplitude map that concerns the strength of the polarization

within a several microns grain size. As one can see (Figure 3.15), some submicron-sized clusters randomly distributed within one grain are superimposed on the maze polarization usually observed by PFM phase. It is worth mentioning that the polarization adapts itself close to the grain boundaries as we have already shown in the previous section. This was explained either by stress accommodation or pinning through defects (most probably La^{3+}). This picture thus visualizes the value of polarization (not well seen in classical PFM images) and reflects the role of the grain boundaries in the development of polarization. Some grain boundaries (probably with low angle between rhombohedral axes) do not affect the polarization and thus can be distinguished from high-angle grain boundaries where the polarization is strongly disrupted.

The spatial inhomogeneities within the grain can be seen as a mixture of polar regions with some sort of glassy correlations, in agreement with earlier suggestions [16]. Indeed, the red zones (in the bottom grain or grain 2) indicate the strongest polarization amplitude. However, the correlation length associated with these polarizations regions is relatively weak as one can judge from the map of correlation length (Figure 3.15(c)).

This situation can be considered as the existence of a core of polarizations with all of them being correlated (mean correlation length) and embedded as a core-shell with a more randomly distributed or glassy-like polarizations. This is well presented on the cross-section showing similar behavior of the amplitude and correlation radius at the grain boundary (Figure 3.15(e)).

It is interesting to remark that the described regions show a rather small width indicating a narrow distribution of length scale and, as a consequence, of relaxation times. A narrow width is also measured in the top grain (grain 2). In this latter grain, the correlation length is rather big as its value is around 60 nm on average. This situation can be interpreted by considering strong enough polarizations interacting with collective dynamics. Such interpretation can be also used for the description of bottom grain (grain 1).

Moreover, interestingly, the shape of the correlation length of the top grain is very similar to that observed with PFM phase but at another scale. This is typical for a fractal behavior. It is remarkable that inside grain 2 the contour of the increased radius (higher correlation length or average domain size) fully corresponds to the distribution of the width (Figure 3.15(d)), i.e., the

width of the spectrum of spatial correlations or roughly the spectrum of relaxation times. The measure of the width of the correlation spectrum is the freezing temperature T_f at which the relaxation spectrum becomes infinitely broad. The rough correspondence of the two parameters (T_f and R_C) reflects the closeness of the selected composition to the non-ergodic state where local change of the correlation length is immediately translated into the variation of T_f. We therefore argue that presented maps are the true images of the relaxation parameters of PLZT near the surface. In this context we should point out that the correlation radius evaluated by FFT is several times greater than that measured by TEM [17]. This can be attested to the influence of the surface as the PFM is sensitive to the piezoelectric vibrations in the layer 50-100 nm deep into the material. The origin of the spatial variation of the relaxor parameters in PLZT can be understood as follows.

In addition to PFM measurements we analyzed EDS spectrum from two neighboring grains of PLZT ceramics. The EDS patterns with SEM micrographs of the fracture surface of the ceramics are shown in Figure 3.16.

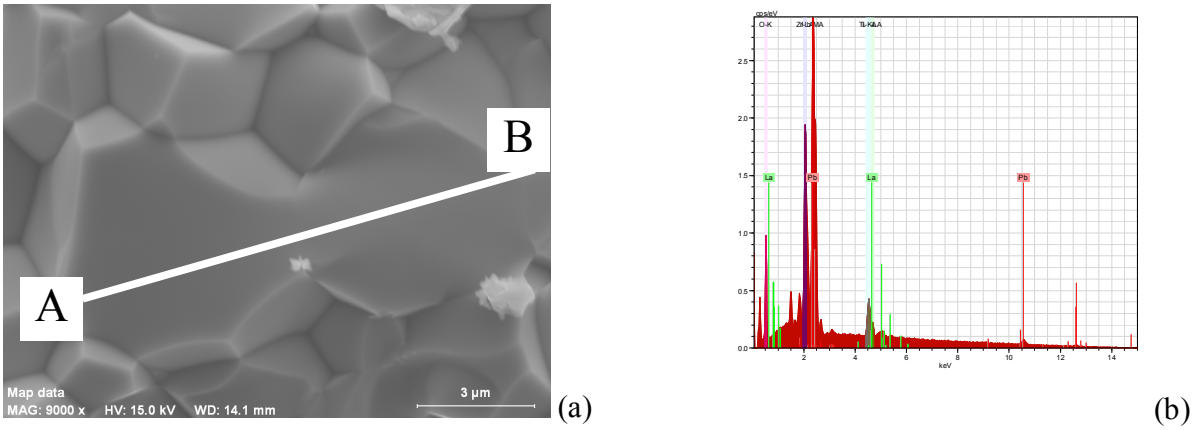

Figure 3.16 SEM images (a) and EDS spectrum (b) of PLZT ceramics.

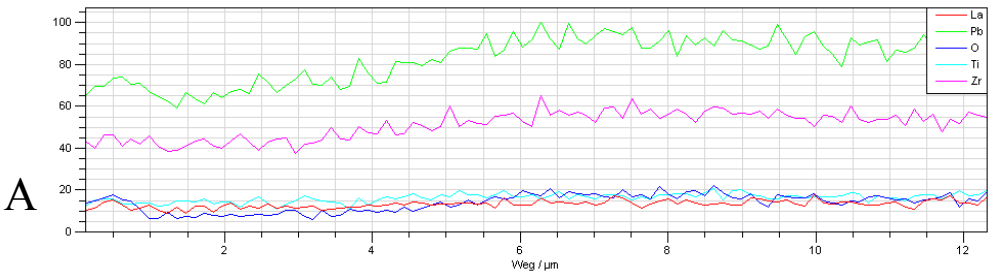

(c)

Figure 3.16 (*Continued*) cross-section along line A-B from (a) of the element analysis of PLZT 9.5/65/35 ceramics (c).

The corresponding EDS spectrum taken from the region in PLZT ceramics (Figure 3.16(b)) clearly shows the presense of the formed phases rich in Pb and Zr with a trace of La. Chemical analysis of PLZT ceramics by emission microanalyzer for Pb, Zr, Ti and La agreed well with the nominal composition of PLZT. The line was drawn across the two grains such that the one grain boundaries and two grains come under line scanning. The different element signals observed in the line scan (shown in the Figure 3.16 (c)) clearly show the homogenous distribution of elements in the entire sample. From the close inspection of the Pb signal we can conclude that Pb concentration is maximized at the grain boundaries. No significant change of La, Ti and O concentration is found at the grain boundaries.

La^{3+} ion substitutes for Pb^{2+} ions in the PZT lattice, and because it possesses a larger positive charge compared with the host ion it creates charge imbalance that depends on volatility of PbO during sintering. If there is PbO loss defect chemistry predicts reduction of oxygen vacancies in the lattice and increase of resistivity. If the PbO loss is not allowed (sintering in a PbO atmosphere) it favors creation of Pb vacancies as the compensating species. In this scenario there is no change in the resistivity but dipolar defects can be easily formed. Typically, both scenarios coexist because it is difficult to prevent evaporation of PbO during liquid sintering. The ionic defects such as Pb and O vacancies can agglomerate [18] and form defect clusters i.e. local random electric fields that may disrupt long-range polarization order and create isolated polarization clusters whose statistical properties reflect the distribution of such defects. It is thus possible that the distribution of relaxor parameters reflects the distribution of random electric fields and thus defect accumulation near the surface.

§3.5 Piezoelectric Hysteresis Loops in PLZT Ceramics

An attempt was made to measure hysteresis loops in both crystallographic directions in order to verify the ability of the PFM tip to induce a phase transition into tetragonal phase and, therefore, a high piezoelectric signal in vicinity of the PFM tip. The results are shown in Figure 3.17. The sequence of the measurements was as follows. First, the PLZT ceramic was prepoled by pulses of variable height and then piezoelectric response was measured at the same location in the absence of electric field. Since the electric field is non uniformly distributed under the surface [19] even small voltages applied by the PFM tip are expected to induce the phase transition. Detailed investigation of hysteresis loops by PFM is observed to clear out the mechanism of ferroelectric switching at the nanoscale. Figure 3.17 shows that the increase in the La mole fraction from 6 to 10 % (for the constant Zr/Ti ratio = 65/35) results in disappearance of the local piezoelectric hysteresis loop.

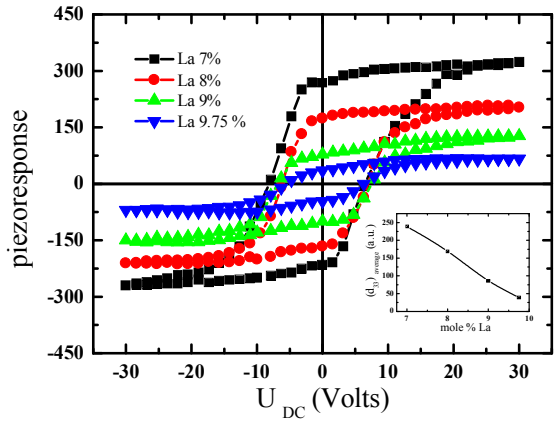

Figure 3.17. Piezoelectric hysteresis loops in PLZT ceramics with different La content. The inset is a value of piezoelectric coefficient d_{33}^{eff} calculated from loops.

This results have good correlation with macroscopic *P-E* ferroelectrics loops from PLZT

ceramic x/65/35 (for x = 6-10 La mole per cent) measured at room temperature (this data have a good compare with Figures 3.6 and literature data from [20]).

Figure 3.18 illustrates of the domain growth process via PFM in PLZT 9.75/65/35 ceramics.

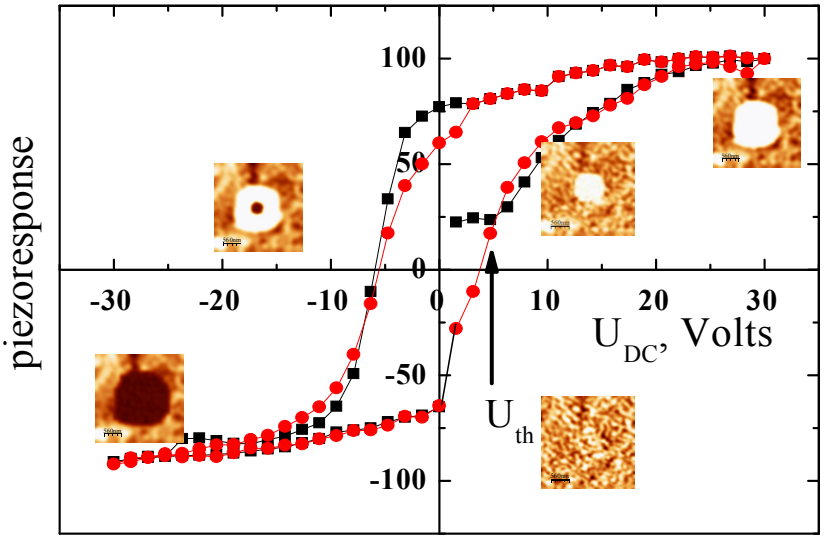

Figure 3.18 PFM hysteresis loop of PLZT 9.75/65/35 ceramics. The insets (scan size 2.5 μm) show the static domain structures obtained by intermediate scanning with V_{AC}=1 V in the corresponding points of the hysteresis.

The tip was positioned in the center of the grain with labyrinth-type domain structure. It should be noted that the increase of the contrast under the application of a dc bias has a threshold-like character and can be attributed to the local phase transition induced by PFM tip. After the threshold (U_{th}≈8-10 V) the local piezoelectric coefficient follows normal hysteresis behavior characteristic of ferroelectric phase with the coercive voltage of about 5-7 V.

In order to understand the hysteresis behavior, the surface of the sample was scanned

between the pulses. Since the applied pulses were sufficiently long (~1 s), the created domains were quite stable and no relaxation occurred, at least during scanning. The changes of the domain structure caused by the applied voltage could be arranged as a sequence of images corresponding to different points of the hysteresis loop (see insets to Figure 3.18).

The measurements of hysteresis loops were performed inside one of the nanodomains, which size is only several times larger than the size of the tip. We observed a threshold-like change of the longitudinal piezoresponse that may signify local transition from the relaxor to ferroelectric phase. In this case, the size of the switched area (Figure 3.18) is much smaller than the grain size. It means that the hysteresis measurements are not sensitive to the bulk of the ceramics and possibly occur in a single grain closest to the surface.

Figure 3.19 represents piezoelectric hysteresis loops obtained in two adjoining PLZT ceramics grains with different crystallographic orientations (Figures 3.19(b–d)). The grains appear as the regions with different contrast in Figures 3.19 (b–d) because the value of the piezoelectric response associated with the contrast scale differs for differently oriented monocrystalline grains. The orientation of polarization vector relative to the orientation of grain surface can vary from vertical one (the maximum piezoresponse value) to parallel to the sample's surface plane (no piezoresponse).

The dependences described above showed that the maximum piezoresponse values obtained in the grains with a maze-type domain structure (Figures 3.19 (a), curve 1) are higher than for grains with more homogeneous distribution of piezoelectric potential across the surface (Figures 3.19 (a), curve 2). It was assumed that such piezoresponse behavior is connected to the grain orientation in the samples of PLZT-9.75 ceramics. Grains with the highest piezoelectric response are most likely oriented in <111> direction. Grains without any observed nanodomain formations are oriented in the directions different from <111>, thus the values of their piezoresponse induced by the same external field are smaller. A comparison of the A and B regions in Figures 3.19(c,d) allows to conclude that the polarization created on the surface of the sample under the cantilever tip after the measurement cycle of the piezoelectric hysteresis loop relaxes sufficiently fast. The local piezoelectric response of the PLZT ceramics samples with

maze-type domain structure (Figures 3.19 (c), point "A") indicates an existence of the polarized state after removing the external field. The remnant polarization nearly vanishes within 45 minutes (Figure. 3.19 (d), point "B").

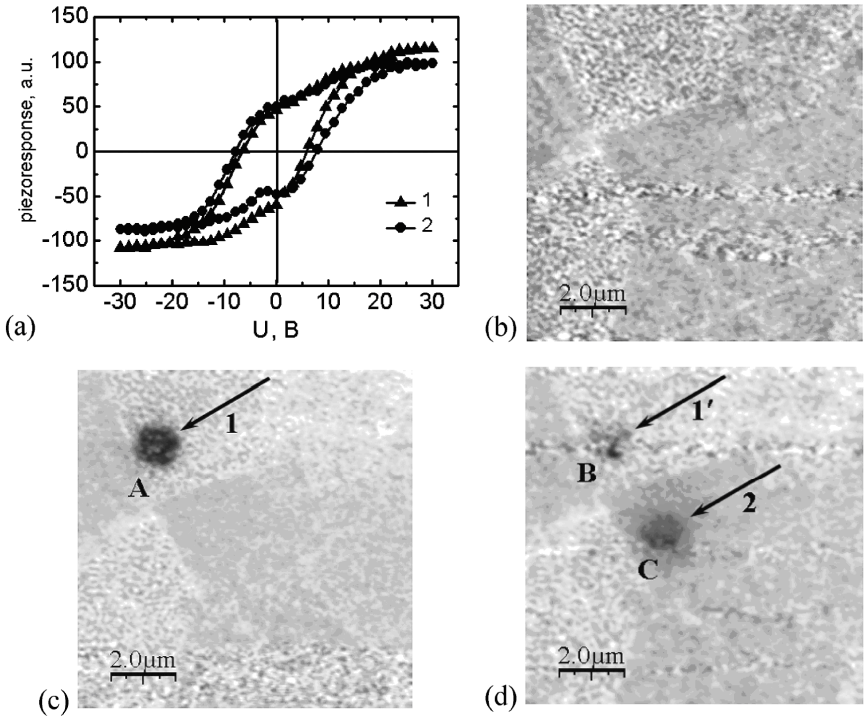

Figure 3.19 (a)—piezoreponse hysteresis loops of PLZT 9.75/65/35 ceramics obtained in grains with different contrast: curve 1—for a grain with the labyrinth domain structure, curve 2—for a grain with a homogeneous piezoresponse. Surface image obtained by means of PFM: (b)—initial state, (c) and (d)—after piezoresponse hysteresis loops measurements (arrows point to the contact of a cantilever tip and PLZT ceramics surface).

The piezoresponse hysteresis loops obtained at two different points on the scanned surface Figure 3.19 (a,b) gave evidence of an existence of the areas with an internal bias field over the surface of PLZT-9.75 ceramics. As it can be seen from Figure 3.20, the orientation of the internal electric field varies along the surface.

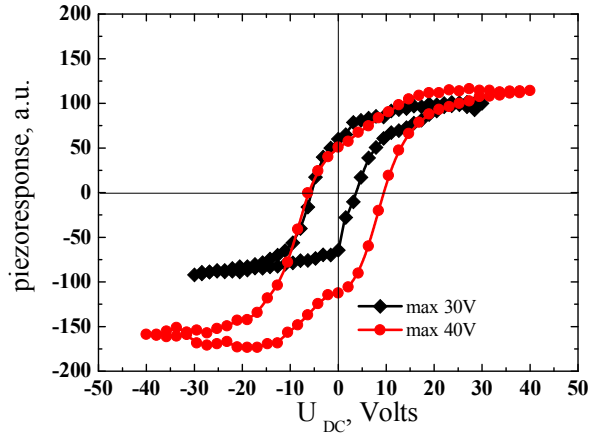

Figure 3.20 Piezoelectric hysteresis loops of PLZT-9.75 ceramics obtained for regions with different directions of the internal electric fields.

The remnant piezoelectric response can be associated with the creation of induced stable polarized state on the ceramics surface under a strong electric field in the vicinity of the sharp PFM probe tip caused by external bias. As in the case of simultaneous effect of an external electric field the remanent polarization can be switched like the spontaneous polarization in ferroelectrics. This is confirmed by piezoelectric hysteresis loop Figure 3.19 (a). The induced ferroelectric state is sufficiently stable and can be observed for several hours after removing the external electric field (Figure. 3.19 c,d).

§ 3.6 Domain Wall Dynamics in PLZT Ceramics

In this section we report on results of the nanoscale measurements of ferroelectric domain wall velocity and static domain wall roughness in disordered (Pb,La)(Zr,Ti)O_3 (PLZT) ceramics prepared by hot press sintering. The origin of the disorder and its dependence on the La content in PLZT are discussed.

Introduction to Domain Wall Motion

Domain walls, twin and interphase boundaries play a key role in a variety of physical processes occurring in crystalline materials, such as reorientations of order parameters, inelastic deformations, and phase transitions. Accordingly, these mobile interfaces may strongly affect the performance and figures of merit of many functional materials employed in electronic devices. The most famous examples are the processes of magnetization switching in ferromagnets and polarization reversal in ferroelectrics, which in fact are controlled by the domain wall motion and are the key factors in functioning of magnetic and ferroelectric non-volatile random access memories [21, 22, 23].

In real crystals, the domain wall motion is hindered not only by the lattice periodic potential relief, but also by their interactions with crystal imperfections. Remarkably, when the pinning of domain walls by immobile defects dominates, the wall motion proceeds via a thermally activated *creep process* [24, 25, 26]. The pinning by randomly distributed defects also influences the statics of domain walls, leading to the appearance of a domain *wall roughness* despite the presence of a surface tension tending to flatten the wall [27]. The behavior of domain walls in crystals with disordered pinning potential is characterized by a dynamical exponent μ and a roughness exponent ζ, which depend on the dimensionality of the wall and on the nature of pinning potential.

For ferromagnetic domain walls, Lemerle *et al.* [28] found that the measured dynamic and roughness exponents are consistent with the theoretical values $\mu = 1/4$ and $\zeta = 2/3$ predicted for one-dimensional interfaces moving in a medium with the so-called random-bond disorder. Although surprising at first glance, this result can be explained by a very small thickness of the investigated ferromagnetic film, which makes the height of domain walls much smaller than their length scale L in the film plane.

On the contrary, the experimental studies of the statics and dynamics of ferroelectric domain walls, which were performed up to now [29, 30, 31, 32], indicated that these walls behave as two-dimensional interfaces. In particular, for walls in epitaxial $PbZr_{0.2}Ti_{0.8}O_3$ films with thicknesses t = 50–90 nm, the roughness exponent at short length scales L < 100 nm was

found to be rather small ($\zeta \sim 0.25$), whereas the measured dynamical exponent is large ($\mu \sim 0.6$) [30]. These results were explained by the random-bond disorder combined with the effective wall dimensionality $d_{eff} = 2.5$, which differs from $d = 2$ due to the existence of long-range dipolar interactions characteristic of ferroelectric materials [31]. A rather large dynamic exponent $\mu \sim 0.5$ has been obtained for ferroelectric walls in ultrathin $BaTiO_3$ films as well, although the monitored in-plane sizes of growing domains were much larger than the film thickness $t = 60$ nm [32]. This value also points to the presence of a random-bond disorder and two-dimensional behavior of domain walls in $BaTiO_3$ films, but a definitive conclusion cannot be made without the wall roughness measurements.

The domain wall roughness is determined with the aid of PFM for the natural domain structure existing in this polycrystalline ferroelectric. Besides, artificial ferroelectric domains are created by the application of voltage pulses to the conducting PFM tip, and the in-plane domain size is measured as a function of pulse duration. Since the obtained roughness and dynamical exponents indicate a *one-dimensional interface*, we additionally studied the shape of artificial domains by sequential layer-by-layer polishing with the subsequent imaging of domains by PFM.

For the investigated PLZT ceramics, PFM clearly distinguishes individual grains (Figure 3.21). The grains have the average sizes ranging from 5 to 7 μm and regular or irregular hexagonal shape typical of the dense packing of hot-pressed ceramics [33].

Figure 3.21 shows the piezoresponse image of an array of five domains reversed by applying +30V of various pulse durations in the range between 1 and 1000 s. It can be seen that the domain diameter strongly depends on the duration of the voltage pulses applied between the AFM tip and the bottom electrode.

The polarized domains demonstrate strong stability for several hours. The smallest stable domain written by AFM tip bias is ~ 100 nm (by a +30V, 0.5 s pulse, not shown here). This is likely the minimum size of the reversed domain by the AFM tip field. According to Molotskii [34] the domain radius under the inhomogeneous AFM tip field depends significantly on the spontaneous polarization value (P_S).

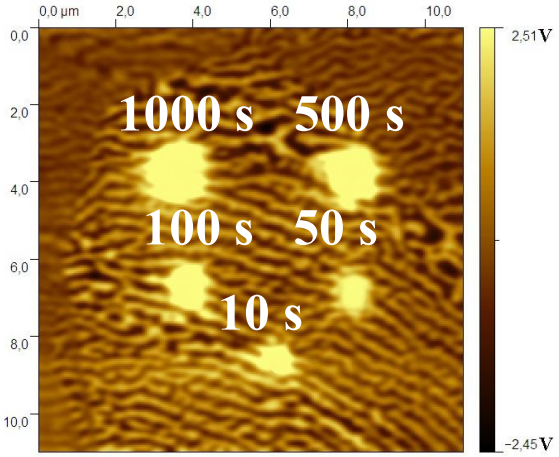

Figure 3.21 Piezoresponse images of the PLZT ceramics after local poling. Ferroelectric 180° domains formed in the PLZT at the voltage V = 30 V applied between the SFM tip and the bottom electrode. The in-plane domain size increases monotonically with increasing writing time τ , which equals 10 s, 50 s, 100 s, 500 s, and 1000 s, respectively.

The equilibrium radius r_m strongly decreases with P_S increasing in the form of $r_m \sim 1/P_S^{2/3}$. Thus nanoscale domains (below 100 nm) for PLZT 9.5/65/35 bulk ceramics under AFM field is difficult to expect due to its smaller P_S value of 10 μC/cm^2, as compared to $LiNbO_3$ (P_S =70 μC/cm^2) and $RbTiOPO_4$ (P_S= ~30 μC/cm^2).

The dependence of domain diameter D on the pulse duration τ at a fixed voltage V_{tip} = +30 V is shown in Figure 3.22(a). It can be seen that the domain growth process is fast at small writing times τ < 500 s but becomes very slow at τ > 1000 s. To understand the mechanism of lateral domain expansion, we determined the velocity $v(\tau)$ of the radial motion of domain boundary at a fixed voltage V_{tip} via the relation $v = 0.25\ dD/d\tau$. The results of our analysis are shown in figure 3.22(b), where v is plotted as a function of the domain diameter D. The revealed exponential type of the dependence $v(D)$ indicates that the motion of domain boundary is governed by a thermally activated process.

To further gain insights into the domain lateral growth, the instantaneous local wall velocity was extracted from the time dependence of the domain diameter, as shown in Figure 3.22 (b). It is very interesting to find that the domain wall velocity behavior fits well to

exponential decay related to the inhomogeneous AFM tip field, which reveals an activation mechanism of the wall motion in bulk PLZT ceramics.

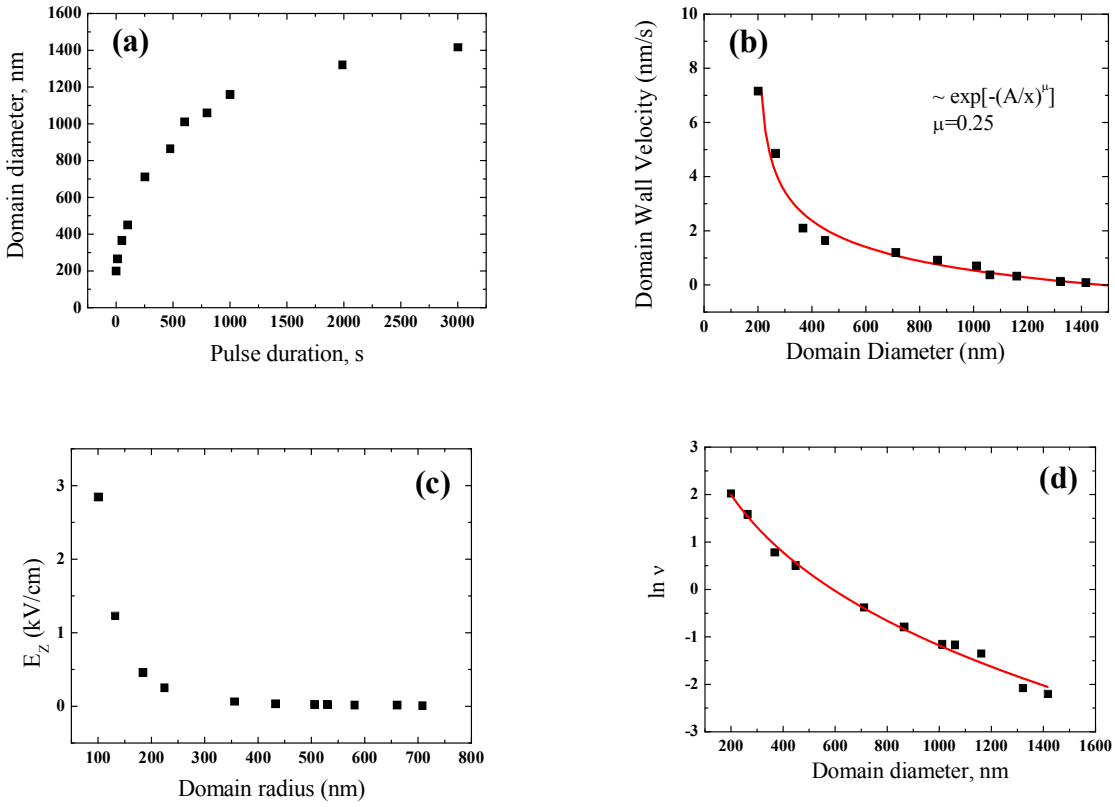

Figure 3.22 (a) Domain diameter vs. the pulse duration for +30 V pulse voltage and (b) domain wall velocity as a function of domain diameter calculated from the data in Figure 3.21(a). The data fit well to v ~ exp[-(A/x)$^{\mu}$] with μ=0.25; (c) the radial distribution E_z for U_{DC}=+30V calculated by Equation (3.8); (d) Logarithm of the domain-wall velocity v as a function of domain diameter at the applied voltage V = +30 V. Symbols denote the values of ln v (with v in nm s−1) calculated from the measured dependence of the domain diameter vs. the writing time, and the solid line shows the fitting of experimental data.

To gain more detailed insight into this process, we have to determine variation of the electric field *E(r)* acting on domain boundary with its distance *r* from the SFM tip. As shown by Pertsev *et al* [32], the most important contribution to the driving field *E(r)* is created by the

conical part of the tip, which can be modeled by a charged line segment. Near the bare surface of a bulk sample, this contribution scales as $E \sim 1/\rho$ with the in-plane distance ρ from the tip apex. Since the electric field *E(r)* also decays with the distance *z* from the sample surface, the maximum driving field acts on the part of domain boundary adjacent to the surface ($z << \rho$). Therefore, we obtain the relation $E \sim 1/D$ for the electric field determining the velocity $v(D)$ of observed lateral domain expansion.

In the literature one may meet several approaches to the calculation of the field distribution under an AFM tip. The authors of [35] calculate it assuming the tip to be a charged sphere and using the electric potential distribution proposed in [36] for a semi-infinitive anisotropic dielectric under an external point charge. In our calculations we used the same approach. This potential distribution produces the normal E_z and lateral E_r field components, whose spatial distributions, that is their decay along the polar axis *z* and the nonpolar (cylindrical) axis *r* from the point of the tip apex projection on the surface are presented by the expressions (3.8) and (3.9), respectively,

$$E_z(z,r) = \frac{2Q_t}{(\sqrt{\varepsilon_a \varepsilon_c} + 1)} \cdot \frac{(z/\gamma + R + \delta)}{\gamma\left[r^2 + (z/\gamma + R + \delta)^2\right]^{3/2}}, \tag{3.8}$$

$$E_r(z,r) = \frac{2Q_t}{(\sqrt{\varepsilon_a \varepsilon_c} + 1)} \cdot \frac{r}{\left[r^2 + (z/\gamma + R + \delta)^2\right]^{3/2}}. \tag{3.9}$$

(Equation (3.8) is identical to the expression for *Ez(r)* in [35] for the one-dimensional case). Here *R* is the tip radius, δ is the distance from the tip apex to the surface, ε_a and ε_c are the dielectric constants, the charge $Q_t = C_t U_{DC}$, where the capacitance tip-to-crystal C_t.

Figure 3.22 (c) presents a tip-field distribution calculated from (1) for δ=0 and U_{DC}=+30 V. From comparison of *v* to $E_z(r)$, one may conclude that in PLZT bulk ceramic, unlike in

$LiNbO_3$, the drop of v follows roughly the dip of E_z.

For the fitting of our experimental data, we also need to specify the electric field dependence of v. If the motion of domain walls in the investigated PLZT ceramics is governed by a creep process, this dependence takes the form

$$v = v_\infty \exp\left[-\frac{U_a}{kT}\left(\frac{E_c}{E}\right)^\mu \right], \tag{3.10}$$

where μ is the dynamical exponent, U_a is the characteristic activation energy, $E_c >> E$ is the critical electric field, T is the temperature and k is Boltzmann's constant [24,25,26]. With $E \sim 1/D$ Equation 3.10 gives $\ln v = \ln v_\infty - \text{const} \cdot D^\mu$ at a given temperature. As can be seen from figure 3.22(d), the experimental results can be fitted by this relation with a very good accuracy. Importantly, the deviation from the linear dependence $\ln v = \ln v_\infty - \text{const} \cdot D$, which could be attributed to the wall motion in a defect-free crystal lattice [37], and the decrease of $|\partial \ln v / \partial D|$ with D ("concave" dependence [32]) are explained by the creep-like motion of domain boundary. For the dynamical exponent, the fitting procedure yields $\mu \approx 0.25$, which points to the dominant role of random-bond disorder in PLZT 9.5/65/35 ceramics.

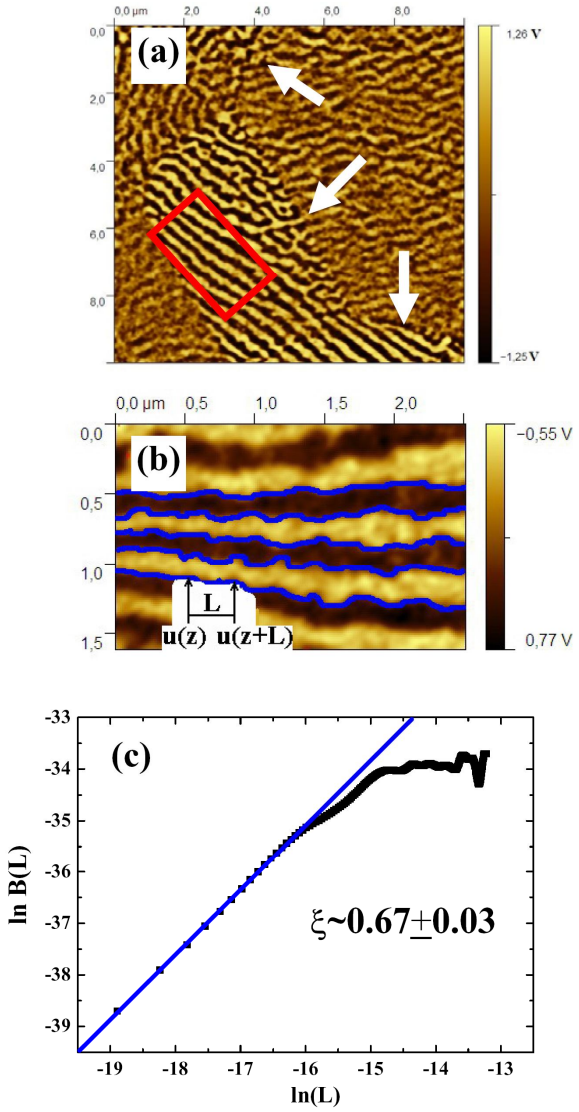

Figure 3.23 As-grown ferroelectric domain structure of the bulk PLZT 9.5/65/35 ceramics (a). Zoom area from (a) with regular domain for determinate roughness of the domain walls (b). Typical correlation function B(L) drawn in a *ln-ln* plot. Fitting the linear part of the curve gives 2ξ (b).

Figure 3.23(a) show very good piezoelectric contrast in the individual grain of the PLZT 9.5/65/35 ceramics with regular domain structures. Light and dark areas correspond to domains with different polarization directions. It is seen that the fractions of domains with different

directions of spontaneous polarization are almost equal. The bend and split of the domain marked by arrows at the grain boundary regions may be attributed to the existence of inhomogeneous lattice distortions or spatial defects which destroyed the continuity of ferroelectric domains and minimized the elastic energy and depolarization fields at the grain boundaries [38]. The fingerprint patterns in Figure 3.23 (a) are relatively regular and are almost periodically spaced in each individual grain. For an analysis of the domain wall roughness we studied five as-grown domain walls (Figure 3.23(b)) with average length 2 μm and effective diameter 150 nm.

The domain wall roughness of elongated as-grown domains the boundary between negative and positive domains with polarization vector oriented normal to the ceramic surface was analyzed (Figure 3.23) using the pair-correlation method described by Paruch *et al.* [30]. The correlation function B(L):

$$B(L) = \overline{\left\langle [u(z+L) - u(z)]^2 \right\rangle}, \tag{3.11}$$

of relative displacements essentially measures the local variance of the wall position from an elastically ideal flat configuration as a function of the length L along the wall, and is predicted to show a power-law growth at equilibrium, governed by a characteristic roughness exponent ζ. As shown in Figure 3.23(c), from a linear fit of the lower part of the $\ln[B(L)]$ versus $\ln(L)$ curve 2ζ allows to be determined. We obtained the average value of the roughness exponent ζ = 0.67±0.03, close to ζ = 2/3 expected for the case of quenched disorder alone and it is higher than that observed in PZT thin films [31]. We found no correlation between the roughness of domain walls and orientation of the grain in the ceramics. This result is in agreement with previous studies [29] pointing to the negligible role of the commensurate potential compared to the effects of disorder. The exact origin of the domain wall roughness is as yet unknown; it may be intrinsic (i.e., disorder caused by La and compensating defects) or due to a combination of low in-plane anisotropy and extrinsic defects, e.g., dislocations or impurities

Combining the results of our static and dynamic measurements, we can determine the effective dimensionality d_{eff} of domain boundary responsible for the lateral domain growth in PLZT 9.5/65/35 ceramics. Indeed, the dynamical exponent μ is related to the roughness exponent

ζ by the formula [31]:

$$\mu = \frac{d_{\text{eff}} - 2 + 2\zeta}{2 - \zeta}. \tag{3.12}$$

The substitution of μ = 0.25 and ξ = 2/3 into equation (3.12) gives d_{eff} = 1, in striking contrast with the value of d_{eff} = 2–2.5 expected for ferroelectric domains in bulk materials.

Evidently, the boundary of a reversed domain created by the SFM tip is two-dimensional. However, if the domain size in the direction orthogonal to the surface is much smaller than its in-plane diameter measured in the dynamic experiment, the radial domain expansion could be similar to a motion of one-dimensional interface. This supposition was confirmed by polishing experiments, where an artificially created domain was sectioned by the consecutive layer-by-layer polishing.

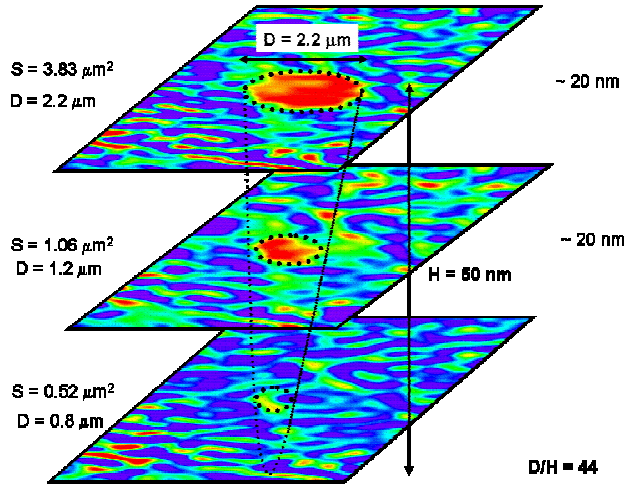

Figure 3.24 PFM images of the PLZT ceramics obtained after several polishing process. Thicknesses of the removed layers were determined from changing of the scratch structures. At the beginning has been induced domain by U_{DC} = +30 V with t = 100 s.

Figure 3.24 shows several PFM images of such induced domain after writing voltage pulse of 100 s duration and +30V amplitude. Slicing the ceramics by polishing was verified to not disturb the grown domains. Figure 3.24 confirms that the domain area (D) is considerably

larger than its depth (H) (i.e., the aspect ratio is D/H=44) which means that the created domain represents quite shallow and flat structures. This eventually verifies that the induced domain wall is quasi one-dimensional and the conclusions drawn from the dynamic and domain roughness experiments are validated. The origin of the shallow and highly anisotropic domains in PLZT ceramics obviously requires further investigation.

In addition, we observed that dynamics exponents in PLZT bulk ceramics depend on La concentration. The value of the dynamic exponent of PLZT ceramics considerably decreases with increasing the La content from 0.33 to 0.25 for 5% and 9.5%, respectively (Figure 3.25). Probably, this effect reflects different nature of defects, the degree of disorder and polar interactions in relaxor ferroelectric materials.

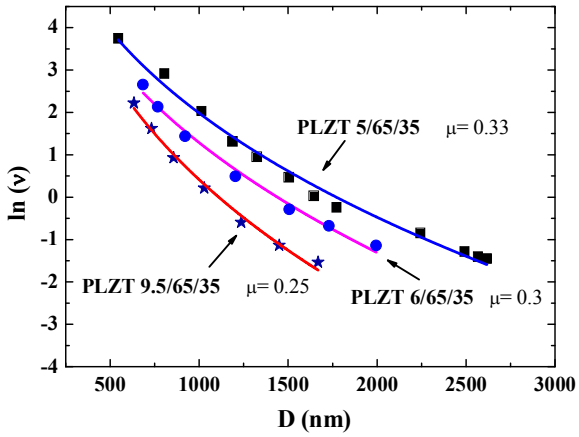

Figure 3.25 Logarithm of the domain-wall velocity v as a function of domain diameter D at the applied voltage V = 30 V for a different La concentration in PLZT ceramics.

Relaxation of the domain walls to their equilibrium configuration at short length scales yields the apparent roughness exponent of $\zeta \approx 0.67$. On the other hand, the dynamic exponent μ was found to be ≈ 0.25 from independent measurements of domain wall creep under point application of electric field. An analysis of these results is indicative of the effective dimensionality $d_{eff} = 1$ for the domain walls. This result is confirmed by the layer-by-layer polishing followed by the imaging of a single domain.

§ 3.7 Local Polarization Relaxation in PLZT Ceramics by PFM

In this paragraph the local relaxation behavior of the PLZT ceramic surface was studied using time-resolved piezoresponse spectroscopy.

Shown in figure 3.26 (a-c) are the results of the poling experiment on the surface with labyrinthine pattern. In classical ferroelectrics, tip-induced switching results in formation of localized domain with well-saturated polarization, i.e. switching proceeds through formation of well-defined area within which polarization switched from state $-P$ to P. The resulting domain can be metastable, and will relax through radial shrinking, albeit maintaining the same phase state in the core. In comparison, the polarization switching in relaxors shows a number of remarkable behaviors.

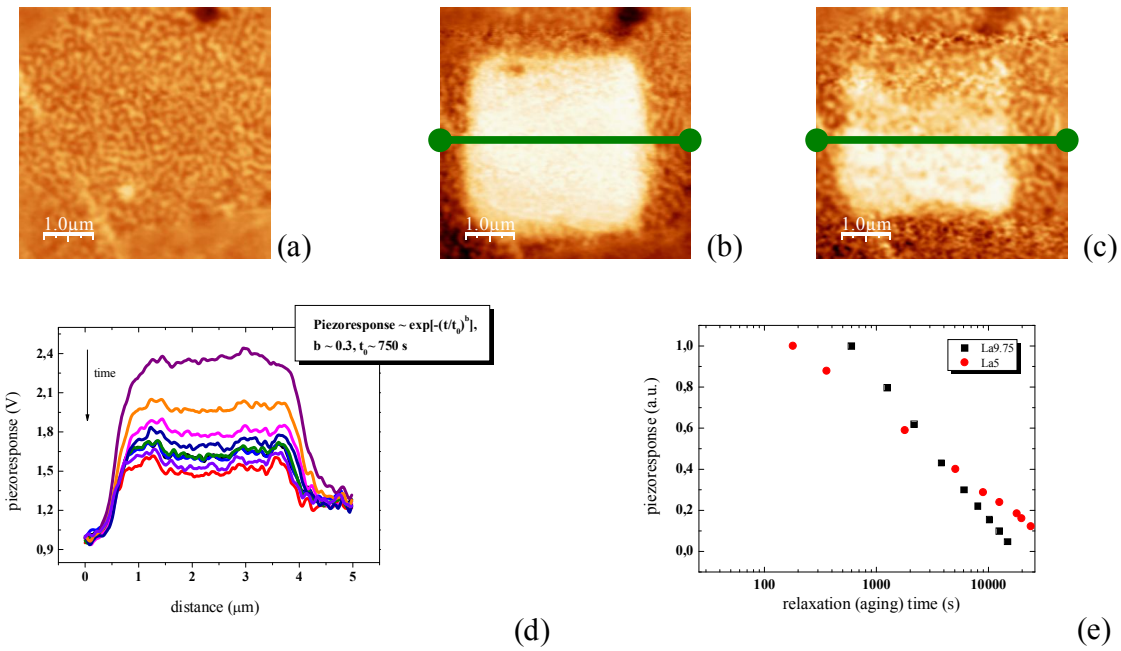

Figure 3.26 PFM images of square polarization patterns written with $V = +30$V in PLZT 9.75/65/35: (a) piezoresponse before poling, (b) initial piezoresponse, (c) piezoresponse after 5 hours, (d) comparison of the piezoresponse cross-sections (obtained along the line in part (b,c)) at different times ($\Delta t = 1024$ s).

Switching proceeds through formation of domain within the scanned region, however. The magnitude of switched contrast is of the order of magnitude higher then preexisting labyrinth structures.

Most strikingly, the labyrinthine domains are not affected by the bias pulse, and are clearly visible on top of the induced polarization pattern. The induced polarization relaxes with time. Unlike in classical ferroelectrics, the polarization decays uniformly within the switched area, rather then through lateral contraction. The relaxation law follows stretched exponential behavior. Notably, the labyrinthine domains emerge unaltered after relaxation. This result stresses the fact that it exist at the same time static (non-switchable) nanodomains in addition to regions with reorientable polarization. This is in agreement with the idea that below a peculiar temperature namely T^*, some static polarization regions take place within a matrix with dynamic polarization [39].

Figure 3.26(a-c) illustrates polarization writing in a regime where the square of about $3\times3\mu m^2$ was written with the same voltage (+30 V) on the surface of PLZT 9.75/65/35 ceramics. Figure 3.26(d) shows the cross-section profile of the piezoresponse signal for PLZT 9.75/65/35 after poling process and relaxation with time. PLZT ceramic shows clear relaxation of electromechanical response consistent with a rapid decay of the bias-induced polarization state (Figure 3.26(e)).

Instead, the stretched exponential dependence was used to fit the experimental data for both polarization directions. The fitting was done with the Kohlrausch–Williams–Watts formula commonly used to describe relaxation in the system with dipole–dipole interactions [40,41]. The response after poling (Figure 3.26(e)) can be well approximated with a stretched exponential dependence:

$$R(t) = R_0 - R_1 \cdot \exp\left(-\left(\frac{t}{t_0}\right)^{\beta}\right), \tag{3.13}$$

where t is the time, β and t_0 are fit parameters. t_0 has the meaning of the effective relaxation time (for $\beta = 1$ the equation reduces to simple *Debye* relaxation). For relaxor PLZT 9.75/65/35 it was

found the relaxation time ~750 sec, and β~0.3.

In comparison, the value of the relaxation time and β for the ferroelectric compound PLZT 5/65/35 (Figure 3.26(e)) were found ~5200 sec and ~0.5, respectively.

It is thus concluded, that for a ferroelectric phase of PLZT 5/65/35 ceramics process of relaxation of polarization proceeds more slowly than for relaxor compositions 9.75/65/35.

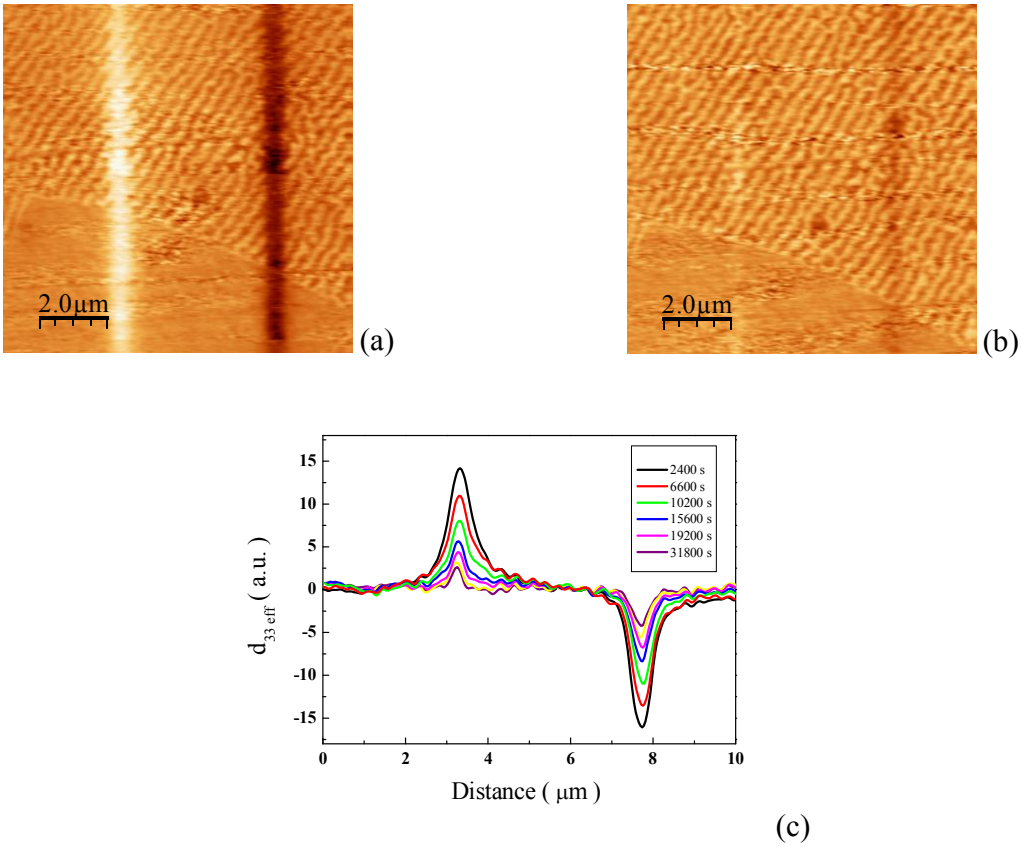

Figure 3.27 Polarization relaxation in PLZT ceramics poled with ±30V: (*a*) initial piezoresponse obtained with +30V (bright line) and −30V (dark line), (*b*) PFM image after about 8 hours, (*c*) piezoresponse cross-sections at different times after poling process.

The effect of polarization relaxation was quantified in the series of measurements shown in Figure 3.27. In this experiment, both negative (V = −30 V) and positive (V = +30 V) polarization patterns were written on the surface of PLZT 9.5/65/35 ceramic. The effective poling

time was about ~60 s that allowed writing of 15 equidistant polarization lines. Figure 3.27(c) represents the cross-section of the resulting piezoresponse signal from relaxation (ageing) time.

Figure 3.28 shows the time dependences of the half-width of the poling lines and maximum piezoresponse in both 'positive' and 'negative' polarization patterns.

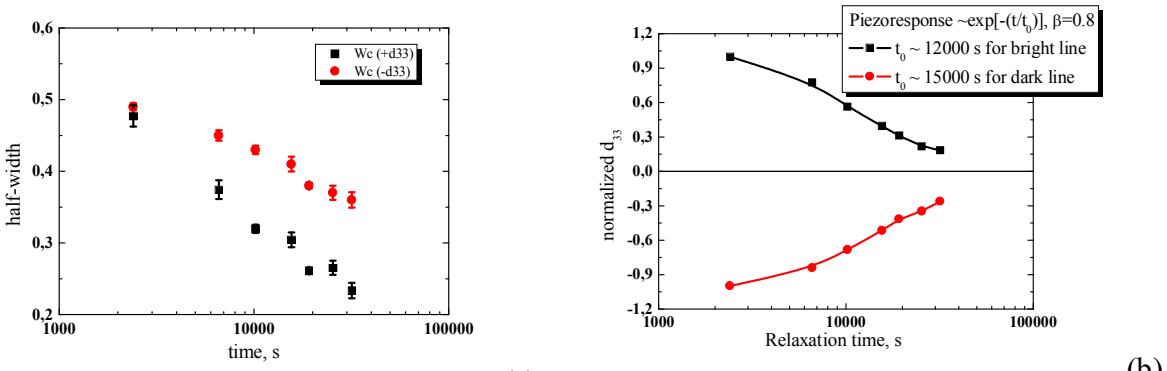

(a) (b)

Figure 3.28 (a) half-width of the poling lines (from Figure 3.27 (a,b)) and (*b*) normalized piezoresponse vs. time. The piezoresponse fits well with stretched exponential dependence. Fitting parameters β and t_0 are shown in the inset.

Figure 3.28(*b*) shows the comparison of the experimental and fitted time dependences of the piezoresponse for both polarization directions.

The dependence of relaxation behavior on the amplitude piezoresponse and time was found to follow a universal logarithmic behavior with a nearly constant slope.

These observations draw a very unusual mesoscopic picture of ferroelectric relaxors in nominally ergodic state. Instead of random fractal polarization distribution, we see a presence of characteristic mesoscopic length scale and non-switchable domains, and switchable polarization that responds locally.

§ 3.8 Temperature Effect on Nanodomains PLZT Ceramics

In this section the domain structures, average correlation radius and piezoelectric loops of PLZT ceramics were also measured as a function of temperature.

Firstly, the temperature of the dielectric permittivity maximum T_m at a frequency 1 kHz for samples are obtained. The results are consistent with literature reports, so for PLZT 8/65/35 T_m≈390 K and for composition 9.5/65/35 T_m≈ 350 K. Investigated PLZT ceramics exhibits a classic relaxor behavior [42]. Three different phases can be distinguished during heating/cooling in wide temperature range: 1) paraelectric phase above Burns temperature ($T > T_B$) representing entirely non-polar matrix, 2) ferroelectric phase below "freezing temperature" ($T < T_f$) representing entirely polar matrix with macro- or nanoscale domain structure, and 3) relaxor phase ($T_f < T < T_B$) representing heterophase state, which is the mixture of nanoscale polar and non-polar regions. Just below T_B the isolated polar nano-regions are immersed in non-polar matrix. With temperature decreasing the total volume of the polar regions increases. As a result, at the temperature range close to T_f the heterophase represents the non-polar regions embedded in multi-domain ferroelectric matrix.

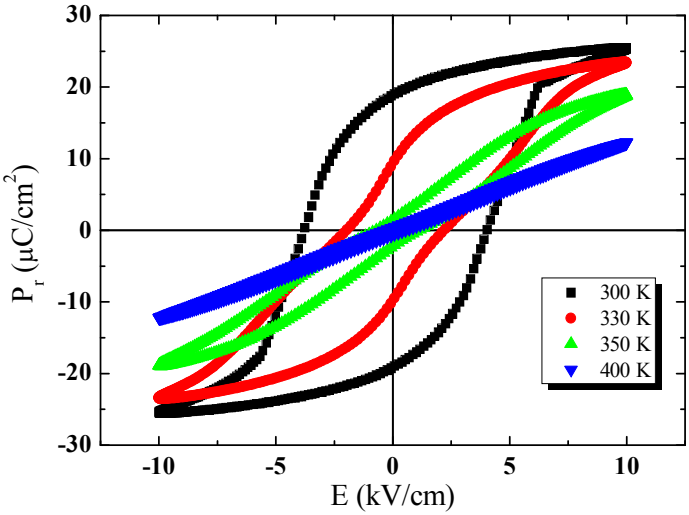

Figure 3.29 The *P–E* hysteresis loops of the PLZT 8/65/35 sample at various temperatures.

The evolution of the macroscopic hysteresis loops of PLZT 8/65/35 ceramics with temperature is shown in Figure 3.29. With the temperature increase, there is a decrease in the area

of the loop, which is a normal characteristic of ferroelectric materials. It can be seen from Figure 3.29 that a change in the temperature leads to a qualitative change in the loop shape.

Figure 3.30 depicts the respective remnant polarization *(P_r)* as a function of *T*. The low-temperature part of P_r was found to follow well the relation [43]:

$$P_r = const \cdot (T_{\max} - T)^{1/2} \tag{3.14}$$

Extrapolation of the remanent polarization with Equation (3.14) gave a zero -P_r value at T_m = 339 K, i.e. essentially it is much less than the temperature of the dielectric permittivity peak on 1 kHz. At the same time, P_r does not disappear at T_m but demonstrates a slow decay above this temperature.

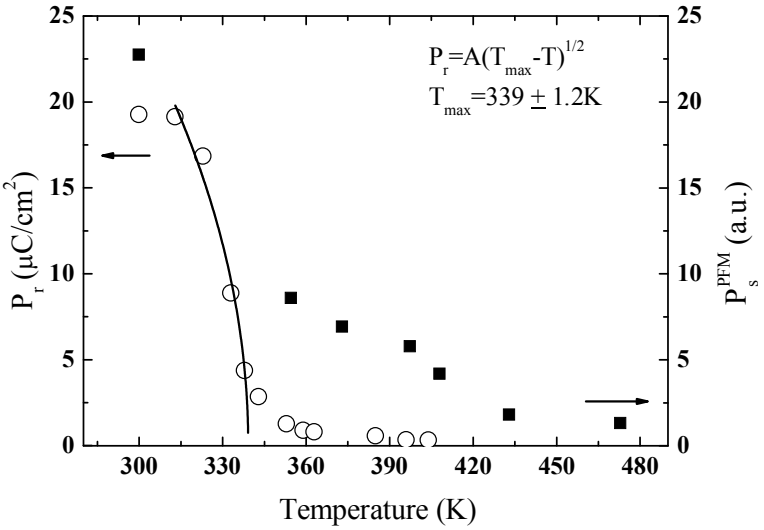

Figure 3.30 Remnant polarization P_r (open circles) and remnant polarization P^{PFM} (solid squares) from local piezoelectric loops as a function of temperature. P_r is fitted by equation (1) (solid curve).

Figure 3.31 shows piezoresponse images acquired at different temperatures for two PLZT ceramics with different La concentrations. At room temperature the labyrinth-type structure with various domain sizes can be observed (Figure 3.31(a, d)). In some locations, the large number of

small nanodomains (about a few tens of nanometers) [44] embedded in the microsized domains are observed. These can be attributed to the local polar nanosized regions induced by random fields (PNRs) similarly to the situation in PMN-*x*PT single crystals [45].

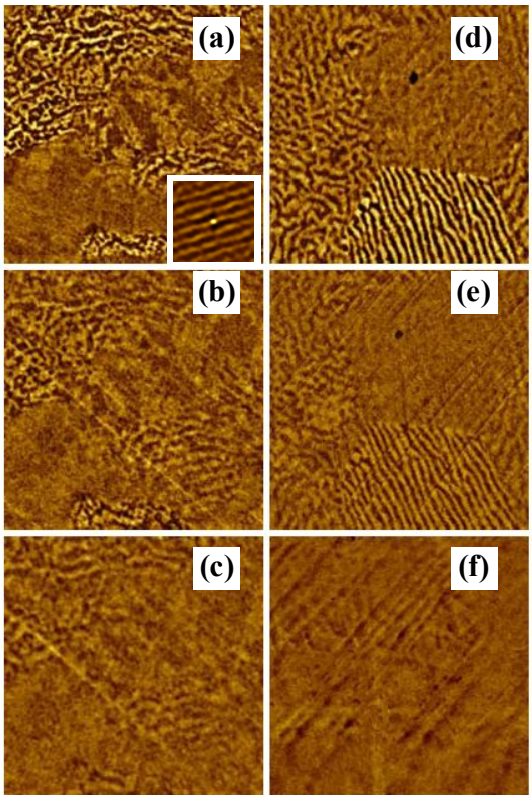

Figure 3.31 PFM images of the PLZT-8 (left column) (T_m =390 K) and PLZT-9.5 (right column) (T_m =350 K) at 315 K (a, d), 350 K(b,e) and 420 K(c,f). The inset to (a) is corresponding autocorrelation image.

In our geometry of applied electric field, the bright and dark areas correspond to domains with the polarization vector pointed correspondingly up and down relative to the Figure plane. The size of these piezoactive regions (referred to as nanodomains) varies in the range from tens to hundreds of nanometers.

To analyze the nanodomain structure we have applied an autocorrelation function technique, which has been successfully used before for topographic data processing. In the

autocorrelation images (inset to Figure 3.31(a) bright and dark contrasts corresponds to positive and negative values of the correlation between "up"- and "down"- oriented polarizations. For fitting of the experimental curves we used only the first central peak. The best fit gives the value of the average correlation length ξ (average domain size). At room temperature the mean correlation length is 230 and 160 nm for PLZT 8/65/35 and 9.5/65/35, respectively. The evolution of the piezoresponse images with temperature was found to correlate with the macroscopic observations.

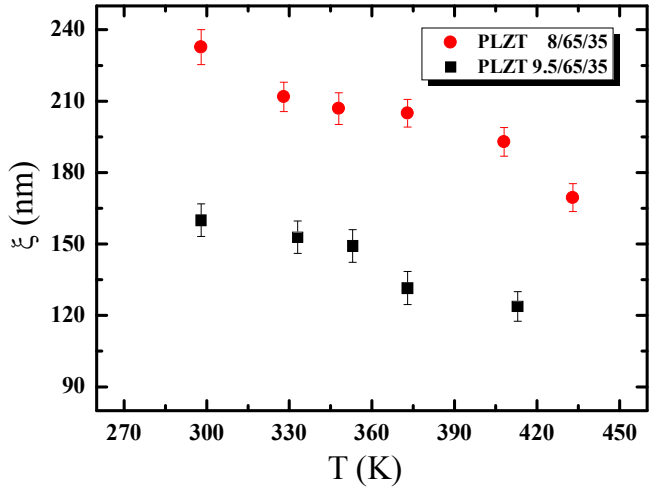

Figure 3.32 Temperature dependence of the average correlation length for PLZT 8/65/35 and 9.5/65/35 ceramics.

On approaching T_m, the piezoresponse signal becomes weaker in accordance with decreasing spontaneous polarization. The domain structure becomes less clear; some domains disappear (Figures 3.31(b)–(f)). Finally, above T_m, most of the grains are in the paraelectric state, manifesting the grey/uniform contrast. No nanodomains have been observed at high temperatures.

The average correlation length estimated from <C(r)> dependencies drops down from 240 to 170 nm and from 160 nm to 120 nm with increasing temperature for PLZT 8% and 9.5%, respectively (Figure 3.32).

An attempt was made to measure nanoscale hysteresis loops in PLZT (8% and 9.5% La) ceramic samples in order to investigate the ability of the phase transition. The hysteresis loops produced at different temperatures of the PLZT samples are shown in Figure 3.33. The local hysteresis measurements were performed by keeping the PFM tip fixed above the surface and applying a bias voltage from −30 to +30 V and the small AC voltage (2.5 V).

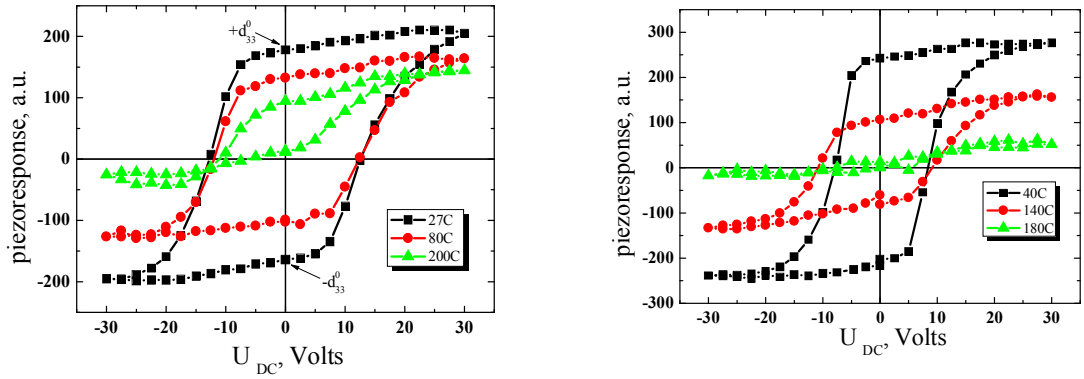

(a) (b)

Figure 3.33 Local piezoresponse hysteresis loops measured in a PLZT ceramics with 8% (a) and 9.5% La (b) at different temperatures.

Figure 3.33 presents typical piezoresponse hysteresis loops obtained in PLZT. The sequence of the measurements was as follows. The loop was prepoled by pulses of variable height and then piezoelectric response was measured at the same location in the absence of electric field. The loops vary with temperature demonstrating significant offset relative to the voltage axis. Detailed investigation of hysteresis loops by PFM show the switching occurs differently on the surface (PFM) and in the bulk (macroscopic polarization measurements). Macroscopically, the switching occurs via the nucleation and growth of a large number of reverse domains in the situation where the applied electric field is uniform. Therefore, the piezoresponse hysteresis reflects the switching averaged over the entire sample under the electrode. In PFM experimental conditions, the electric field is strongly localized and inhomogeneous, and therefore

the polarization switching starts with the nucleation of a single domain just under the tip on sample surface. Under applied voltage, this newly formed domain elongates to the bottom electrode, simultaneously expanding in lateral dimensions until it reaches an equilibrium size, which depends on the value of the maximum applied voltage. Saturation of the piezoresponse is achieved when the size of the induced domain is much larger than the penetration depth of the measuring ac voltage and the coercive voltage is simply a voltage at which the piezoresponse of the newly appeared domain cancels the piezoresponse of the oppositely oriented background signal. In this case, the coercive voltage is a complex function of the electric-field distribution, dielectric constant, domain wall energy and contact area [46]. Coercive voltage, maximal switchable polarization, offset positions all change with temperature and concentration. The hysteresis loops produced for PLZT ceramics are quite symmetric, but the values for the coercive field drop down with increasing temperature. The loop produced in PLZT 8/65/35 has a maximum polarization offset at 470 K. This can be due to capacitance change as described below. The $Z_{1\omega}$ amplitude of first harmonic of piezoresponse can be written as:

$$Z_{1\omega} = \frac{1}{k} \cdot \frac{dC}{dz} \cdot \left(U_{DC} + U_C\right) \cdot U_{AC} \cdot \sin \varphi t + d_{33}^{eff} \cdot U_{AC} \cdot \sin \varphi t \,, \tag{3.15}$$

where C is the electric capacitance between the tip–cantilever system and the Si wafer, k is the spring constant of the cantilever, U_C is the contact potential difference between the Si wafer and the tip– cantilever system, U_{DC} is the DC voltage applied by pulses, and U_{AC} *sin* φt is the ac voltage applied to the tip. $Z_{1\omega}$ is proportional to $1/k$, dC/dz and the absolute value of the difference between applied voltage and contact potential difference. From imaging under U_{DC} voltage it is possible to determine U_C. We find what U_C is about 1 V and does not depend on temperature. Thus the loop offset is determined only by the variation of dC/dz.

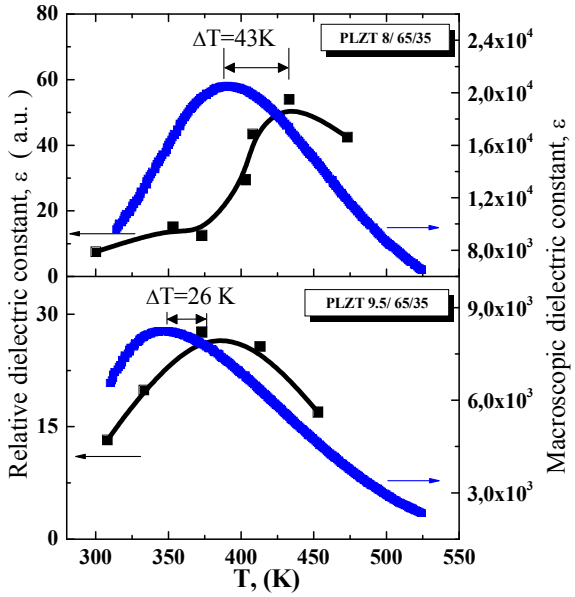

Figure 3.34 Relative dielectric constant (black line) and macroscopic dielectric constant (blue line) measured on f_{AC}=2 kHz.

So, loop offset allows to determine the variation of the surface dielectric constant ε (Figure 3.33), i.e. $\varepsilon^{surf} = \left(\left(-d_{33}^{0}\right) - \left(+d_{33}^{0}\right)\right)/2$, where $\pm d_{33}^{0}$ is remanent value of d_{33}^{eff} by V_{DC}=0 V (see arrows in Figure 3.33(a)). Macroscopic dielectric measurements showed a broad ferroelectric-to-paraelectric phase transition with a maximum permittivity of 20000 at 390 K (La 8% mol) and (blue lines on Figure 3.34) while the extracted permittivity gave a higher maximum of the dielectric constant ; in this case at about 433K. This results would tell us that at the nanoscale the phase transition occurs at higher tempearure. However, several explanations might be invoked. First, the process we used to extract the dielectric constant is not completely rigorous as the dielectric constant in relaxor-like system is frequency dependent and thus both measurements, macroscopic and nanoscopic, are not made at the same frequency. Secondly, it is also well-known [47] that the surface structure of relaxors is different compared to the bulk one; indeed a larger ferroelectric distortion on the surface was evidenced by X-ray synchrotron.

However, based on the hysteresis loops one can extract a local polarization P_S which is

plotted in figure 3.30. Compared to macroscopic P_r it is clear that a residual polarization persists up to T_m~339K and there is still a significant hysteresis loop until the highest investigated temperature i.e. 470 K. This persistence of P_S at high temperature can not be explained just by different surface phase transition as discussed previously. Indeed, knowing that at T^* there are some static polar domains which nucleate it is believable that these regions participate to the piezoelectric response measured by PFM. Of course, the difference of ferroelectric-to-paraelectric phase transition on the surface may also act on the local polarization, but we believe that based on our data, we also measured the response coming from the static polar nanodomains that occur at T^* which value is close to 500K for lead-based relaxors [39].

Temperature evolution of the domain structure detected by piezoresponse force microscopy also testifies the intermediate (between ferroelectric and relaxor) nature of PLZT ceramics with 8% and 9.5% La concentrations.

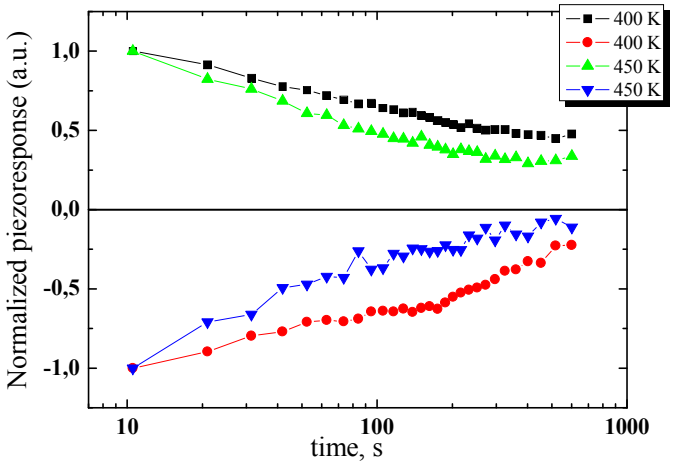

Figure 3.35 Relaxation of piezoreponse with time at different temperatures.

In addition, we investigated dependence of the piezoresponse relaxation at different temperatures (Figure 3.35). It was established that with the increase in temperature the relaxation process of relaxation becomes appreciably faster than at low temperature. We found that the

values of the relaxation time t and parameter β are ~ 52 sec and ~0.51 (at 400 K) and ~33 sec and 0.55 at 450 K, respectively. Faster relaxation at high temperature referes to higher mobility of domain walls at higher temperature.

§ 3.9 Fractal Analysis of PLZT Ceramics

It is well known that fractal analysis of any complicated geometrical object allows one to obtain additional information about the self-similarity of the structure in terms of fractal dimension.

Note that while fractal domain structure are expected for these systems, the labyrinthine pattern with domain period 100 nm is consistent only with the transversally-isotropic symmetry of material (e.g. often observed in ultrathin magnetic films). In the systems closer to ferroelectric limit, these labyrinthine structures often coexist with classical ferroelectric domains.

We believe that the observed contrast is due to the agglomerates of polar clusters stabilized by surface defects. Since random fields and mechanical stresses play important roles in the formation of these agglomerates, they are expected to obey the fractal laws even in the presence of the stabilizing effect of the surface.

We applied the dimensional analysis or so-called "island statistics" to the obtained images [48]. In this calculation, we determined the dependence of the perimeter P of the ensemble of the individual domains as a function of their area S. The results could be fitted by the power law:

$$P(S) = P_0 S^{D/2} \tag{3.16}$$

It is interesting that the fractal (self-affine) domains shown in Figure 3.35 in fact demonstrate two characteristic length scales with two different fractal dimensions as is clear from Figure 3.7. This points to the hierarchical structure of nanodomains and interaction between ''true'' (dynamic) PNRs at the mesoscopic scale.

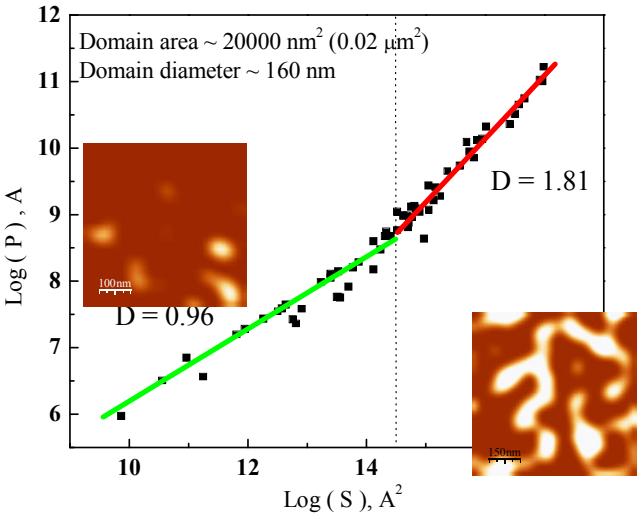

Figure 3.36 Variation of fractal dimension with length scale in PLZT 9.5/65/35 ceramics. Hausdorff fractal dimension is about 0.96 and 1.81 below and above inflection point, respectively.

The best fit for second part of the fractal dimension *D* gives the value of about 1.81 (Figure 3.36). If the formation of as-grown domain structure is a random spatially non-correlated process one would expect *D*=1.81 (e.g., as observed in the case of random Brownian surfaces [49]). Slight increase of the fractal dimension as compared to the case of Brownian interfaces may be explained by the short-range order and finite correlation length of the agglomerated PNRs.

These regions were attributed to the "mesoscopic" PNRs, which grow in the vicinity of the phase transition and become immobilized on the time scale of the PFM experiment due to their large size.

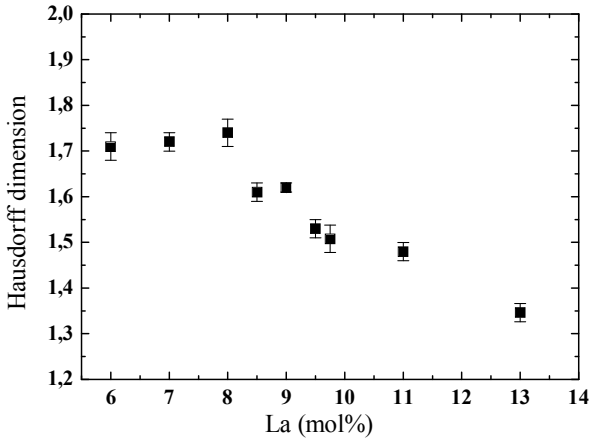

Figure 3.37 Average Hausdorff dimension as a function of La content, for PLZT x/65/35 ceramics with x = 6 − 13 La mol %.

Figure 3.37 shows the Hausdorff dimension for different La concentrations in PLZT ceramics. One can see that the fractal dimension of domain walls decreases with increasing La content.

It is interesting to compare the experimental data with the theoretical predictions. Theoretically determined fractal dimensions for the 2D RFIM have been reported to be $D_H = 1.18$ using Monte Carlo simulations [50] and $D_H = 1.96$ from the exact solution for the ground state [51]. The large difference between these two theoretical values is partly due to the large deviation of the Monte Carlo simulations from thermal equilibrium. In addition, their small D_H value refers to rather weak RFs and finite temperatures [50], parameters both of which favor weak domain wall roughness, since local pinning can easily be overcome by thermal fluctuations. The experimental values obtained from the analysis of PFM images: D(La 6%) = 1.72, D (La 8%) = 1.65, D(La 9.75 %) = 1.5 and D(La 13 %) = 1.35 lie between these two theoretical predictions.

Instead of random fractal polarization distribution, we see a presence of characteristic mesoscopic length scale and non-switchable domains, and switchable polarization that responds locally.

§ 3.10 Summary

In summary, this chapter is devoted to the characterization of ferroelectric properties of PLZT ceramics at nanoscale in comparison to the macroscopic properties. The PLZT system exhibits a highly uniform microstructure consisting of randomly oriented equiaxial grains (crystallites). The microstructure of the PLZT 6÷11/65/35 system, generally has grain size that may vary from 2 to 10 μm.

The PLZT 6÷11/65/35 ceramics was also confirmed by dielectric and ferroelectric measurements. Firstly, addition of lanthanum shifts T_m lo lower temperatures (T_m = 390, 335 and 300 K for 8, 9.75 and 13/65/35, respectively, for measurement frequency of 1 kHz), and secondly, dielectric constant decreases with increasing lanthanum content (21000, 5500 and 1700 for 8, 9.75 and 13/65/35, respectively, for measurement frequency of 1 kHz). Dilutions of the permittivity and a reduction in T_m as a function of increasing La concentration have both been previously observed.

The first reliable measurements of the domain structure of high-quality PLZT 5÷13/65/35 ceramics were reported by piezoresponse force microscopy. As reported many times, the key element in lead-based relaxors are Pb^{2+}-ions as they bring huge local polarization because of their lone pair and the hybridization with the oxygen neighbors. Therefore increasing lanthanum substitution on A-sites weakens the coupling between the ferroelectrically active ions, destroying *long-range-ordered* inducing a ferroelectric/relaxor transformation. This effect is observed in PFM as a gradual decrease in domain width and, finally, the appearance of “labyrinth-type” domain structures.

The PLZT ceramics with high concentration of La (>9 mol. %) preserve the domain contrast at the nanoscale, even if the macroscopic properties do not exhibit any ferroelectricity. Random network of maze nanopolar patterns is a direct consequence of La-induced disorder and

we have observed them as a function of temperature in order to observe the freezing of polar nanoclusters. It is proved that the PFM technique is well suited for the inspection of polar mesoscopic structures on the surface of relaxor ferroelectrics. Fractal and correlation analysis of the observed images is presented. The fractal dimension close to 1.8 is consistent with the random distribution of charge defects in this material.

Also, we have observed a distinct grain size effect in PLZT 9.75/65/35 relaxor ceramics demonstrating that the degree of disorder in these materials varies as a function of the local position inside the grain. The surface polarization correlation length is directly extracted from these measurements and is shown to depend on the grain size. The variation of the correlation length is tentatively attributed either to the mechanical stress arising upon cooling the ceramics from the sintering temperature or to the La gradient across the grain.

References

[1] Haertling G. H. "Ferroelectric Ceramics: History and Technology" *J. Am. Ceram. Soc.,* **82**, 797 (1999).

[2] Tan Q., Viehland D. "ac-field-dependent structure-property relationships in La-modified lead zirconate titanate: Induced relaxor behavior and domain breakdown in soft ferroelectrics" *Phys. Rev. B* **53**, 14103 (1996).

[3] Viehland D., Li J. F., Jang S. J., Cross L. E., and Wuttig M., "Glassy polarization behavior of relaxor ferroelectrics" *Phys. Rev. B* **46**, 8013 (1992).

[4] Viehland D., Ph.D. thesis, Pennsylvania State University, (1991).

[5] Akbas M. A., Reaney I. M., Lee W. E. "Domain structure-property relations in lead lanthanum zirconate titanate ceramics" *J. Mater. Res.*, **11**, 2293 (1996).

[6] Viehland D., Li J.F., Jang S.J., Cross L.E., Wuttig M., "Dipolar-glass model for lead magnesium niobate" *Phys. Rev. B* **43**, 8316 (1991).

[7] Marssi M. El, Farhi R., Dellis J.-L., Glinchuk M. D., Seguin L., Viehland D. "Ferroelectric and glassy states in La-modified lead zirconate titanate ceramics: A general picture" *J Appl Phys*, **83**, 5371 (1998).

[8] Munoz R. C., Vidal G., Mulsow M., Lisoni J. G., Arenas C., and Concha A., "Surface roughness and surface-induced resistivity of gold films on mica: Application of quantitative scanning tunneling microscopy" *Phys. Rev. B* **62**, 4686 (2000).

[9] Vakhrushev S. B., Naberezhnov A. A., Dkhil B., Kiat J.-M., Shvartsman V., Kholkin A., Dorner B., and Ivanov A., Fundamental Physics of Ferroelectrics 2003, Williamsburg, VA, USA, 2003, edited by P. K. Davies and D. J. Singh, *AIP Conf. Proc.* **677**,74 (AIP, Melville, NY, 2003).

[10] Samara G. A., "The relaxational properties of compositionally disordered ABO_3 perovskites" *J. Phys.: Condens. Matter* **15**, R367 (2003).

[11] Samara G. A., "Pressure as a probe of the glassy properties of compositionally disordered soft mode ferroelectrics: $(Pb_{0.82}La_{0.12})(Zr_{0.40}Ti_{0.60})O_3$ (PLZT 12/40/60)" *J. Appl. Phys.* **84**, 2538 (1998).

[12] Chaabane B., Kreisel J., Dkhil B., Bouvier P. and Mezouar M. " Pressure-Induced Suppression of the Diffuse Scattering in the Model Relaxor Ferroelectric $PbMg_{1/3}Nb_{2/3}O_3$ ", *Phys. Rev. Lett.* **90**, 257601 (2003).

[13] Okazaki K. and Nagata K., "Effects of grain size and porosity on electrical and optical properties of PLZT ceramics" *J. Am. Ceram. Soc.* **56**, 82 (1973).

[14] Smolensky G. A., Bokov V. A., Isupov V. A., Krainik N. N., Pasynkov R. E., Sokolov A. I., Yushin N. K., *Physics of ferroelectric phenomena*, Leningrad, Nauka (1985) (in Russian).

[15] Lin W. K., Chang Y. H. "Properties and microstructures of PLZT ceramics hot-pressed from commercial powders" *Ferroelectrics* **99**, 133 (1989).

[16] Blinc R., Laguta V, Zalar B "Field cooled and zero field cooled ^{207}Pb NMR and the local structure of relaxor $PbMg_{1/3}Nb_{2/3}O_3$" Phys.Rev.Lett 91, 247601 (2003).

[17] Viehland D. " Origin of F spots and stress sensitivity in lanthanum lead zirconate titanate" *J.Appl.Phys.* **74** 7454 (1993).

[18] Dawber M. and Scott J. "A model for fatigue in ferroelectric perovskite thin films" *Appl. Phys. Lett.* **76**, 1060, (2000).

[19] Gruverman A., Auciello O., and Tokumoto H., "Imaging and control of domain structures in ferroelectric thin films via scanning force microscopy" *Annu. Rev. Mater. Sci.* **28**, 101 (1998)

[20] Płońska M., Czekaj D., Surowiak Z., "Application of the sol-gel method to the synthesis of ferroelectric nanopowders $(Pb_{1-x}La_x)(Zr_{0.65}Ti_{0.35})_{1-0.25x}O_3$, $0.06 \leq x \leq 0.1$ " *Materials Science*, *Vol.* **21**, No. 4, 431 (2003).

[21] Hubert A.and Schäfer R., *Magnetic domains: the analysis of magnetic microstructures* (Berlin: Springer) (1998).

[22] Spaldin N.A., *Magnetic materials: fundamentals and device applications* (Cambridge: University Press) 2003.

[23] Scott J.F., *Ferroelectric Memories*, Berlin. Springer (2000).

[24] Ioffe L.B. and Vinokur V.M. "Dynamics of interfaces and dislocations in disordered media" *J. Phys.* C **20**, 6149 (1987).

[25] Nattermann T., Shapir Y and Vilfan I "Interface pinning and dynamics in random systems" *Phys. Rev. B* **42**, 8577 (1990).

[26] Chauve P., Giamarchi T and Le Doussal P, "Creep and depinning in disordered media" *Phys. Rev. B*, **62**, 6241 (2000).

[27] Fisher D.S., "Interface fluctuations in disordered systems: 5-ε expansion and failure of dimensional reduction" *Phys. Rev. Lett*. **56**, 1964 (1986)

[28] Lemerle S., Ferré J, Chappert C, Mathet V, Giamarchi T and Le Doussal P "Domain wall creep in an ising ultrathin magnetic film" *Phys. Rev. Lett*. **80**, 849 (1998).

[29] Tybell T., Paruch P, Giamarchi T and Triscone J-M "Domain wall creep in epitaxial ferroelectric $Pb(Zr_{0.2}Ti_{0.8})O_3$ thin films" *Phys. Rev. Lett.* **89**, 097601 (2002).

[30] Paruch P., Giamarchi T. and Triscone J.-M. "Domain wall roughness in epitaxial ferroelectric $PbZr_{0.2}Ti_{0.8}O_3$ thin films", *Phys. Rev. Lett.* **94**, 197601 (2005).

[31] Paruch P., Giamarchi T, Tybell T and Triscone J-M "Nanoscale studies of domain wall motion in epitaxial ferroelectric thin films" *J. Appl. Phys*. **100**, 051608 (2006).

[32] Pertsev N.A., Petraru A, Kohlstedt H, Waser R, Bdikin I K, Kiselev D and Kholkin A L "Dynamics of ferroelectric nanodomains in $BaTiO_3$ epitaxial thin films via piezoresponse force microscopy",*Nanotechnology* **19**, 375703 (2008).

[33] Dambekalne M., Antonova M, Livinsh M, Garbarz-Glos B, Smiga W and Sternberg A " PLZT—Synthesis, sintering and ceramics microstructure" *J.Europ Ceram Soc.* **26**, 2963 (2006).

[34] Molotskii M."Generation of ferroelectric domains in atomic force microscope" *J. Appl. Phys.* **93**, 6234 (2003).

[35] Rosenman G., Urenski P., Agronin A., Rosenwaks Y., Molotskii M., " Submicron ferroelectric domain structures tailored by high-voltage scanning probe microscopy" *Appl. Phys. Lett.* **82**, 103 (2003).

[36] Mele J., „Screening of a point charge by an anisotropic medium: Anamorphoses in the method of images" *Am. J. Phys.* **69**, 557 (2001).

[37] Miller R.C. and Weinreich G. "Mechanism for the sidewise motion of 180° domain walls in barium titanate" *Phys. Rev.* **117**, 1460 (1960).

[38] Abplanalp M., Barosova D, Bridenbaugh P, Erhart J, Fousek J, Günter P, Nosek J and Sulc M "Scanning force microscopy of domain structures in $Pb(Zn_{1/3}Nb_{2/3})O_3$-8% PbTiO3 and $Pb(Mg_{1/3}Nb_{2/3})O_3$-29% $PbTiO_3$" *J. Appl. Phys.* **91**, 3797 (2002).

[39] Dkhil B., Gemeiner P., Al-Barakaty A., Bellaiche L., Dul'kin E., Mojaev E., and Roth M., "Intermediate temperature scale T* in lead-based relaxor systems" *Phys. Rev. B* **80**, 064103 (2009).

[40] Jonscher A.K., Universal Relaxation Law (London: Chelsea Dielectric Press, 1996).

[41] Shvartsman V.V., Kholkin A L, Tyunina M and J. Levoska "Relaxation of induced polar state in relaxor $PbMg_{1/3}Nb_{2/3}O_3$ thin films studied by piezoresponse force microscopy" *Appl. Phys. Lett.* **86**, 222907 (2005).

[42] Marssi M. El., Farhi R., Dellis J. L., Glinchuk M. D., Seguin L., and Viehland D., "Ferroelectric and glassy states in La-modified lead zirconate titanate ceramics: A general picture" *J. Appl. Phys*. **83**, 5371 (1998).

[43] Kittel C., *Introduction to Solid State Physics* New York: Wiley, (1996).

[44] Yin Q. R., Zeng H. R., Yu H. F., Li G. R. "Near-field acoustic and piezoresponse microscopy of domain structures in ferroelectric material " *Journal of Materials Science* **41**, 259 (2006).

[45] Shvartsman V. V.,. Kholkin A. L, "Evolution of nanodomains in $0.9PbMg_{1/3}Nb_{2/3}O_3$-$0.1PbTiO_3$ single crystals" *J. Appl. Phys*. **101**, 064108 (2007).

[46] Kalinin S. V.,, Morozovska A.N., Long Qing Chen L.Q. and Rodriguez B. J., "Local polarization dynamics in ferroelectric materials" *Rep. Prog. Phys.* **73**, 056502 (2010).

[47] Guangyong Xu, Z. Zhong, Y. Bing, Z.-G. Ye, C. Stock, and G. Shirane, "Anomalous phase in the relaxor ferroelectric $Pb(Zn_{1/3}Nb_{2/3})O_3$" *Phys. Rev. B* **70**, 064107 (2004).

[48] Russ J., *Fractal Surfaces*, Plenum Press, NY (1994).

[49] Feder J., *Fractals,* Plenum Press, NY (1988).

[50] Cambier J. L. and Nauenberg M., "Formation of domains in the random-field Ising model" *Phys. Rev. B* **34**, 7998 (1986).

[51] Esser J., Nowak U., and Usadel K. D., "Exact ground-state properties of disordered Ising systems" *Phys. Rev. B* **55**, 5866 (1997).

Chapter 4

Nanopolar Domain Structure of Relaxor Single Crystals

In this chapter we used PFM tools to investigate the complex polar domain configuration of relaxor single crystals. The crystals we consider in this chapter belong to the main and mostly studied systems namely $(1-x)Pb(Zn_{1/3}Nb_{2/3})O_3–xPbTiO_3$ *(PZN-PT) and* $(1-x)Pb(Mg_{1/3}Nb_{2/3})O_3–xPbTiO_3$ *(PMN-PT). These solid solutions display the highest electromechanical properties and the main relaxor-like features. As most of the PFM measurements we did are performed at room temperature, we selected different samples in order to highlight some specific properties we discovered at the nanoscale.*

Indeed, we shall first analyze the case of PZN-4.5%PT which is representative of most relaxor-like compounds exhibiting at room temperature a rhombohedral ferroelectric phase with T_m *characterizing the maximum of the dielectric constant occurring around 430K. The consequences on the nanofeatures going toward and through the so-called morphotropic phase boundary (MPB) by increasing the* $PbTiO_3$ *(PT) amount will be then investigated.*

We shall then turn on the prototype relaxor $Pb(Mg_{1/3}Nb_{2/3})O_3$ *(PMN) which in contrast to PZN-4.5%PT, displays only relaxor behavior as the average macroscopic structure remains cubic down to 5K. We will also study the effect of* $PbTiO_3$ *substitution by investigating the relaxor compound PMN-10%PT, which overcomes a ferroelectric phase transition only below room temperature (at Tc~280K) and richer PT concentration belonging to the MPB region.*

§ 4.1 Macroscopic Ferroelectric Properties of PZN-PT Single Crystals

Here, we introduce Ferroelectric/Piezoelectric Properties of PZN-PT Single Crystals knowing that these properties are similar to all relaxor-PT single crystals as PMN-PT.

Due to the remarkable piezoelectric and electromechanical properties in domain engineered $(1-x)Pb(Zn_{1/3}Nb_{2/3})O_3–xPbTiO_3$ (PZN-*x*PT) single crystals, they have been studied extensively in recent years for potential applications in many electromechanical devices, such as transducers and actuators [1,2]. PZN-PT system is a complete solid solution of the relaxor $Pb(Zn_{1/3}Nb_{2/3})O_3$ and ferroelectric PT and there is a morphotropic phase boundary (MPB) between tetragonal and rhombohedral phases near 8%PT component at room temperature. It

was found that [001] poled rhombohedral phase crystals close to the MPB composition have the outstanding piezoelectric and electromechanical properties [2].

The phases present in relaxor-ferroelectric PZN-*x*PT single crystals strongly depend on their composition and temperature [3]. High-resolution diffraction studies have revealed the intricate structure of morphotropic phase boundary compositions, which involves the rhombohedral, tetragonal, orthorhombic/monoclinic phases [4]. Figure 4.1 displays the phase diagram of PZN-*x*PT in a broad concentration range comprising the MPB [5] Due to the very high piezoelectric properties, PZN-PT has been studied mainly in the composition range close to the morphotropic phase boundary.

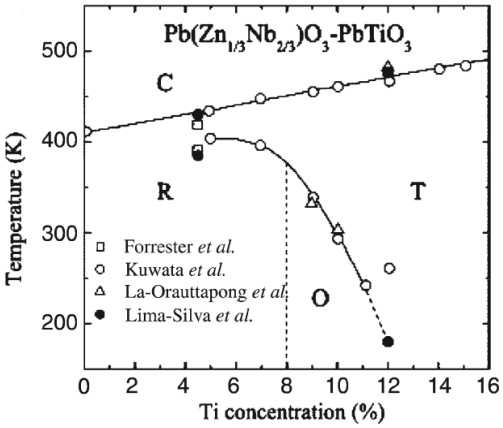

Figure 4.1 Phase diagram of PZN-PT [5].

When the composition is close to the morphotropic phase boundary, relaxor ferroelectric crystals exhibit a maximum in various electromechanical properties (such as piezoelectric coefficients, coupling factors and high-field strain) (Figure 4.2). Investigations have shown that the MPB of the PZN-*x*PT system allows for the coexistence of several phases making easier the rotation of the polarization with for instance the switching from rhombohedral into tetragonal phase under sufficiently high electric field. Several researchers [4,6] have observed the coexistence of rhombohedral and tetragonal domains in PZN-*x*PT crystals at room temperature. Actually there is not yet any consensus concerning the real structure of the relaxor-PT structure and the reason of the huge electromechanical responses is still debated. Indeed, the large piezoelectric coefficients observed in the vicinity of the so-called MPB are related to the 'polarisation rotation' between the adjacent rhombohedral and

tetragonal phases through one (or more) intermediate phases of low-symmetry, i.e. a monoclinic (orthorhombic or triclinic) phase [7]. It is believed that the monoclinic phase is not limited to the MPB region but rather exists at a nanoscale in a more expanded composition region and may even originally exists within the relaxor composition itself. The transformation pathway through the monoclinic phase and associated features such as the tweed-like domain patterns observed in MPB systems has lead some authors to consider that the monoclinic phase is an adaptive phase [8]. The adaptive phase is issued from martensitic-like phase transitions and is based on stress-accommodating twinned domains. According to this, the 'monoclinic phase' observed on the average scale would not truly exist on the local scale but would be rather constructed by tetragonal and/or rhombohedral twinned nanodomains [9]. Therefore, the huge electromechanical response can be explained by the energy release because of the large number of domain walls of the nanodomains instead of an easy rotation of the polarization. Note that both monoclinic phase (then rotation of the polarization) and nanodomains (then several domain walls) were also observed at the same time [10] indicating that the origin of the giant piezoelectricity may finally come from these both contributions.

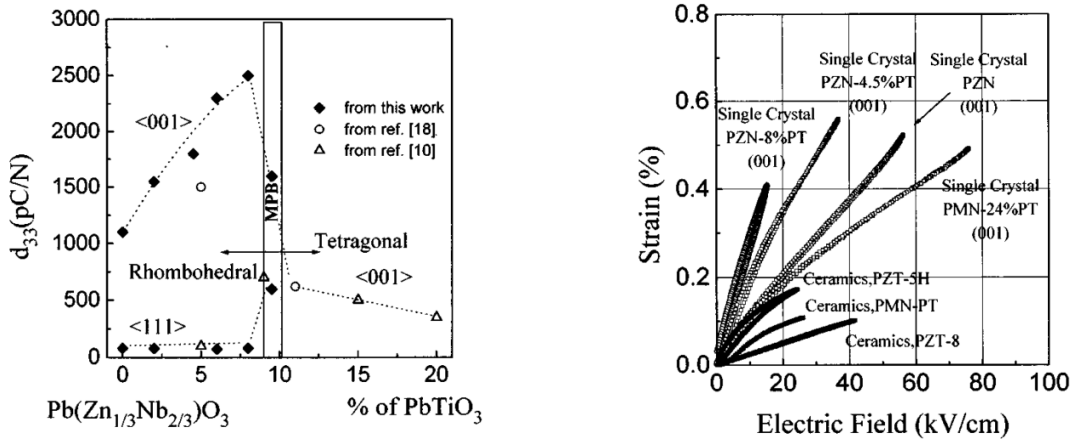

(a) (b)

Figure 4.2 (a) – Longitudinal piezocoefficient d_{33} as a function of PT concentration x and orientation in PZN-xPT crystals, (b) – Comparison of strain vs *E*-field behavior in (001) oriented PZN-PT and PMN-PT crystals and in several piezoelectric ceramics [11].

The domain structure and electromechanical properties of ferroelectric single crystals of solid solutions PZN-xPT specifically have been intensively investigated during the last several years. As it is already noted, the attracting feature of this system is the extremely high piezoelectric effect (piezoelectric coefficient up to 2500 pm/V) and electrically induced strain (up to 1.7%) measured for (001)-cut faces for the compositions close to the phase boundary with tetragonal phase (x~0.08-0.1) [11] (Figure 4.2). It was also observed that the corresponding coupling coefficients are very high (~95%) making these crystals a promising material for piezoelectric transducers for medical imaging, active vibration damping, and underwater sensing [1,12]. It was shown [13] that unusually high strain in these crystals is due to the phase transition from rhombohedral to tetragonal phase when the electric field is applied along the <001> pseudocubic direction. For compositions close to the morphotropic phase boundary a new monoclinic phase (intermediate between rhombohedral and tetragonal phases) has been observed by both x-ray diffraction and direct domain study [14,15]. This phase provides the path for the domain rotation between rhombohedral and tetragonal phases and was suggested as a reason for the extraordinary electromechanical response of PZN-PT [16]. Several domain studies have been performed on PZN-PT crystals that revealed the existence of ferroelastic twins that survive even in poled specimens [17,18,19]. In another publication, a peculiar dendritic domain pattern formed under pulse poling conditions has been documented making domain structure very complicated [20]. The disadvantage of these investigations is that they have been performed using mainly optical techniques with a resolution limited to the wavelength of the light. However, submicron-size domains can exist in such materials due to their relaxor nature and can contribute to their final electromechanical performance. Another complication is that the surface state of these crystals seems to be ferroelectric but the bulk is in the so-called X phase that exhibit only weak tetragonal distortion for unpoled material [21].

In contrast to pure ferroelectric crystals, such as PT, PZN-PT with low PT concentration is a typical relaxor, which exhibits a diffuse phase transition and a frequency dependent dielectric response.

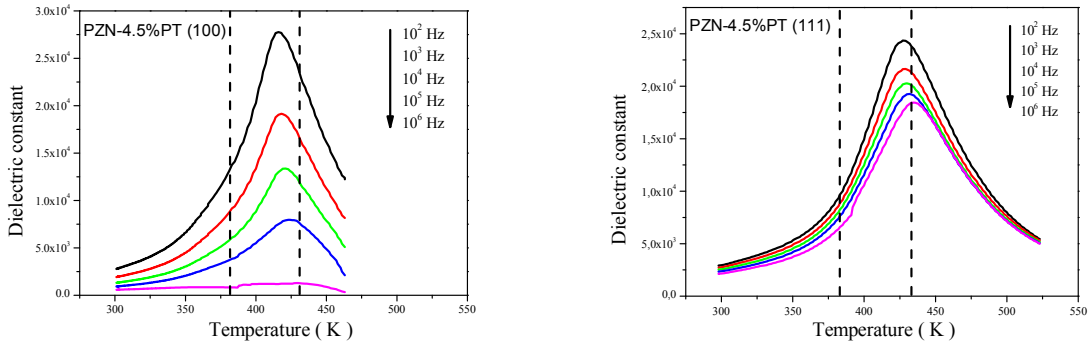

Figure 4.3. Temperature dependence of the dielectric constant for (100) and (111) orientations of PZN-4.5 %PT single crystals.

The dielectric measurements for (100) and (111) orientations were done in the investigated PZN-4.5%PT crystals to confirm their relaxor nature (Figure 4.3.). The measurements were performed on heating from room temperature up to 250 ºC in unpoled specimens at different frequencies in the range 10^2-10^6 Hz.

For PZN–4.5PT, the phase transition to cubic phase appears as a diffused peak with frequency dispersion characteristic of the relaxor-like phase transition. According to Forrester *et al*. [22], PZN–4.5%PT exhibits two phase transitions above room temperature: a rhombohedral (or X-phase)-to-tetragonal (at ~380 K) and a tetragonal-to-cubic (~430 K). The temperatures of these phase transitions are indicated by dashed lines in Figure 4.3, where the the high-temperature phase transition is hardly seen due to its diffuse character. The low-temperature phase transition could be observed as a shoulder on the dielectric curve.

§ 4.2 Temperature Dependence of the Complex Domain Structures in PZN-4.5%PT Single Crystals

In this section, we report on the evolution of domains observed in as-grown rhombohedral PZN-4.5%PT single crystals of both orientations. It is worth recalling that in such compound exhibiting both ferroelectric (T_{c2}~380K) and relaxor behavior (T_m~T_{c1}~430K) one would expect at room temperature a rather complex polar domains configuration as both

"classical" ferroelectric domains and "relaxor"-like nanodomains should coexist. The domain structure of PZN-4.5%PT at room temperature is representative of mostly relaxor-based systems and may be considered as a reference system.

These studies are motivated by the inability to follow the evolution of nanodomains with temperature by using conventional methods. Only few studies have been reported (e.g. [23]). Especially interesting are the surface contributions to the ferroelectric phenomena in relaxors in view of recently observed surface phases and rich physics of systems with low-dimensionality.

Ferroelectric domain structures and their evolution in the as-grown samples of PZN-4.5%PT were studied by means of temperature-dependent piezoresponse force microscopy and main results are reproduced in Figure 4.4.

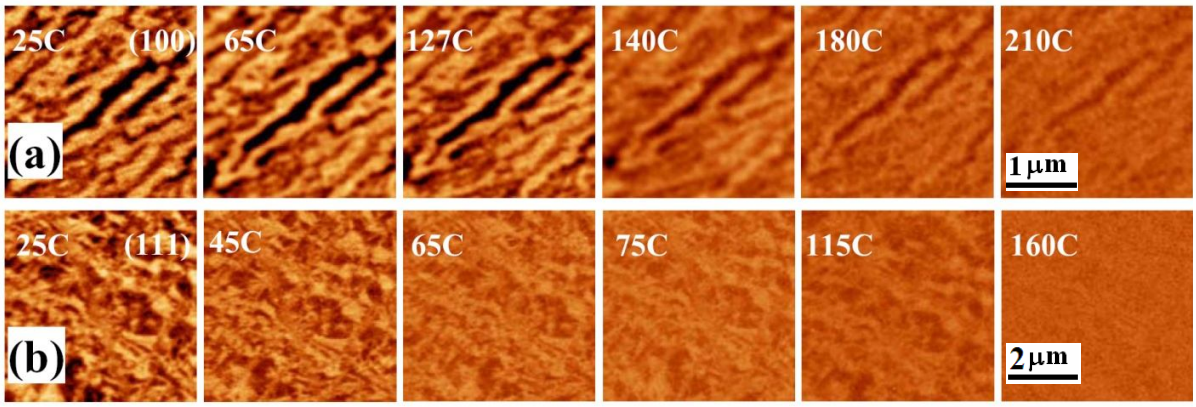

Figure 4.4 Evolution of surface domain structures for PZN-4.5PT single crystals for (a) (100) and (b) (111) crystal cuts. Note the difference in the initial domain patterns for both orientations and persistence of domains at much higher temperature for (100) orientation.

First of all no macroscopic regular "classical"-like domains related to the ferroelectric character is observed. Instead of that, this Figure 4.4 shows irregular labyrinth-type domains with preferred direction (stripes along one of the equivalent [111] directions) and more irregular structure for (100) cut. Nanodomains were observed for both orientations in contrast to early results probably because of different growth procedures.

As can be seen, the contrast between the oppositely oriented domains gradually decreases on heating and the boundaries of the domains become rougher, while there is a little change in the overall shape and number of domains. Surprisingly, some nanodomains can still be seen when the temperature is above the transition temperature, T_{c1}~T_m~160°C. Indeed and surprisingly, while no more contrast is detected at 160°C for (111) cut, there are still some residual domains for (100) orientation up to 210 °C. Therefore, the nanodomains persist at much higher temperature for (100) orientation (about 50 ºC) and their disappearance is not related to any bulk transition.

The nanoscale piezoelectric hysteresis loops obtained at different temperatures are shown in Figure 4.5., where hysteresis curves are plotted for two crystal orientations in the temperature range 25-210 ºC. These loops are representative for both crystal cuts and did not depend on the locations on the crystal surface.

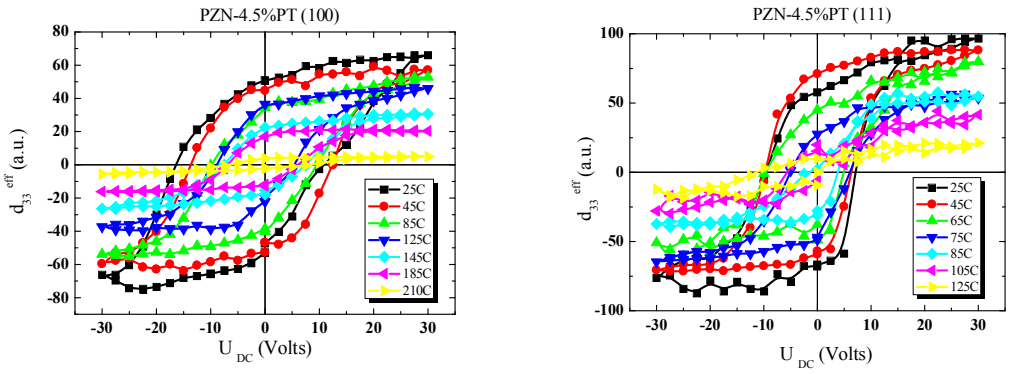

Figure 4.5 Temperature dependence of the local piezoresponse hysteresis loops for (100) and (111) oriented PZN-4.5%PT single crystals.

The results are summarized in Figure 4.6 which shows the temperature dependencies of the involved parameters such as correlation length (or average domain period), average piezoresponse (taken from images) and several characteristics of the hysteresis loops such as apparent coercive bias and area of the hysteresis loops (actually work produced by the electric field applied by the tip). The latter parameter is a measure of the ferroelectric order in the crystals.

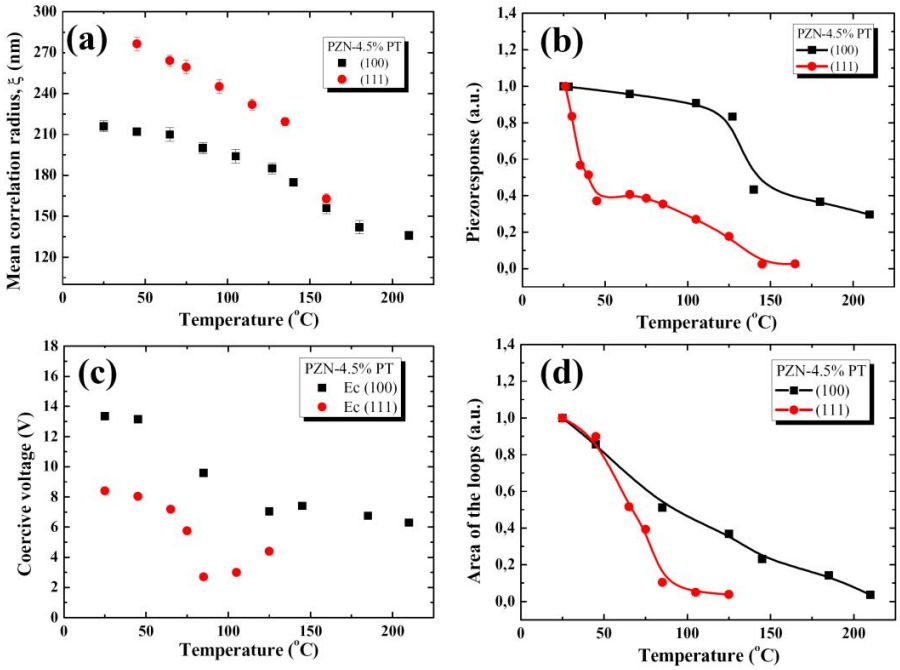

Figure 4.6 Temperature dependencies of (a) correlation length, (b) normalized average piezoresponse, (c) apparent coercive bias, and (d) normalized area of the hysteresis loops (proportional to switchable local polarization).

The average correlation length ξ estimated from correlation function dependencies varied from 290 to 170 nm for (111)- and from 210 to 135 nm for (100)-oriented with increasing temperature (Figure 4.6(a)).

It can be seen that the piezoresponse for (100)-oriented PZN-4.5%PT changes very little at lower temperatures (Figure 4.6 (b)). However, when the sample is heated to a temperature near the transition temperature, T_{c1}=160ºC, piezoresponse contrast decreases sharply, but then persists to a temperature much higher than T_m. This means that static nanodomains exist in the macroscopic paraelectric phase as expected for relaxor-like systems. This is also in line with the hysteresis measurements where a notable hysteretic behavior can be seen even at 210 ºC. Note furthermore that close to our maximum temperature of investigation (i.e. 210°C), the area of the loop for (100) is going towards zero. This is very interesting as this temperature is very close to T^*. Indeed, it was demonstrated that whatever the lead-based relaxor compound T^* is almost the same and is close to 500K (230°C) [24]. T^*

corresponds to the temperature where the PNRs adopt a static components. Based on this, one can suggest that the observed piezoresponse in fig 4.6 may correspond to the static PNRs which are believed to appear at T^*. In Ref [24], it was shown that T^* can be evidenced by x-ray diffraction, Raman spectroscopy, acoustic emission and first-principle calculations. Here, we showed that such temperature can also be evidenced using PFM tool. It is not obvious to give a real size of those domains as we will see later by depth profiling experiments, the size domain change with depth and one may also imagine that defects can favor at least near the surface increase of the polarization.

Interestingly for the crystal (111) cut, the contrast disappears at T_{C2}~110ºC (rhombohedral phase transition) and some features as the average correlation length or the area of the hysteresis loop also go to zero which is directly related to (111)-like rhombohedral polarization. However, in case of (100) cut while the local polarization feels the rhombohedral phase transition T_{C2} with a clear change of the piezoresponse it does not feel the tetragonal transition at T_{C1}~160°C. Therefore by assuming that this response arises from static PNRs, one can suggest that indeed tetragonal static PNRs appear at T^* and by decreasing the temperature these PNRs grow (their size and/or their number) and it is only when their size/number is big enough that diffraction technique can detect them. We believe that such size/number is reached at T_{C1}~160°C in case of PZN-4.5%PT. Moreover, the tetragonal symmetry we found is of interest as it was already suggested by several authors [25,26,27] and might be related to Pb-atoms which prefer to be displaced along <100>-tetragonal direction. Besides, as we stresses in the previous section, the high electromechanical response is observed in the rhombohedral region by applying the external electric field along the tetragonal-like (001) direction. Based on the suggested picture from the PFM measurements i.e. PZN-4.5%PT is composed of rhombohedral like domain with some embedded tetragonal nanodomain, one can understand easily imagine that the macroscopic piezoresponse can be huge because some tetragonal nuclei already exist in the material and can serve as embryos for having macroscopic polarization along [001] direction. In other word in such microscopic picture, it is easy to switch the polarization and then to have high piezoelectric response.

§ 4.3 Annealing Effect on the Domain Structure of (111)-Oriented PZN-4.5%PT Single Crystal

The interesting result was obtained after annealing the sample at a temperature above T_m (i.e. in the macroscopic cubic phase) The nanoscale domain structure of (111)-oriented PZN-4.5%PT single crystal has been studied after annealing at ~200 ºC in air for 1 hour (zero field heating) and cooling to room temperature (zero field cooling), with heating and cooling rates of about 1 ºC/min.

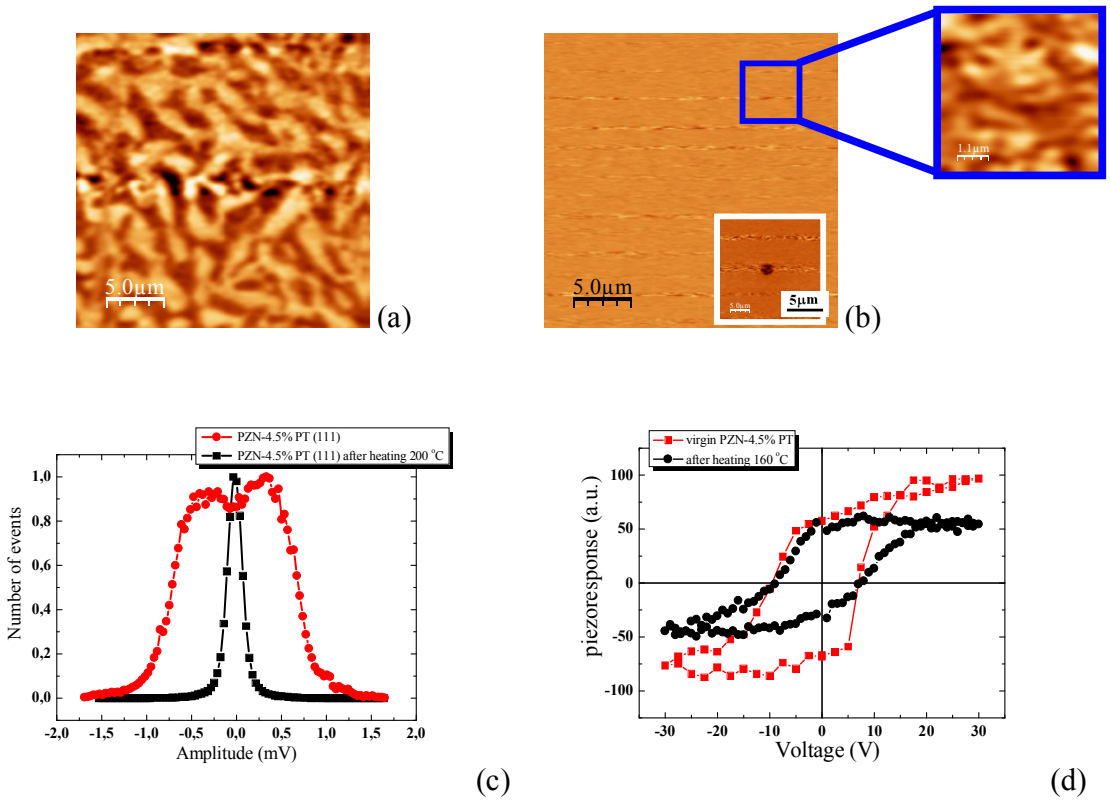

Figure 4.7 (a) Domain structure of as-grown sample of (111)-oriented PZN-4.5%PT single crystal, (b) piezoresponse structure after annealing at 200 ºC. (c) Histrograms of piezoresponse signal and (d) local piezoelectric hysteresis loops for PZN-4.5%PT before and after annealing.

Figure 4.7 presents piezoresponse domain images scanned in a 25x25 μm^2 area for the (111)-oriented PZN-4.5%PT single crystal before (a) and after annealing at 200 ºC (b). For

virgin crystal we can see regular ferroelectric domain structure with characteristic domain period of ~ 0.5÷1 μm. After heating the as-grown domain structure disappears, and we observed only nanodomains with sizes less than 100 nm (not visible at the bigger scale). Figure 4.7(c) illustrates histograms of the piezoresponse signal where two distinct peaks are characteristic of the ferroelectric phase (with "up" and "down" polarizations) and only single maximum is obtained for nanodomains of much smaller dimensions and piezoresponse amplitude. We believe that the changes in domain structure, is related to the defect annealing at the surface. Also it means that the curves shown in Figures 4.4-4.6 are partly affected and the abrupt changes of the polarization can be related to the annealing effects. This is proved by the existence of d_{33} hysteresis loops after annealing (but with reduced value of the switching polarization), Figure 4.7(c). Note however that despite the single maximum around zero for the piezoeresponse, a hysteresis loop and contrast are still measured attesting that indeed polar domains exist. It can be concluded that annealing at 200 ºC causes irreversible ferroelectric-relaxor features at the surface and if one want to properly investigate the properties one should make investigation as a function of depth as we shall do in a next section.

Annealed surface is an "ideal" surface (without defects) and then can be analyzed in terms of stability and relaxation. For testing the PNRs polarizability and stability after poling the following experiment was performed. The surface was periodically poled as shown in Figure 4.8 and thus artificial ferroelectric domains made from nanodomains were created.

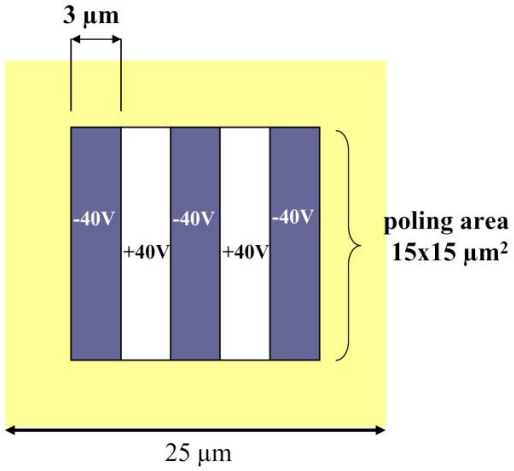

Figure 4.8 Schematic of the poling experiment by PFM.

In this experiment, both negative (V = −40 V) and positive (V = +40 V) polarization patterns were written on the surface of annealed PZN-4.5%PT single crystal. The results are shown in Figure 4.9. The sample was then left in the polarized state and the relaxation of polarization was evaluated at room temperature.

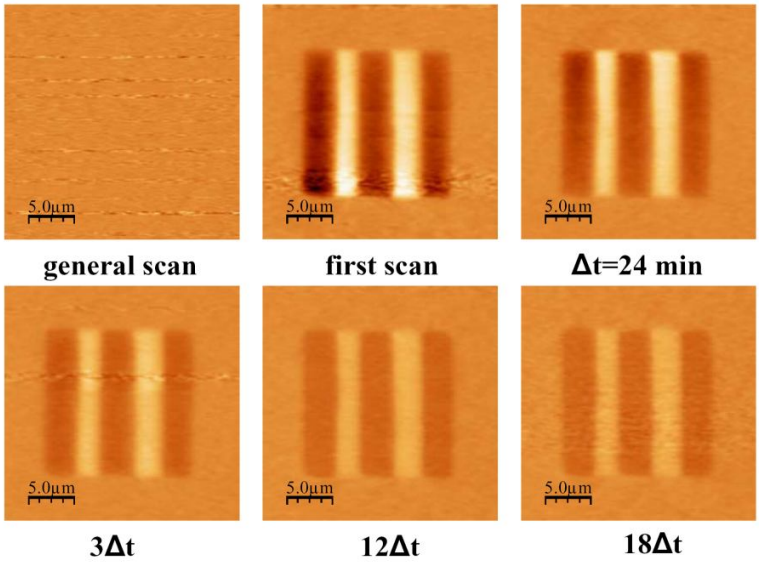

(a)

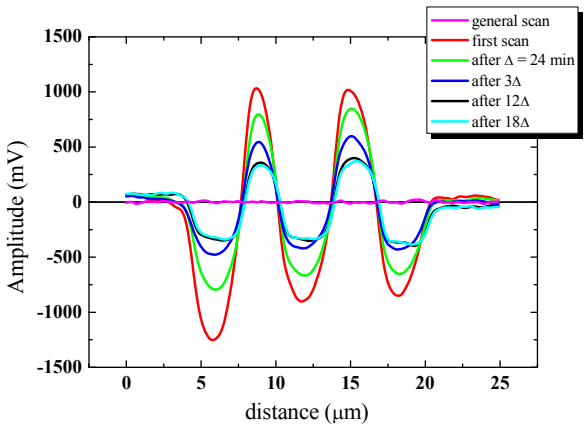

(b)

Figure 4.9 (a) Polarization relaxation in (111)-oriented PZN-4.5%PT single crystal poled with ±40V, (b) Cross-sections of piezoresponse at different times (Δt=24 min).

Figure 4.9(a) displays the relaxation of thus created polarization pattern. Comparison of the piezoresponse cross-sections (obtained along the middle line of the scan) at different

times is shown in Figure 4.9(b). The fit using stretched exponential dependence is shown in Figure 4.10. Simple exponential fit was unable to explain the relaxation of the polarization in PZN-4.5%PT single crystals, and it is understood as a signature of the relaxor behavior consistent with macroscopic measurements in relaxors.

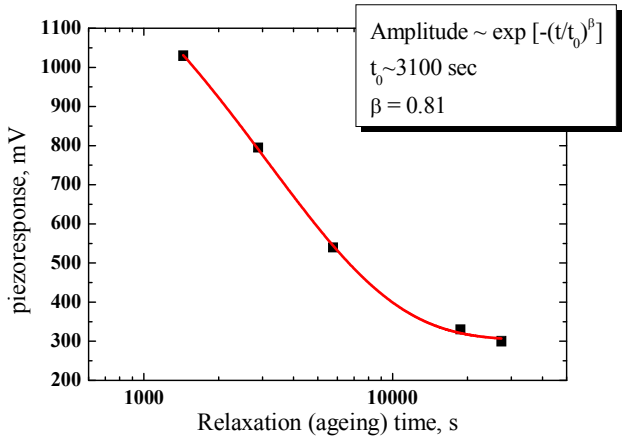

Figure 4.10 Piezoresponse relaxation fitted with stretched exponential dependence. Fitting parameters β and t_0 are shown in the inset.

We found that stretched exponential dependence (Kohlrausch-Williams-Watts type) gives the best fit and the parameters of the relaxation are close to those found in PLZT ceramics (Chapter 3). We can make a conclusion that the induced "classical" ferroelectric domains in PZN-4.5%PT are not stable and disappear with time. This behavior can be understood either by considering defects at the surface that stabilize bigger domains or/and by the relaxor nature of this compound which in somehow forces the polar arrangement to be irregular. It is believed that the induced polarization can be stabilized with time by the surface layer as evidenced by the more square shape of the polarization profile after relaxation. But at the same one may imagine that some other domains (with tetragonal-like orientation for instance as suggested in the previous section) or random fields that are characteristic of relaxors can fight against a homogeneous polarization.

§ 4.4 Domain Branching in PZN-PT Single Crystals

In this section we present our findings on the domain structures vs. depth evolution in ferroelectric relaxor crystals of PZN-4.5%PT with different orientations

Introduction to Domain Branching

The domain widths are known to vary as a square root of the lamellar thickness, the behavior is known as Kittel's law (later extended by Mitsui and Furuichi to ferroelectrics and by Roytburd to ferroelastics) [28,29,30].

The proportionality between the square of the domain width (*w*) and the thickness of a parallel-sided slab (*d*) was initially proposed by Kittel for ferromagnetic materials, but later it has been proposed as a general property of ferroic domains of any kind: *ferromagnetic* (Kittel, 1946 [28]), *ferroelectric* (Mitsui and Furuichi, 1953 [29]), and *ferroelastic* (Roytburd, 1976 [30]). This is because the free energy associated with the domains in a ferroic material has at least two components, one from the energy of the domains themselves, which is proportional to the domain size (ω), and another coming from the domain walls. The number of domain walls is inversely proportional to the domain size ($1/\omega$), while the domain wall energy is proportional to the domain wall area, which itself scales directly with the film thickness (*d*).

Using *U* and γ as constants of proportionality, we obtain an expression

$$F = U\omega + \gamma \frac{d}{\omega} \ . \tag{4.1}$$

Under equilibrium conditions $dF/d\omega = 0$, i.e.

$$\omega^2 = \frac{\gamma}{U} d \tag{4.2}$$

When *U* is the magnetostatic energy this becomes a Kittel's law [28], for the case of electrostatic - Mitsui and Furuichi's law [29], and in the case of elastic energy Roytburd's law [30]. For ferroelectrics, the formation of antiparallel (180°) *c*-axis stripe domains is driven by

the electrostatic energy of the uncompensated dipoles at the surface. Anti-parallel lamellar domains are formed in the presence of an anisotropic surface energy density σ and a depolarization field E_d in unelectroded ferroelectrics. The period $2L$ of the lamellar domain structure is enlarged by σ but diminished by E_d. The equilibrium value of $2L$ is determined by the balance between the electrostatic energy U_E generated by E_d and the domain wall energy U_W proportional to σ. In the case of a thin plate shown in Figure 4.11(a) [28,29], the domain walls run through the thickness d of the plate and the square root law, $2L \sim d^{1/2}$, holds in the case of a thick plate shown in Figure 4.11(b) [31]. On the other hand, the branched domain structure is energetically favorable and has the period $2L \sim d^{2/3}$. Although polarization charges are also generated in the bulk, the decreases of U_W in the bulk and U_E on the surfaces exceed the increase of U_E in the bulk. The branched domain structure was experimentally verified in ferromagnets [32], but rarely in ferroelectrics [33].

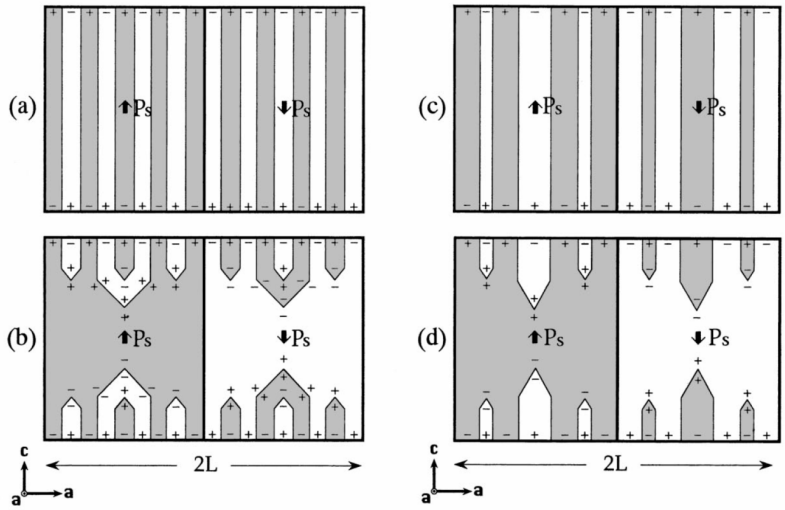

Figure 4.11 Models of anti-parallel lamellar domain structure of ferroelectrics. (a) Kittel-Mitsui model, (b) Kaczer's branching model, (c) Pentad Cantor set model (the second pre-fractal), (d) branched pentad Cantor set model (the second pre-fractal) [31].

Okazi *et al.* have found that the anti-parallel domain structure is not only periodic but also fractal in the presence of the strong E_d and anisotropic σ in hydrogen-bounded ferroelectrics TGS, CDP and KDP crystals [34, 35]. The domain structure is described by the pre-fractals of the pentad Cantor sets in each half-period, as shown in Figure 4.11(c). The

period of the pre-fractal domain structure obeys the square root law, $2L \sim d^{1/2}$. This is verified in TGS for a wide thickness ranges, $0.5 < d < 11$ mm. If the pre-fractal domain structure was branched as shown in Figure 4.11(d), the period should obey $2L \sim d^{2/3}$.

For example in KDP the measurement of the thickness dependence of $2L$ is difficult, because each rectangular domain block has a different value of $2L$ [36].

Pre-fractal Domain Structure in Ferroelectrics

As illustrated in Figure 4.12, each half-period of the periodic domain patterns is characterized by the pre-fractals of the pentad Cantor set having the fractal dimension D ~ 0.756 along the wall normal.

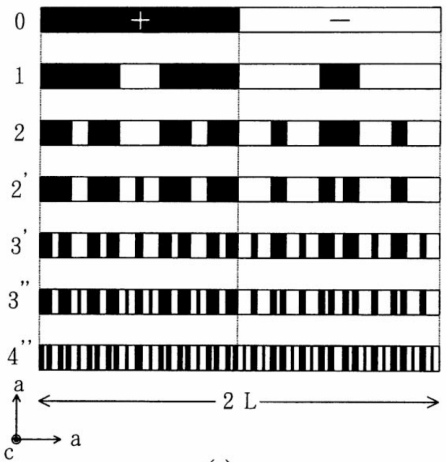

Figure 4.12 A period $2L$ of pre-fractal domain structures (PFDS). The generation n of PFDS increases by one after reversing the polarity of P_S normal to this page in a central fifth part of each + domain in the left half period and of each -domain in the right half period [35]

The domain walls generating the zero and the first pre-fractal domain structures run through the thickness, while those newly generating the second pre-fractal one and the derivatives of the second, the third and the fourth pre-fractal ones, 2'-4", only stick on the c surface. The domain structure increases its generation by sticking a fifth domain on the end of each domain widest in the structure. Thus, the branched domain structures become more complex than the unbranched pre-fractal domain structures of the pentad Cantor set.

PZN-4.5%PT (100) and (111) Orientations

Figure 4.13 shows the evolution of the ferroelectrics domain structures of PZN-4.5%PT (two orientations) versus depth from virgin surface after polishing with diamond and colloid pastes. It was verified that gentle polishing does not lead to the disruption of the domain structure and only intrinsic variations of the domain sizes could be observed.

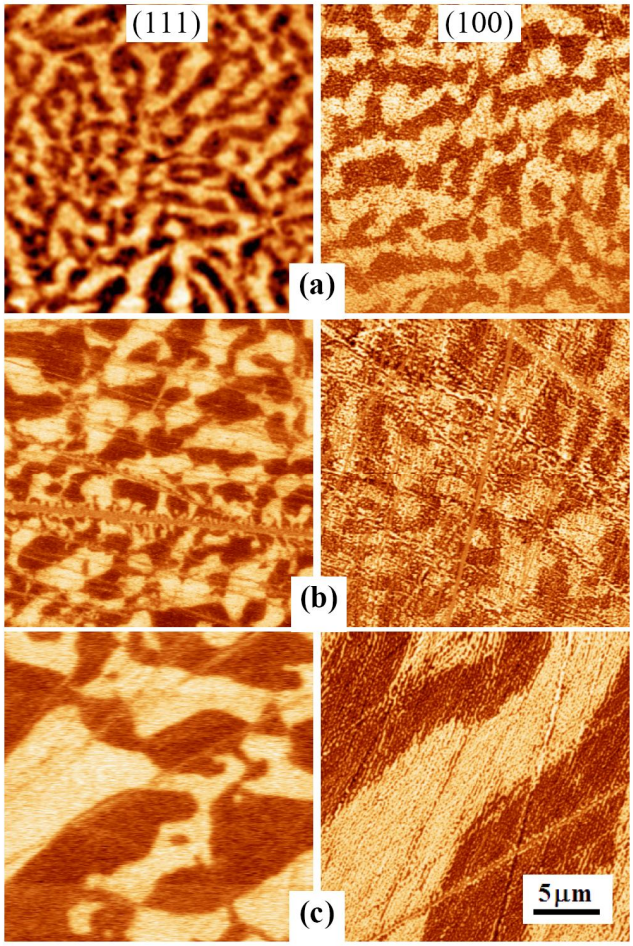

Figure 4.13 Piezoresponse images of $Pb(Zn_{1/3}Nb_{2/3})O_3$-4.5%$PbTiO_3$ single crystal: left column (111)-oriented sample, right – (100)-oriented sample for different polishing depths. (a) – as-grown domain structure, (b) – polished 25 μm and (c) polished 50 μm from virgin surface. Scan size for all images is 25×25 μm^2.

It is seen that the domain size increases with depth for both crystal orientations but the labyrinthine-like shape that is a relaxor-feature is conserved. This result means that even if the size that we determine from the classical PFM measurement i.e. the near surface is the wrong one, the shape of the domains remains unchanged. We shall see later in case of pure relaxor i.e. PMN how we succeed to extract the real size of the PNRs.

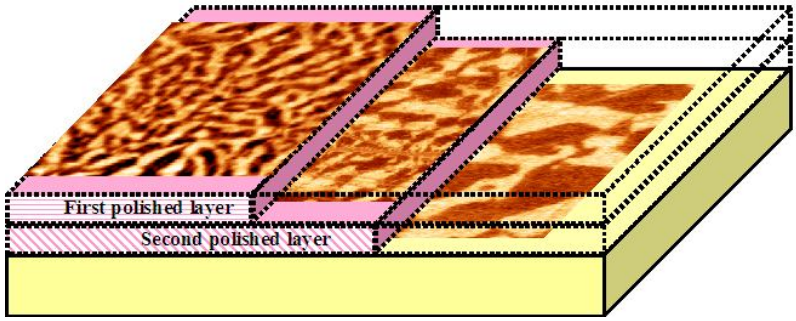

Figure 4.14 3D PFM images in PZN-4.5%PT (100) obtained after polishing.

Figure 4.14 illustrates the evolution of domain configurations during polishing. It is found that 3D domain representation is possible by cross-sectioning (repeated polishing) of ferroelectric material (similar to AFM microtomy).

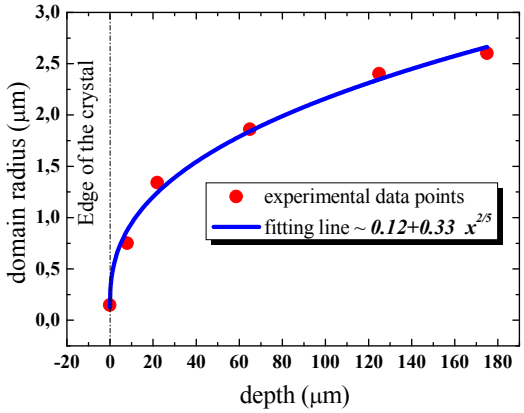

Figure 4.15 Domain size vs. depth of the PZN-4.5% PT (100)-oriented single crystal.

Figure 4.15 presents the correlation length s (roughly average domain size) as a function of depth l in PZN-4.5% PT (100)-oriented single crystal. If this dependence would just follow from the Kittel's law [28], it would give a square root dependence on l ($s \sim l^{1/2}$). As is seen from the Figure 4.15 the domain size actually follows the 2/5 power law and it cannot be explained by the Marchenko's model [37] that requires the exponent 2/3.

Very interesting results were observed on the edge of single crystals after polishing process.

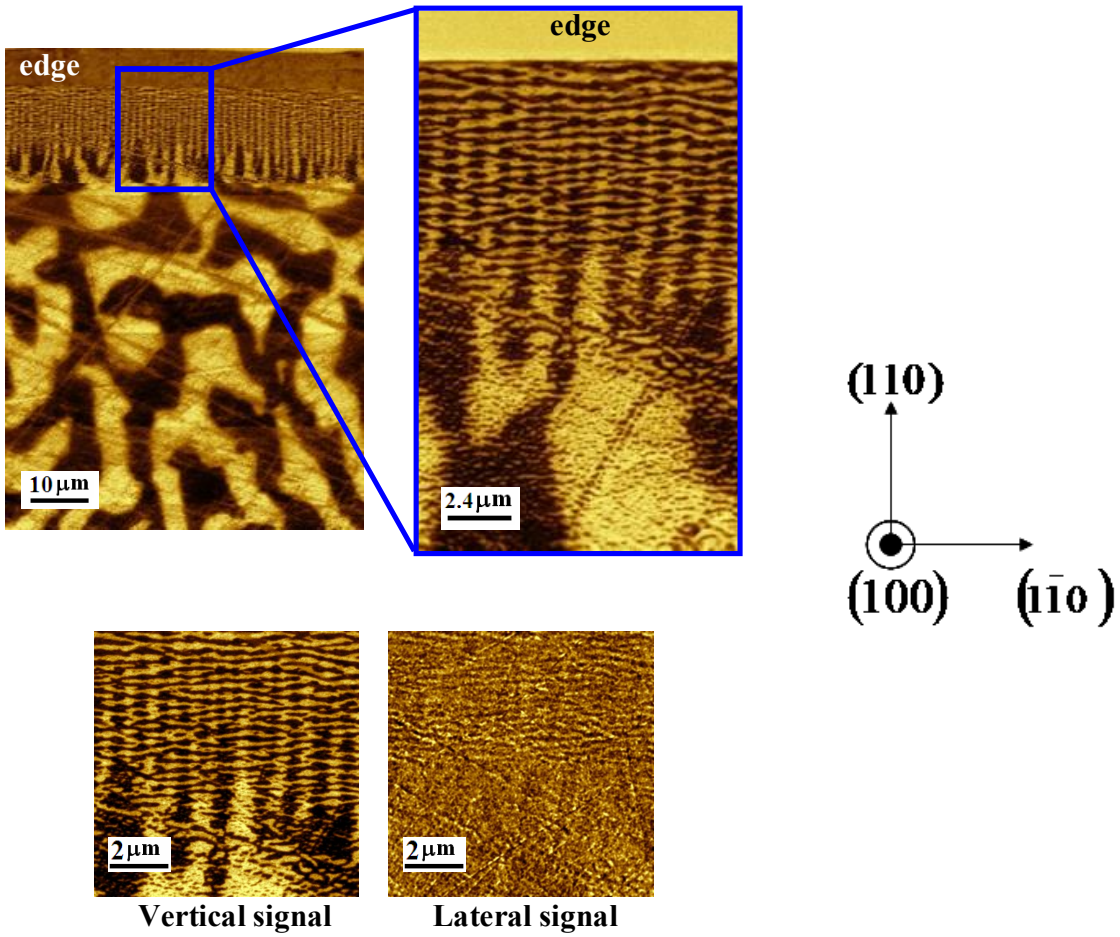

Figure 4.16 Wedge-like domain structures on edge of the (100)-oriented PZN-4.5%PT single crystal.

Figure 4.16 presents the domain branching from the edge to center for (100)-oriented PZN-4.5%PT. We observed wedge-type domains with the characteristic length of about ~ 10

μm and lateral size $d \sim 300$ nm oriented along [110] direction. Only ou-of-plane signal was found and no indication of the lateral polarization was indeed detected.

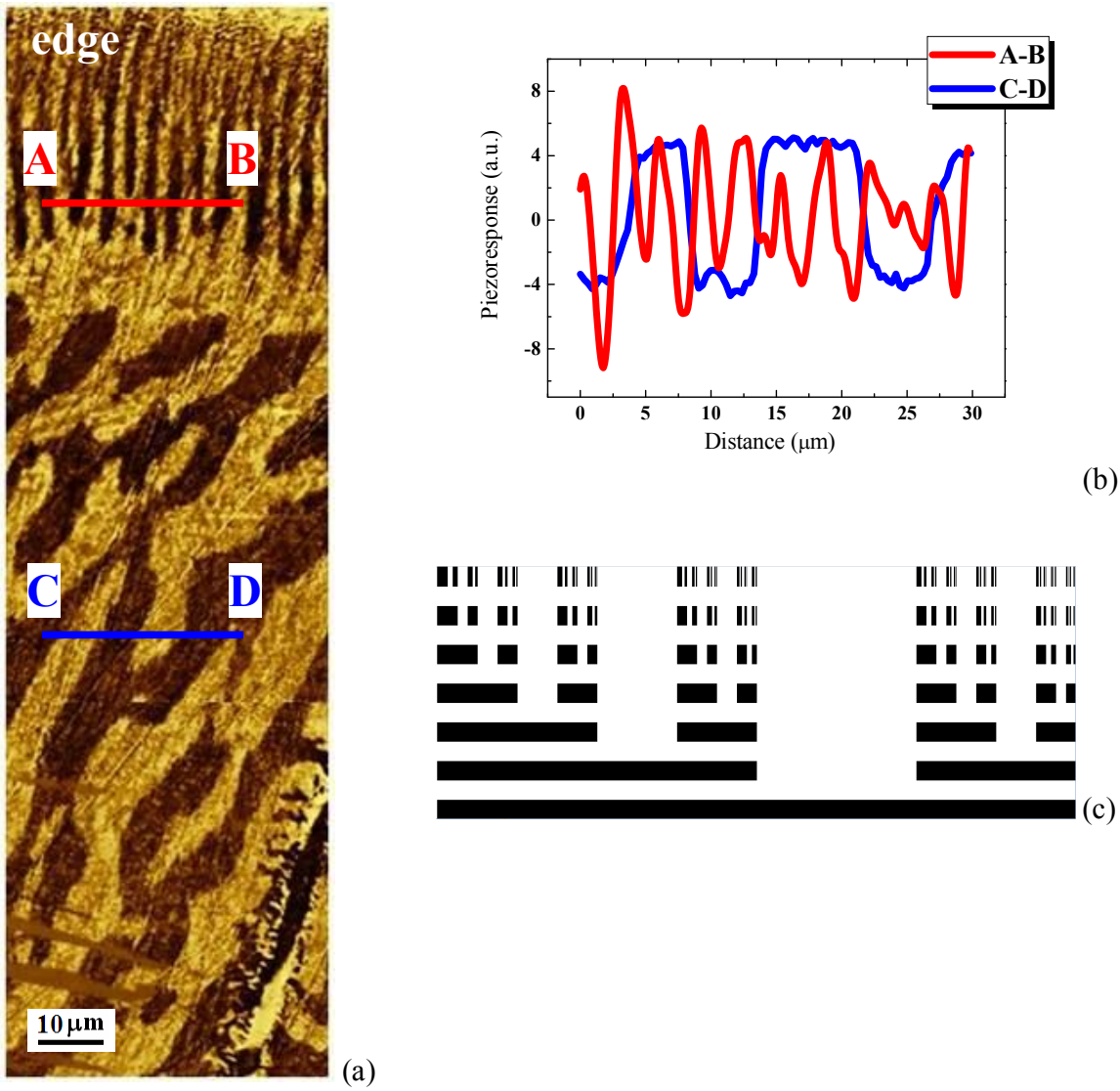

(a) (b) (c)

Figure 4.17 (a) – wedge domain structure of the (100)-oriented PZN-4.5%PT single crystal, (b) – cross-section along lines *A-B* and *C-D*, (c) - asymmetric Cantor set with fractal dimension 0.6942.

Figure 4.17 (a) shows a periodic domain structure with branching at the edge of the crystal. Cross-sections along lines *A-B* and *C-D* (Figure 4.17 (b)) illustrate decreasing period

of the domain patterns to edge of the crystal. Domain branching is observed and explained by the appearance of inverse domains to compensate the depolarizing field. On the other hand, the fractal dimension obtained from Figure 4.17 (a) is ~ 0.69. This value is close to fractal dimension for asymmetric cantor set, where D=0.6942 (Fig. 4.17(c)). The near coincidence of the fractal dimension with the theoretical value is the indication of one-dimensional domain growth and continuous splitting into finer domains when approaching the surface.

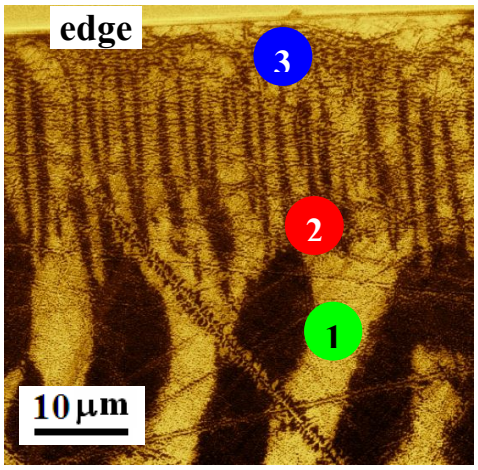

(a)

1 – white domain

2 – boundary nano&micro domains

3 – edge of the crystal

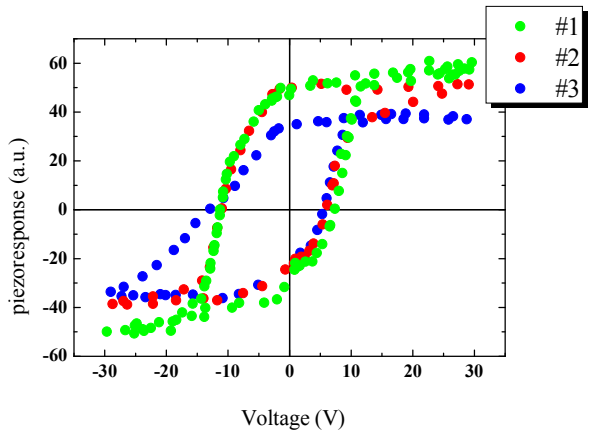

(b)

Figure 4.18 Piezoresponse hysteresis loops acquired on PZN-4.5%PT (111) single crystal in different locations: #1- in the bulk, #2 near - domain splitting, #3 – at the surface.

To investigate the local switching properties in a more detail, piezoresponse hysteresis loops were measured in different locations (close to the edge and in places with different domain size). The switching parameters (imprint, remanent piezoresponse, etc.) can then be extracted from the loops. In this manner, the dynamics of the local switching characteristics can be probed and the switching properties can be visualized to show how these characteristics vary from the bulk to the surface. In Figure 4.18 a PFM image of PZN-4.5PT with domain branching structure within a 50×50 μm^2 area and representative hysteresis loops demonstrating a variation in the vertical and horizontal shifts are shown. They illustrate that the materials property does not change dramatically at the edge and all described above phenomena are of intrinsic, rather than extrinsic character and domain branching cannot be cause by polishing induced damage,

Domain patterns in the vicinity of the edge of (100) and (111) -oriented PZN-4.5%PT were also studied by SEM (Figures 4.19 and 4.20, respectively).

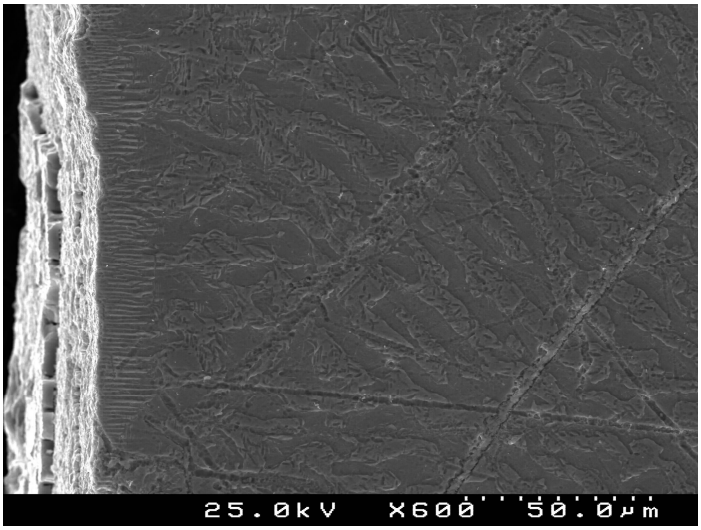

Figure 4.19 SEM image of the edge of (100)-oriented PZN-4.5%PT single crystal.

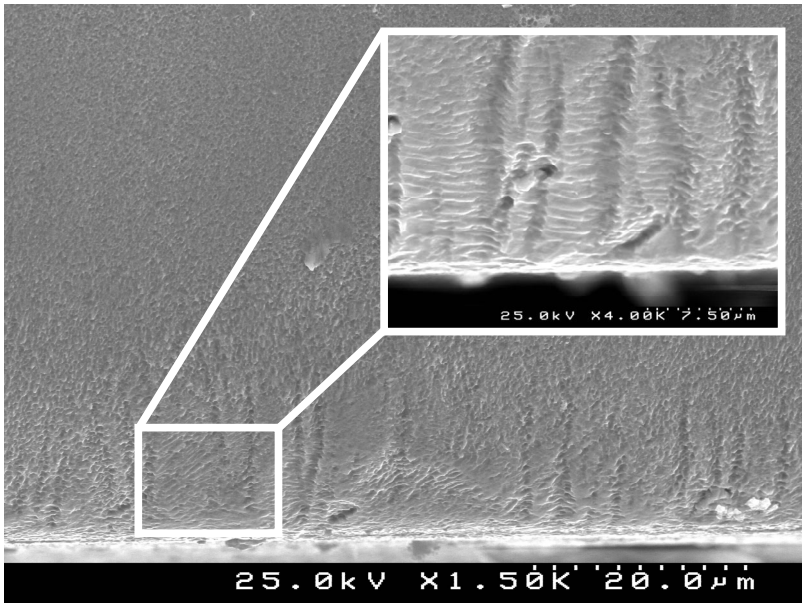

Figure 4.20 SEM image of (111)-oriented PZN-4.5%PT single crystal.

These Figures indicate that the domain branching can be also observed by SEM and prove once again that the domain size decreases at the surface and is of purely intrinsic nature, i.e., cannot be caused by polishing/etching or measurements procedures.

§ 4.5 Nanoscale Domains and Local Piezoelectric Hysteresis in $Pb(Zn_{1/3}Nb_{2/3})O_3$-$xPbTiO_3$ Single Crystals close to the MPB

In this section we present our findings on the domain structures and local piezoelectric hysteresis loops of the single crystals of PZN-x%PT for x>7%. We go far away from the representative PZN-4.5%PT compound and investigate the domain features going through the MPB.

In order to understand the relaxor behavior of the PZNT-xPT system (low concentration of PT) the measurements were also done on various compositions with high (x>7 %) ferroelectric component concentration. Figure 4.21 shows piezoresponse images of

ferroelectric domains in PZN-xPT single crystals of above mentioned compositions. The imaging contrast is determined by the out-of-plane component of the piezoelectric signal, in which the dark and bright areas correspond to the opposite polarization orientations.

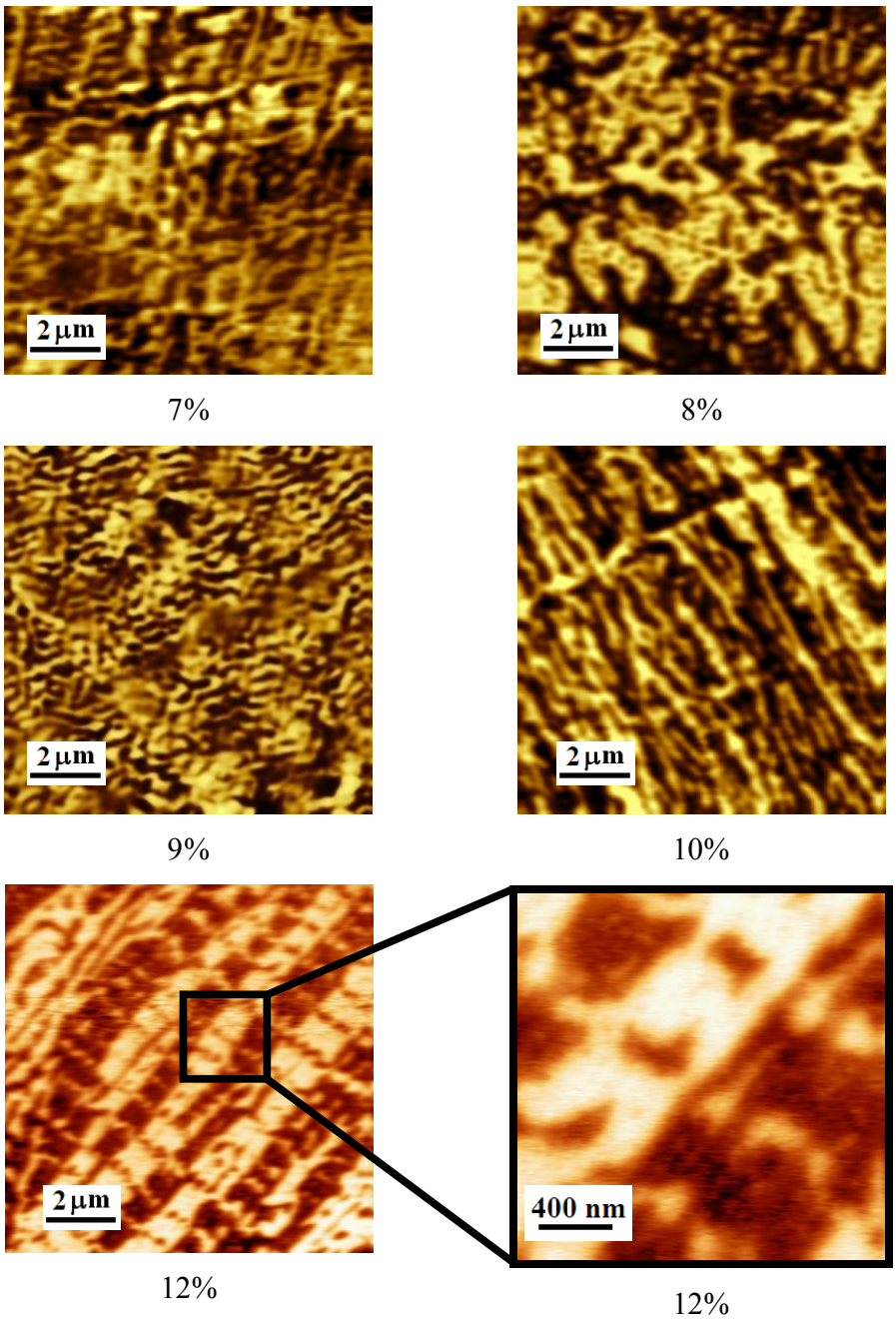

Figure 4.21 Piezoresponse images of ferroelectrics domains in (111)-oriented PZN-*x*%PT single crystals (x≥7%).

In general, the trend is a transition from irregular (relaxor type) domain structures characteristic for low x to banded (stripe-like) domains of the compositions with higher x concentrations. For the compositions close to the morphotropic phase boundary, a mixture of domains belonging to several phases can be noted (e.g., for x=9% where both rhombohedral and tetragonal domains are evident). Irregular domains can be still observed in x=12% crystals away from the MPB. This is very interesting because in such composition *T** the temperature where static nanodomains appear was also evidenced [26]. Therefore we have here, in these PFM images, the direct evidence of the nanodomains suggested by the evidence of *T** in ref [26]. It is of interest to recall that for PZN-12%PT the structure is usually considered as not relaxor but based on our finding we believe that some relaxation should exist for this sample and therefore one need to make further investigations on the tetragonal-side of the relaxor-PT systems.

It was suggested in the past that general mechanism for the difference in domain regularity and polar cluster size between the compositions is related to the role of titanium ions in the polar cluster interaction. It is expected that highly polarizable Ti^{4+} ions play an important role in promoting interaction between the clusters. In this way, higher PT concentration in PZN-12%PT facilitates long-range ferroelectric order formation. Such process undoubtedly accelerates growth and coalescence of polar clusters into microsized domains upon cooling.

Nanoscale piezoelectric hysteresis loops (shown in Figure 4.22) were measured in the PZN-x%PT single crystals by applying voltage cycles of maximum 40 V to the PFM tip. The measurements were done under identical conditions, so that to directly relate the changes in the loop shape to the variation of the compositions.

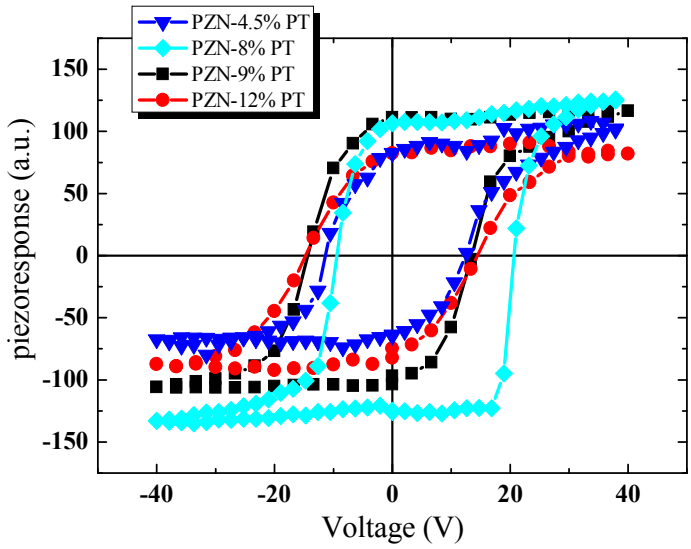

Figure 4.22 Local piezoresponse hysteresis loops of (111)-oriented PZN-x%PT single crystals.

The piezoresponse hysteresis loops presented in Figure 4.22 clearly prove the existence of ferroelectricity in all PZN-xPT single crystals. The shape of the hysteresis is very similar (except of the x=8% composition close to MPB). Globally, the amplitude is higher for 8% and 9% compared to 4.5% and 12% and therefore reflect the location of the MPB regions that is around 9%. As an additional feature, piezoresponse hysteresis loops were found to be shifted vertically towards positive (4.5%, 7% of PT) or negative (8% and 12% of PT) values. This shift can be related to the contact potential difference in the investigated crystals (i.e., to the electrostatic contribution to the piezoresponse) or more likely to the fixed polarization offset (e.g., due to frozen polarization at the surface or static PNRs). The origin of the surface polarization offset in the studied PZN-PT crystals is not currently clear and cannot be adequately explained based on the modern theory of the surface states in relaxor ferroelectrics. It can be related, for example, to the flexoelectric effect in the surface that may promote the appearance of internal field and small residual non-switchable domain of certain orientation. The loop for the 8%PT concentration can be explained by the rhombohedral-tetragonal phase induced by the electric field applied to the PFM tip.

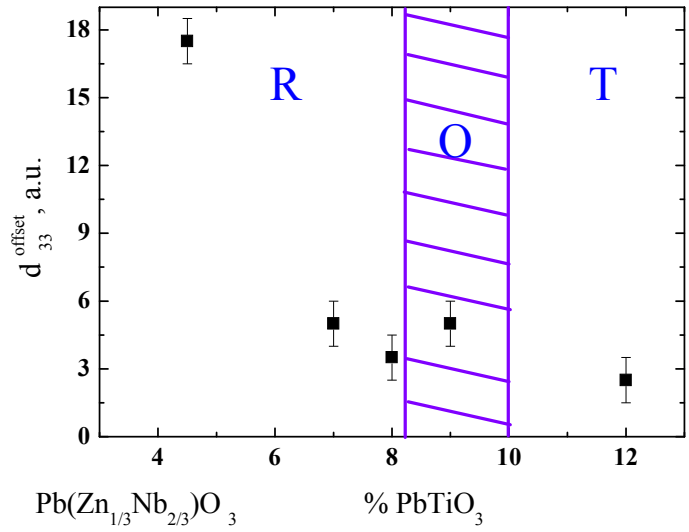

Figure 4.23 Dependence of the vertical shift of the hysteresis loops in PZN-PT single crystals on the concentration of PT.

The absolute values of the piezoelectric offset ($\left|d_{33}^{offset}\right|$) calculated from the hysteresis loops measured in PZN-xPT crystals (Figure 4.22) are presented in Figure 4.23. Monotonous decrease of the piezoelectric offset with increasing PT concentration is observed without appreciable anomaly near the MPB. As we mentioned previously, the offset might be related to the static PNRs. Going far from the relaxor-like or low-Ti composition can then be explained by the continuous decrease of the static PNRs that still continue to exist even for PZN-12%PT as we have shown in fig 4.21.

§ 4.6 Nanoscale Properties of PMN Single Crystals: case of pure relaxor without any ferroelectric phase transition

In this section, the properties of PNRs are accessed via PFM. The contrast and size distribution of polar nanoregions is studied in pure PMN as a prototypical example of the relaxor family. The measure of the short range order – the correlation length - is directly

extracted from the images. These measurements are complemented with local piezoelectric hysteresis where the available electric fields can induce local ferroelectric state.

Introduction to PMN Singe Crystals

As was shown in the previous Chapters, relaxors are characterized by a frequency dispersion in their maximum permittivity temperature with no macroscopic phase transition into a ferroelectric state at T_m. These behaviors are fundamentally different from those of normal ferroelectrics and the dielectric dispersion does not fit the classical Debye relaxation model. Pure $PbMg_{1/3}Nb_{2/3}O_3$ (PMN) is considered to be a prototype relaxor, and has been studied extensively over last 50 years. Efforts to understand the dynamical properties of relaxors have focused on the polar nanoregions (PNRs) present in these compounds. Evidence for the existence of local polarization in PMN was deduced from optical and strain measurements [38] (T_B =620 K for PMN).

For the first time PNRs were observed in optical measurements by Burns and Dacol [38]. It was shown, that PNRs appear at the temperature T_B a few hundred degrees above the temperature T_m of a dielectric constant maximum. The characteristic size of PNR obtained from these optical measurements was 10-15 nm. In recent neutron experiments in PMN it was also shown that PNR appear at T_B. Thus PNRs are believed to be dynamic in nature and acquire a static component at T^*~500K [39].Correlation length of polarization was determined to increase with decreasing temperature and reach 6 nm followed by a significant jump at freezing temperature T_f~210K. Neutron scattering measurements [40,41] have demonstrated that diffuse scattering appears in PMN between 600 and 650 K, consistent with previous optical studies. Various neutron and x-ray measurements using diffuse scattering have been carried out in order to investigate how PNR are formed, and to determine average sizes and polarizations (atomic shifts) at different temperatures [42,43,44,45,46,47].

Recently, neutron measurements [44,45] provided evidence for both local atomic displacements and for medium-range (5–50 Å) ordering. The temperature dependence of the volume fraction of the PNRs was also found, and it was shown that the three-dimensional percolation is reached below 200 K, where the PNR start to overlap. The sizes of PNR have

characteristic values of 10-15 nm and polarization correlations are observed at distances of the order 2-6 nm.

The PFM measurements were few and carried out only at room temperature for solid solutions with PT [48,49,50].

In our experiments we used pure PMN single crystals with (111) orientation and carry out the measurement at room temperature, i.e., above T_m and T_f for PMN. Figure 4.24 shows piezoresponse images of (111)-oriented PMN single crystal obtained at room temperature after different treatments. Figure 4.24(a) displays PFM signal after annealing above Burns temperature. No domains were found after zero field cooling (ZFC) conditions. The absence of the contrast is consistent with a dynamical nature and small size of the polar clusters (PNRs) in PMN and is in agreement with the measurements in PZN-4.5%PT crystals (fig. 4.7). However, a strong piezoelectric signal could be induced by applying a dc voltage exceeding a threshold value of 5–10 V indicating an onset of a polar state on the surface of the sample (Figure 4.24 (b)). At higher voltages (10–20 V), a hysteresis could be measured on the surface of the bulk PMN as shown in Figure 4.25.

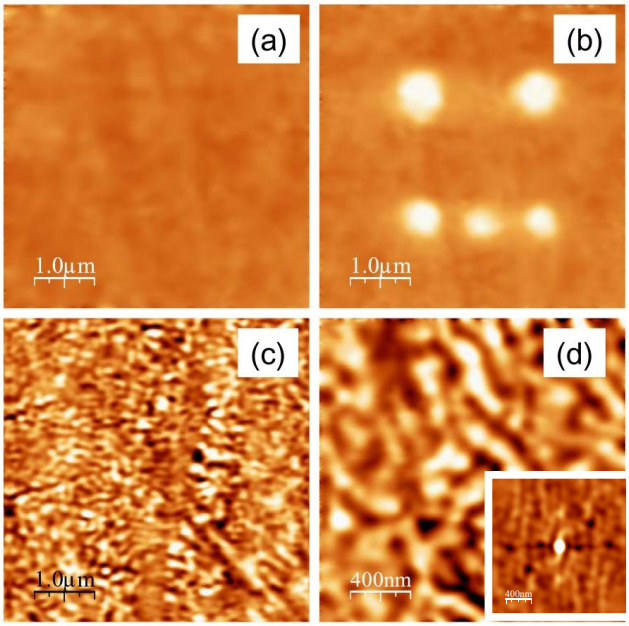

Figure 4.24 Piezoresponse images of PMN [111] single crystal at room temperature: (a) being acquired after annealing to 650 K; (b) – after local poling by tip with voltage 30 V during different pulse durations (10; 3; 1; 0.3 and 0.1 seconds); (c) and (d) after poling at 180 K – different scan size.

Figure 4.24 (b) displays the results of the application of *dc*-field during different pulse durations. It was found that the induced piezoresponse is unstable and relaxed within few thousands of seconds after switching off the *dc* bias. But after the initial relaxation the residual ferroelectric domains do not change with size and can persist on the surface during several days. After poling at low temperature, random domain patterns characteristic of frozen PNRs are reproduced. Thus PFM is able to follow relaxor-ferroelectric phase transition induced both by the electric field and by the temperature.

The hysteresis obtained before and after annealing above Burns temperature (Figure 4.25) confirms the results obtained on PZN-4.5%PT and once again illustrates the possibility of the stabilization of the static polarization at the surface.

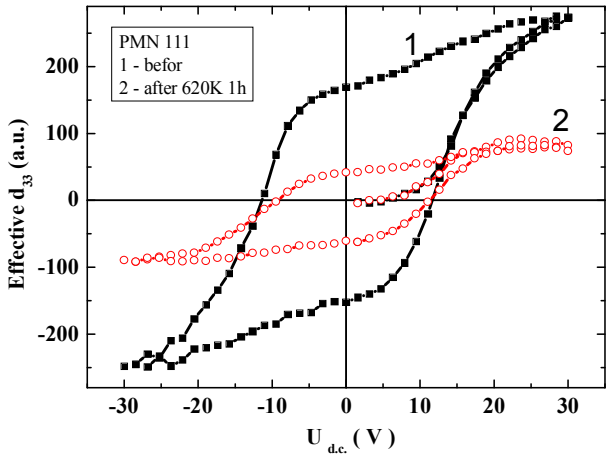

Figure 4.25 Local piezoelectric hysteresis loops of PMN (111) single crystal measured by PFM after poling at 180 K and before (1) and after (2) 1 hour annealing at 620 K.

The time dependence of the domain radius for three different pulse amplitudes is shown in Figure 4.26. Apparently, there is saturation in the domain size with time. We analysed the kinetics of the sidewise domain growth using the classical activation model of wall motion in the tip-generated field assuming a weak indentation regime.

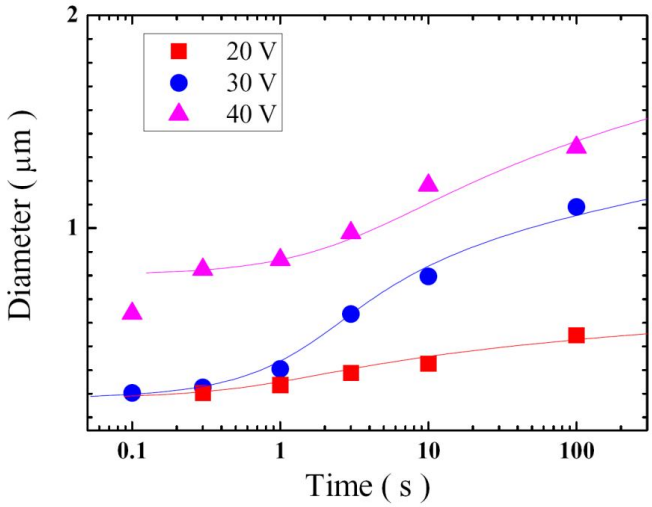

Figure 4.26 Domain diameter vs. pulse duration for various pulse magnitudes in PMN. The data are fitted using Eqs. (4.3) and (4.4) and are shown by solid lines.

According to the Miller and Weinreich model [51], the sidewise growth of the domain develops as an activation process via nucleation at the existing 180° domain wall. This nucleation process determines the exponential field dependence of the wall velocity. The normal component of this electric field at a section of the 180° domain wall with the sample surface at a distance r from the tip was calculated using an expression for the electric potential derived by Mele [52]:

$$E(r) = \frac{C_t V_t}{2\pi\varepsilon\sqrt{\varepsilon_c \varepsilon_a} + 1}\sqrt{\frac{\varepsilon_a}{\varepsilon_c}}\frac{R+\delta}{((R+\delta)^2 + r^2)^{3/2}} \tag{4.3}$$

where C_t and V_t are the tip capacitance and bias, respectively, and ε_a and ε_c are the dielectric constants along the nonpolar and polar axes of the sample, respectively. In the present study, we used the following values: R = 50 nm, d = 1 nm, $\varepsilon_a \approx \varepsilon_c \approx 12000$. The tip capacitance was calculated to be 1.63 10^{-17} F. The data in Figure 4.26 were fitted using the following expression for the time dependence of the domain radius:

$$t = \int \frac{dr}{v(r)},$$

$$t = t_a + t_d$$

$$t_a = \frac{r_a}{v_a},$$

$$t_d = \int \frac{dr}{v(r)} = \int_{r0}^{r} \frac{dr}{v_0 \exp(-\frac{\alpha}{E(r)})}, \qquad (4.4)$$

where $v(r)$ is a local wall velocity ($v_d = v_0 \exp(-\alpha/E(r))$, α is the activation field). The meaning of the fitting parameter r_0 can be understood as follows. Underneath the probing tip, the generated field is much larger than the local coercive field and the domain growth develops as a nonactivated process. The spatial inhomogeneity of the external field results in a transition from the nonactivated to the activated process. Therefore, r_a can be considered as the domain radius at which the activation type of the wall motion begins. The r_a value was found to be 200 nm for the applied voltage of 20 and 30 V and 780 nm for the 40 V.

We must note that these activation fields are small enough. We empasize that a strong decrease of the external field with the distance from the tip as well as nonlocal tip effect might result in a different mechanism of domain wall motion that may explain a less adequate fitting of $r(t)$ for large domains.

These results should be compared with the macroscopic experiments. In bulk PMN single crystals the induced transition into ferroelectric state was observed only at low temperatures (230 K), where the threshold field of 1.7 kV/cm was required for (111) oriented bulk PMN. However, it should be taken into account that in PFM experiment the surface contribution apparently dominates and the electric field is highly nonuniform. In the subsurface layer (giving the main contribution to measured piezoresponse), the field could considerably exceed the one used in macroscopic experiments. The rough estimation shows that the value of electric field corresponding to the threshold voltage is 25 kV/cm at the depth of 50 nm and it can be even higher just below the surface. It is thus obvious that the macroscopic data cannot be used as a guideline for the explanation of PFM experiments and, thus allowing observation of ferroelectric like phenomena in the surface of bulk PMN at room

temperature. Thus we have shown that the influence of a strong local field at the PMN surface at room temperature results in the formation of local nanosized domains. By finding out this fact we decided to investigate the regime of zero field heating after field cooling (ZFHaFC).

Figure 4.24 (c,d) shows piezoresponse images of PMN obtained at room temperature following ZFHaFC. An irregular system of individual polar regions with an alternating piezoresponse signal (polarization directions) is observed on a larger scale (see Figure 4.24 (c)). These nanodomains are similar to those observed in PZN-PT and PLZT in previous Chapters. A pattern of labyrinth-type interpenetrating polar regions is well resolved on the surface with the boundaries corresponding to 180° domain walls. This structure did not change with time during few days. The nanodomains were not continuous stripes (like in PLZT), rather we could say that the small interpenetrating labyrinth-type structures prevail (see Figure 4.24 (d)). There is no preferred orientation of domain walls and their orientation was not connected to the topography. The typical width of the domains determined from the piezoresponse image is in the range 70–120 nm. At higher magnification, a fine structure of nanodomains of opposite orientation is observed (Figure 4.24(d)). We believe that the appearance of such nanodomain structure is a distinctive feature of relaxor single crystals, and it is closely related to the distribution of PNRs in the volume of a sample. Indeed, PNRs and local random fields due to charge disorder in PMN-type relaxors are considered as one of the main reasons responsible for the relaxor behaviour.

For the quantitative data treatment, we used a correlation function technique, which has been already used for the analysis of PLZT ceramics and PZN-PT single crystals. The two-dimensional image of $C(x_1, y_1)$ is shown in the inset to Figure 4.24 (d). Here, the bright contrast represents areas with correlated polarization, and dark contrast corresponds to a negative value of $C(x_1, y_1)$, which implies the probability to find an antiparallel polarization direction. The autocorrelation function was used for the estimation of the average size of the nanodomains. The average of the autocorrelation function, $C(r)$, is shown in the Figure 4.27 (a). Form these data the value of the correlation length, ξ_{corr}, of about 70 nm was found.

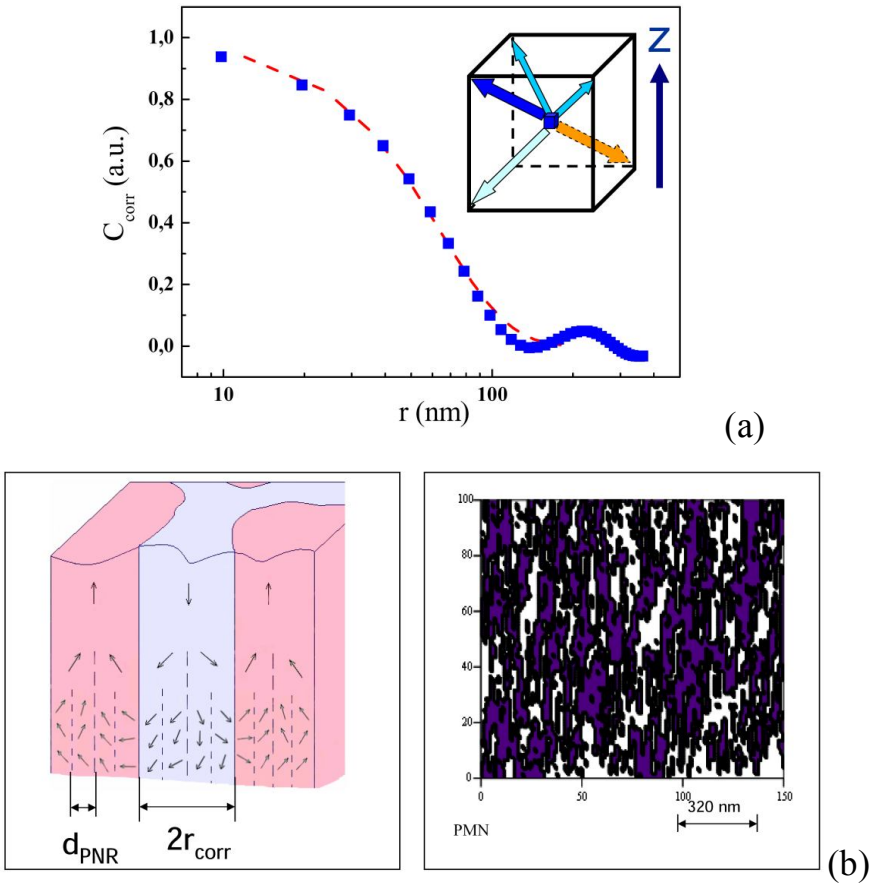

Figure 4.27 Absolute value of averaged autocorrelation function vs radius (a), modelling of PNRs with based on observed surface nanodomains (b).

There exists a contradiction between the characteristic sizes of nanoregions obtained in our experiments and data on neutron scattering. In order to explain this controversy we propose a simple model based on the combinatory approach. Let us believe that the PNRs exist in the volume of the sample. We suppose that on one hand the direction of polarization must differ only weakly in two nearest neighbour PNRs. On the other hand, in PNRs the polarization takes one of the preferred directions determined by the symmetry of an order parameter (one of <111> direction). Then the polarization direction from neighbour to neighbour will change, but only through the nearest directions and so that they are aligned in one direction (see Figure 4.27 (b)).

Let us suppose that, due to the dipolar interaction between the nearest PNRs in the intermediate area, the direction of polarization in the nearest PNR can be still the same or change via the nearest direction (see inset to Figure 4.27(a)). Then to a first approximation the probability p_1 that the projection of polarization along axis z will be the same is 3/4 (for (100)-plane) or 5/8 (for (111)-plane). And we also assume that this condition must be valid for all nearest neighbours. When we take this in account than we will find that this probability will be $p_1 \approx 0.92\text{-}0.94$ (and depends on the number of the neighbours taken on consideration). Generally, it is possible to speak that the probability p_1 should vary with temperature from 0.85 up to 1 in all area of existence of PNR, but in enough broad range of temperatures, when nanoregions are in direct contact with each other (if there is a percolation according to work [47]), the magnitude p_1 must vary near the value 0.94 weakly increasing with decreasing temperature). Now we suppose that all PNRs (see Figure 4.28(b)) which polarization projection along Z is positive will appear as positive (polarization up) domains on the surface, and those with negative projections will appear as down domains. Then the correlation function for nanodomains as function of the distance t (or the function of the number of PNRs) is easily determined as

$$C_{corr}(r) = \prod_{k=1}^{r} P_k \,, \tag{4.5}$$

where P_k is the probability for each next neighbour according to $[P_k \sim 1 - (P_{k-1}(1-P_1) + (1-P_{k-1})P_1)]$. Thus we obtain the fitting curve for Figure 4.27 (a). The results of the computer simulation of the surface nanodomains are shown in Figure 4.27 (b). The average size of PNRs was about 12 nm, and this value is in line with the results of neutron measurements at freezing temperature. Thus according the discussed model the value of correlation length R_{corr} could be compared with the value of $\xi_{corr} \approx 70$ nm obtained by PFM

Thus, in line with the previous reports [44, 45], it is possible to offer the following picture of polarization correlation at the relaxor surface. The true static polar nanoregions have characteristic scale of 10-15 nm. They appear at T^* and their number and/or size is increased gradually with decreasing temperature. Inside PNRs, the polarization is directed along one of the easy polarization axis ([111] for PMN). Besides, there is a correlation between directions

of polarization in separate polar nanoregions, which has characteristic correlation length ξ_{corr} ($\xi_{corr} \approx 70$ nm for PMN). It results from the branching of nanodomains at the surface, which has the same characteristic size and characteristic symmetry determined by the symmetry of polarization in PNR. In our experiments the stable branchy structure were observed in PMN after ZFHaFC regime at room temperature, which is above T_f and T_m and below T^*.

The domain growth kinetics in the tip-generated electric field has been investigated in PMN single crystals using piezoresponse force microscopy. For the used range of pulse magnitudes and durations the domain size could be described in domain motion limit. The written domains exhibit strong retention behaviour. The sidewise domain growth can be well approximated by calculating the lateral field distribution in the charged sphere model under the assumption of the exponential field dependence of the domain wall velocity. The activation field is found to be a function of the external field. The measured growth kinetics reflects the complex nature of the ferroelectric domain formation and stabilization process in the inhomogeneous electric field. Furthermore based on simple approach, we reconcile the correlation length observed by PFM measurements and that determined using neutron of x-ray diffraction techniques, revealing a PNR average size of 10-15 nm.

§ 4.7 Piezoresponse Force Microscopy Imaging and Hysteresis Loops in PMN-PT Single Crystals

In this paragraph, we explore the dynamic aspects of disorder in relaxors and gain an understanding of local phase stability and evolution under an electric field by studying the static domain structures and domain dynamics as a function of composition by PFM and switching spectroscopy PFM (SS-PFM). Using such approach we show that several features can be revealed and confirm our previous findings in case of PZN-PT solid solution by studing another system i.e. PMN-PT. The case of PMN-PT10% is of interest because it is a relaxor with a ferroelectric phase transition but in contrast to PZN-4.5%, this ferroelectric phase appears only below room temperature (T_C~280K).

The dependence of relaxation behavior on voltage pulse amplitude and time was found to follow a universal logarithmic behavior with a nearly constant slope. This behavior is indicative of the progressive population of slow relaxation states, as opposed to a linear relaxation in the presence of a broad relaxation time distribution. The role of relaxation behavior, ferroelectric non-linearity, and the spatial inhomogeneity of the tip field on hysteresis loop behavior is analyzed in detail. The hysteresis loops for ergodic PMN-10%PT are shown to be kinetically limited, while in PMN with larger PT content, true ferroelectric hysteresis loops with low nucleation biases are observed.

Here, we explore the dynamic aspects of disorder in relaxors and gain an understanding of local phase stability and evolution under an electric field by studying the static domain structures and domain dynamics as a function of composition by PFM and switching spectroscopy PFM (SS-PFM).

As a model system, we have chosen several members of the (1-x) $Pb(Mn_{1/3}Nb_{2/3})O_3 - x$ $PbTiO_3$ family, including relaxor PMN-10%PT and ferroelectric PMN-32%PT and PMN-35%PT, the latter having a composition close to the morphotropic phase boundary. PMN-10%PT is a relaxor with a small rhombohedral distortion below T_C=275 K. The dielectric maximum occurs at T_{max} = 300 K (at 1 kHz). PMN-32%PT and PMN-35%PT already exhibit a long-range ferroelectric order at room temperature described by the monoclinic *Pm* phase [53, 54]. In all three samples, T_B and T^* are about 650 K and 500K respectively. The (001) crystal surfaces were mirror-polished using a series of diamond pastes for PFM examination and supplied with counter electrodes (silver paste).

Static Domain PFM Imaging

Topography and domain structure for the three chosen PMN-PT compositions (PMN-10%PT, PMN-32%PT, and PMN-35%PT) are shown in Figure 4.28. The domain structure in PMN-10%PT (Figure 4.28 (a,d)) is formed by well-defined labyrinthine domains of 100-200 nm characteristic size. The domain boundaries are generally smooth and the amplitude contrast is non-uniform on the length scale above the characteristic domain size, possibly due to variations in surface topography. Note once again that the observed domain pattern, highly

reminiscent of the labyrinthine domains in ferromagnetic films [55] is unusual for classical ferroelectrics.

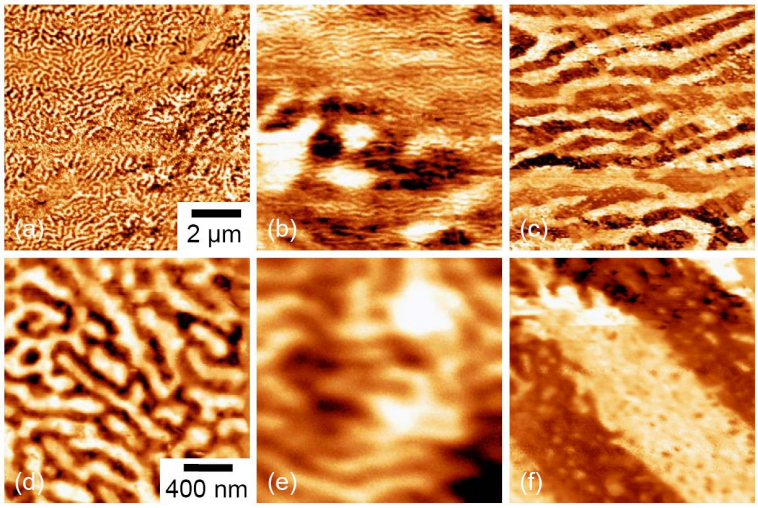

Figure 4.28 Domain structures (mixed VPFM images at two scan sizes) in PMN-xPT as a function of composition for (a,d) 10%PT, (b,e) 32%PT, and (c,f) 35%PT.

This is further reinforced by the fact that at room temperature, PMN-10%PT is well above the *Tc* (≅ 280 K) and, according to the focused x-ray measurements, is in the nominally cubic state in the near-surface regions [56]. The presence of these domains strongly suggests that the symmetry of the surface phase in PMN-10%PT is lower than cubic, *albeit* with very small lattice distortion. While similar domain structures were observed in the ergodic phases of several relaxor systems including also PLZT and PZN-PT [48,57,58] their exact origin is unknown.

In contrast to the labyrinthine structure in PMN-10%PT, where the domain walls can have arbitrary, seemingly uncorrelated directions, PMN-32%PT and PMN-35%PT show banded domain structure (Figure 4.28 (b,d) and (c,f), respectively) as observed in PZN-PT solid solution. The thickness of the banded domains may vary from ~ 100 nm (*i.e.*, the same as for labyrinthine domains in PMN-10%PT) to ~ 1 μm. As already observed in case of PZN-12%PT, a number of small (10-50 nm) domain "islands" of opposite polarity within the macroscopic domains are clearly seen (note that such small islands are practically absent in PMN-10%PT). The domain boundaries are strongly roughened and the PFM amplitude

changes rapidly at the domain wall. Note that the PFM amplitude is much higher within normal domains than within the labyrinthine pattern of PMN-10%PT. This difference can be related to the fact that at room temperature the PMN-32%PT and PMN-35%PT crystals are both in the monoclinic ferroelectric phase [59] while PMN-10%PT is in the macroscopically cubic ergodic relaxor phase. Close inspection of amplitude and phase images illustrates that labyrinthine domains are superimposed over macroscopic domains, *i.e.*, the two can coexist in each point for the PMN-32%PT solid solutions.

To gain insight into the behavior of in-plane polarization components, the three compositions were imaged using lateral PFM. The comparison of vertical and lateral PFM (VPFM and LPFM, respectively) data is shown in Figure 4.29. For all compositions, the LPFM image shows a clearly visible contrast that could be, in principle, interpreted as the presence of an in-plane polarization component. However, in both PMN-32%PT and PMN-35%PT crystals one can observe a clear correspondence between the vertical and lateral domains so that the domain walls in both images coincide. This behavior is consistent with LPFM behavior at 180º-domain walls [60] and thus can be ascribed to a cross-talk with the vertical signal.

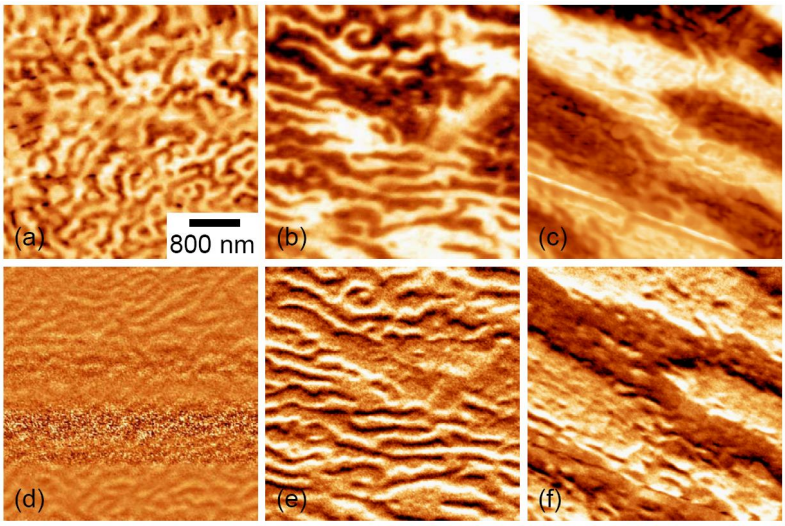

Figure 4.29 Vertical and lateral PFM in PMN-xPT as a function of composition. (a-c) VPFM and (d-f) mixed LPFM images for (a,d) 10%PT, (b,e) 32%PT, and (c,f) 35%PT. VPFM and LPFM data were measured sequentially and have not been corrected for possible tip-drift.

Based on the examination of the images, we conclude that the in-plane component contribution to the LPFM signal is below the detection limit (less than ~20% of vertical signal). Hence, while in the monoclinic *Pm* phase the spontaneous polarization vector may have 24 different directions none of which are perpendicular to the (001) plane (crystal surface) [61] the observed vertical and lateral PFM images are consistent with *purely* out-of-plane polarization orientation for all compositions. PFM data on PMN-10%PT suggests that the close correspondence between VPFM and LPFM exists only in some areas. However, the small size of the observed domains does not allow identifying their orientation and the pure out-of-plane polarization component should be confirmed in future studies.

Relaxation Dynamics

The local relaxation behavior of the PMN-10%PT crystal surface is studied using time-resolved piezoresponse spectroscopy. We utilize the approach based on point-response measurements [62]. Briefly, dc bias pulses of specified magnitude and duration are applied to the conducting AFM tip in contact with the sample, and the resulting vertical electromechanical response is measured as a function of time for a specified duration. An example of single-point measurements on mica, $LiNbO_3$, and PMN-10%PT are shown in Figure 4.30(a).

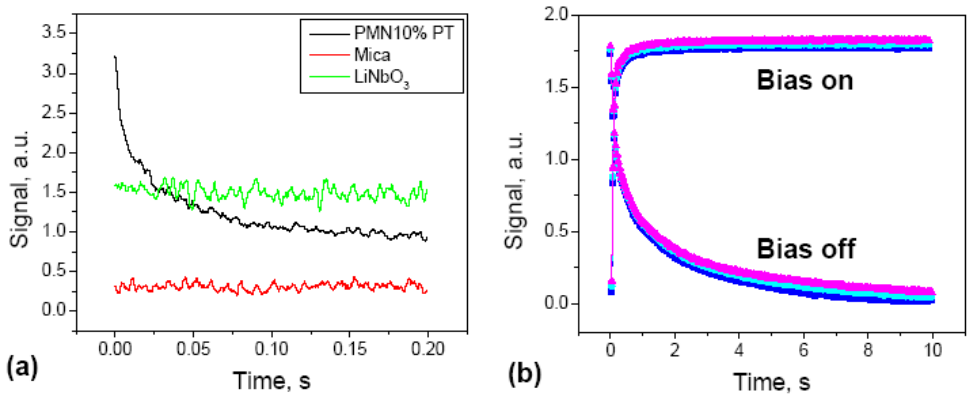

Figure 4.30 (a) Relaxation curves for PMN-10%PT, LiNbO3, and mica. The observed dynamics suggest that the contribution of possible instrumental and atmospheric artifacts (*e.g.*, electrocapillary effect) to relaxation is minimal. (b) Relaxation curves for PMN-10%PT in bias-on (during the

application of 10 V pulse) and bias-off (after bias pulse) states. Several superimposed curves illustrate typical repeatability of experiments.

While the electromechanical response on mica is (as expected) essentially zero, the response on $LiNbO_3$ is generally independent on time. These observations illustrate the absence of instrumental and environmental (*e.g.*, electrocapillary) artifacts that can lead to spurious relaxation behavior after application of a dc bias. In comparison, PMN-10%PT shows clear relaxation of electromechanical response consistent with a rapid decay of the bias-induced polarization state. The response for bias-on and bias-off states for PMN-10%PT is shown in Figure 4.30 (b), and illustrates much faster response saturation for the in-field state. The response after poling can be well approximated with a Kolrausch-Williams-Watts (KWW) stretched exponential dependence

$$R(t) = R_0 - R1\exp\left(-\left(\frac{t}{\tau_{KWW}}\right)^{\beta}\right), \tag{4.6}$$

with β <0.5, or (over shorter time intervals) by a logarithmic time dependence,

$$R(t) = R_0 - R_1 \ln t \tag{4.7}$$

To determine the dependence of relaxation behavior on voltage pulse parameters, the measurements were performed as a function of pulse magnitude and length. The results of these bias experiments are shown in Figure 4.31 (a).

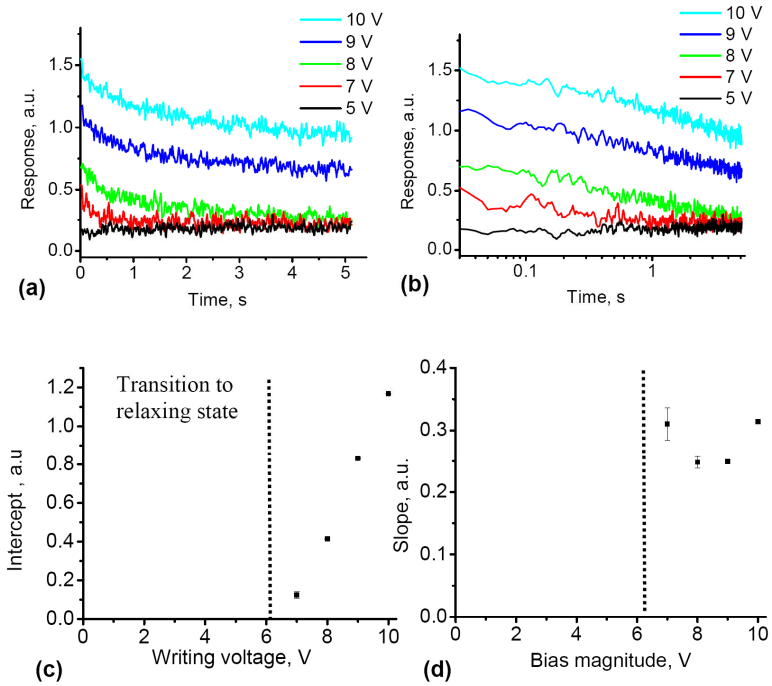

Figure 4.31 Relaxation behavior in PMN-10%PT after switching off the 30 ms pulses of different magnitude in (a) linear and (b) logarithmic coordinates. Bias dependence of (c) intercept and (d) slope of the relaxation curve in logarithmic coordinates. Vertical dashed line corresponds to the onset of the state with induced polarization.

For small bias pulses (below 5 V), no relaxation is observed and the electromechanical response is time-independent. For larger biases, the formation and decay of the bias-induced polar state is clearly observed. Within the noise level of the experiment, the relaxation kinetics follows a logarithmic law (Figure 4.31 (b)) (which is also consistent with a stretched exponential if the time interval is too short). The data was fitted using

$$\Delta PR(t) = a_1(V) - b_1(V)\log t \tag{4.9}$$

and the bias dependence of the intercept, $a_1(V)$, and slope, $b_1(V)$, are shown in Figure 4.31 (c,d) ($\Delta PR(t)$ represents the piezoresponse signal with subtracted initial background). Note that the slopes are essentially bias independent while the intercept grows linearly with voltage. The lack of relaxation below 5 V is consistent with either the absence, or a short relaxation

time (within the limits of experimental error) of an induced polar state as expected for such composition.

The relaxation behavior as a function of pulse length, τ, is shown in Figure 4.33. The relaxation behavior is again well-approximated by the logarithmic law,

$$\Delta PR(t) = a_2(\tau) - b_2(\tau)\log t. \tag{4.10}$$

The intercept, $a_2(\tau)$, is initially linear with log(t) and then saturates at several seconds. The slope, $b_2(\tau)$, slightly increases with τ but in general varies by less than a factor of two even while τ changes by three orders of magnitude.

In the first approximation, the relaxation behavior as a function of pulse parameters can be represented by the phenomenological dependence

$$\begin{aligned} &\Delta PR(t) = a(V,\tau) - b(V,\tau)\log t \quad for \quad t < t_{crit} \\ &\Delta PR(t) = 0 \quad for \quad t > t_{crit}, \end{aligned} \tag{4.11}$$

where $\log(t_{crit}) = a(V,\tau)/b(V,\tau)$ is the generalized lifetime of the bias induced polar state. Given that $b_1(V,\tau) \approx b$, does not vary significantly with V and τ, the relaxation kinetics are determined primarily by the amount of switched polarization, *i.e.*, by an offset $a(V,\tau)$. The latter is determined by the pulse bias and duration (before saturation) as

$$a(V,\tau) = (\alpha + \beta\log\tau) f(V), \tag{4.12}$$

where $f(V)=0$ for $V<V_{crit}$ and $f(V)=kV$ for $V>V_{crit}$, and β = const. Note that numerically $b \approx \beta$, suggesting the universality of bias-on (writing) and bias-off (reading) relaxation behavior.

Piezoresponse Force Spectroscopy on PMN-PT Single Crystals

The goal of spatially-resolved spectroscopy of relaxor materials is obtaining insight into the spatial distribution of relaxation behavior and its relationship with existing domain structures, surface topography, and structural and morphological defects. The time-resolved

studies reported above provide insight into local relaxation behavior at a single point. However, the detailed studies of relaxation behavior over a dense spatial grid required to map spatial variability of relaxation behavior involve extremely large times, rendering these measurements challenging due to limitations of the microscope platform (thermal drift, data acquisition times) [56].

At the same time, single point spectroscopy measurements suggest universality between voltage and time dynamics (see below). The fact that responses are linear in bias and logarithmic in time suggests that voltage spectroscopy allows a more rapid and efficient approach to probe local relaxation behavior. In this section, we present the results of voltage spectroscopy on relaxor surfaces.

Voltage versus Time Spectroscopy

To establish the relationship between voltage- and time spectroscopy, we assume that the bias- and voltage dynamics follows Eqs. (4.11) and (4.12) as $\Delta PR\left(t = a\left(V,\tau - b\log t\right)\right)$, where $a\left(V,\tau\right) = \left(\alpha + \beta\log t\right)kV$ for $V > V_{crit}$ (bias-induced state) and 0 for $V < V_{crit}$ (no bias induced state or short-lived state). In other words, we assume that at $V > V_{crit}$ relaxation depends only on the amount of induced polarization with universal relaxation rate, *b*, independent of writing process conditions.

In a PFM spectroscopy experiment, a series of rectangular pulses of length τ_p spaced at τ_o (typically, $\tau_p \sim \tau_o$ and is of the order of 1-10 ms) is applied to the tip. The envelope of the waveform is a triangular wave with amplitude $V_{\max}$ (bias window) (Figure 4.32). Note that in spatially resolved experiments the loops are acquired on a dense mesh, *i.e.*, the pixel spacing is smaller than the characteristic size of the electric field produced by the probe. Hence, we are in the "quasistationary" state where we have created a "poled" state everywhere. In other words, we assume that each pixel prior to measurement cycle has experienced multiple other cycles and is in the stationary response regime.

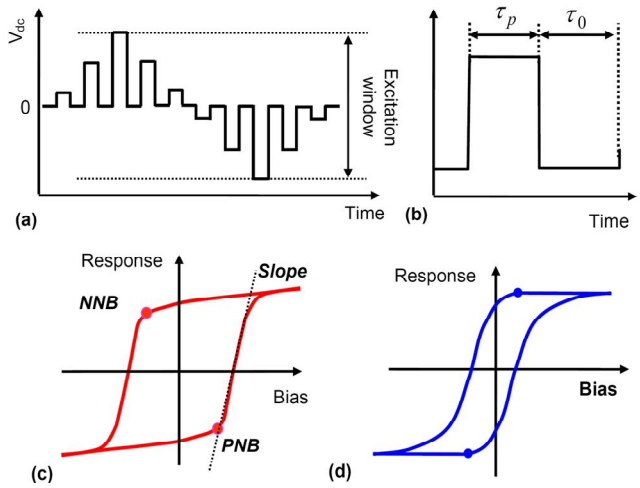

Figure 4.32 (a) Pulse sequence during the acquisition of a PFM hysteresis loop and (b) sequence of measurements at a single pulse. Schematics of a hysteresis loop for (c) ferroelectric and (d) ergodic relaxor state. In a classical ferroelectric material, the hysteresis loop shape is dominated by the *spatial dispersion* of the signal. The nucleation biases define the conditions for nucleation of stable domain of opposite polarity, and the slope of the loop after nucleation is determined by bias and time dependence of the domain size. In comparison, in relaxor ferroelectric the hysteresis loop is dominated by *time dispersion* of the signal, and nucleation bias corresponds to bias at which the lifetime of bias-induced state becomes larger than measurement time. The slope after nucleation is determined by bias-dependence of the life time. Finally, for PNB > NNB, the bias-induced state is stable, whereas for PNB < NNB relaxation is unstable.

The behavior of the hysteresis loops can be reconstructed from time dynamics as follows. If the life time of bias-induced state is less than the point measurement time, τ_p, or the tip bias V is less than V_{crit}, the response is constant. For larger voltages, a bias-induced state is created. From $a(V,\tau)=(\alpha+\beta\log\tau)kV$ we get $da/dt=\beta kV/t$. Hence, for a linear ramp $V=ct$, we get $da/dt=\beta kc$ for $V > V_{crit}$ and hence the hysteresis loop is linear in voltage above a critical voltage with a slope proportional to the slope in Eq. (4.12), *i.e.*, the bias-dependence of the decay constant in the tip-induced state.

The total amount of switched polarization is $a(V,\tau)=(\alpha+\beta\log\tau_0)kV_{\max}$. On decreasing the bias, the polarization relaxes approximately logarithmically as

$\Delta PR(t) = a_{\max} - b\log(V/c)$. The relaxation will be observable if the state induced by the maximal tip bias is stable (changes by less than ~3%) on the time scale of the experiment. This difference between a linear increase and log decay results in the hysteresis loop having a characteristically "rhomboid" shape. The nucleation biases (inflection points) are determined by the lifetime of the tip bias-induced state for both polarities. Note that the built–in fields affects both positive and negative nucleation biases (PNB and NNB) differently, as discussed below. The electrostatic fields will shift the hysteresis loop, similar to imprint in conventional ferroelectrics. Hence, PNB+NNB allow mapping built-in fields. At the same time, PNB-NNB determines the stability of tip-induced state on the time of experiment, and will further be referred as the stability gap.

The key observation in this section is that hysteresis loop formation in relaxor ferroelectrics is kinetically limited and local and is only weakly sensitive to the spatial dispersion effect. Hence, it is controlled by local properties (*e.g.*, defined as the local relaxation time spectrum). In comparison, in classical ferroelectrics, the hysteresis loop formation is defined by non-local domain wall dynamics, *i.e.*, purely by the spatial dispersion of the polarization dynamics.

Switching Spectroscopy PFM (SS-PFM)

The switching spectroscopy PFM (SS-PFM) maps and representative hysteresis loops from selected locations for PMN-10%PT, 32%PT, and 35%PT are shown in Figure 4.33. In all cases, 2D SS-PFM maps exhibit clearly visible spatially resolved features, suggesting that the spatial variability of ferroelectric behavior is larger compared to the pixel spacing (dense regime).

The SS-PFM maps for PMN-10%PT were recorded using a 1 V, 640 kHz ac-bias and 39.06 ms writing pulses, τ_p , followed by a 39.06 ms OFF state, τ_0 , during which time the response was recorded for 15 ms following a 15 ms delay. For 32%PT and 35%PT, the writing pulse was 110 ms, the OFF state was 47 ms, the response was recorded for 15 ms following a 15 ms delay, and the data was recorded at 5 V ac, 1.47 MHz and 1 V ac, 680 kHz, respectively.

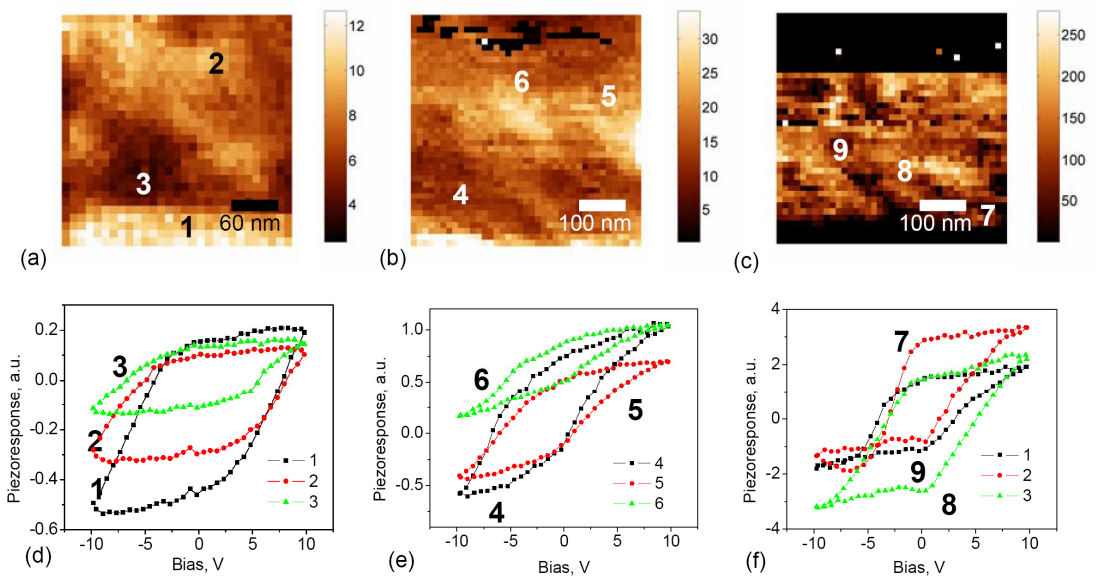

Figure 4.33 Hysteresis loops in PMN-*x*PT as a function of composition. Shown are (a,b,c) work of switching maps (in the [-10, 10V] bias window) and (d,e,f) selected hysteresis loops for (a,d) 10%PT, (b,e) 32%PT and (c,f) 35%PT.

In general, in order to measure loops on 32%PT and 35%PT, a longer writing time, τ_p , was required compared to 10%PT. In PMN-10%PT, the loop shape was qualitatively the same with longer writing times and the nucleation biases remained larger than for the other compositions. The results were not very sensitive to experimental conditions (such as tips and *ac* voltage amplitudes and measurement frequency (away from resonances)).

The hysteresis loops for PMN-10%PT are shown in Figure 4.33 (d). The loops have a characteristic "diamond" shape with relatively constant response for small biases and linear increase of the response for large bias. This behavior agrees with that predicted from the observed relaxation behavior. The shape of the loops is relatively weakly position dependent, and the observed nucleation bias corresponds to the formation of a slowly (on the time scale of the measurement) relaxing polar state, as will be analyzed below.

In PMN-35%PT (Figure 4.33 (f)), the hysteresis loops have well-defined "ferroelectric" shape with clear nucleation biases and abrupt onset of nucleation. The corresponding nucleation bias is typically small, on the order of 0.5 – 2 V, and weakly position dependent. The hysteresis loops are often saturated (*i.e.*, for high enough voltages

forward and reverse branches coincide). In several locations, the formation of characteristic "noses" are observed, consistent with the presence of movable domain wall in the vicinity of the probe [63,64]. The overall behavior agrees with that expected for highly disordered ferroelectrics where a high density of random field and random bond defects allows for lower nucleation biases ~1 V (as compared to, *e.g.*, 30 V for $LiNbO_3$ single crystals and ~5-10 V for lead zirconate titanate ferroelectric thin films) and due to proximity to T_C.

Finally, the hysteresis loops for 32%PT (Figure 4.33 (e)) illustrate an intermediate shape between the PMN-10%PT and PMN-35%PT cases. After nucleation, the loop shape has profound curvature, possibly due to the stronger ferroelectric non-linearity induced by the ferroelectric phase. Similarly, the switchable component of the bias-induced polar state relaxes much faster. We ascribe this behavior to the simultaneous presence of a switchable polarization component and a non-switchable frozen polarization.

Stability Gap Mapping

The SS-PFM maps allow the stability of bias induced states (the "stability gap") to be mapped as the lifetime exceeding the experimental time for the applied 10 V bias. Shown in Figure 4.34 (a-d) are mixed PFM, switchable polarization, stability gap, and built-in field maps for PMN-10%PT. The image shows large scale features of ~100 nm size, indicative of the presence of mesoscopic range disorder in the material. Note that all three maps are generally uncorrelated, indicative of the veracity of the measurements. The corresponding histograms of PNB (positive nucleation bias) and NNB (negative nucleation bias) and PNB-NNB (their difference) are shown in Figure 4.34 (e,f). Note that a significant fraction of the sample surface has a negative PNB-NNB. This shows that the bias-induced polar state is unstable as expected for the ergodic relaxor phase.

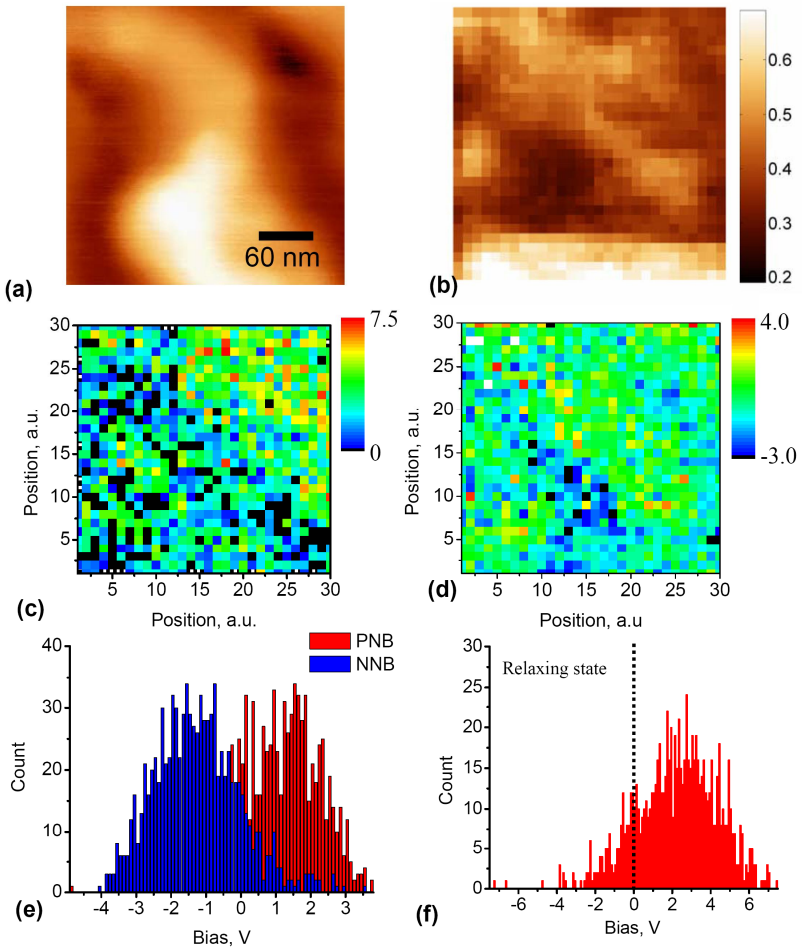

Figure 4.34 Switching spectroscopy mapping of PMN-10%PT. (a) Mixed PFM signal, (b) switchable polarization, (c) stability map [PNB-NNB] and (d) built-in field [PNB+NNB] map. Histograms of (e) PNB and NNB and (f) PNB-NNB.

In comparison, mixed PFM and SS-PFM maps for PMN-32%PT are shown in Figure 4.35. In this case, stability gap, switchable polarization, and built-in field maps show clear contrast correlated to the remnant ferroelectric domains. Note that a larger switchable polarization corresponds to a smaller stability gap. This is anticipated, since the driving force for switching is proportional to polarization, *P*. Also, there are no regions with zero stability gap, *i.e*., the bias-induced states are stable.

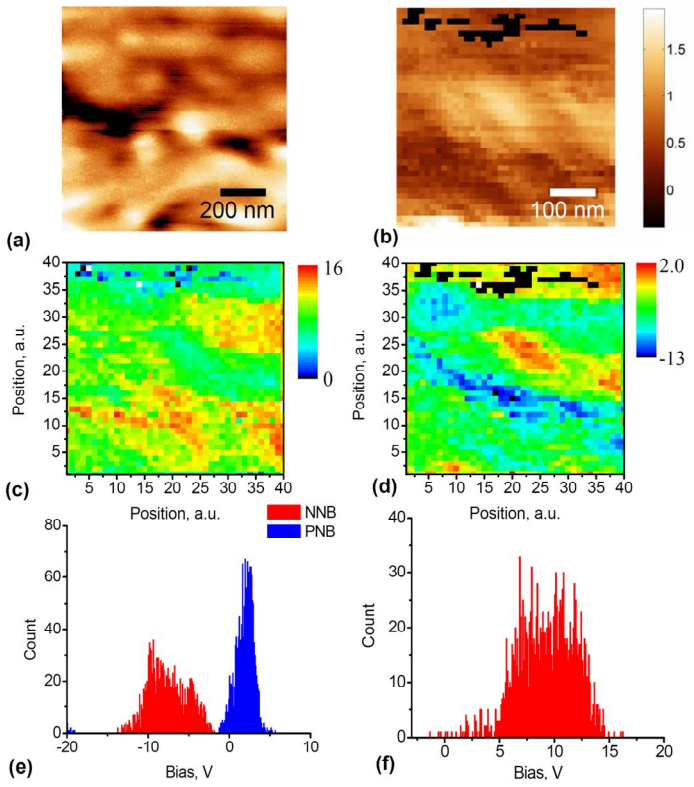

Figure 4.35 Switching spectroscopy mapping of PMN-32%PT. (a) Mixed PFM signal, (b) switchable polarization, (c) stability map [PNB-NNB] and (d) built-in field [PNB+NNB] map. Histograms of (e) PNB and NNB and (f) PNB-NNB. Panel (b) was measured from the center of (a). Panels (c) and (d) have the same scale as (b).

This behavior is further illustrated in the histograms in Figure 4.35 (e,f). Here, the PNB and NNB are well separated, and PNB-NNB is always positive in contrast to PMN-10%PT. This is because the PMN-32%PT is in a ferroelectric state and the poled state induced by large enough bias field is stable. A field of opposite polarity is required to switch the polarization.

§ 4.8 Summary

In summary, as-grown crystals of PZN-PT, PMN and PMN-PT show a complicated pattern of antiparallel domains (fingerprint, labyrinth-type or other patterns) as reflected in the

piezoresponse mode measurements. The domain structure depends on the concentration of the ferroelectric component and exhibit specific temperature and electric field dependencies. The domain structure is influenced by the annealing and can be restored by te application of electric field at low temperatures.

3D domain imaging was found to be possible by cross-sectioning (repeated polishing) of ferroelectric material (similar to AFM microtomy). Domain branching is observed and explained by the appearance of inverse domains to compensate the depolarizing field (Marchenko's model). Temperature dependence contains both reversible and irreversible components (reflecting surface phase transition) and persists well above bulk phase transition.

The domain growth kinetics in the tip-generated electric field has been investigated in PMN single crystals using PFM. For the used range of pulse magnitude and duration the domain size could be described in domain motion limit. The written domains exhibit strong retention behaviour. The sidewise domain growth can be well approximated by calculating the lateral field distribution in the charged sphere model under the assumption of the exponential field dependence of the domain wall velocity. The activation field is found to be a function of the external field. The measured growth kinetics reflect the complicated nature of the ferroelectric domain formation and stabilization process in the inhomogeneous electric field.

Domain structures and time- and bias- controlled local polarization dynamics in the PMN–xPT family of relaxor ferroelectrics are studied using piezoresponse force microscopy and spectroscopy. The PFM imaging indicates the presence of labyrinthine domain structures even in ergodic PMN-10%PT compositions, indicative of a non-cubic symmetry at least in the surface layer. In PMN-35%PT, ferroelectric domains with high wall roughness are observed, whereas PMN-32%PT demonstrates the coexistence of ferroelectric and labyrinthine domains. The comparison of vertical and lateral PFM suggests that the observed in-plane contrast can be ascribed purely to cross-talk between vertical and lateral signals, and no evidence for in-plane domains is obtained.

The dependence of relaxation behavior on the pulse amplitude and time was found to follow a universal logarithmic behavior with a nearly constant slope. This behavior is indicative of the progressive population of high energy slow relaxation states, as opposed to the linear relaxation in the presence of a broad relaxation time spectrum. The contribution of

ferroelectric non-linearity and spatial dispersion of the tip field to the relaxation is analyzed in detail, and the effects of spatial dispersion are shown to be relatively small. Hence, PFM-based relaxation experiments provide information similar to that in a uniform field.

The relationship between relaxation and hysteresis loop formation is analyzed in detail. It is shown that local hysteresis loops in relaxors are fundamentally different form those in ferroelectrics. In relaxors (PMN-10%PT), the local loops are kinetically limited, while in "normal" ferroelectrics (PMN-32%PT and PMN-35%PT) the loops seem to be dominated by the spatial dispersion of the polarization only. Finally, switching spectroscopy mapping of relaxor and ferroelectric PMN-PT compositions is performed, and the mapping of built-in fields and the stability gap is demonstrated.

References

[1] Kuwata J., Uchino K., and Nomura S., "Dielectric and piezoelectric properties of 0.91Pb(Zn1/3Nb2/3)O3-0.09PbTiO3 single crystals" *Jpn. J. Appl. Phys*., Part 1 **21**, 1298 (1982).

[2] Park S. E. and Shrout T. R., "Characteristics of relaxor-based piezoelectric single crystals for ultrasonic transducers" *IEEE Trans. Ultrason. Ferroelectr. Freq. Control* **44**, 1140 (1997).

[3] Ye Z.-G., "Crystal chemistry and domain structure of relaxor piezocrystals" *Curr. Opin. Solid State Mater. Sci.* **6**(1), 35 (2002).

[4] Fujishiro K., Vlokh, R., Uesu, Y., Yamada, Y., Kiat, M., Dkhil, B., Yamashita, Y. "Optical observation of heterophase and domain structures in relaxor ferroelectrics $Pb(Zn_{1/3}Nb_{2/3})O_3$-9%$PbTiO_3$". *Jpn. J. Appl. Phys.* Part 1 **37**, 5246 (1998).

[5] La Orauttapong, D. Noheda, B. Ye, G., Gehring, P.M., Toulouse, J., Cox, D.E., Shirane, G. "Phase diagram of the relaxor ferroelectric $(1 - x)Pb(Zn_{1/3}Nb_{2/3})O_3$- $xPbTiO_3$" *Phys. Rev. B* **65**, 144101 (2002).

[6] Ye Z.-G., Dong M., Zhang L. "Domain structure and phase transitions in relaxor-based piezo-/ferroelectric $(1-x)$ $Pb(Zn_{1/3}Nb_{2/3})O_3$-$xPbTiO_3$ single crystals" *Ferroelectrics* **229**, 223 (1999).

[7] Noheda B., "Structure and high-piezoelectricity in lead oxide solid solutions" *Curr. Opin. Solid* State Mater. Sci 6, 27 (2002).

[8] Viehland D., "Symmetry-adaptive ferroelectric mesostates in oriented Pb(BI1/3BII2/3)O3–PbTiO3 crystals" *J. Appl. Phys.* **88**, 4794 (2000).

[9] Theissmann R., Schmitt L.A., Kling J., Schierholz R., Schonau K.A., Fuess H., Knapp M., Kungl H., and Hoffmann M.J., "Nanodomains in morphotropic lead zirconate titanate ceramics: On the origin of the strong piezoelectric effect" *J. Appl. Phys.* **102**, 024111 (2007).

[10] Bhattacharyya S., Jinschek J.R., Cao H., Wang Y.U., Li J.F., and Viehland D., „Direct high-resolution transmission electron microscopy observation of tetragonal nanotwins within the monoclinic M_C phase of $Pb(Mg_{1/3}Nb_{2/3})O_3$-0.35$PbTiO_3$ crystals"*Appl. Phys. Lett.* 92, 142904 (2008).

[11] Park S.-E. and Shrout T. R.," Ultrahigh strain and piezoelectric behavior in relaxor based ferroelectric single crystals" *J. Appl. Phys.* **82**, 1804 (1997).

[12] Ogawa T., Yamauchi Y., Numamoto Y., Matsushita M., and Tachi Y., "Giant electromechanical coupling factor of k_{31} mode and piezoelectric d_{31} constant in $Pb[(Zn_{1/3}Nb_{2/3})_{0.91}Ti_{0.09}]O_3$ piezoelectric single crystal" *Jpn. J. Appl. Phys.* **41**, L55 (2002).

[13] Paik D.-S., Park S.-E., Nada S., Liu S.-F., and Shrout T. R., "*E*-field induced phase transition in (001)-oriented rhombohedral 0.92$Pb(Zn_{1/3}Nb_{2/3})O_3$–0.08$PbTiO_3$ crystals" *J. Appl. Phys.* **85**, 1080 (1999).

[14] Durbin M. K., Hicks J. C., Park D.-E., and Shrout T. R., "X-ray diffraction and phenomenological studies of the engineered monoclinic crystal domains in single crystal relaxor ferroelectrics" *J. Appl. Phys.* **87**, 8159 (2000).

[15] Xu G., Luo H., Hu H., and Yin Z., "Third ferroelectric phase in PMNT single crystals near the morphotropic phase boundary composition" *Phys. Rev. B* **64**, 020102 (2001).

[16] Noheda B., Cox D. E., Shirane G., Park S.-E., Cross L. E., and Zhong Z., "Polarization rotation via a monoclinic phase in the piezoelectric 92% $PbZn_{1/3}Nb_{2/3}O_3$-8% $PbTiO_3$" *Phys. Rev. Lett.* **86**, 3891 (2001).

[17] Yin J. and Cao W., "Domain configurations in domain engineered 0.955$Pb(Zn_{1/3}Nb_{2/3})O_3$–0.045$PbTiO_3$ single crystals" *J. Appl. Phys.* **87**, 7438 (2000).

[18] Lee J.-K., Yi J. Y., Hong K.-S., Park S.-E., and Millan J., "Domain configuration and crystal structure of $Pb(Zn_{1/3}Nb_{2/3})O_3$–5%$PbTiO_3$ crystals as a function of the electric-field direction" *J. Appl. Phys.* **91**, 4474 (2002).

[19] Abplanalp M., Barosova D., Bridenbaugh P., Erhart J., Fousek J., Guenter P., Nosek J., and Sulc M., "Scanning force microscopy of domain structures in $Pb(Zn_{1/3}Nb_{2/3})O_3$-8%$PbTiO_3$ and $Pb(Mg_{1/3}Nb_{2/3})O_3$-29% $PbTiO_3$" *J. Appl. Phys.* **91**, 3797 (2002).

[20] Yu H. and Randall C. A., "Dendritic domain configurations in $Pb(Zn_{1/3}Nb_{2/3})O_3$–$PbTiO_3$ single crystals" *J. Appl. Phys.* **86**, 5733 (1999).

[21] Xu G., Zhong Z., Bing Y., Ye Z.-G., Stock C., Shirane G., "Ground state of the relaxor ferroelectric $Pb(Zn_{1/3}Nb_{2/3})O_3$" *Phys Rev B* **67**, 104102 (2003).

[22] Forrester J.S., Piltz R. O., Kisi E. H. and McIntyre G. J., "Temperature-induced phase transitions in the giant-piezoelectric-effect material PZN-4.5%PT" *J. Phys.: Condens. Matter* **13**, L825 (2001).

[23] Iwata M, Araki T, Maeda M, Suzuki I, Ohwa H, Yasuda N, Orihara H and Ishibashi Y, "Domain observation in $Pb(Zn_{1/3}Nb_{2/3})O_3$–$PbTiO_3$ mixed crystals", Jpn. J. Appl. Phys. 41, 7003 (2002).

[24] Dkhil B., Gemeiner P., Al-Barakaty A., Bellaiche L., Dul'kin E., Mojaev E., and Roth M., "Intermediate temperature scale T* in lead-based relaxor systems" *Phys. Rev. B* **80**, 064103 (2009).

[25] Dkhil B., Kiat J.M., Calvarin G., Baldinozzi G., Vakhrushev S.B., Suard E., "Local and long range polar order in the relaxor-ferroelectric compounds $PbMg_{1/3}Nb_{2/3}O_3$ and $PbMg_{0.3}Nb_{0.6}Ti_{0.1}O_3$" *Phys. Rev. B* **65**, 024104 (2002).

[26] Vakhrushev S.B., Ivanov A., Kulda J., "Diffuse neutron scattering in relaxor ferroelectric $PbMg_{1/3}Nb_{2/3}O_3$ " *Phys. Chem. Chem. Phys*. **7**, 2340 (2005).

[27] Roth M., Mojaev E., Dul'kin E., Gemeiner P., Dkhil B., "Phase transition at a nanometer scale detected by acoustic emission within the cubic phase $Pb(Zn_{1/3}Nb_{2/3})O_3$-$xPbTiO_3$ relaxor ferroelectrics" *Phys. Rev. Lett.* **98**, 265701 (2007).

[28] Kittel C., "Theory of the structure of ferromagnetic domains in films and small particles" *Phys. Rev.* **70**, 965 (1946).

[29] Mitsui T. and Furuichi J., "Domain structure of rochelle salt and KH_2PO_4" *Phys. Rev*. **90**, 193 (1953).

[30] Roytburd A. L., "Equilibrium structure of epitaxial layers" *Phys. Stat. Sol. A* **37**, 329 (1976).

[31] Ozaki T., Miyoshi N., Aoyagi S. "Ferroelectric domain branching in KDP", *Ferroelectrics*, **269**, 183 (2002)

[32] Kaczer J., "On the domain structure of uniaxial ferromagnets" *Sov. Phys. JETP* **19**, 1204 (1964) and references therein.

[33] Strukov B.A., Levanyuk A.P., Ferroelectric phenomena in crystals, Chap. 10 (Springer, Berlin, 1998).

[34] Ozaki T., Senju T. and Nakamura E., "Fractal aspects of the ferroelectric domain structures in KH2PO4 crystal" *J. Phys. Soc. Jpn.*, **62**, 3027 (1993).

[35] Ozaki T., Kitamura T., Ohgami J. and Nakamura E., "Self-similarity of the ferroelectric domain structures optically observed in electroded KDP crystals" *Ferroelectrics*, **157**, 87 (1994).

[36] Ozaki T., "Ferroelectric domain structure characterized by prefractals of the pentad cantor sets in KH2PO4" *Ferroelectrics*, **172**, 65 (1995).

[37] Marchenko V.I. "On ferroelectric domain structure" *Zh. Eksp. Teor. Fiz*. **77**, 2419 (1979).

[38] Burns G. and Dacol F.H., "Crystalline ferroelectrics with glassy polarization behavior" *Phys. Rev. B* **28**, 2527 (1983).

[39] Dmowski W., Vakhrushev S. B., Jeong I.-K., Hehlen M. P., Trouw F., and Egami T., "Local lattice dynamics and the origin of the relaxor ferroelectric behavior" *Phys. Rev. Lett.* **100**, 137602 (2008).

[40] Naberezhnov A., Vakhrushev S., Doner B., Strauch D., and Moudden H., "Inelastic neutron scattering study of the relaxor ferroelectric $PbMg_{1/3}Nb_{2/3}O_3$ at high temperatures", *Eur. Phys. Jour B* **11**, 13 (1999).

[41] Vakhrushev S.B., Kvyatkovksy B.E., Naberezhnov A.A., Okuneva N.M., and Toperverg B., "Glassy phenomena in disordered perovskite-like crystals" *Ferroelectrics* 90, 173 (1989).

[42] Hirota K., Ye Z.-G., Wakimoto S., Gehring P.M., and Shirane G.," Neutron diffuse scattering from polar nanoregions in the relaxor $Pb(Mg_{1/3}Nb_{2/3})O_3$ " *Phys. Rev. B* **65**, 104105 (2002).

[43] Dkhil B., Kiat J.M., Calvarin G., Baldinozzi G., Vakhrushev S.B., and Suard E., "Local and long range polar order in the relaxor-ferroelectric compounds $PbMg_{1/3}Nb_{2/3}O_3$ and $PbMg_{0.3}Nb_{0.6}Ti_{0.1}O_3$" *Phys. Rev. B* **65**, 024104 (2001).

[44] You H. and Zhang Q.M., "Diffuse X-Ray Scattering Study of Lead Magnesium Niobate Single Crystals" *Phys. Rev. Lett.* **79**, 3950 (1997).

[45] La-Orauttapong D., Toulouse J., Robertson J.L., and Ye Z.-G., "Diffuse neutron scattering study of a disordered complex perovskite $Pb(Zn_{1/3}Nb_{2/3})O_3$ crystal" *Phys. Rev. B* **64**, 212101 (2001).

[46] Xu G., Shirane G., Coplay G.R.D. and Gehring P.M., "Neutron elastic diffuse scattering study of $Pb(Mg1/3Nb2/3)O_3$" *Phys. Rev. B* **69**, 064112 (2004).

[47] Jeong I.-K., Darling T. W., Lee J. K.," Direct Observation of the Formation of Polar Nanoregions in Pb(Mg1/3Nb2/3)O3 Using Neutron Pair Distribution Function Analysis" *Phys. Rev. Lett.* **94**, 147602 (2005).

[48] Shvartsman V. V., Kholkin A. L., Orlova A., Kiselev D., Bogomolov A. A., and Sternberg, A. "Polar nanodomains and local ferroelectric phenomena in relaxor lead lanthanum zirconate titanate ceramics" *Appl. Phys. Lett.* **86**, 202907 (2005).

[49] Shvartsman V.V., Kholkin A.L.. "Domain structure of 0.8Pb(Mg1/3Nb2/3)O3-0.2PbTiO3 studied by piezoresponse force microscopy" *Phys. Rev. B* **69**: 014102, (2004).

[50] *Nanoscale Characterization of Ferroelectric Materials: Scanning ProbeMicroscopy Approac*h, edited by M. Alexe and A. Gruverman (Springer, Berlin, 2004).

[51] Miller R.C., Weinreich G "Mechanism for the Sidewise Motion of 180° Domain Walls in Barium Titanate" *Phys. Rev.* **117**, 1460 (1960).

[52] Mele E. J., "Screening of a point charge by an anisotropic medium: Anamorphoses in the method of images" *Am. J. Phys.* **6**9, 557 (2001).

[53] Singh A. K., Pandey D., and Zaharko O., "Powder neutron diffraction study of phase transitions in and a phase diagram of (1−x)[$Pb(Mg_{1/3}Nb_{2/3})O_3$]-x$PbTiO_3$" *Phys. Rev. B*. **74,** 024101 (2006).

[54] Zekria D., Shuvaeva V. A., and Glazer A. M., "Birefringence imaging measurements on the phase diagram of $Pb(Mg_{1/3}Nb_{2/3})O_3$–$PbTiO_3$ " *J. Phys.: Condens. Matter*. **17**, 1593 (2005).

[55] O'Handley R. C., *Modern Magnetic Materials: Principles and Applications,* Wiley-Interscience (2000).

[56] Kalinin S. V., Rodriguez B. J., Budai J. D., Jesse S., Morozovska A. N., Bokov A. A., and Ye Z.-G., "Spatially resolved mapping of local polarization dynamics in an ergodic phase of ferroelectric relaxor" *Appl. Phys. Lett* **95**, 142902 (2009).

[57] Bdikin I.K., Shvartsman V.V., and Kholkin A.L., "Nanoscale domains and local piezoelectric hysteresis in $Pb.Zn_{1/3}Nb_{2/3}O_3$-4.5%$PbTiO_3$ single crystals" *Appl. Phys. Lett.* **83**, 4232 (2003).

[58] Kiselev D. A., Bdikin I. K., Selezneva E. K., Bormanis K, Sternberg A., and Kholkin A. L., "Grain size effect and local disorder in polycrystalline relaxors via scanning probe microscopy" *J. Phys. D: Appl. Phys*. **40,** 7109 (2007).

[59] Noheda B., Cox D. E., Shirane G., Gao J., and Ye Z.-G., "Phase diagram of the ferroelectric relaxor (1-x)$PbMg_{1/3}Nb_{2/3}O_3$-x$PbTiO_3$" *Phys. Rev. B* **66**, 054104 (2002); Ye Z.-G., Noheda B., Dong M., Cox D., and Shirane G., "Monoclinic phase in the relaxor-based piezoelectric/ferroelectric $Pb(Mg_{1/3}Nb_{2/3})O_3$-$PbTiO_3$ system" *ibid*. **64**, 184114 (2001).

[60] Abplanalp M., PhD Thesis, ETHZ, Zurich, 2001.

[61] Bokov A. A. and Ye Z. G., "Domain structure in the monoclinic *Pm* phase of $Pb(Mg_{1/3}Nb_{2/3})O_3$–$PbTiO_3$ single crystals" *J. Appl. Phys*. **95**, 6347 (2004).

[62] Rodriguez B.J., Jesse S., Kim J., Ducharme S., and Kalinin S. V., "Local probing of relaxation time distributions in ferroelectric polymer nanomesas: Time-resolved piezoresponse force spectroscopy and spectroscopic imaging" *Appl. Phys. Lett.* **92**, 232903 (2008).

[63] Tagantsev A.K., Muralt P., and Fousek J., "Shape of piezoelectric hysteresis loop for non-ferroelastic switching," *Mat. Res. Soc. Symp. Proc.* **784**, 517 (2004).

[64] LeRhun G., Vrejoiu I., Pintilie L., Hesse D., Alexe M., and Gösele U., "Increased ferroelastic domain mobility in ferroelectric thin films and its use in nano-patterned capacitors" *Nanotechnology,* **17**, 3154 (2006).

Chapter 5

General Conclusions

and

Future Work

§ 5.1 General Conclusion

In this thesis, the first systematic measurements of the nanoscale properties of several families of ferroelectric relaxors have been undertaken. The domain configurations and various polarization-related nanoscale properties were studied via PFM technique for two major relaxor systems: (i) PLZT x/65/35 ceramics and (ii) PZN-xPT, pure PMN and PMN-xPT single crystals. The investigations performed included detailed mapping of ferroelectric domains, recording local piezoelectric hysteresis loops (all with a lateral resolution down to 10 nm) and study of the propagation of the domain walls and their relaxation after electrical excitation (as a function of temperature and sample depth). As was demonstrated in this thesis, PFM offers unique opportunities for studying relaxor ferroelectrics that cannot be done by any other techniques. Besides, for a better understanding of the microscopic mechanism involved in relaxors we also developed new multiscale approaches and methodologies that might be transferred to other complex and inhomogeneous systems involving nano- and meso-scale investigations. The measurements were complemented by several nanoscale methods (such as SEM and TEM) and by traditional macroscopic electrical techniques. As a result of this dissertation, valuable information necessary for the understanding of the fundamental processes underlying the relaxor nature was uncovered and many novel phenomena were discovered for the first time in this work.

The following conclusions can be drawn from the thesis:

PLZT x/65/35 Ceramics

- PLZT 6÷11/65/35 ceramics obtained by various methods were tested by the conventional dielectric spectroscopy and ferroelectric measurements. It was confirmed that addition of La shifts the dielectric maximum T_m lo lower temperatures (T_m = 390, 335 and 300 K for 8, 9.75 and 13/65/35, respectively), and increases the dielectric constant to (21000, 5500 and 1700 for 8, 9.75 and 13/65/35, respectively). These measurements confirmed high quality of ceramics and are in line with previous reports on this material.

- The first reliable measurements of the domain structures in PLZT 5÷13/65/35 ceramics were performed. A gradual decrease in domain size and, finally, the appearance of "labyrinth-type" domain structures was documented as a direct consequence of local disorder quantified via autocorrelation analysis. This was attested to La doping that weakens the coupling between the ferroelectrically active oxygen octahedral leading to a progressive domain splitting and randomization. PLZT ceramics with high concentration of La (>9 at.%) preserve the domain contrast at the nanoscale, even if the macroscopic properties do not exhibit any ferroelectricity. It was found that for the relaxor PLZT ceramics the images of the autocorrelation function are regular in two different directions revealing the local rhombohedral (rather than cubic) symmetry.
- Random network of nanopolar patterns in PLZT relaxors was investigated as a function of temperature in order to follow the evolution of polarization clusters while approaching Burns temperature. This lead to the conclusion that the local phase transition temperature at the relaxor surface is higher than in the bulk (43 K for 8/65/35 and 26 K for 9.5/65/35 compositions) in accordance with previous x-ray results. The correlation length was found to decrease gradually with temperature being 170 nm (8/65/35) and 120 nm (9.5/65/35). Local polarization persists up to 200 ºC at the surface (i.e. 100 ºC higher than the macroscopic one) in PLZT 9.5/65/35. The fractal dimension close to 1.8 is consistent with the random distribution of charge defects pinning polarization in this material. Such local polarization might be the signature of the recently discovered T^* temperature which corresponds to the nucleation of static Polar NanoRegions (PNRs).
- An origin of macroscopic grain size effect in PLZT observed as early as in 70s was uncovered by PFM. It is shown in this work that the degree of disorder in PLZT varies as a function of the local position inside the grain. The polarization correlation length decreases while approaching to grain boundaries and gradually diminishes by decreasing the grain size. The variation of the correlation length is attributed either to the mechanical stress arising upon cooling the ceramics from the sintering temperature or to the La gradient across the grain. Indeed by replacing the Pb-lone pair, La ions

affect drastically the polarization and its correlation. This finding explains the grain size effect on the macroscopic dielectric constant and polarization in PLZT.

- It was found that relaxation of local polarization in PLZT is described by stretched exponential time dependence with parameters strongly varying with La content.
- The lateral domain growth in the AFM tip-generated electric field was for the first time studied by PFM. Our studies demonstrate that lateral domain wall motion in ferroelectric relaxors is a creep process, governed by a characteristic dynamical exponent μ close to 0.25 for PLZT 9.5/65/35. These studies combined with the measurements of domain wall roughness lead to the conclusion that the domain walls in PLZT are quasi one-dimensional.
- Local 2D FFT analysis in PLZT was done by PFM and it was possible to map the important parameters of relaxor ferroelectrics such as correlation length, local polarization, and crystallographic quality as a function of the position.

PZN-4.5%PT Single Crystals

- For both (100) and (111) orientations, irregular domain patterns with the typical sizes 20-200 nm were observed in the mixed ferroelectric-relaxor PZN-4.5%PT. For (100)-oriented crystals typical dimensions of domain structure are one order of magnitude smaller than the (111)-oriented single crystals; [111]-direction corresponding to the main polar axis of PZN-4.5%PT at room temperature.
- Evolution of the domain structures and hysteresis in PZN-4.5%PT was studied as a function of temperature. The intensity of piezoresponse decreases with temperature and finally disappears at 160 ºC for (111) orientation while for (100) orientation still some nanodomains persist up to 200 ºC which is far above.the temperature of the ferroelectric phase transitions. It is suggested (as in case of PLZT) that such nanodomains correspond to the static PNRs appearing at T^* (~500K). Interestingly, we revealed that (100) orientation is a peculiar direction in relaxor as was suggested by previous reports. Based on our findings we proposed to describe PZN-4.5%PT as composed of rhombohedral like domain with some embedded tetragonal

nanodomains. Such microscopic picture allowed us to explain the macroscopic piezoresponses or relaxor-based systems. Indeed, as some tetragonal nuclei already exist in these relaxors they can serve as embryos for favoring the easy switching from [111]-rhombohedral macroscopic polarization towards the tetragonal [001] direction.

- ZFC and FCZFH regimes were reproduced in (111) oriented PZN-4.5%PT crystals. They show that the irregular mesoscale domain structure can be "erased" by heating but smaller nanoscale irregular domains still exist. Such experiment allowed us to reveal the effect of the surface and especially pinning by surface defects. Electrically induced polarization on the "cleaned" surfaces relaxes with the characteristic relaxation time of several hours obeying stretched exponential time dependence.
- We demonstrated that 3D domain imaging is possible by cross-sectioning (repeated polishing) of ferroelectric material (similar to AFM tomography). Domain branching is observed and explained by the appearance of inverse domains to compensate the depolarizing field (Marchenko's model).
- Domain structure and hysteresis loops were studied in PZN-x%PT (x>7%) single crystals of (111) orientations. It was found that the domain structure becomes more regular with increasing PT content reflecting ferroelectric ordering. However and interestingly, nanodomains are still present through the morphotropic phase boundary region and until the expected "normal" ferroelectric PZN-12% compound. Offset of the hysteresis loops might be an indication of the presence of such nanodomains. Indeed, the piezoelectric offset was found to gradually decrease with increasing PT content.

PMN and PMN-xPT Single Crystals

- Domain structures and time- and bias- controlled local polarization dynamics in the PMN–xPT family of relaxor ferroelectrics were studied in detail using PFM and PFS (switching spectroscopy). The PFM imaging indicates the presence of labyrinthine domain structures even in ergodic PMN-10%PT compositions, indicative of a non-cubic symmetry at least in the surface layer. PMN-32%PT demonstrates the coexistence of ferroelectric and labyrinthine domains. In PMN-35%PT, ferroelectric

domains with high wall roughness are observed with nanodomains embedded within these domains as observed in case of PZN-PT solid solution. The comparison of vertical and lateral PFM suggests that the observed in-plane contrast can be ascribed purely to cross-talk between vertical and lateral signals and no evidence for in-plane domains is obtained.

- The dependence of relaxation behavior on the pulse amplitude and time was found to follow a universal logarithmic behavior with a nearly constant slope. This behavior is indicative of the progressive population of high energy slow relaxation states, as opposed to the linear relaxation in the presence of a broad relaxation time spectrum. The contribution of ferroelectric non-linearity and spatial dispersion of the tip field to the relaxation is analyzed in detail, and the effects of spatial dispersion are shown to be relatively small. Hence, PFM based relaxation experiments provide information similar to that in a uniform field.
- The relationship between relaxation and hysteresis loop formation is analyzed in detail. It is shown that local hysteresis loops in relaxors are fundamentally different from those in ferroelectrics. In relaxors (PMN-10%PT), the local loops are kinetically limited, while in "normal" ferroelectrics (PMN-32%PT and PMN-35%PT) the loops seem to be dominated by the spatial dispersion of the polarization only. Finally, switching spectroscopy mapping of relaxor and ferroelectric PMN-PT compositions is performed, and the mapping of built-in fields and the stability gap is demonstrated.
- The PFM contrast and hysteresis were observed for the first time in pure PMN crystals and their evolution with electric field and time were performed. We developed a simple methodology to extract the real correlation length revealing a PNR average size of 10-15 nm which reconciles the correlation length observed by PFM measurements and that determined using neutron of x-ray diffraction techniques.

§ 5.2 Recommendation of Future Work

The results obtained in this thesis emerged due to the systematic examination of the nanoscale properties of PLZT ceramics, PZN-PT, PMN and PMN-PT single crystals by using

several nanoscale methods (e.g., PFM, PFS and SEM). Further studies regarding these materials are required to answer some unsolved questions in this work. Accordingly, the future work should be focused on the following issues.

- The variation of the correlation length is tentatively attributed either to the mechanical stress arising upon cooling the ceramics from the sintering temperature or to the La gradient across the grain. Other local techniques such as Electron Energy Loss Spectroscopy (EELS) should be used to choose between these possibilities.
- Dynamic PFM modes (i.e. measurements at higher frequencies) and high-resolution imaging should be both used to identify the origin of the switchable polarization component existing at the relaxor surface.
- Temperature-dependent measurements should be extended to cryotemperatures in order to undertsand the behavior of nanodomains close to freezing point and spontaneous relaxor-ferroelectric phase transition.

List of Publications of the Thesis

Book Chapters and Reviews:

1. V.V. Shvartsman, W. Kleemann, **D. A. Kiselev**, I.K. Bdikin, and A.L. Kholkin, "Polar structures in relaxors by piezoresponse force microscopy" in *Scanning Probe Microscopy of Functional Materials*, S.V. Kalinin and A. Gruverman (eds.), Springer Science + Business Media (*in press*).

2. A. L. Kholkin, I. K. Bdikin, **D. A. Kiselev**, V. V. Shvartsman, S.-H. Kim, "Nanoscale piezoelectric characterization of polycrystalline ferroelectrics" *Journal of Electroceramics* **19**, 81-94 (2007).

3. A.L. Kholkin, V.V. Shvartsman, **D.A. Kiselev**, I.K. Bdikin "Nanoscale characterization of ferroelectric materials for piezoelectric applications" *Ferroelectrics* **341**, 3-19 (2006).

Journal Papers:

1. A. L. Kholkin, A.N. Morozovska, **D. A. Kiselev**, I. K. Bdikin, B.J. Rodriguez, P. Wu, A. Bokov, Z. Ye, B. Dkhil, L.Q. Chen, M. Kosec, S.V. Kalinin, "Surface domain structures and mesoscopic phase transition in ferroelectrics relaxors", *Adv. Func. Mat. (submitted)*.

2. **D.A. Kiselev**, I.K. Bdikin, N.A. Pertsev, M. Kosec, and A.L. Kholkin, "Quasi-one-dimensional domain walls in ferroelectric ceramics: Evidence from domain dynamics and wall roughness measurements" *Nanotechnology* (*submitted*).

3. A.L. Kholkin, **D.A. Kiselev**, I.K. Bdikin, A. Sternberg, B. Dkhil, S. Jesse, O. Ovchinnikov, S. V. Kalinin "Mapping Disorder in Polycrystalline Relaxors: a Piezoresponse Force Microscopy Approach" *Special Issue of Materials "Advances in Ferroelectrics & Piezoelectric Materials*, *Materials* **3**, 4860 (2010).

4. B. J. Rodriguez, S. Jesse, A. N. Morozovska, S. V. Svechnikov, **D. A. Kiselev**, A. L. Kholkin, A. A. Bokov, Z.-G. Ye, S. V. Kalinin, "Real space mapping of polarization dynamics and hysteresis loop formation in relaxor-ferroelectric PMN-PT solid solutions" *J. Appl. Phys.* **108**, 042006-1 (2010).

5. A.A. Bogomolov, A.V. Solnyshkin, A.Yu Lasarev, **D.A. Kiselev**, A. L. Kholkin, "Polarization of surface layer in PLZT relaxor ceramics" *Ferroelectrics* **374**, 144 (2008).

6. N. Pertsev, A. Petraru, I. Bdikin, **D. A. Kiselev**, A. L. Kholkin**,** "Dynamics of ferroelectrics domains in $BaTiO_3$ ferroelectric thin films via Piezoresponse Force Microscopy" *Nanotechnology* **19**, 375703 (2008).

7. **D. A. Kiselev**, I. K. Bdikin, E. K. Selezneva, K. Bormanis, A. Sternbergand and A. L. Kholkin "Grain size effect and local disorder in polycrystalline relaxors via scanning probe microscopy" *J. Phys. D: Appl. Phys*. **40**, 7109-7112 (2007).

8. V. V. Shvartsman, A. L. Kholkin, A.N. Orlova, **D. A. Kiselev**, A. A. Bogomolov, A. Sternberg "Polar nanodomains and local ferroelectric phenomena in relaxor lead lanthanum zirconate titanate ceramics" *Appl. Phys*. *Lett* **86**, 202907 (2005).